4-14-2020 2:30 PM

Characterization of Impact Melt Rocks and Hydrothermal Mineralization at the Haughton Impact Structure, Devon Island, Canada: An Investigation of Impacts into Carbonate Targets

Cassandra L. Marion, *The University of Western Ontario*

Supervisor: Osinski, Gordon R., *The University of Western Ontario*
Co-Supervisor: Linnen, Robert L., *The University of Western Ontario*
A thesis submitted in partial fulfillment of the requirements for the Doctor of Philosophy degree in Geology
© Cassandra L. Marion 2020

Recommended Citation

Abstract

Impact cratering is a fundamental and ubiquitous geological process on all solid planetary bodies in our solar system. Impacts into carbonate-rich sedimentary target rocks on Earth are still poorly understood. The fate of carbonates during impact, in particular whether they undergo melting or decomposition, is actively debated. The dominant process is significant as decomposition would cause severe climatic effects due to release of large amounts of carbon dioxide into the atmosphere. At the root of the problem is the difficulty to distinguish and characterize the genesis of the variety of impactite carbonates produced. The Haughton impact structure in the Canadian High Arctic was formed in the Paleozoic Arctic Platform which overlies Precambrian metamorphic rocks. In order to better understand impactite formation and hydrothermal mineralization in impacts into calcareous targets, this study conducts a thorough investigation and characterization of the impactites and mineralization at the centre and around the central uplift periphery at Haughton. A variety of petrographic, geochemical and mineralogical techniques are applied to characterize the rocks, including microbeam analysis and cathodoluminescence. Recent shallow drill cores at the centre of structure reveal melt rocks unlike those previously identified at Haughton. The first, is a crystalline carbonate-sulfate-silicate melt rock classified based on a series of igneous textures. The second, is a silicate impact melt rock. Both cores are pervasively hydrothermally altered. Finally, we re-evaluate the hydrothermal mineralization at the centre and periphery within the cores and faulted target rocks. Overall this work confirms the presence of crystalline carbonate melt rocks at Haughton; presents detailed methodologies on how to distinguish between a wide range of carbonate and sulfate impactite products, hydrothermal replacement and diagenetic carbonate; presents an updated hydrothermal model and paragenesis for mineralization at the centre of the structure; and confirms impacts into mixed targets produce heterogeneous impactites and hydrothermal mineralization.

Keywords

Summary for Lay Audience

Impact cratering is the process through which a projectile from space, such as an asteroid, impacts the surface of a planetary body like Earth. Impacts into igneous or metamorphic rocks such as granite or gneiss, are well understood. Impacts into sedimentary rocks, particularly those rich in volatiles such as carbonate and sulfate, however, are less well understood. Whether these carbonate rocks melt or break down into a carbon dioxide and lime, for example, as a result of the impact is actively debated. The principal challenge lies both in the difficulty to recognize and distinguish between the different carbonate and sulfate rocks produced or altered; and the lack of detailed studies at impact craters hosted in carbonate- or sulfate-rich rocks. The Haughton impact structure in the Canadian High Arctic was formed in a mixture of carbonate- and sulfate-rich rocks from the Paleozoic Arctic Platform and metamorphic rocks. In order to better understand impacts into carbonate-rich targets, this study conducts a thorough investigation and characterization of the rocks from the centre of the Haughton impact and new minerals formed by heated circulating fluids generated by the impact (a.k.a. hydrothermal minerals). A variety of petrographic, geochemical and mineralogical techniques are applied to characterize the rocks. Recent shallow drill cores at the centre of structure reveal two new melt rocks unlike those previously identified at Haughton. The first, is a mixed crystalline carbonate-sulfate-silicate melt rock classified based on a series of textures. The second, is a silicate impact melt rock. Both cores are pervasively hydrothermally altered. Finally, we re-evaluate and create a new model for hydrothermal mineralization within the structure. This study confirms the presence of carbonate impact melt rocks at Haughton; presents detailed methods on how to distinguish between a wide range of pre-, syn- and post-impact carbonate and sulfate products; presents an updated hydrothermal model for mineralization at the centre of the structure; and confirms impacts into mixed types of rocks result in diverse crater deposits and varied mineralization.

Co-Authorship Statement

This thesis is divided into five chapters, three of which are in manuscript format. Chapter 1 is an introduction to the thesis and literature review on the relevant thesis topic. Dr. Osinski and Dr. Linnen assisted in editing this section. Chapter 2 was submitted to the journal Geology in 2018 and will soon be re-submitted. This manuscript, in addition to the yet to be published Chapter 3 were researched and written by C.L. Marion, as well as doctoral supervisors Gordon R. Osinski and Robert L. Linnen who provided critical feedback and ed12its. It also includes collaborators Richard A. F. Grieve, William Zylberman, Pierre Rochette, Yoann Quesnel, Jérôme Gattaccecca and Roberta Flemming. Dr. Grieve assisted with textural interpretations; Dr. Flemming directed XRD analysis; Dr. Zylberman recently published an article on the geophysics of this new lithology, Zylberman et al. (2017) and the remaining authors are part of the geophysics team that conducted the drilling operations in the field and geophysical ground surveys at Haughton, see Quesnel et al. (2013). Chapter 4 is yet to be submitted for publication; it was researched and written by C.L. Marion under the supervision of, and co-authored by G.R.Osinski and R.L.Linnen. Nigel Blamey completed the quantitative gas analysis on hydrothermal quartz.

Acknowledgments

To our friends and forever neighbours the Thorpes, thank you for being our London family, and supporting us in all things. You mean the world to us!

Finally, to my thesis examiners, thank you in advance for taking the time to read and provide constructive feedback on this work. Greatly appreciate it!

Land Acknowledgment

I acknowledge that Western University is located on the traditional lands of the Anishinaabek, Haudenosaunee, Lūnaapéewak and Attawandaron peoples, on lands connected with the London Township and Sombra Treaties of 1796 and the Dish with One Spoon Covenant Wampum. This land continues to be home to diverse Indigenous peoples (e.g. First Nations, Métis and Inuit) whom we recognize and thank as contemporary stewards of the land.

Table of Contents

List of Tables

List of Figures

Figure 2.2 A) Cross section of the F2 core. B-E, G-I, and L are backscattered electron photomicrographs whereas K-L are panchromatic cathodoluminescence maps of the F2 core: B) Porphyritic silicate groundmass altered to Mg-rich clay minerals; C) Partially digested K-feldspar clast within silicate groundmass; D) A jellybean-shaped silicate corona on relict clast, now replaced with calcite. This relict clast is embedded within a groundmass containing acicular silicate-calcite intergrowth shoen in the inset and Figure A.2; E) Garnet clast with reaction rim hosted within calcite groundmass; F) Acicular silicate crystals intergrown within anhydrite groundmass; G) Radial acicular or spherulitic calcite and altered silicate hosted in calcite; H) Radial acicular calcite and dendritic Mg -silicate hosted in calcite; I) Porous calcite core overgrown with non-porous calcite and porousring-like flow in adjacent grain; J) Clast boundary (far right) showing wormy to vermicular intergrowth textures that suggest emulsionbetween silicate and carbonate melts, porous calcite (bright CL), sulfur-rich calcite overgrowth and sulfur poor overgrowth in contact with anhydrite (far left); K) Evolution of calcite crystallization: small crystals with silicate coronas closest to the silicate clast contact, followed by resorption features, oscillatory zoned calcite, porous calcite with some sulfate amygdules, terminated by sulfur-rich calcite overgrowth (dark CL), all of which hosted in sulfate groundmass. Note also the radial

List of Appendices

List of abbreviations

ASD   Analytical Spectral Devices Inc.

BSE   backscattered electron

CRISM   Compact Reconnaissance Imaging Spectrometer for Mars

CL   cathodoluminescence

D   partition coefficient

EDS   energy-dispersive spectrometry

EPMA/EMPA   electron microprobe analysis

EVA   DIFFRAC PLUS Evaluation software

GADDS   General Area Detector Diffraction System

gl   glass

ICDD   International Center for Diffraction Data

OMEGA   Visible and Infrared Mineralogical Mapping Spectrometer (Observatoire pour la Minéralogie, l'Eau, les Glaces et l'Activité

NIR   near-infrared

NRM   natural remanent magnetization

REE   rare earth elements

SE   secondary electron

SWIR   short-wavelength infrared

USGS   United States Geological Survey

μXRD   micro X-ray diffraction

VNIR   visible near-infrared

Vis-NIR   visible and near-infrared

vol%   volume percent

WDS   wavelength-dispersive spectrometry

XRD   X-ray diffration

wt%   weight percent

List of Minerals and Formulas

Mineral	Abbreviation	Formula
Actinolite	Act	$Ca_2(Mg,Fe)_5Si_8O_{22}(OH)_2$
Anhydrite	An	$Ca(SO_4)$
Apatite	Ap	$Ca_5(PO_4)^3(OH)_{0.33}F_{0.33}Cl_{0.33}$
Barite	Ba	$Ba(SO_4)$
Bassanite	Bas	$2CaSO4 \cdot H2O$
Biotite	Bt	$KMg_{2.5}Fe_{0.5}AlSi_3O_{10}(OH)_{1.75}F_{0.25}$
Calcite	Cal	$Ca(CO_3)$
Celestite	Cls	$Sr(SO_4)$
Chlorite (clinochlore)	Chl (Ccl)	$(Mg,Fe)_5Si_3Al_2O_{10}(OH)_8$ (variable)
Chalcopyrite	Chc	$CuFeS_2$
Copiapite	Cpp	$Fe_5(SO_4)_6(OH)_2 \bullet 20(H_2O)$
Diopside	Di	$CaMg(Si_2O_6)$
Dolomite	Dol	$CaMg(CO_3)_2$
Epidote	Ep	$Ca_2(Fe,Al)Al_2(SiO_4)(Si_2O_7)O(OH)$
Fibroferrite	Ff	$Fe(SO_4)(OH) \bullet 5(H_2O)$
Fluorite	Fl	CaF_2
Goethite	Geo	$FeO(OH)$
Gypsum	Gyp	$Ca(SO_4) \bullet 2(H_2O)$
Illite	Ill	$(K,H_3O)(Al,Mg,Fe)_2(Si,Al)_4O_{10}[(OH)_2,(H_2O)]$
Jarosite	Jar	$KFe_3(SO_4)_2(OH)_6$
Magnesite	Mgs	$Mg(CO_3)$
Magnetite	Mt	Fe_3O_4
Marcasite	Mrc	FeS_2
Melanterite	Mel	$Fe(SO_4) \bullet 7(H_2O)$
Montmorillonite	Mont, Mm	$Na_{0.2}Ca_{0.1}Al_2Si_4O_{10}(OH)_2(H_2O)_{10}$
Forsterite (Olivine)	Fo (Ol)	$Mg_2(SiO_4)$
Pyrite	Py	FeS_2
Quartz	Qtz	SiO_2

Rozenite	Rz	$Fe(SO_4) \cdot 4(H_2O)$
Saponite	Sap	$(Ca/2,Na)_{0.3}(Mg,Fe^{++})_3(Si,Al)_4O_{10}(OH)_2 \cdot 4(H_2O)$
Sepiolite	Sep	$Mg_4Si_6O_{15} \cdot 6(H_2O)$
Serpentine (lizardite, antigorite, chrysotile)	Sp	$Mg_3Si_2O_5(OH)_4$
Szomolnokite	Szo	$Fe(SO_4) \cdot (H_2O)$
Talc	Tlc	$Mg_3Si_4O_{10}(OH)_2$
Titanite	Tit	$CaTiSiO_5$
Zircon	Zr	$ZrSiO_4$

Formulas acquired from webmineral.com

Chapter 1

1   Introduction

An impact crater is a circular depression with a raised rim caused by the collision of a celestial body. Impact cratering is a ubiquitous process which occurs on all solid planetary surfaces in our solar system. It is an essential part of the history of the accretion and geological evolution of the Earth, Moon and Solar System as a whole. Impact cratering has also played a significant role in the biological evolution of the Earth (Alvarez et al., 1980). While impacts on other planetary bodies are well-preserved, the physical markers of Earth's impacts are subjected to tectonics, volcanism and erosion. Even so, terrestrial craters remain our primary source to ground-truth the processes and products produced during impact. Where the crater morphology has been altered by geological processes, as is generally the case on Earth, it is referred to as an impact 'structure'. Much has been learned about cratering processes and their resulting products (French, 1998; Osinski and Pierazzo, 2013); but much remains to be understood, particularly for impacts into carbonate-rich sedimentary targets.

1.1   Impact Crater Formation

The formation of an impact crater is a high energy event that occurs over the span of a few seconds to minutes. Impact crater formation has been divided and organized into three distinct but overlapping stages: 1) contact and compression; 2) excavation; and 3) modification (Gault et al., 1968; Melosh, 1989), as summarized below (Fig. 1.1). These stages are followed by a post-formational final stage of hydrothermal alteration (Kieffer and Simonds, 1980; Kirsimäe and Osinski, 2013) described further in section 1.3.

Beginning with the contact and compression stage, a projectile, i.e., an asteroid or comet, makes contact and collides with another planetary body. The kinetic energy of the projectile, one with a large enough mass and hypervelocity (>11 km/s for Earth) (French, 1998), is transferred into the target to produce high pressure shock waves (>100 GPa) (Fig. 1.1a). The shock waves travel radially into the target from the point of impact as well as upwards back into the projectile.

Once the shock waves reach the free upper surface of the projectile, they are reflected back as rarefaction waves (Ahrens and O'Keefe, 1972). These rarefaction waves, also known as tensional or decompression waves, result in unloading from high pressures (Melosh, 1989). Under these conditions, the target rocks are set in motion (excavation stage), fractured, brecciated, melted, vapourized and metamorphosed (Ahrens and O'Keefe, 1972; Grieve et al., 1977; Melosh, 1989). The projectile itself is commonly completely melted and/or vapourized. The end of this stage is marked by the complete unloading of the projectile (Melosh, 1989).

The excavation stage, as the name denotes, opens up and excavates the crater. The shock waves propagate hemispherically into the target from the depth of penetration of the projectile. This accelerates the target material radially in an outward trajectory, whereas the rarefaction waves generally propagate downward. The complex interaction between these waves creates an excavation flow field that results in the formation of a transient cavity (Dence, 1968). The excavation flow lines unearth material from the upper third to half of the transient cavity (Grieve, 1987), termed the 'excavated zone' and displace material in the lower half, termed the 'displacement zone' (Melosh, 1989; Stöffler and Gault, 1975) (Fig. 1.1b). Material in the excavated zone is ejected ballistically beyond the transient cavity rim to form the continuous ejecta blanket (Oberbeck, 1975). The ejecta consists of a wide range of lithologies and shock levels including melted material as it is sourced from the full range of shock pressure contours. It may also be emplaced as melt-rich flows during the later stages of crater formation (Osinski et al., 2011). In simple impact structures, the final crater rim and transient cavity rim are generally one and the same. However, in complex craters the transient cavity is typically unrecognizable as a result of the modification stage. Here the ejecta are present within the inner crater rim region of the structure as well as outside the final crater rim (Osinski et al., 2013; Osinski et al., 2011). A series of displaced material remain within the transient cavity, but the excavation stage ends when there is no longer enough energy to continue to transport material outwards (French, 1998; Osinski and Pierazzo, 2013), and the maximum crater diameter has been reached (Melosh and Ivanov, 1999).

The modification stage begins as the force of gravity takes over (Figs. 1.1c - 1.1e). The effects depend on the size of the structure and the lithological properties of the target rocks (Melosh and Ivanov, 1999). On Earth, simple craters are bowl like structures smaller than 2 to 4

kms in diameter where very minor modification occurs. In larger impacts, those over ~2 km in diameter for sedimentary targets and ~4 km for crystalline targets, a complex impact structure is formed. The transition diameter on other planetary bodies increases with decreasing acceleration of gravity (Melosh, 1989). Complex craters are characterized by an uplifted crater floor that formed a central uplift and collapsed crater rim walls wherein fault-bounded blocks have moved inward and downward forming terraces. The resulting impact structure has final crater diameter significantly larger than that of the original transient cavity. Impact structures will be forever modified by common geological processes such as tectonics and erosion; therefore the modification stage has no marked end.

a CONTACT/COMPRESSION STAGE

Ballistic ejecta
Rarefraction (release wave)
Shock wave

b EXCAVATION STAGE

Displaced zone (allochthonous target rocks and melt)
Excavated zone
Ballistic ejecta
Transient cavity
Displaced zone (autochthonous target rocks)

c END EXCAVATION STAGE/ START TECTONIC MODIFICATION STAGE

Lining of melt and clasts (proto crater-fill deposits)
Ballistic ejecta
Uplift of crater floor
Displaced zone (autochthonous target rocks)

d TECTONIC MODIFICATION STAGE

Ballistic ejecta
Flow of melt and clasts off oversteepened central upift
Gravitational collapse of crater walls

e END OF TECTONIC MODIFICATION STAGE

Impact melt-bearing impactites emplaced as flows
Ballistic ejecta
Final crater rim
Crater-fill impactites
Central Uplift
Listric extensional faults

Figure 1.1 Schematic diagram showing the formation of a complex impact structure beginning with a) the contact and compression stage; b) the excavation stage; c) end of the excavation stage; d) modification stage; and e) end of the modification stage. Modified from Osinski et al. (2011).

1.2 Shock metamorphism and impactites

Impactite is a term used to describe all rocks that have been affected by a hypervelocity impact event (Stöffler and Grieve, 2007). The physical movement and shock metamorphism of the target rocks during crater formation result in significant phase changes as well as mixing of all the target lithologies. These impactites can range from fractured, brecciated, and melted material deposited both within and outside the structure. At the point of impact, the target rocks are subjected to the highest shock pressures, which decrease radially away from the point of impact. At low shock levels (<5 GPa), the target is simply fractured and brecciated. As pressures increase, there may be a variety of shock effects, wherein each rock and mineral type tend to react differently. In general, shock metamorphic features occur as follows: planar fractures and shatter cones (~5-7 GPa); planar deformation features and high pressure polymorphs such as stishovite and coesite (~10-30 GPa); diaplectic glass and partial melting (~35-45 GPa); loss of diaplectic glass,planar features and flow features (~45-55 GPa); whole rock melting and glasses (>60 GPa); and finally vapourization (>100 GPa) (Stöffler et al., 2018a; Stöffler and Grieve, 2007).

An impactite classification scheme recommended by the IUGS by Stöffler and Grieve (2007) is illustrated in Figure 1.2. The classification is largely based on the physical properties of the lithologies as well as the extent to which they have been displaced from their original pre-impact locations, and their current location. The typical stratigraphy of crater-fill impactites occurs from bottom to top as unshocked to shocked autochthonous and parautochthonous fractured rocks and faulted blocks; parautochthonous and allochthonous monomict to polymict breccias overlain by impact melt rocks. Complications arise with this classification scheme, for example, it does not offer more detailed classification of the variety of impact melt rocks. Osinski et al. (2008) proposed a clarification to this classification scheme of impact melt-bearing impactites which

further describe the rocks by their textural characteristics including: phaneritic, aphanitic, vitric/glassy, vesicular, particulate and fragmental, as well as their clast content.
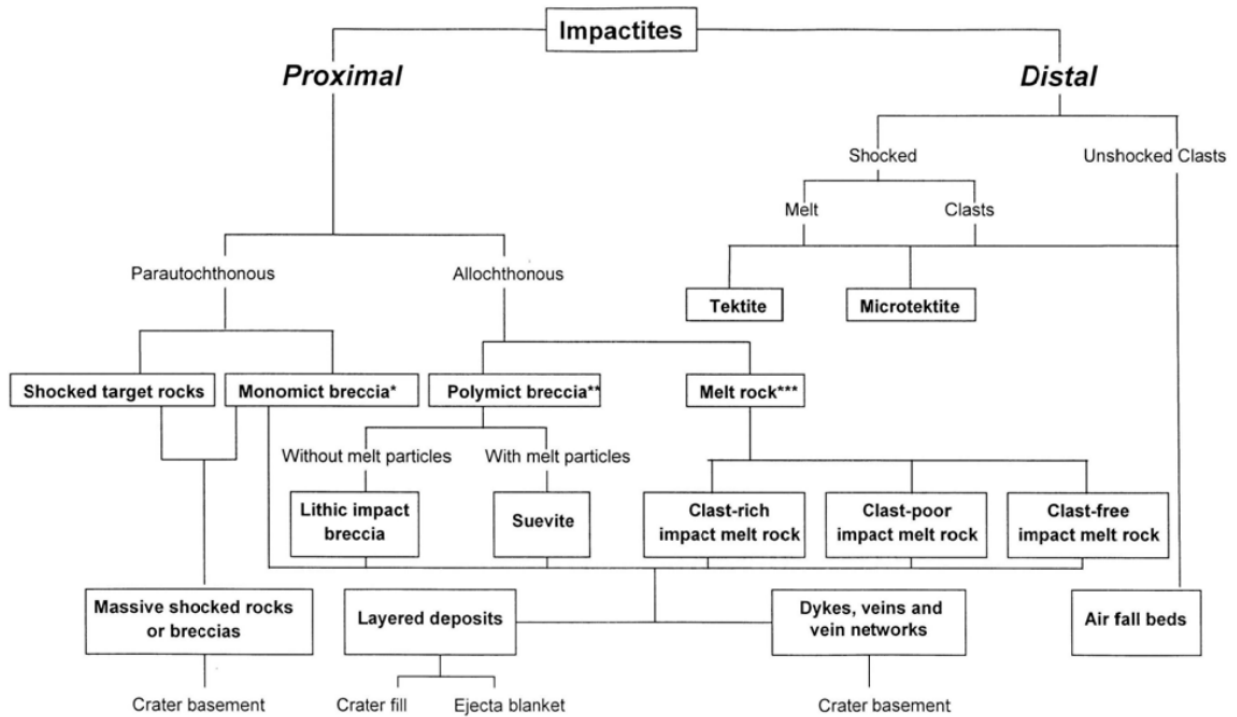
Figure 1.2 Stöffler and Grieve (2007)'s impactite classification scheme.

1.3 Impact-induced melting of sedimentary rocks: carbonates and sulfates

The range of products in impact structures set in dominantly sedimentary targets are still not well understood (see Osinski et al. (2008b) for a review). Impact melting results in a complex set of lithologies in any target, but even more so in dominantly sedimentary targets relative to impacts into crystalline targets. In a crystalline target, a thick coherent impact melt 'sheet', essentially a large volume of well-mixed silicate melt (or 'lava') would be emplaced overlying melt-bearing breccias; whereas in sedimentary and mixed targets, heterogeneous particulate impact melt and melt-bearing breccias are emplaced (Osinski et al., 2008b, 2008a). These impact melt rocks are not only texturally and chemically distinct from those in crystalline targets, but are

quite difficult to distinguish in situ from various types of melt-bearing ('suevite') and lithic breccias (Osinski et al., 2008). For this reason, it was proposed that less melt is formed in impacts into sedimentary targets than into crystalline targets of comparable size (Grieve and Cintala, 1992; Kieffer and Simonds, 1980). However, numerical modelling and field and analytical studies have shown this proposed difference in melt volume to be inaccurate (Osinski et al., 2008 and references therein; Pierazzo et al., 1997; Wünnemann et al., 2008).

Sedimentary rocks differ from crystalline rocks (igneous and metamorphic rocks) in many ways: 1) they are rich in volatiles such as H_2O in hydrous mineral phases, CO_2 in carbonates, and SO_x in evaporites; 2) they commonly have higher porosities; and 3) they have pre-existing structures such as layering etc. The response of carbonate and sulfate target rocks to meteorite impact continue to be debated (Langenhorst and Deutsch, 2012; Osinski et al., 2008b). The main point of debate rests on whether carbonates and sulfates decompose (e.g., $CaSO4_{(s)} \rightarrow CaO_{(s)} + SO_{2(g)} + 0.5O_{2(g)}$; $CaCO3_{(s)} \rightarrow CaO_{(s)} + CO_{2(g)}$; $CaMg(CO_3)_{2(s)} \rightarrow CaO_{(s)} + MgO_{(s)} + 2CO_{2(g)}$) and liberate CO_2 and SO_x species (Agrinier et al., 2001; Hörz et al., 2015; Kieffer and Simonds, 1980; O'Keefe and Ahrens, 1989; Pope et al., 1994) or whether they melt and crystallize to form carbonate-rich and/or sulfate-rich melt rocks (Graup, 1999; Hörz et al., 2015; Jones et al., 2000; Osinski et al., 2008b; Osinski and Spray, 2003, 2001; Walton et al., 2017, 2019). The amount of decomposition and devolatilization of CO_2 and SO_x is important in the context of atmospheric changes in composition and stability of the atmosphere as it directly impacts short and long term changes in climate and conditions for life (Alvarez et al., 1980; Artemieva and Morgan, 2017), see section 1.5.

Ivanov et al. (2004) re-evaluated the phase relationships of anhydrite and showed that it may either decompose (when released from pressures of 60 to 70 GPa) or melt (when released from pressures of 80 to 90 GPa). At the melting point of anhydrite (1738 K) at 1 atm, which is very close to the temperature of decomposition, the resulting products of decompression depend on whether the system is open or closed. In a closed system, the partial pressure of SO_2 suppresses decomposition, resulting in complete melting, whereas in an open system, a fraction of the anhydrite decomposes and a fraction melts (Ivanov et al., 2004).

Ivanov and Deutsch (2002) re-evaluated phase relationships for calcite during compression and decompression. Their results show that melting is the dominant response to impact into carbonate target rocks, whereas decomposition occurs strictly during the post-shock cooling. A recent in situ study of the Steen River impact identified post-impact carbonate decomposition as the result of thermal equilibration-related heating of carbonate clasts upon incorporation into hot impact breccias (Walton et al., 2019). The decomposition reaction of calcite may be shifted to the products or reactants depending primarily on the partial pressure of CO_2 and reaction kinetics (Agrinier et al., 2001; Hamann et al., 2018a; Ivanov and Deutsch, 2002). Preservation of carbonate impact melt is possible under the following conditions: small post-shock temperature differences and/or fast cooling and/or high pCO_2 and/or slow reaction kinetics (Hamann et al., 2018). Like anhydrite, carbonate melting and decomposition likely occur in parallel in an open system. It is also worth noting that both primary igneous carbonate and sulfate minerals have been observed in other geological settings, such as carbonatites (Jones et al., 2013).

1.4 Impact-generated Hydrothermal Systems

Hydrothermal circulation can develop where a source of heat, a porous and permeable medium and a reasonable amount of fluids are present (Naumov, 2005). In medium to large impacts, a hydrothermal system is generated post-impact wherein heated groundwater and pore waters circulate throughout the newly formed, porous and permeable structure and precipitate new minerals as it cools. The large volume of impact melted rocks and melt-rich breccias result in a thermal anomaly, and provide a heat source capable of causing convection of near-surface waters, inducing a hydrothermal system (Abramov and Kring, 2007). Additional sources of heat may be elevated geothermal gradients in the central uplifts of large impact structures and remnant energy deposited into the central uplift via the shock wave (Kirsimäe and Osinski, 2013).

The resulting hydrothermal mineralization is a direct product of the permeability and reactivity of impactite lithologies, which are controlled by target lithology and paleogeographic characteristics. The more varied the target rock composition, the more varied the secondary mineral phases (Naumov, 2005). Hydrothermal activity in the form of cavity and fracture-filling minerals and pervasive alteration of impactites has been observed in impact structures varying in

size from the 1.8 km Lonar Crater, India, to the ~250 km Sudbury structure, Canada (Kirsimäe and Osinski, 2013). Evidence of hydrothermal activity has been observed in ~40% of the 198 impact structures on Earth but less than 20 have been studied in detail (see Table 1-1).

Hydrothermal cooling and circulation histories vary with the size of impacts and the nature of the target rocks. Numerical modelling shows that in small to medium-sized craters (up to 30 km, a simple convective cell system develops in the most-heated central part of the crater as that region has the most gained heat from the impact melt-bearing crater-fill breccias. At depth, where permeability is decreased, heat is transported by conduction. As the heat source and volume of melted impactites is proportional to the size of the impact, and convection is the most effective form of heat transfer, cooling is much faster in smaller craters (Kirsimäe and Osinski, 2013). The lifetime of impact generated hydrothermal systems can be several hundred to many thousands of years long. The Sudbury structure is the best constrained case in which the hydrothermal system is known to have lasted up to 2 Ma (Ames et al., 1998).

The distribution and morphology of the mineralized localities are a function of porosity and permeability of the host rock and relationship to the thermal zones throughout the structure (Kirsimäe and Osinski, 2013). In sedimentary targets, porosity and permeability are higher than in their crystalline counterparts. Figure 1.3 illustrates many of the type-localities within a complex impact structure where hydrothermal mineralization may occur. These include: cavity and fracture fillings within crater-fill impact melt-bearing breccias and impact melt rocks; fractured target rocks in the interior and around the outer margin of the central uplift; along faults in the crater rim; ejecta deposits, and post-impact crater-fill deposits such as crater lake sediments (Osinski et al., 2013; Osinski et al., 2005a).

The composition of a hydrothermal fluid is a function of the fluid source(s) and host rock composition. To date, studies show the that dominant fluid sources in impact-generated systems originate from meteoric waters and/or seawater (Naumov, 2005). However, additional sources are possible, such as pore waters, deep formational brines, magmatic fluids from the impact melt sheet or decomposed volatiles, such as those in carbonate targets. Most trapped fluids are low to medium salinity (0–13%) aqueous fluids with rare $CaCl_2$–$NaCl$ species and low CO_2 gas phases (Kirsimäe et al., 2002a; Naumov, 2005). Mineralization in these systems typically corresponds

with an intermediate Ca-Mg or K-series alteration (metasomatism), based on temperature and dissolved species activities. Zoning of mineralization is controlled by the composition and nature of the hydrothermal fluids and the stage of the development of the hydrothermal system (Kirsimäe and Osinski, 2013).

As the system cools and fluid composition evolves, the resulting mineralization in any specific locality will vary. Overall however, there is a retrograde sequence of alteration minerals and it is common for multiple generations of hydrothermal minerals to be present (Osinski et al., 2013). The principal sequence of mineralization in a hydrothermal system follows several stages. The first is vapour-dominated during which silicate alteration occurs through reactions of infiltrating water with shocked silicates and silicate melt rocks to form Fe-Mg sheet silicates. This is followed by a vapour-liquid-dominated silicate mineralization brought on by dissolution of silicates and silica-rich metastable glasses to form iron smectites and zeolites (silicate targets). Lastly, there is a late stage of liquid-dominated carbonate-sulfide/iron-oxyhydrate mineralization. For example, mineral assemblages observed at the Kara, Popigai and Puchezh-Katunki structures indicate alteration at 50 - 350°C, and pH values of 6-8 (Jõeleht et al., 2005; Naumov, 2002; Versh et al., 2005). The precipitation of calcite and dolomite is controlled by the availability of Ca and Mg ions and may continue through the second to third stage. Previous studies suggest that the hydrothermal fluid composition and resulting alteration minerals evolve as the temperature of the fluids decreases with time (e.g. Naumov (2005)).

Most of the detailed work on hydrothermal mineralization has been completed at impact structures in dominantly crystalline target rocks, which results in formation of silicate-rich minerals. Only a few hydrothermal studies have been completed in carbonate-rich targets: the Lockne (Sturkell et al., 1998), Haughton (Osinski et al., 2005a, 2001), Ries (Muttik et al., 2008; Newsom et al., 1986; Osinski, 2005) and Chicxulub (Abramov and Kring, 2007; Ames et al., 2004; Hecht et al., 2004; Zürcher and Kring, 2004) impact structures. The main correlation observed when carbonates are present in the target, is a widespread association of calcite-quartz-sulfide mineralization (Naumov, 2005).

Hydrothermal systems in impact craters have many beneficial products and consequences, in particular, the production of economically viable natural resources (e.g. the formation of the Ni-

Cu-PGE deposits at the famous mining camp at the Sudbury impact structure, and the Pb-Zn deposits in the Siljan structure in Sweden (Reimold et al., 2005)). In addition, impact-generated hydrothermal systems can provide new habitats rich in nutrients for microbial communities and have potential implications for the origin and evolution of life on Earth, Mars and elsewhere in the Solar System.

Alteration indices and mass balance equations are common methods used to quantify alteration in a wide range of settings (Mathieu, 2018). In the case of impact structures like Haughton, quantifying alteration is a challenge as the precursor is a dynamic mixture of many rock types, and unaltered samples of breccia or impact melt rocks are not available for mass balance equations. Alteration indices have limited usability in impacts into alkali-poor rocks. Therefore, alteration interpretations are based dominantly on the minerals present, petrographic relationships and common alteration forming reactions.
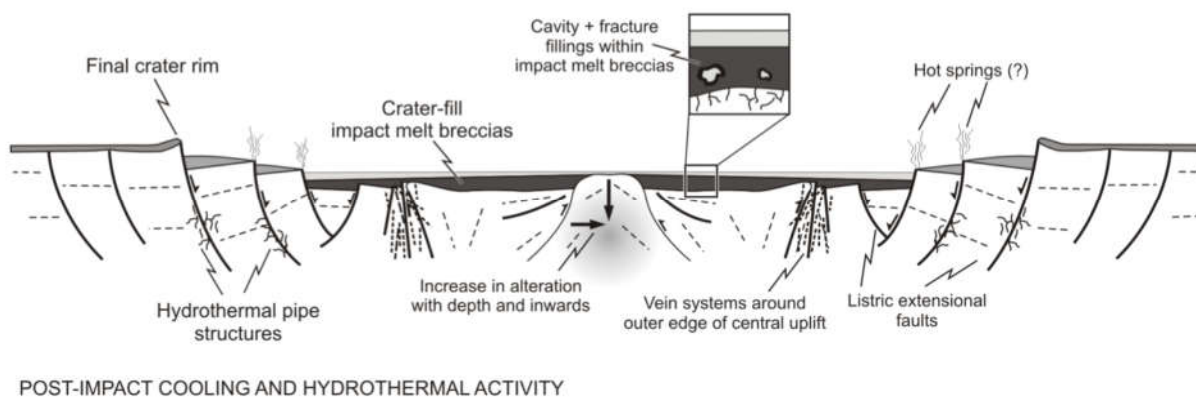
Figure 1.3 **Schematic cross-section of post-impact hydrothermal deposits, showing type localities of mineralization, modeled from the Haughton impact structure. Modified from (Osinski et al., 2005a).**

Table 1-1 Selection of studied impact structures with evidence of hydrothermal activity

Impact structure	Location	Diameter (km)	Target Rocks	Hydrothermal mineralogy	S.I. Studies	F.I. Studies
Lonar	India	1.8	Crystalline	Mont	-	-
Roter Kamm	Namibia	2.5	Crystalline	Qtz, Sulf, Chl, Ill, Ca	-	-
Kardla	Estonia	4	Mixed*	Chl, Corr, Hem, Sulf, Ill	X	X
Saaksajarvi	Finland	6	Crystalline	Ze, Chl, Qtz, Chc	-	X
Lockne	Sweden	7.5	Mixed*	Cc, Sulf, Ze, Qtz	X	X
Haughton	Nunavut, Canada	23	Mixed*	Cc, Qtz, Py, Marc, Fl, Ba, Gyp	X	X
Lappajarvi	Finland	23	Mixed*	Ze, Sm, Cc, Chl, Chc, Hem	X	-
Ries	Germany	24	Mixed*	Sm, Cc, Chl, Ze, Anh, Corr, Qtz, Ill	X	-
Tunnunik	NWT, Canada	28	Sedimentary*	Qtz, Cal, Dol, Marc	-	-
Manson	Iowa, USA	35	Mixed	Chl, Corr, Qtz, Sm, Ill, Grt, Act, Pyh, Ep, Za, Sulf	-	X
Carswell	Saskatchewan, Canada	39	Mixed*	Chl, Ill, Sulf, Ca, Hem, Coff, Pb, Qtz, Ze	-	X
Siljan	Sweden	52	Mixed*	Sm, Chl, Ze, Ep, Ab, Sulf, Hem	X	X
Charlevoix	Québec, Canada	54	Mixed*	Ze, Cc, Prh, Qtz, Chl, Sm	-	X
Kara	Russia	65	Mixed	Cc, Sulf, Ze, Apf, Ba, Sm, Op, Sm, Chl	X	
Puchezh-Katunki	Russia	80	Mixed	Sm, Ze, Chl, Anh, Cc, Sulf, Apf, Act, Op	X	-
Popigai	Russia	100	Crystalline	Sm, Cc, Anh, Chl, Ze, Prh, Grt, Gp, Sulf, Qtz, Ill, Act	X	-

| Chicxulub | Yucatan, Mexico | 170 | Mixed* | Kfds, Mag, Sm, Anh, Sulf, Chl, Py, Qtz, Ab, Mag, Ep, Cc | X | X |
| Sudbury | Ontario, Canada | 250 | Crystalline | Chl, Act, Sulf, Cc, Sm, Ep, Sph | - | - |

*Data compiled from Naumov (2005), Osinski et al. (2013) and Kirsimäe and Osinski (2012) and references therein in addition to the Impact Earth database. * Indicates the presence of carbonates. Abbreviations: S.I. = Stable Isotope; F.I. = fluid inclusion; Ab = albite; Act = actinolite; An = anatase; Anh = Anhydrite; Ba = barite; Cc = calcite; Chc = chalcopyrite; Chl = Chl; Ep = epidote; Fl = Fluorite; Hem = hemitite; Kfps = K-feldspar; Ill = Illite; Mag = magnetite; Marc = Marcasite; Mont = Montmorillonite; Qtz = quartz; Prh = prehnite; Pyh = pyrrohtite; Sm smectite; Sulf = sulfur; Sph = sphalerite; Ze = zeolite.*

1.5 Haughton Impact Structure

The ~23 km Haughton impact is a complex impact structure located on Devon Island, Nunavut in the Canadian High Arctic (Fig. 1.4). It was first suggested as a possible impact site by Dence (1972). The impact occurred into an ~1880 m thick sequence of Lower Paleozoic carbonate-rich sedimentary rocks of the Arctic Platform. These sedimentary rocks consist primarily of limestones, dolostones and interbedded gypsum, with minor shales and sandstones, which overly a Precambrian gneiss basement (Metzler et al., 1988; Thorsteinsson and Mayr, 1987). The impact has been dated by several studies that identified contradictory ages of ~22.4 - 23.5 Ma (Jessberger, 1988; Omar et al., 1987; Young et al., 2013) and ~39 Ma (Sherlock and Kelley, 2005). Since that time, DevonIsland has remained tectonically stable. It is a young well-preserved, well-exposed impact structure located in a remote Arctic desert. Consequently, it is an ideal case study and model for investigation of impact cratering processes and products in a carbonate-rich targets when most other structures are heavily eroded, buried, underwater or anthropogenically altered.

A number of studies have characterized the structure (Osinski and Spray, 2005; Robertson and Sweeney, 1983), impactite lithologies (Osinski et al., 2005c, 2005b; Osinski and Spray, 2003, 2001; H. J. Redeker and Stöffler, 1988), geophysical properties (Hajnal et al., 1988; Pohl et al., 1988; Quesnel et al., 2013; Zylberman et al., 2017) and astrobiological implications (Fike et al., 2002; Lacelle et al., 2009; Parnell et al., 2010b; Pontefract et al., 2012) at Haughton. The oldest rocks are exposed in the centre, surrounded by concentrically arranged fault-bounded blocks of progressively younger formations. The youngest exposed stratigraphic unit is the

Silurian-aged Allen Bay Formation, whereas the oldest unit present in the impactites deposits originates from the Precambrian crystalline basement. The Haughton impactites, in stratigraphic order, consist of parautochthonous target rocks, overlain by lithic monomict breccias, polymict breccias and finally pale grey allochthonous clast-rich particulate impact melt rocks. The latter is the dominant crater-fill impactite, which covers ~54 km^2 at the present-day and consists of a microcrystalline calcite-anhydrite-silicate glass groundmass with clast contents from all of the target lithologies (Osinski et al., 2005b, 2005c). In this same unit, evidence for melting of carbonates and sulfates has been identified (Osinski and Spray, 2003, 2001). Post-impact erosion and recent modification of the structure by glaciation and seasonal periglacial processes is evident. In the west-central region of the structure, crater-fill melt rocks are uncomformably overlain by Neogene lacustrine sediments of the post-impact Haughton Formation as well as Quaternary glacial and fluvial deposits (Osinski and Lee, 2005).

The hot impact melt rocks and breccias provided the main heat source for the post-impact hydrothermal system. Hydrothermal mineralization at Haughton was studied previously by Osinski et al. (2005a, 2001), and Parnell et al., (2010b), wherein the distribution and nature of the hydrothermal deposits were determined. Mineralization has been identified at several localities within the crater structure: as cavity fillings within impact melt breccias; as mineralized breccias around the margin of the central uplift; as veins and vugs around the margin of the central uplift, and as hydrothermal pipe structures and along faults in the crater-rim region (Fig. 1.3). The dominant hydrothermal minerals identified consist of calcite, selenite and marcasite with minor occurrences of quartz, goethite, celestite, barite, fluorite, pyrite and fibroferrite. Osinski et al., (2005c) proposed a three-stage model for the Haughton hydrothermal system based on micro-analytical techniques and fluid inclusions results. The early stage is a vapour-dominated regime generating temperatures >200°C in the near surface and two-phase vapour-liquid dominated regime at depth; followed by a main stage with temperatures ranging from 200-80°C, characterized by progressive cooling of the heat source and two-phase fluid inclusions; and finally, a late-stage liquid-dominated episode of cooling to below 80°C. Salinities calculated from fluid inclusions indicated a possible meteoric to surface water source for the hydrothermal fluids.
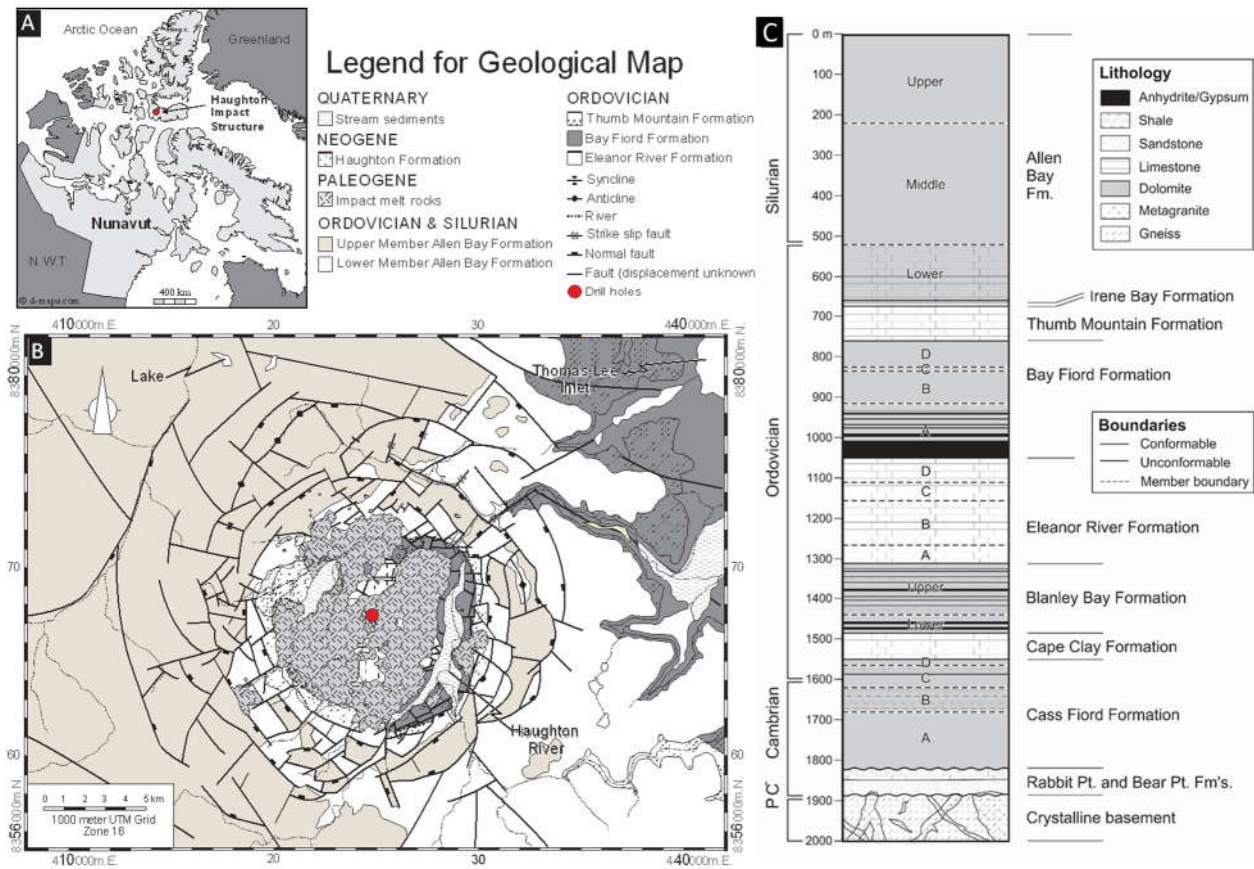
Figure 1.4 Location (A), geologic map (B), and stratigraphy of the target rocks (C), of the Haughton impact structure, on Devon Island in Nunavut, Canada, modified from Osinski et al. (2005c).

In an unpublished M.Sc. thesis, Auclair (2011) investigated stable carbon and oxygen isotopes in hydrothermal calcite from varying structural/stratigraphic localities at Haughton. Results indicate a strong depletion in heavy isotopes of carbon and oxygen relative to the target rocks, typical of a hydrothermal origin. Some distinctions were identified between mineralized localities and assemblages, interpreted as a function of the evolution of the fluid composition over time as well as local variations in temperature. Calcite veins showed the largest variations between localities and may be the best proxy for the fluid characterization. Comparatively, Martinez et al. (1994) investigated carbon and oxygen isotope compositions of shocked carbonates in the impact breccias and identified enriched ^{13}C values and slightly depleted [18]O

15

values relative to the target reference materials. The study concluded that this fractionation is a result of outgassing and disassociation of CO_2 followed by a fast back-reaction, combining CO_2 with residual oxides. However, experimental studies of this phenomenon show contradictory results, and suggest it is more likely that calcite melts in the early stages of impact, and decomposition may occur only later during post-shock cooling (Osinski et al., 2008 and references therein).

1.6 Post-impact effects of climate

Meteorite impact events have a wide range of devastating consequences from a local to global scale, depending on the size and energy of the event. In addition to the formation of the crater itself, there are catastrophic effects to the impacted region, such as emission of high levels of thermal radiation from the impact plume, hurricane force winds, wildfires, earthquakes, landslides and tsunamis (Bourgeois et al., 1988; Bralower et al., 1998; Kring, 2007; Melosh et al., 1990; Schulte et al., 2010). Small impacts tend to have localized effects, whereas large meteorite impacts have the potential to cause global devastation and mass extinctions, largely as a result of the massive amounts of rock debris and gases ejected into the atmosphere (Alvarez et al., 1980; Brugger et al., 2017; Pierazzo and Melosh, 2013).

The ~ 200 km Chicxulub impact in the Yucatàn Peninsula, Gulf of Mexico resulted in the ~66 Ma sudden global mass extinction of plant and animal life on Earth, including the non-avian dinosaurs (Pope et al., 1997; Renne et al., 2013; Schulte et al., 2010). The preserved, although buried impact structure and K-Pg boundary deposits all over the world provide the best source of data we have on Earth's climatic response to large impacts (Pierazzo and Melosh, 2013). Alvarez et al. (1980) was the first study of impactite material in the Cretaceous-Paleogene (K/Pg) boundary to propose that the mass extinction was related to an impact event. Their results were compelling, concluding that the extinction was the result of a global shutdown of photosynthesis due to the debris ejected into the atmosphere. This study ignited a series of studies including computer modelling, experimental and field studies, as well as the identification and link between the K-Pg extinction and the Chicxulub impact in the early 90s (e.g., Hildebrand et al., 1991; Pope et al., 1997).

It is proposed that the Chicxulub structure was formed by the impact of a projectile ~10 km in diameter, at a velocity of over 22 km/s, with the energy equivalent of 10^8 Megatons TNT-equivalent into an ~3 km thick section of shallow marine carbonates and evaporites overlying metamorphic target rocks (Covey et al., 1994; Pope et al., 1997). The ejecta rose in a rapidly expanding hot plume that reached beyond Earth's atmosphere: deposited hot fine dust particles into the upper atmosphere (Covey et al., 1994; Melosh et al., 1990), gigatons of SO_x, H_2O vapour and CO_2 from the impact target's carbonates and evaporites into the stratosphere, as well as smoke and soot from the combustion of organic matter (Artemieva and Morgan, 2017; Melosh et al., 1990). All of the above was distributed around the globe.

The proposed extinction processes consist mainly of a short-term blackout and cooling period, and a long-term warming period. Cooling was caused by a global decrease in solar radiation as the sun was blocked by ejected dust and soot, as well as backscattered and absorbed by the newly, rapidly-formed evaporite that derived sulfuric aerosols in the atmosphere that stalled photosynthesis (Artemieva and Morgan, 2017; Covey et al., 1994; Sigurdsson et al., 1992). Computer simulations suggest surface temperatures were reduced by over 25°C (Brugger et al., 2017). When the dust particles had begun to settle out of the atmosphere, the temperature and light levels began to rebound with the help of heat stored in the oceans. However, the longer residence time of SO_x and water vapour in the atmosphere continued to block 50% sunlight for up to 10 years, and it took over 30 years post-impact for the temperatures to recover (Brugger et al., 2017). The sulfuric and nitric aerosols converted from SO_x and NO formed by reactions in the stratosphere, settled into the troposphere, where they were deposited as acid rain (Brett, 1992; D'Hondt et al., 1994; Park, 1978). This acid rain may also have contributed to surface-ocean acidification, with the potential to reduce the ocean's pH to lethal levels (D'Hondt et al., 1994). The long-term warming period was due to the release of a large volume of greenhouse gases: CO_2 and water vapour (O'Keefe and Ahrens, 1989; Pope et al., 1994). Like our current state of global warming, the more CO_2 added to the atmosphere, the stronger the greenhouse effect. Scientists continue to work and debate over the estimates of released gases as they are important inputs to the global climate models simulate the short and long-term environmental changes post-impact. The uncertainties in the models exist due to the angle of impact and amount of relative carbonates and evaporites in the target rocks, and the limitations due to computational

costs (Artemieva and Morgan, 2017). The quantities of ejected carbonate and sulfate particles versus disassociated sulfate and carbonate gases ejected into the atmosphere directly and significantly affect the resulting climate models and our understanding of post-impact climate-related extinctions.

1.7 Thesis objectives

The reaction of calcareous sedimentary rocks to impact is ambiguous. In the field, the principal obstacle preventing clarity lies in the difficulty to distinguish between impact-generated carbonate melt products, lithic carbonate products (e.g. lithic breccias), impact-generated hydrothermal carbonates and pre-impact diagenetic carbonate. The same ambiguity exists for impacts into sulfates. To address this obstacle, this thesis presents new petrographic and microanalytical results of both impact-generated melt products and post-impact hydrothermal alteration of dominantly calcareous sedimentary target rocks at the Haughton impact structure, Canadian High Arctic.

In order to better understand the impact melt products of impacts into calcareous targets, Chapter 2 presents new textural and mineralogical evidence for a newly recognized melt rock lithology at the Haughton impact structure, identified in a recent drill core collected in the central region of the structure: a coherent body of crystalline carbonate-silicate-sulfate impact melt. This series of melt textures provide new tools to recognize carbonate- and sulfate-derived impact melt at other impact craters and provides insight into the formation of impactites in the central region of the structure.

In order to better understand the impact-generated products at the centre of the Haughton impact structure, Chapter 3 presents a thorough characterization of two shallow drill cores from the structure's centre. The F2 core, described predominantly in the context of impact melt textures in Chapter 2, is in fact far more complex due intense hydrothermal alteration. The F3 core is similar in appearance to the previously documented particulate melt at Haughton but has a groundmass of clay minerals. Both cores represent new lithologies and types of hydrothermal alteration, and a means to explore the crystallization and hydrothermal history at the centre of the crater-fill at Haughton.

Chapter 4 aims to re-evaluate the impact-generated hydrothermal system and distinguish between its products and the carbonate target rocks within the Haughton impact structure. Mineralization is characterized in each stratigraphic unit in the interior and periphery of the central uplift through a systematic micro-analytical approach. Cathodoluminescence is used extensively for characterizing hydrothermal carbonate and differentiation between multiple generations of calcite precipitation. Recent shallow drilling efforts in the central uplift at Haughton also provide new opportunities to examine the extent of alteration at unexposed depths. Combined with previous studies and Chapter 3, a new stratigraphic model of mineralization at the centre of the Haughton structure is presented.

Chapter 5 concludes the thesis with a discussion on the impactites on the central uplift and central uplift periphery at Haughton and the progress made towards understanding the impacts into calcareous sedimentary target rocks. In addition, it reviews the economic and astrobiological potential at Haughton, the potential influence on past, present and future global climate, and work for the future.

1.8 References

Abramov, O., Kring, D.A., 2007. Numerical modeling of impact-induced hydrothermal activity at the Chicxulub crater. Meteorit. Planet. Sci. 42, 93–112. https://doi.org/10.1111/j.1945-5100.2007.tb00220.x

Agrinier, P., Deutsch, A., Schärer, U., Martinez, I., 2001. Fast back-reactions of shock-released CO_2 from carbonates: An experimental approach. Geochim. Cosmochim. Acta 65, 2615–2632. https://doi.org/10.1016/S0016-7037(01)00617-2

Ahrens, T.J., O'Keefe, J.D., 1972. Shock melting and vaporization of Lunar rocks and minerals. Moon 4, 214–249.

Alvarez, L.W., Alvarez, W., Asaro, F., Michel, H. V., 1980. Extraterrestrial Cause for the Cretaceous-Tertiary Extinction. Science (80-.). 208, 1095–1108.

Ames, D., Watkinson, D., Parrish, R., 1998. Dating of a regional hydrothermal system induced by the 1850 Ma Sudbury impact event. Geology 26, 447–450.

Ames, D.E., Kjarsgaard, I.M., Pope, K.O., Dressler, B., Pilkington, M., 2004. Secondary
alteration of the impactite and mineralization in the basal Tertiary sequence, Yaxcopoil-1,
Chicxulub impact crater, Mexico. Meteorit. Planet. Sci. 39, 1145–1167.
https://doi.org/10.1111/j.1945-5100.2004.tb01134.x

Artemieva, N., Morgan, J., 2017. Quantifying the Release of Climate-Active Gases by Large
Meteorite Impacts With a Case Study of Chicxulub. Geophys. Res. Lett. 1–9.
https://doi.org/10.1002/2017GL074879

Auclair, S., 2011. Stable carbon and oxygen isotopic study of impact-induced hydrothermal
calcite at the Haughton impact structure, Devon Island, Nunavut, Canada. M.Sc. thesis.
University of Western Ontario.

Bourgeois, J., Hansen, T.A., Wiberg, P.L., Kauffman, E.G., 1988. A tsunami deposit at the
Cretaceous-Tertiary boundary in Texas. Science (80-.). 241, 567–570.

Bralower, T.J., Paull, C.K., Leckie, R.M., 1998. The Cretaceous-Tertiary boundary cocktail:
Chicxulub impact triggers margin collapse and extensive sediment gravity flows. Geology
26, 331–334.

Brett, R., 1992. The Cretaceous-Tertiary extinction: a lethal mechanism involving anhydrite
target rocks. Geochim. Cosmochim. 56, 3603–6306.

Brugger, J., Feulner, G., Petri, S., 2017. Baby, it's cold outside: Climate model simulations of the
effects of the asteroid impact at the end of the Cretaceous. Geophys. Res. Lett. 44, 419–427.
https://doi.org/10.1002/2016GL072241

Covey, C., Thompson, S.L., Weissman, P.R., MacCracken, M.C., 1994. Global climatic effects
of atmospheric dust from an asteroid or comet impact on Earth. Glob. Planet. Change 9,
263–273. https://doi.org/10.1016/0921-8181(94)90020-5

D'Hondt, S., Pilson, M.E.Q., Sigurdsson, H., Hanson, A.K., Carey, S., 1994. Surface-water
acidification and extinction at the Cretaceous- Tertiary boundary. Geology 22, 983–986.
https://doi.org/10.1130/0091-7613(1994)022<0983:SWAAEA>2.3.CO;2

Dence, M.R., 1972. The nature and significance of terrestrial impact structures, in: 15th International Geological Congress. pp. 77–89.

Dence, M.R., 1968. Shock zoning at Canadian craters: petrography and structural implications, in: Fench, B.M., Short, N.M. (Eds.), Shock Metamorphism in Natural Materials. Mono Book Corp., Baltimore, MD., pp. 169–184.

Fike, D.A., Cockell, C., Pearce, D., Lee, P., 2002. Heterotrophic microbial colonization of the interior of impact-shocked rocks from Haughton impact structure, Devon Island, Nunavut, Canadian High Arctic. Int. J. Astrobiol. 1, 311–323. https://doi.org/10.1017/S1473550403001290

French, B.M., 1998. Traces of Catastrophe, LPI Contri. ed. Lunar and Planetary Institute, Houston Texas.

Gault, D.E., Quaide, W.L., Oberbeck, V.R., 1968. Impact Cratering mechanics and structures, in: Shock Metamorphism in Natural Materials. Mono Book Corp., Baltimore, MD., pp. 87–99.

Graup, G., 1999. Carbonate-silicate liquid immiscibility upon impact melting: Ries Crater, Germany. Meteorit. Planet. Sci. 34, 425–438.

Grieve, R.A.F., 1987. Terrestrial Impact Structures. Annu. Rev. Earth Planet. Sci. 15, 245–270.

Grieve, R.A.F., Cintala, M.J., 1992. An analysis of differential impact melt-crater scaling and implications for the terrestrial impact record. Meteoritics 57, 526–538.

Grieve, R.A.F., Dence, M.R., Robertson, P.B., 1977. Cratering processes: As interpreted from the occurrence of impact melts, in: Roddy, D.J., Pepin, R.O., Merrill, R.B. (Eds.), Impact and Explosion Cratering. Pergamon Press, New York, pp. 791–814.

Hajnal, Z., Scott, D., Robertson, P.B., 1988. Reflection study of the Haughton impact structure. J. Geophys. Res. 93, 11930–11942.

Hamann, C., Bläsing, S., Hecht, L., Schäffer, S., Deutsch, A., Osterholz, J., Lexow, B., 2018. The reaction of carbonates in contact with laser-generated, superheated silicate melts:

Constraining impact metamorphism of carbonate-bearing target rocks. Meteorit. Planet. Sci. 43. https://doi.org/10.1111/maps.13133

Hecht, L., Wittmann, A., Schmitt, R.-T., Stoeffler, D., 2004. Composition of impact melt particles and the effects of post-impact alteration in suevitic rocks at the Yaxcopoil-1 drill core, Chicxulub Crater, Mexico. Meteorit. Planet. Sci. 39, 1169–1186.

Hildebrand, A.R., Penfield, G.T., Kring, D.A., Pilkington, M., Antonio, C.Z., Jacobsen, S.B., Penfield, G.T., Boynton, W. V., 1991. Chicxulub crater: a possible Cretaceous/Tertiary boundary impact crater on the Yucatan Peninsula, Mexico. Geology 19, 867–871. https://doi.org/10.1130/0091-7613(1991)019<0867:CCAPCT>2.3.CO;2

Hörz, F., Archer, P.D., Niles, P.B., Zolensky, M.E., Evans, M., 2015. Devolatilization or melting of carbonates at Meteor Crater, AZ? Meteorit. Planet. Sci. 50, 1050–1070. https://doi.org/10.1111/maps.12453

Ivanov, B. a, Deutsch, A., 2002. The phase diagram of CaCO3 in relation to shock compression and decomposition. Phys. Earth Planet. Inter. 129, 131–143. https://doi.org/10.1016/S0031-9201(01)00268-0

Ivanov, B.A., Langenhorst, F., Deutsch, A., Horneemann, U., 2004. Anydrite EOS and phase diagram in relation to shock decomposition. Lunar Planet. Sci. XXXV 3–4.

Jessberger, E., 1988. 40Ar-39Ar Dating of the Haughton Impact Structure. Meteoritics 23, 233–234.

Jõeleht, A., Kirsimae, K., Plado, J., Versh, E., Ivanov, B., 2005. Cooling of the Kärdla impact crater : II . Impact and geothermal modeling. Meteorit. Planet. Sci. 40, 21–33.

Jones, A.P., Claeys, P., Heuschkel, S., 2000. Impact melting of carbonates from the Chicxulub crater, in: Gilmour, I., Koeberl, C. (Eds.), Impacts and the Early Earth, Lecture Notes in Earth Sciences, Vol 91. Springer, Springer-Verlag Berlin Heidelberg, pp. 343–361.

Jones, A.P., Genge, M., Carmody, L., 2013. Carbonate Melts and Carbonatites. Rev. Mineral. Geochemistry 75, 289–322. https://doi.org/10.2138/rmg.2013.75.10

Kieffer, S.W., Simonds, C.H., 1980. The role of volatiles and lithology in the impact cratering process. Rev. Geophys. 18, 143–181. https://doi.org/10.1029/RG018i001p00143

Kirsimäe, K., Osinski, G.R., 2013. Impact-induced hydrothermal activity, in: Osinski, G.R., Pierazzo, E. (Eds.), Impact Cratering Processes and Products. Wiley-Blackwell, p. 316.

Kirsimäe, K., Suuroja, S., Kirs, J., 2002. Hornblende alteration and fluid inclusions in Kärdla impact crater, Estonia: Evidence for impactâ€ induced hydrothermal activity. … Planet. Sci. 37, 449–457.

Kring, D.A., 2007. The Chicxulub impact event and its environmental consequences at the Cretaceous-Tertiary boundary. Palaeogeogr. Palaeoclimatol. Palaeoecol. 255, 4–21. https://doi.org/http://dx.doi.org/10.1016/j.palaeo.2007.02.037

Lacelle, D., Pellerin, A., Clark, I.D., Lauriol, B., Fortin, D., 2009. (Micro)morphological, inorganic-organic isotope geochemisty and microbial populations in endostromatolites (cf. fissure calcretes), Haughton impact structure, Devon Island, Canada: The influence of geochemical pathways on the preservation of isotope bioma. Earth Planet. Sci. Lett. 281, 202–214. https://doi.org/10.1016/j.epsl.2009.02.022

Langenhorst, F., Deutsch, A., 2012. Shock Metamorphism in Minerals. Elements 8, 31–36.

Martinez, I., Agrinier, P., Schaerer, U., Javoy, M., 1994. A SEM-ATEM and stable isotope study of carbonates from the Haughton impact crater, Canada. Earth Planet. Sci. Lett. 121, 559–574.

Mathieu, L., 2018. Quantifying Hydrothermal Alteration: A Review of Methods. Geosciences 8, 245. https://doi.org/10.3390/geosciences8070245

Melosh, H.J., 1989. Impact Cratering A Geologic Process, Oxford mon. ed. Oxford University Press, New York.

Melosh, H.J., Ivanov, B. a., 1999. Impact Crater Collapse. Annu. Rev. Earth Planet. Sci. 27, 385–415. https://doi.org/10.1146/annurev.earth.27.1.385

Melosh, H.J., Schneider, N.M., Zahnle, K.J., Latham, D., 1990. Ignition of global wildfires at the K/T boundary. Nature 373, 399–404.

Metzler, A., Ostertag, R., Redeker, H.J., Stöffler, D., 1988. Composition of the Crystalline Basement and Shock Metamorphism of Crystalline and Sedimentary Target Rocks at teh Haughton Impact Crater, Devon Island, Canada. Meteoritcs 23, 197–207. https://doi.org/10.1017/CBO9781107415324.004

Muttik, N., Kirsimäe, K., Somelar, P., Osinski, G.R., 2008. Post-impact alteration of surficial suevites in Ries crater, Germany: Hydrothermal modification or weathering processes? Meteorit. Planet. Sci. 43, 1827–1840. https://doi.org/10.1111/j.1945-5100.2008.tb00646.x

Naumov, M., 2002. Impact-generated hydrothermal systems: Data from Popigai, Kara, and Puchezh-Katunki impact structures, in: Plado, J., Pesonen, L.J. (Eds.), Impacts in Precambrian Shields. Springer-Verlag, Berlin, pp. 117–171.

Naumov, M.V., 2005. Principal features of impact-generated hydrothermal circulation systems: mineralogical and geochemical evidence. Geofluids 5, 165–184.

Newsom, H., Graup, G., Sewards, T., Keil, K., 1986. Fluidization and hydrothermal alteration of the Suevite deposit at the Ries Crater, West Germany, and implications for Mars. J. Geophys. Res. 91, E239–E251. https://doi.org/http://dx.doi.org/10.1029/JB091iB13p0E239

O'Keefe, J.D., Ahrens, T.J., 1989. Impact production of CO2 by the Cretaceous/Tertiary extinction bolide and the resultant heating of the Earth. Nature. https://doi.org/10.1038/338247a0

Oberbeck, V.R., 1975. The Role of Ballistic Erosion and Sedimentation in Lunar Stratigraphy. Rev. Geophys. Sp. Phys. 13, 337–362.

Omar, G., Johnson, K.R., Hickey, L.J., Robertson, P.B., Dawson, M.R., Cathy, B.W., 1987. Fission-Track Dating of Haughton Astrobleme and Included Biota, Devon Island, Canada. Science (80-.). 237, 1603–1605.

Osinski, G., 2005. Hydrothermal activity associated with the Ries impact event, Germany.

Geofluids 5, 202–220.

Osinski, GR, Tornabene, L.L., Banerjee, N.R., Cockell, C.S., Flemming, R., Izawa, M.R., McCutcheon, J., Parnell, J., Preston, L.J., Pickersgill, A.E., Pontefract, A., Sapers, H.M., Southam, G., 2013. Impact-generated hydrothermal systems on Earth and Mars. Icarus 224, 347–363. https://doi.org/10.1016/j.icarus.2012.08.030

Osinski, G.R., Grieve, R.A.F., Collins, G.S., Marion, C., Sylvester, P., 2008a. The effect of target lithology on the products of impact melting. Meteorit. Planet. Sci. 43, 1939–1954. https://doi.org/10.1111/j.1945-5100.2008.tb00654.x

Osinski, Gordon R., Grieve, R.A.F., Tornabene, L.L., 2013. Excavation and impact ejecta emplacement, in: Osinski, G.R., Pierrazzo, E. (Eds.), Impact Cratering Processes and Products. WILEY-BLACKWELL, pp. 43–59.

Osinski, G.R., Lee, P., 2005. Intra-crater sedimentary deposits at the Haughton impact structure, Devon Island, Canadian High Arctic. Meteorit. Planet. Sci. 40, 1887–1899.

Osinski, G.R., Lee, P., Parnell, J., Spray, J.G., Baron, M., 2005a. A case study of impact-induced hydrothermal activity: The Haughton impact structure, Devon Island, Canadian High Arctic. Meteorit. Planet. Sci. 40, 1859–1877. https://doi.org/10.1111/j.1945-5100.2005.tb00150.x

Osinski, G.R., Lee, P., Spray, J.G., Parnell, J., Lim, D.S.S., Bunch, T.E., Cockell, C.S., Glass, B., 2005b. Geological overview and cratering model for the Haughton impact structure, Devon Island, Canadian High Arctic. Meteorit. Planet. Sci. 40, 1759–1776. https://doi.org/10.1111/j.1945-5100.2005.tb00145.x

Osinski, G.R., Pierazzo, E. (Eds.), 2013. Impact Cratering processes and products. WILEY-BLACKWELL, Hoboken, NJ.

Osinski, G.R., Spray, J.G., 2005. Tectonics of complex crater formation as revealed by the Haughton impact structure, Devon Island, Canadian High Arctic. Meteorit. Planet. Sci. 40, 1813–1834. https://doi.org/10.1111/j.1945-5100.2005.tb00148.x

Osinski, G.R., Spray, J.G., 2003. Evidence for the shock melting of sulfates from the Haughton impact structure, Arctic Canada. Earth Planet. Sci. Lett. 215, 357–370. https://doi.org/10.1016/S0012-821X(03)00420-5

Osinski, G.R., Spray, J.G., 2001. Impact-generated carbonate melts: evidence from the Haughton structure, Canada. Earth Planet. Sci. Lett. 194, 17–29. https://doi.org/10.1016/S0012-821X(01)00558-1

Osinski, G.R., Spray, J.G., Grieve, R.A.F., 2008b. Impact melting in sedimentary target rocks: An assessment, in: Evans, K.R., Horton, J.W., King, J.D.T., Morrow J.R. (Eds.), The Sedimentary Record of Meteorite Impacts, Geological Society of America Special Publication 437. Geological Society of America, Boulder, pp. 1–18. https://doi.org/10.1130/2008.2437(01).For

Osinski, G.R., Spray, J.G., Lee, P., 2005c. Impactites of the Haughton impact structure, Devon Island, Canadian High Arctic. Meteorit. Planet. Sci. 40, 1789–1812. https://doi.org/10.1111/j.1945-5100.2005.tb00147.x

Osinski, G.R., Spray, J.G., Lee, P., 2001. Impact-induced hydrothermal activity within the Haughton impact structure, arctic Canada: Generation of a transient, warm, wet oasis. Meteorit. Planet. Sci. 36, 731–745. https://doi.org/10.1111/j.1945-5100.2001.tb01910.x

Osinski, G.R., Tornabene, L.L., Grieve, R.A.F., 2011. Impact ejecta emplacement on terrestrial planets. Earth Planet. Sci. Lett. 310, 167–181. https://doi.org/10.1016/j.epsl.2011.08.012

Park, C., 1978. Nitric oxide production by Tunguska meteor. Acta Astronaut. 5, 523–542.

Parnell, J., Taylor, C.W., Thackrey, S., Osinski, G.R., Lee, P., 2010. Permeability data for impact breccias imply focussed hydrothermal fluid flow. J. Geochemical Explor. 106, 171–175. https://doi.org/10.1016/j.gexplo.2009.12.002

Pierazzo, E., Melosh, H.J., 2013. Environmental effects of impact events, in: Osinski, G.R., Pierazzo, E. (Eds.), Impact Cratering Processes and Products. WILEY-BLACKWELL, Hoboken N.J., p. 316.

Pierazzo, E., Vickery, A.M., Melosh, H.J., 1997. A reevaluation of impact melt production. Icarus 127, 408–423. https://doi.org/10.1006/icar.1997.5713

Pohl, J., Eckstaller, A., Robertson, R.B., 1988. Gravity and magnetic investigations in the Haughton impact structure, Devon Island, Canada. Meteoritcs 23, 235–238.

Pontefract, A., Osinski, G.R., Lindgren, P., Parnell, J., Cockell, C.S., Southam, G., 2012. The effects of meteorite impacts on the availability of bioessential elements for endolithic organisms. Meteorit. Planet. Sci. 47, 1681–1691. https://doi.org/http://dx.doi.org/10.1111/maps.12004

Pope, K.O., Baines, K.H., Ocampo, A.C., Ivanov, B.A., 1997. Energy, volatile production, and climatic effects of the Chicxulub Cretaceous / Tertiary impact. J. Geophys. Res. 102.

Pope, K.O., Baines, K.H., Ocampo, A.C., Ivanov, B.A., 1994. Impact winter and the Cretaceous/Tertiary extinctions; results of a Chicxulub asteroid impact model. Earth Planet. Sci. Lett. 128, 719–725. https://doi.org/http://dx.doi.org/10.1016/0012-821X(94)90186-4

Quesnel, Y., Gattacceca, J., Osinski, G.R., Rochette, P., 2013. Origin of the central magnetic anomaly at the Haughton impact structure, Canada. Earth Planet. Sci. Lett. 367, 116–122. https://doi.org/10.1016/j.epsl.2013.02.032

Redeker, H.J., Stöffler, D., 1988. The Allochtonous Polymict Breccia Layer of the Haughton Impact Crater, Devon Island, Canada. Meteoritics 23, 185–196.

Reimold, W., Koeberl, C., Gibson, R., Dressler, B., 2005. Economic mineral deposits in impact structures: a review. Impact tectonics 479–552.

Renne, P.R., Deino, A.L., Hilgen, F.J., Kuiper, K.F., Mark, D.F., Mitchell III, W.S., Morgan, L.E., Mundil, R., Smit, J., 2013. Time scales of critical events around the Cretaceous-Paleogene boundary. Science (80-.). 339, 684–687. https://doi.org/http://dx.doi.org/10.1126/science.1230492

Robertson, P.B., Sweeney, J.F., 1983. Haughton impact structure: structural and morphological aspects. Can. J. Earth Sci. 20, 1134–1151.

Schulte, P., Alegret, L., Arenillas, I., Arz, J.A., Barton, P.J., Bown, P.R., Bralower, T.J., Christeson, G.L., Claeys, P., Cockell, C.S., Collins, G.S., Deutsch, A., Goldin, T.J., Goto, K., Grajales-Nishimura, J.M., Grieve, R.A.F., Gulick, S.P.S., Johnson, K.R., Kiessling, W., Koeberl, C., Kring, D.A., MacLeod, K.G., Matsui, T., Melosh, J., Montanari, A., Morgan, J. V., Neal, C.R., Nichols, D.J., Norris, R.D., Pierazzo, E., Ravizza, G., Rebolledo-Vieyra, M., Reimold, W.U., Robin, E., Salge, T., Speijer, R.P., Sweet, A.R., Urrutia-Fucugauchi, J., Vajda, V., Whalen, M.T., Willumsen, P.S., 2010. The chicxulub asteroid impact and mass extinction at the cretaceous-paleogene boundary. Science (80-.). 327, 1214–1218. https://doi.org/10.1126/science.1177265

Sherlock, S., Kelley, S., 2005. Re   evaluating the age of the Haughton impact event. … Planet. Sci. 40, 1777–1787. https://doi.org/10.1111/j.1945-5100.2005.tb00146.x

Sigurdsson, H., D'Hondt, S., Carey, S., 1992. The impact of the Cretaceous/Tertiary bolide on evaporite terrane and generation of major sulfuric acid aerosol. Earth Planet. Sci. Lett. 109, 543–559. https://doi.org/10.1016/0012-821X(92)90113-A

Stöffler, D., Gault, D.E., 1975. Experimental hypervelocity impact into quartz sand: distribution and shock metamorphism of ejecta. J. Geophys. Res. 80, 4062–4077.

Stöffler, D., Grieve, R.A.F., 2007. Impactites, in: Fettes, D., Desmons, J. (Eds.), Metamorphc Rocks: A Classification and Glossary of Terms; Recommendations of the Iternational Union of Geological Sciences. Cambridge University Press, Cambridge, pp. 82–92.

Stöffler, D., Hamann, C., Metzler, K., 2018. Shock metamorphism of planetary silicate rocks and sediments: Proposal for an updated classification system. Meteorit. Planet. Sci. 53, 5–49. https://doi.org/10.1111/maps.12912

Sturkell, E.F.F., Broman, C., Forsberg, P., Torssander, P., 1998. Impact-related hydrothermal activity in the Lockne impact structure, Jamtland, Sweden. Eur. J. Mineral. 10, 589–606. https://doi.org/10.1127/ejm/10/3/0589

Thorsteinsson, R., Mayr, U., 1987. The sedimentary rocks of Devon Island, Canadian Arctic Archipelago. Geological Survey of Canada Memoir 411, Ottawa, Canada.

Versh, E., Kirsimäe, K., Jõeleht, A., Plado, J., 2005. Cooling of the Kärdla impact crater: I. The mineral paragenetic sequence observation. Meteorit. Planet. Sci. 40, 3–19. https://doi.org/10.1111/j.1945-5100.2005.tb00361.x

Walton, E., Hughes, A., Maclagan, E., Herd, C.D.K., Dence, M., 2017. A previously unrecognized high-temperature impactite from the Steen River impact structure , Alberta , Canada. Geology 291–294. https://doi.org/10.1130/G38556.1

Walton, E.L., Timms, N.E., Hauck, T.E., Maclagan, E.A., Herd, C.D.K., 2019. Evidence of impact melting and post-impact decomposition of sedimentary target rocks from the Steen River impact structure ,. Earth Planet. Sci. Lett. 515, 173–186. https://doi.org/10.1016/j.epsl.2019.03.015

Wünnemann, K., Collins, G.S., Osinski, G.R., 2008. Numerical modelling of impact melt production in porous rocks. Earth Planet. Sci. Lett. 269, 530–539. https://doi.org/10.1016/j.epsl.2008.03.007

Young, K.E., van Soest, M.C., Hodges, K. V., Watson, E.B., Adams, B. a., Lee, P., 2013. Impact thermochronology and the age of Haughton impact structure, Canada. Geophys. Res. Lett. 40, 3836–3840. https://doi.org/10.1002/grl.50745

Zürcher, L., Kring, D. a., 2004. Hydrothermal alteration in the core of the Yaxcopoil-1 borehole, Chicxulub impact structure, Mexico. Meteorit. Planet. Sci. 39, 1199–1221. https://doi.org/10.1111/j.1945-5100.2004.tb01137.x

Zylberman, W., Quesnel, Y., Rochette, P., Osinski, G.R., Marion, C., Gattacceca, J., 2017. Hydrothermally enhanced magnetization at the center of the Haughton impact structure? Meteorit. Planet. Sci. 52, 2147–2165. https://doi.org/10.1111/maps.12917

Chapter 2

2 A coherent carbonate-sulfate melt rock at the Haughton impact structure

2.1 Introduction

A characteristic outcome of hypervelocity impact into igneous and metamorphic terrains is melting through shock decompression (Osinski et al., 2018). Although it has been established that impact melting does occur in sedimentary rocks, complications arise due to the presence of porosity and volatiles (Osinski et al., 2008 and references therein). This is particularly true for carbonate- and sulfate-bearing target rocks, where there is an ongoing debate about the relative importance of melting versus decomposition (Osinski et al. 2008). This lack of consensus has led to the exclusion of impact melting of these lithologies from the newly revised classification for shock metamorphism (Stöffler et al., 2018b). Furthermore, the decomposition and devolatilization of carbonates and evaporites during impact has been proposed to have a severe effect on the global climate. The Chicxulub impact event, for example, is thought to be responsible for the K-Pg mass extinction, through the release of large amounts of sulfur species and debris into the atmosphere causing global cooling (Artemieva and Morgan, 2017).

The presence of silicate, carbonate and sulfate minerals that crystallized from an impact-generated melt at the Haughton impact structure was first proposed by Osinski and Spray (2001) and Osinski and Spray (2003). In these works, the melt is represented primarily by a fine-grained particulate groundmass consisting of quenched melt particles of calcite, anhydrite and Mg-silicate glass which hosts clasts of all target lithologies. In the present study, we provide new textural and mineralogical evidence for the presence of a different type of impact melt rock: a coherent body of crystalline carbonate-silicate-sulfate impact melt in the centre of the Haughton structure. This new lithology expands our understanding of the products of impact into sedimentary rocks and has implications for the recognition of impact melt rocks at other craters, such as Chicxulub.

2.2 Geological Setting

The 23-km diameter Haughton impact structure is located on Devon Island, Nunavut, in the Canadian High Arctic. The impact occurred into an ~1880 m thick sedimentary sequence of Lower Paleozoic sediments of the Arctic Platform, which consist primarily of limestone, dolostone and interbedded gypsum, with minor shale and sandstone, that unconformably overly a Precambrian basement (Thorsteinsson and Mayr, 1987) (Fig. 2.1). The crater-fill impactites at Haughton consist of thin lithic breccias passing upwards into pale grey clast-rich impact melt rocks with a particulate groundmass that hosts clasts from all target lithologies (Osinski et al., 2008a, 2005c). In 2013, two cores, targeting a magnetic anomaly, were collected from the centre of the impact structure (Quesnel et al., 2013). The F2 core was collected within the anomaly (75.38220° N, 89.67453° W) and the F3 core just outside of it. Preliminary petrography and magnetometry of the cores were completed by Zylberman et al. (2017). This study is focused on the F2 core, which comprises a unique new lithology not previously documented at Haughton.
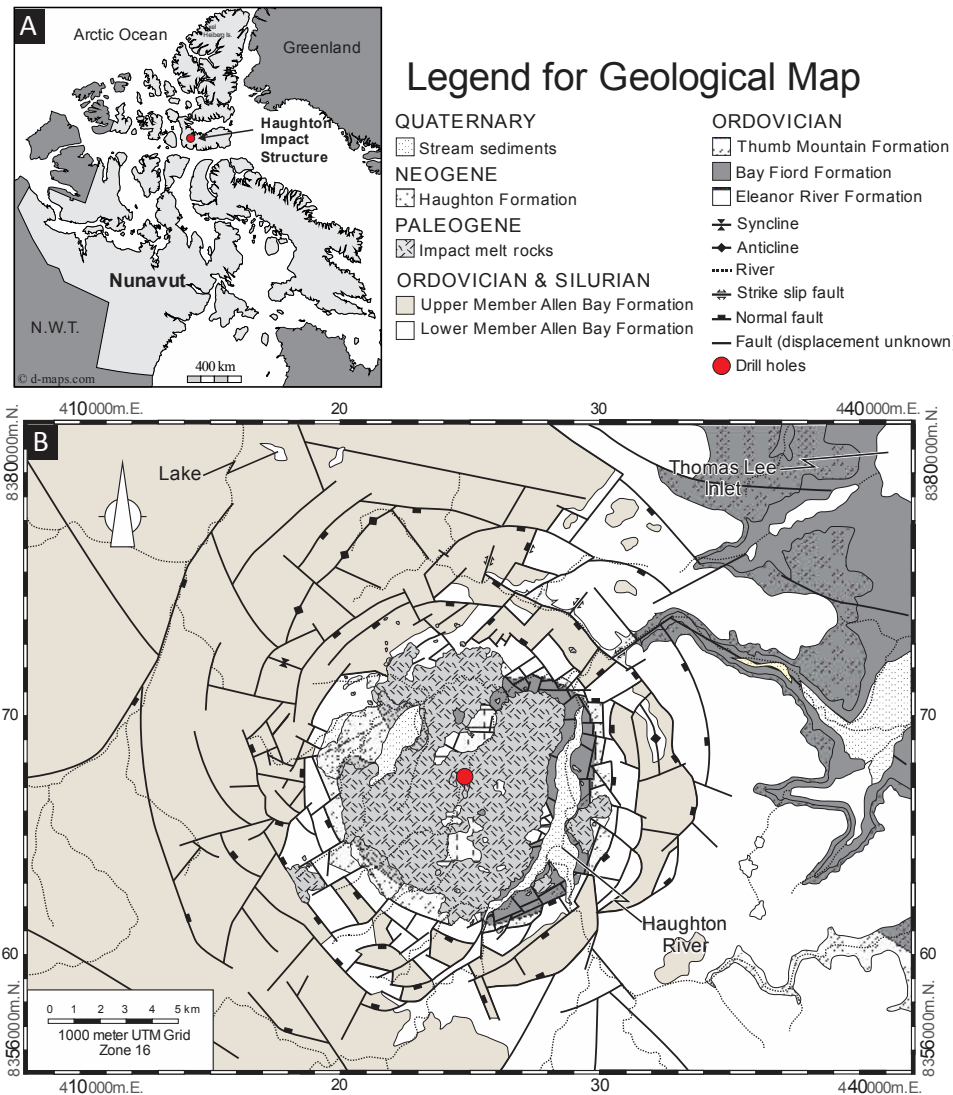
Figure 2.1 Location (A) and geologic map (B) of the Haughton impact structure, on Devon Island in Nunavut, Canada, modified from Osinski et al. (2005b).

2.3 Methodology

Polished thin sections were made every ~20 cm over 4 m of core. Micro-textural analysis was completed using optical microscopy, where backscattered electron (BSE) and cathodoluminescence (CL) imaging, as well as geochemical analysis and mapping of the groundmass and clast phases by wavelength dispersive (WDS) and energy dispersive spectrometry (EDS) using a JEOL JXA-8530F field-emission electron microprobe.

32

Complementary mineralogical investigations of the core samples were conducted using *in situ* micro X-ray diffraction. Full details of all the analytical techniques are provided in Appendix A.

2.4 Results

The F2 core intersected a white to pale green, mainly clast-supported, clast-rich polymict impactite (Fig. 2.2A and Fig. A.1). The groundmass is heterogeneous with three compositional zones dominated by carbonate, sulfate, and Mg-rich silicate minerals, respectively. Low wt% oxide totals in individual microprobe analyses and major element composition indicate the silicate groundmass and the majority of clasts are hydrated Mg-silicates. The groundmass proportion is variable, but generally comprises a visually estimated 20–40% of the rock, increasing up to 60% in some silicate-dominant zones. The clasts consist predominantly of Mg-rich clay minerals, >300 μm in diameter, rounded and commonly zoned. Remnant gneissic textures can be observed in some clasts, whereas other clasts are filled by replacement calcite or anhydrite. There are no observable dolomite or sulfate clasts. Notable textures present within the groundmass are described below (Fig. 2.1).

The silicate groundmass is dominated by Mg-rich clay minerals and has an overall porphyritic texture (Fig. 2.1B). Smaller mm-size clasts are present as well as partially digested clasts (Fig. 2.1C). Silicate coronas or relict coronas (Fig. 2.1D and E) are common and can be replaced by selenite.

The groundmass calcite occurs in various forms but is generally fine-grained and fills interstitial and intra-clast space. Acicular to radial acicular silicate intergrowth textures are observed in both calcite (Fig. 2.1D) and anhydrite (Figs. 2.1F inset; Fig. A.2). The acicular inclusions are less than 5 μm in width, and range in length from 1 to 80 μm. Microprobe analysis show that these are Mg-silicates with minor to trace amounts of Al_2O_3 (average of 6.4 wt%) and CaO (up to 1 wt%), respectively. The calcite that hosts the needles is far less luminescent than the surrounding calcite. Highly acicular to spherulitic calcite mantled by clay minerals (Figs.2.1G and 1H; Fig. A.3) also occurs adjacent to dendritic Mg-silicate that grew outwards from silicate clasts, which is currently contained within a carbonate groundmass (Fig. 2.1H). Porous calcite commonly occurs near the nucleation sites of acicular grains. Some calcite has porous cores with non-porous overgrowths; whereas, adjacent grains have a ring-shaped zone of

porous calcite that displays flow textures (Fig. 2.1I). Globular regions with an abundance of micrometre-scale spherical voids are also common. Wormy to vermicular intergrowth of silicate and calcite are pervasive along clast boundaries (Figs. 2.1J-K; Fig. A.4). Resorption and overgrowth textures in calcite are commonly observed in CL maps of the calcite growth along silicate clast boundaries (Figs. 2.1J-K). Included within the overgrowths are normal and oscillatory zoned in calcite, a S-rich calcite overgrowth (up to 3% SO_3), followed by a S-poor overgrowth in contact with the sulfate groundmass. The sulfur-rich calcite is partially replaced by porous calcite.

The sulfate groundmass consists of fine- to medium-grained anhydrite, bassanite, and/or a selenite variety of gypsum. Skeletal Mg-rich silicate grains are hosted within anhydrite groundmass and range from euhedral to subhedral, tabular to dipyramidal, with their hollowed centre or embayment filled primarily with anhydrite (Fig. 2.1L). Element mapping shows that the skeletal crystals are irregularly zoned and consist primarily of Si, Mg and O near the core, with increasing Al and decreasing Si outwards, followed by an outer edge that is Al-poor (Fig. A.5). WDS spot analyses confirm this compositional change (Table A.1) but also indicate low totals in the range of 76–91wt % of oxides. Other major elements such as Ca, Fe, K and Na are found in trace amounts or are below detection limits. μXRD analyses of these grains demonstrates the presence of bassanite, talc, serpentine and diopside (Appendix A Fig. A.6); Raman was acquired as well, but no peaks could be distinguished due to fluorescence and the strength of the bassanite spectra (Appendix G). The presence of talc and an Al-rich serpentine have been confirmed with stoichiometric calculations of the skeletal grains, using WDS analyses (Table A.1), as well as a hydrated Mg-rich silicate similar in stoichiometry to anthophyllite but with a higher volatile content, based on lower wt% oxide totals on the outer edge of the grain. The skeletal grains occur in a single thin section, and are located adjacent a large diopside clast.
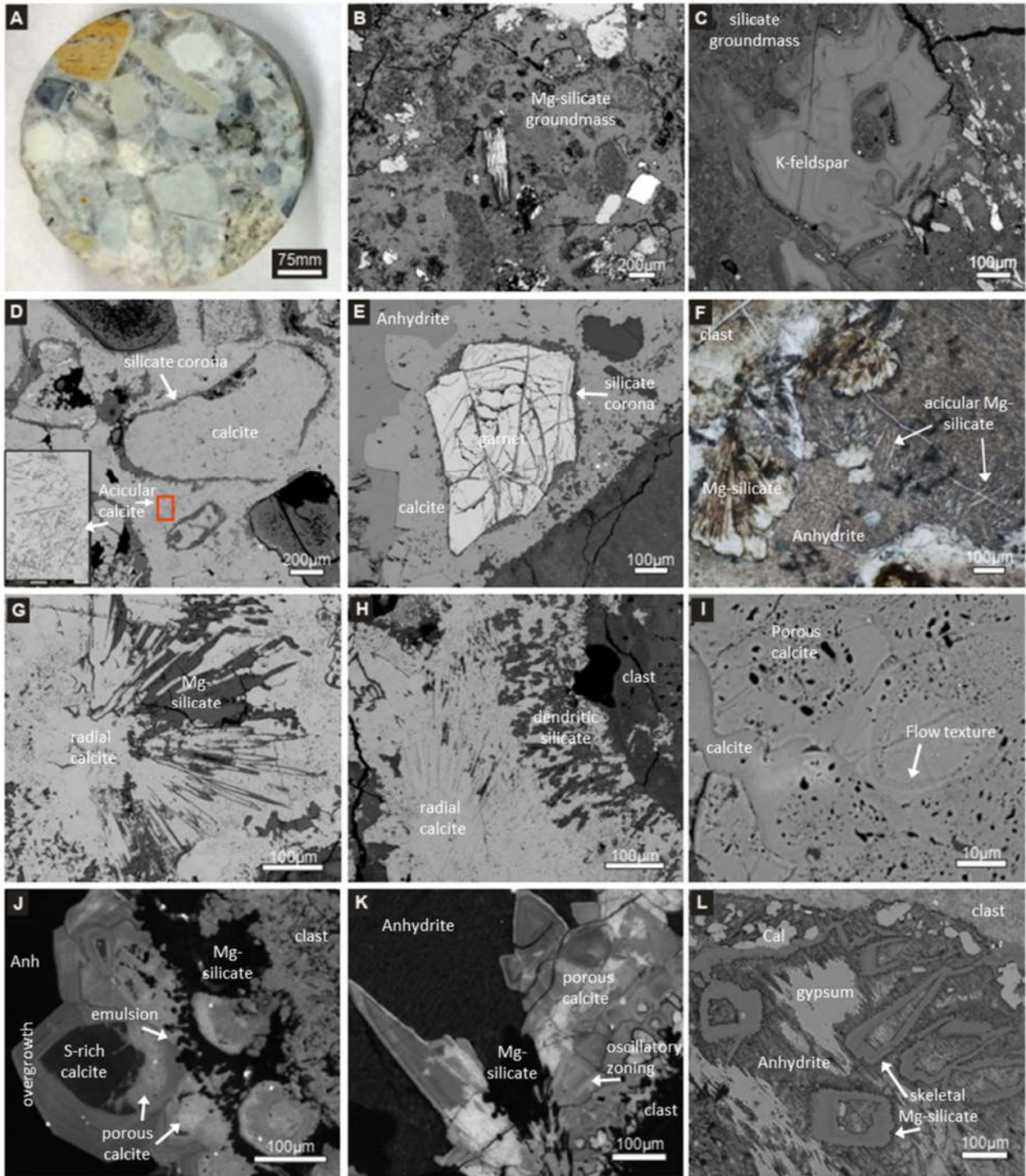
Figure 2.2 A) Cross section of the F2 core. B-E, G-I, and L are backscattered electron photomicrographs whereas K-L are panchromatic cathodoluminescence maps of the F2 core: B) Porphyritic silicate groundmass altered to Mg-rich clay minerals; C) Partially digested K-feldspar clast within silicate groundmass; D) A jellybean-shaped silicate corona

on relict clast, now replaced with calcite. This relict clast is embedded within a groundmass containing acicular silicate-calcite intergrowth shown in the inset and Figure A.2; E) Garnet clast with reaction rim hosted within calcite groundmass; F) Acicular silicate crystals intergrown within anhydrite groundmass; G) Radial acicular or spherulitic calcite and altered silicate hosted in calcite; H) Radial acicular calcite and dendritic Mg -silicate hosted in calcite; I) Porous calcite core overgrown with non-porous calcite and porousring-like flow in adjacent grain; J) Clast boundary (far right) showing wormy to vermicular intergrowth textures that suggest emulsion between silicate and carbonate melts, porous calcite (bright CL), sulfur-rich calcite overgrowth and sulfur poor overgrowth in contact with anhydrite (far left); K) Evolution of calcite crystallization: small crystals with silicate coronas closest to the silicate clast contact, followed by resorption features, oscillatory zoned calcite, porous calcite with some sulfate amygdules, terminated by sulfur-rich calcite overgrowth (dark CL), all of which hosted in sulfate groundmass. Note also the radial silicate in contact with both the calcite and sulfate as well as the emulsion contact with calcite; L) Skeletal Mg-silicate hosted in sulfate groundmass.

2.5 Discussion

The cores were collected in an outcrop-free area on so-called Anomaly Hill and are the first consolidated samples acquired at the very centre of the structure (Fig. 2.1). The presence of impact melt rocks at this location are expected within the typical stratigraphic context of a complex impact structure (Grieve et al., 1977).

The textures exhibited by the calcite, sulfate and silicate in the groundmass of the F2 core are interpreted as classic igneous textures, that serve as physical evidence of crystallization from a melt(s). The textures observed here include interlocking grains, zoning and coronas. Particularly convincing are the variety of intergrowth and overgrowth textures, skeletal grains, and vesicular carbonate, which were not expected to form through post-impact hydrothermal alteration and mineralization based on the existing knowledge of mineralization at Haughton and other impact sites (Naumov, 2002, 2005; Osinski et al., 2005a).

Reaction rims or coronas are common in impact melt rocks and result from a chemical disequilibrium reaction between the melt and clast or simply the partial melting or assimilation

36

of the clast (Grieve, 1975). Radial to parallel aggregates of elongated calcite, such as the large acicular to spherulitic calcite observed in the core, are diagnostic of quenched carbonate melt over a wide range of pressure-temperature conditions (Jones et al., 1998), as quenched carbonate melts do not form glasses.

The intergrowth of acicular to radial silicate minerals that occurs within both the carbonate and sulfate groundmass, and within single calcite and anhydrite grains (acting as oikocrysts), strongly suggest that these phases resulted from coeval crystallization. Co-crystallization of silicate and carbonate is possible within certain a pressure-temperature range; the silicate will form first before reaching the carbonate liquidus to precipitate calcite (Lee and Wyllie, 1998). Indeed, the graphic intergrowth of olivine and calcite has been documented in calcite carbonatites (Chakhmouradian et al., 2016). A hydrothermal fluid of this composition is neither likely to form nor to precipitate intergrowths, as silicates and carbonates dissolve and precipitate under different conditions, e.g., solubilities, pH etc. Moreover, the acicular silicate would not remain suspended in a less dense water-rich fluid, while the calcite consistently crystallized around it. The gypsum is a late-stage hydrothermal replacement of anhydrite (Osinski et al., 2005a).

Porosity in the form of spherical voids or vesicles, are commonly formed by trapped gases during rapid crystallization from a melt. Vesicular melt rocks are common at many impact structures (e.g. Palme et al., 1979; Graup, 1999) and in some carbonatites (e.g. Lorenz et al., 2000). Vesicles are strictly igneous in origin, though they may be confused with secondary porosity. The core may have both vesicular calcite and secondary porosity. We propose that the very spherical voids, which also exhibit flow features (Figs. 2.1H-I) and that are isolated within particular grains, are vesicles. Growth zones of porous calcite with wispy terminations are likely replacement of an alteration prone carbonate. It is impossible to know if the primary carbonate, in this case, was vesicular as well. (Fig. 2.1J). Post-impact dissolution and fracturing would also occur along fluid pathways or adjacent fractures.

Overgrowth textures are formed through sequential primary crystallization. As the melt evolves compositionally and thermally, it may partially resorb primary phases and then continue growth. This results in discordant or truncated boundaries and overgrowths of somewhat

different composition (Fig. 2.1J) (Ginibre et al., 2007). These variations within the melt can also result in various types of zoning. Normal zoning results in lower temperature composition towards the rims, while oscillatory zoning represents cyclic changes, or rapid crystal growth as shown in Figure 2.1K.

The intermingling and wormy contacts between calcite and silicate are interpreted as emulsion textures, i.e. that originate from a mechanical mixture of mutually insoluble melts, independent of the original mixing status. Low viscosity carbonate melt has a high migration potential within a silicate melt and could form an interconnected melt network within the silicate melt (Martin et al., 2012).

Porphyritic and aphanitic textures, reaction rims and digested clasts, as well as the general appearance of the silicate groundmass are typical of silicate impact melt rocks (e.g., Osinski et al., 2018). We document the first melt rock with a silicate groundmass dominated by Mg-rich clay minerals at Haughton. Although impact melt glasses, are typically the first phases to alter through hydrothermal or weathering processes (Osinski et al., 2018), alteration of multiple crystalline phases or an interstitial groundmass would more likely form the current combination of groundmass clay minerals.

Serpentine and talc are typical alteration products of the mineral olivine; the serpentinization of olivine is a common pseudomorphic replacement reaction (Putnis, 2009). The morphology of the skeletal serpentine crystals is consistent with olivine crystal shapes, e.g. tabular and dipyramidal shapes represent the (010) and (100) planes, respectively. Olivine forms a large variety of crystal morphologies based on temperature and growth rate (Donaldson, 1976). These conditions are consistent with a superheated impact melt followed by significant undercooling. At high temperature and relatively low silica activity, it is likely the melt would crystallize the high temperature end member of olivine rather than pyroxene. As olivine is not present in the silicate targets rocks at Haughton, we conclude that these skeletal grains are serpentine pseudomorphs after olivine, which crystallized as a primary phase in Haughton's impact melt, prior to the crystallization of the sulfate groundmass.

2.6 Implications

This study recognizes a new lithologic unit, with strong textural evidence for silicate-carbonate-sulfate impact melting, which is manifest as a clast-rich crystalline impact melt rock at Haughton. This finding is in contrast to the heterogeneous particulate to glassy impact melt rocks reported previously by Osinski et al., (2005b), which form the bulk of the crater-fill at Haughton. The presence of these two melt rock types at Haughton is consistent with other medium to large impacts into heterogeneous targets, in which multiple melt rock lithologies are observed at each structure (e.g., Vishnevsky and Montanari, 1999; Osinski, 2004; Sapers et al., 2014). This observation suggests that multiple impact melt lithologies are a common occurrence at impact structures with heterogeneous targets.

Importantly, the presence of carbonate- and sulfate-rich impact melt rocks is in contrast to the concept that both carbonates and sulfates do not melt but decompose to release CO_2 (Pope et al., 1994) and sulfur-bearing gases (O'Keefe and Ahrens, 1989) during impact. Furthermore, this previously unrecognized lithology adds to the growing body of evidence for melting in sedimentary target rocks.

Recent geophysical results describing the morphology of the geophysical anomaly (Quesnel et al., 2013) suggest that this core may represent a much larger unexposed body of crystalline impact melt on the order of 1 km wide. This body, we suggest, represents a lens of crystalline impact melt at the centre of the Haughton structure, closest to the uplifted crystalline basement. Furthermore, as the localized geophysical study encompassed only a small area within the crater, it is possible there is more crystalline melt to be discovered.

2.7 References

Artemieva, N., Morgan, J., 2017. Quantifying the Release of Climate-Active Gases by Large Meteorite Impacts With a Case Study of Chicxulub. Geophys. Res. Lett. 1–9. https://doi.org/10.1002/2017GL074879

Bell, M.S., 2016. CO2 release due to impact devolatilization of carbonate: Results of shock experiments. Meteorit. Planet. Sci. 51, 619–646. https://doi.org/10.1111/maps.12613

Chakhmouradian, A.R., Reguir, E.P., Zaitsev, A.N., 2016. Calcite and dolomite in intrusive carbonatites. I. Textural variations. Mineral. Petrol. 110, 333–360. https://doi.org/10.1007/s00710-015-0390-6

Donaldson, C.H., 1976. An experimental investigation of olivine morphology. Contrib. to Mineral. Petrol. 57, 187–213. https://doi.org/10.1007/BF00405225

Ginibre, C., Wörner, G., Kronz, A., 2007. Crystal zoning as an archive for magma evolution. Elements 3, 261–266. https://doi.org/10.2113/gselements.3.4.261

Graup, G., 1999. Carbonate-silicate liquid immiscibility upon impact melting: Ries Crater, Germany. Meteorit. Planet. Sci. 34, 425–438.

Grieve, R.A.F., 1975. Petrology and chemistry of the impact melt at Mistastin Lake crater, Labrador. Geol. Soc. Am. Bull. 86, 1617–1629.

Grieve, R.A.F., Dence, M.R., Robertson, P.B., 1977. Cratering processes: As interpreted from the occurrence of impact melts, in: Roddy, D.J., Pepin, R.O., Merrill, R.B. (Eds.), Impact and Explosion Cratering. Pergamon Press, New York, pp. 791–814.

Jones, A.P., Claeys, P., Heuschkel, S., 2000. Impact melting of carbonates from the Chicxulub crater, in: Gilmour, I., Koeberl, C. (Eds.), Impacts and the Early Earth, Lecture Notes in Earth Sciences, Vol 91. Springer, Springer-Verlag Berlin Heidelberg, pp. 343–361.

Jones, A.P., Heuschel, S., Claeys, P., 1998. Comparison between carbonate textures in Chicxulub impact rocks and synthetic experiments, in: Meteoritical Society 61st Annual Meeting. abstract #5212, Dublin Ireland.

Kieffer, S.W., Simonds, C.H., 1980. The role of volatiles and lithology in the impact cratering process. Rev. Geophys. 18, 143–181. https://doi.org/10.1029/RG018i001p00143

Lee, W.J., Wyllie, P.J., 1998. Petrogenesis of carbonatite magmas from mantle to crust, constrained by the system $CaO-(MgO + FeO^*)-(Na_2O + K_2O)-(SiO_2+ Al_2O_3+ TiO_2)-CO_2$. J. Petrol. 39, 495–517. https://doi.org/10.1093/petroj/39.3.495

Lorenz, V., Stachel, T., Kurszlaukis, S., Stanistreet, I.G., 2000. Volcanology of the Gross Brukkaros Field, southern Namibia. Commun. Geol. Surv. Namib 12, 395–401.

Marion, C.L., 2009. Geology, distribution and geochemistry of impact melt at the Mistastin Lake impact crater, Labrador. Memorial University of Newfoundland.

Martin, A.M., Righter, K., Treiman, A.H., 2012. Experimental constraints on the destabilization of basalt+calcite+anhydrite at high pressure-high temperature and implications for meteoroid impact modeling. Earth Planet. Sci. Lett. 331–332, 291–304. https://doi.org/10.1016/j.epsl.2012.03.026

Naumov, M., 2002. Impact-generated hydrothermal systems: Data from Popigai, Kara, and Puchezh-Katunki impact structures, in: Plado, J., Pesonen, L.J. (Eds.), Impacts in Precambrian Shields. Springer-Verlag, Berlin, pp. 117–171.

Naumov, M.V., 2005. Principal features of impact-generated hydrothermal circulation systems: mineralogical and geochemical evidence. Geofluids 5, 165–184.

O'Keefe, J.D., Ahrens, T.J., 1989. Impact production of CO2 by the Cretaceous/Tertiary extinction bolide and the resultant heating of the Earth. Nature. https://doi.org/10.1038/338247a0

Osinski, G.R., 2004. Impact melt rocks from the Ries structure, Germany: An origin as impact melt flows? Earth Planet. Sci. Lett. 226, 529–543. https://doi.org/10.1016/j.epsl.2004.08.012

Osinski, G.R., Grieve, R.A.F., Bleacher, J.E., Neish, C.D., Pilles, E.A., Tornabene, L.L., 2018. Igneous rocks formed by hypervelocity impact. J. Volcanol. Geotherm. Res. 353, 25–54. https://doi.org/10.1016/j.jvolgeores.2018.01.015

Osinski, G.R., Grieve, R.A.F., Collins, G.S., Marion, C., Sylvester, P., 2008a. The effect of target lithology on the products of impact melting. Meteorit. Planet. Sci. 43, 1939–1954. https://doi.org/10.1111/j.1945-5100.2008.tb00654.x

Osinski, G.R., Lee, P., Parnell, J., Spray, J.G., Baron, M., 2005a. A case study of impact-induced

hydrothermal activity: The Haughton impact structure, Devon Island, Canadian High Arctic. Meteorit. Planet. Sci. 40, 1859–1877. https://doi.org/10.1111/j.1945-5100.2005.tb00150.x

Osinski, G.R., Spray, J.G., 2003. Evidence for the shock melting of sulfates from the Haughton impact structure, Arctic Canada. Earth Planet. Sci. Lett. 215, 357–370. https://doi.org/10.1016/S0012-821X(03)00420-5

Osinski, G.R., Spray, J.G., 2001. Impact-generated carbonate melts: evidence from the Haughton structure, Canada. Earth Planet. Sci. Lett. 194, 17–29. https://doi.org/10.1016/S0012-821X(01)00558-1

Osinski, G.R., Spray, J.G., Grieve, R.A.F., 2008b. Impact melting in sedimentary target rocks: An assessment, in: Evans, K.R., Horton, J.W., King, J.D.T., Morrow J.R. (Eds.), The Sedimentary Record of Meteorite Impacts, Geological Society of America Special Publication 437. Geological Society of America, Boulder, pp. 1–18. https://doi.org/10.1130/2008.2437(01).For

Osinski, G.R., Spray, J.G., Lee, P., 2005b. Impactites of the Haughton impact structure, Devon Island, Canadian High Arctic. Meteorit. Planet. Sci. 40, 1789–1812. https://doi.org/10.1111/j.1945-5100.2005.tb00147.x

Palme, H., Göbel, E., Grieve, R., 1979. The distribution of volatile and siderophile elements in the impact melt of East Clearwater/Quebec. Lunar Planet. Sci. X 2465–2492.

Pope, K.O., Baines, K.H., Ocampo, A.C., Ivanov, B.A., 1994. Impact winter and the Cretaceous/Tertiary extinctions; results of a Chicxulub asteroid impact model. Earth Planet. Sci. Lett. 128, 719–725. https://doi.org/http://dx.doi.org/10.1016/0012-821X(94)90186-4

Putnis, A., 2009. Mineral Replacement Reactions. Rev. Mineral. Geochemistry 70, 87–124. https://doi.org/10.2138/rmg.2009.70.3

Quesnel, Y., Gattacceca, J., Osinski, G.R., Rochette, P., 2013. Origin of the central magnetic anomaly at the Haughton impact structure, Canada. Earth Planet. Sci. Lett. 367, 116–122.

https://doi.org/10.1016/j.epsl.2013.02.032

Sapers, H.M., Osinski, G.R., Banerjee, N.R., Ferriere, L., Lambert, P., Izawa, M.R.M., 2014. Revisiting the Rochechouart impact structure, France. Meteorit. Planet. Sci. 49, 2152–2168. https://doi.org/http://dx.doi.org/10.1111/maps.12381

Stöffler, D., Hamann, C., Metzler, K., 2018. Shock metamorphism of planetary silicate rocks and sediments: Proposal for an updated classification system. Meteorit. Planet. Sci. 53, 5–49. https://doi.org/10.1111/maps.12912

Thorsteinsson, R., Mayr, U., 1987. The sedimentary rocks of Devon Island, Canadian Arctic Archipelago. Geological Survey of Canada Memoir 411, Ottawa, Canada.

Vishnevsky, S., Montanari, A., 1999. Popigai impact structure (Arctic Siberia, Russia): Geology, petrology, geochemistry, and geochronology of glass-bearing impactites, in: Dressler, B.O., Sharpton, V.L. (Eds.), Large Meteorite Impacts and Planetary Evolution II Special Paper 339. Geological Society of America, Houston, TX, United States (USA).

Zylberman, W., 2014. Magnetometry and petrography of a core from the Haughton impact structure, Nunavut, Canadian High Arctic.

Zylberman, W., Quesnel, Y., Rochette, P., Osinski, G.R., Marion, C., Gattacceca, J., 2017. Hydrothermally enhanced magnetization at the center of the Haughton impact structure? Meteorit. Planet. Sci. 52, 2147–2165. https://doi.org/10.1111/maps.12917

Chapter 3

3 Characterization of drill cores from the Haughton impact structure, Canada: Implications for impact melting and hydrothermal mineralization

3.1 Introduction

Over seventy percent of known hypervelocity impacts on Earth occurred in targets with sedimentary or mixed crystalline and sedimentary lithologies (Osinski et al., 2008a). Despite this fact, the response of carbonate- and sulfate-rich sedimentary rocks to hypervelocity impact remains poorly understood (Osinski et al., 2008b). Numerous studies have been completed on the topic (e.g., O'Keefe and Ahrens, 1989; Graup, 1999; Agrinier et al., 2001; Langenhorst and Deutsch, 2012; Hörz et al., 2015; Osinski et al., 2015; Bell, 2016; Walton et al., 2019) yet researchers continue to debate the dominant process responsible for impact products in carbonate and sulfate targets: impact-induced melting or thermal decomposition (see Osinski et al. (2008b) for a review). A large part of the problem stems from the difficulty in recognizing and distinguishing between diagenetic, hydrothermal, and impact melt derived carbonate and sulfate minerals. These complexities, in turn, make it difficult for numerical models to quantify volatiles released to the atmosphere. These models are important as the volatiles released as a result of decomposition can have severe and long-lasting effects on climate (Artemieva and Morgan, 2017; Pope et al., 1994).

A better understanding of post-impact hydrothermal processes is also needed, as out of 73 impact structures with evidence of hydrothermal systems, only a dozen have been studied in detail (Kirsimäe and Osinski, 2013; Osinski et al., 2013). Two things are clear, however. First, the chemistry and heterogeneity of the target rocks significantly influence the products of impact melting as well as hydrothermal mineralization, and second, this type of hydrothermal system is characterized by a sequence of retrograde alteration (e.g., Kieffer and Simonds, 1980; Naumov, 2005; Osinski et al., 2013; Osinski et al., 2008a). Mineralization within impact structures is an

important source of economic resources, for example, the formation of the Zn-Pb-Cu deposits at the famous mining camp at the Sudbury impact structure and the Pb-Zn deposits in the Siljan structure in Sweden (Reimold et al., 2005). In addition, impact-generated hydrothermal systems can provide new habitats for thermophilic microorganisms and have potential implications for the origin and evolution of life on Earth, Mars and elsewhere in the Solar System.

In this study, carbonate and sulfate target rocks from the centre of the Haughton impact structure in the Canadian Arctic are thoroughly characterized by examining two shallow drill cores, F2 and F3. The F3 core is similar in appearance to the particulate impact melt rocks previously documented at Haughton (Osinski et al., 2005c), but has a clay mineral groundmass. The F2 core intersected a recently identified lithology: a carbonate-silicate-sulfate melt rock, dominated by a crystalline groundmass that has been intensely hydrothermally altered to clay minerals (Chapter 2). This is the first time that clay minerals have been documented at Haughton. In addition, the F2 core provides important insight into the formation of carbonate and sulfate melt rocks (Osinski et al., 2008b; Stöffler et al., 2018b), as well as a means to differentiate between impact melted and hydrothermal carbonate and sulfate. Together these cores provide the means to explore the crystallization and hydrothermal history at the centre of the crater-fill at the Haughton impact structure and give insight into the heterogeneity of impact melt rocks from mixed sedimentary-crystalline targets.

3.2 Geological Setting and Previous Studies

Haughton is a 23 km diameter complex impact structure located on Devon Island, Nunavut, in the Canadian High Arctic (Fig. 3.1). It was first suggested as an impact structure by Dence, (1972), and later confirmed by the identification of shatter cones (Robertson and Mason, 1975) and coesite within the impactites (Frisch and Thorsteinsson, 1978). It is a relatively young structure with two reported ages, Ar-Ar and (U-Th)/He ages of ~23 Ma (Jessberger, 1988; Young et al., 2013, respectively) and an Ar-Ar age of 39 Ma (Sherlock and Kelley, 2005). The target rocks consist of a 1.8 km thick sequence of Lower Paleozoic Arctic Platform sedimentary rocks overlying the Precambrian crystalline basement of the Superior Province. The Arctic Platform consists of limestone, dolostone, interbedded with sulfate horizons and minor shale and sandstone (Thorsteinsson and Mayr, 1987). The basement rocks consist primarily of a series of

amphibolite to granulite facies quartzofeldspathic and tonalitic gneisses, metasedimentary rocks, metabasalt, and Proterozoic diabase dykes (Frisch and Trettin, 1991; Metzler et al., 1988). No significant geologic events have taken place in the region since the impact, with the exception of some glacial and periglacial erosion. Given its young age and its ideal location in a geologically stable, uninhabited arctic environment, Haughton is one of the best-preserved and well-exposed impact structures on Earth.

Extensive mapping and geological investigations of the structure began in the late 1970s and continue today (e.g. Robertson and Mason, 1975; Frisch and Thorsteinsson, 1978; Robertson and Plant, 1981; Grieve, 1988; Pohl et al., 1988; Redeker and Stöffler, 1988a, 1988b; Robertson, 1988; Osinski et al., 2005c; Osinski and Spray, 2005; Singleton et al., 2011; Greenberger et al., 2016). The cratering model and geology of the exposed impactites at Haughton have been well documented (Osinski et al., 2005c, 2005b). The crater rim consists of faulted blocks of the target lithologies, where the fractured and brecciated target rocks exposed become older towards the centre of the structure. A significant part of the centre of the structure is covered by crater-fill impactites consisting of grey clast-supported lithic breccias overlain by groundmass-supported, particulate impact melt rocks with a groundmass of microcrystalline calcite, anhydrite and silicate glass with clasts of all known target lithologies. The term 'particulate' has been applied to the Haughton impactites, describing a heterogeneous aphanitic or glassy groundmass comprising intermingled melt phases (Osinski et al., 2008a) which is different from coherent crystalline groundmass. Carbonate melt rocks at Haughton were first examined by Osinski and Spray (2001) wherein microcrystalline calcite in the particulate melt rocks shows igneous textures: spherules and globules within silicate glass, and micro-immiscibility textures. This interpretation is supported by experimental work on the phase relations of calcite, which show that carbonates respond to hypervelocity impact by melting (Ivanov and Deutsch, 2002). These same authors later investigated anhydrite within the impact melt rocks at Haughton and suggest that they crystallized from an impact-generated melt (Osinski and Spray, 2003) on the basis of the presence of sulfate-carbonate-silicate immiscibility textures and possible quench and flow textures in the groundmass-supported crater fill.

Preliminary characterization of the hydrothermal activity at Haughton identified quartz-carbonate-sulfate-sulfide mineralization within four distinct settings and styles: vugs and veins

46

within impact breccias, as cement in the central uplift impactites, veining within the faulted target blocks in the outer margin of the central uplift and as hydrothermal pipes within the faulted crater rim (Osinski et al., 2005a, 2001). Quartz was the only hydrothermal phase identified in impactites at the centre of the structure (Osinski et al., 2005a). Minor montmorillonite is suspected in one calcite-marcasite vug in the periphery of the central uplift, as well as sulfate and iron oxide mineralization as a result of weathering (Greenberger et al., 2016; Izawa et al., 2011), but no other clay minerals have been documented to date. A model for the evolution of the hydrothermal system was defined in three stages (Osinski et al., 2001). The first was a high temperature (>200°C) stage that consisted dominantly of quartz precipitation; the second occurred at moderate temperature (200–80 °C) and consisted of calcite, marcasite, pyrite and minor celestite, barite and fluorite. Finally, a low temperature (<80 °C) stage was dominated by further carbonate and selenite precipitation. The sulfides were further altered through weathering to form fibroferrite, jarosite, goethite, copiapite, rozenite, melanterite and szomolnokite (Greenberger et al., 2016; Izawa et al., 2011).

Quesnel et al. (2013) conducted localized geophysical surveys to explain the unique coupled negative gravity anomaly and positive magnetic anomaly at Haughton. They concluded that a km-sized body with enhanced magnetization is the result of hydrothermal alteration in the porous crater-fill deposits located at Anomaly Hill, in the centre of the structure (Fig. 3.1). Shallow drilling was subsequently completed to sample the anomaly near the surface. Two cores were successfully collected, F2 within the anomaly and F3 just outside of it. The F3 core consists of fragments collected between depths of 2.9 m to 4.9 m; by comparison, the F2 core consists of nearly continuous core from a depth of 8.6 m to 12.8 m (Zylberman, 2014). Preliminary petrography and magnetometry of the cores were conducted by Zylberman et al. (2017) whom confirmed that the F2 and F3 cores were very different from one another, and that the F2 core was more intensely hydrothermally altered than F3. To date, these are the only cores of impactites at Haughton.

Chapter 2 describes the F2 core as a heterogeneous crystalline silicate-carbonate-sulfate impact melt rock on the basis of igneous textures. Textures include intergrowths between silicate and carbonate and silicate and sulfate groundmass, reaction rims of clasts, and textures representative of rapid crystal growth, such as acicular, dendritic and skeletal grains of silicate

47

and carbonate. These rapid growth textures were not observed in the sulfate groundmass. The study inferred that the core represents a body of new impact melt rock at Haughton, one completely unexposed but likely on the order of a kilometre in diameter.
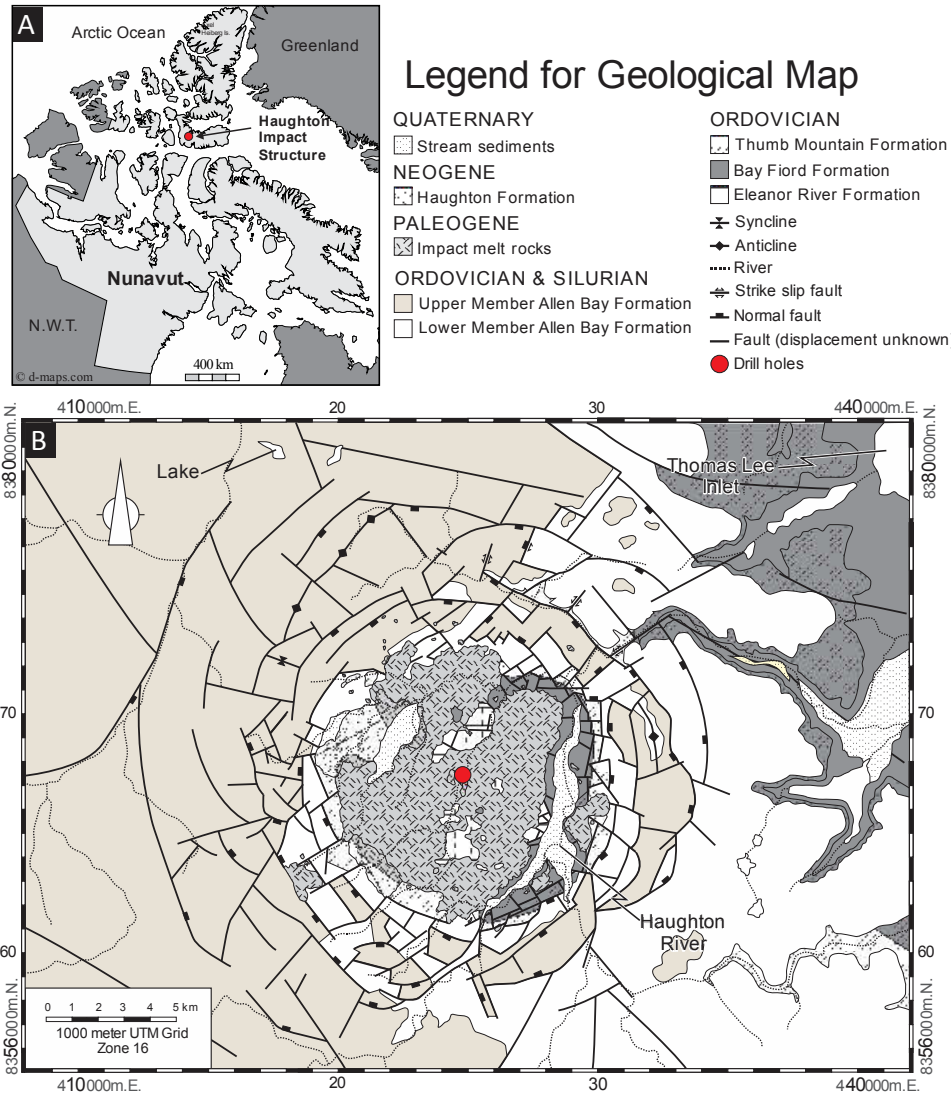
Figure 3.1 Geologic map of the Haughton impact structure, identifying the location of the drill core. Modified from Osinski et al. (2005).

3.3 Methodology

3.3.1 Petrography

Petrography of 15 polished thin sections of both the F2 and F3 cores were completed using a Nikon LV100POL petrographic microscope. Microanalyses were completed using the JEOL JXA-8530F Field-Emission Electron Probe Microanalyzer at the University of Western Ontario's Earth and Planetary Materials Analysis Laboratory. Imaging and petrography were complicated by poor polishing, a result of the very soft, sulfate-rich sample material. Examination of the groundmass and clast phases were completed first with backscattered electron (BSE) imagery, secondary electron, and panchromatic cathodoluminescence imaging and energy dispersive spectrometry (EDS) for geochemical context. Element maps were constructed of areas of interest with a step size of 0.26 μm and a dwell time of 10 ms. Wavelength dispersive spectrometry (WDS) was used to map Mg, Ca, Mn, Fe, Al, K, S and Cl and energy dispersive spectrometry (EDS) was used to map Si, C, F, Na, Sr and Ba. Element maps, spectrometry and associated BSE images were collected with the probe current set to 15 kV and 50 nA. EPMA-cathodoluminescence mapping was completed concurrently under the same conditions to produce greyscale panchromatic images.

For carbonate analyses, WDS were collected at 15 keV and 5nA, using a 25 μm spot size. The spot size was locally reduced to accommodate the area available for analysis. Elements included were Ca, Mg, Fe, Mn, Sr, Ba, Si, S, Cl, F and Al, with standards calcite, dolomite, siderite, siderite, strontianite, barite, quartz, anhydrite, sodalite, fluorite and corundum, respectively. For silicates, wavelength dispersive spectrometry was collected for Si, Ti, Cr, Al, Mg, Mn, Fe, Ca, Na, K, P, Cl, F and S, with standards enstatite, rutile, chromite, albite, enstatite, rhodonite, hematite, diopside, albite, orthoclase, apatite, sodalite, fluorite and anhydrite, respectively, at 15 keV, 20nA, a 2 to 5 μm spot size, and peak and background count times of 30 s and 15 s, respectively. Microprobe detection limits range from 100 to 500 ppm for major element oxides, and from approximately 200 to 800 ppm for minor element oxides.

Backscattered electron (BSE) mosaics were completed on 2 entire thin sections, one representative section each for the F2 and F3 cores. The BSE maps were collected at 15 keV accelerating voltage, 20 nA probe current, with brightness and contrast selected to distinguish the

minerals of interest, using the GuideNet mapping option in the JEOL software at a magnification of 40x. The program automatically measures a series of adjacent areas and stitches them together at the seams. The maps were then processed and analyzed using ImageJ software, wherein images were smoothed or blurred, edges identified when necessary and brightness and contrast settings were adjusted. Corrections were completed by hand to account for software errors and holes in the thin section. This was followed by bilevel thresholding to make specific features of interest stick out. F3 core was especially difficult to differentiate clasts from groundmass given the groundmass composition is similar to a large portion of the clasts. Proportions of groundmass and clasts were attained through ImageJ calculations of the resulting black and white pixel images.

3.3.2 Raman

Most of the principal mineral phases (e.g., calcite, anhydrite, bassanite, gypsum, quartz), were identified or confirmed by laser Raman spectroscopy on both core samples. Other phases, including a series of clay minerals were analyzed but were unsuccessful, mainly due to florescence. Analyses were completed on a Renishaw InVia Reflex Raman spectrometer at Surface Science Western. Samples were viewed using an optical microscope integrated with the Raman. Laser wavelengths used were 785, 633 and 514 nm, the latter most frequently, with two gratings 1800 and 1200 l/mm. Each laser is equipped with a polarizer and half waveplate. Spot size is 1-2 μm. Most spectra were collected with a spectral range of 50 to 1250 cm^{-1}, some hydrated phases and fluid inclusions were also analyzed from 2000 to 4000 cm^{-1}. The data was processed using both Renishaw Wire 4.2 and CrystalSleuth software, and phases were identified using comparisons to Raman spectra from the RRUFF sample database (Appendix G). Spectra were interpreted individually, without stacking. The Raman spectrometer also has a confocal mode for focusing the beam below the surface of the sample, but this in turn lowered the resolution of the results.

3.3.3 Reflectance Spectroscopy

Hydrated minerals in the F2 and F3 cores were identified using an ASD Incorporated PANanalytical Company TerraSpec Halo handheld spectrometer. The Halo instrument captures visible near-infrared (VNIR 350-1000 nm) and near-infrared (NIR: 1001-2500 nm) spectra. The

reflectance data is displayed as a function of wavelength. The instrument calibrates itself at the beginning of each use with a Spectralong white reference disk. The Halo light source is a quartz tungsten halogen bulb, with spectral resolution of 3nm @ 700 nm, 9.8 nm @ 1400 nm and 8.1 nm @ 2100 nm. The spectrometer uses a 512 element silicon array VNIR detector and a InGaAs photodiode, TE cooled SWIR q and 2 detectors. The signal to noise ratio for VNIR and SWIR 1 is 9000:1 at 700 and 1400 nm, respectively, and SWIR 4 is 4000:1 @ 2100 nm. The internal fiber optic has a numerical aperture of 0.22. Spectra were collected on offcuts of the cores. Spectral processing was performed using the Environment for Visualizing Images (ENVI) software, wherein spectra were compared to the USGS Spectral Library mineral database for absorption features characteristic of molecular bond vibrations within specific mineral phases. Eighteen analyses were collected of the F2 core, and seven of the F3 core.

3.4 Results

Visible differences between the F2 and F3 cores were immediately apparent: F2 is light green to white in colour with dominantly light-coloured large clasts and a coarse-grained groundmass (Chapter 2), whereas F3 is dark grey with a range of clast sizes and a fine-grained groundmass (Figs. 3.2 and 3.3). A comparative summary of the properties of the two cores, including previously documented impact melt rock at Haughton, is presented in Table 3-1.

Table 3-1 Summary characteristics of the three types of impact-generated melt rocks at Haughton.

Characteristic	F2 Core	F3 Core	Particulate impact melt rocks, crater interior (Osinski et al., 2005)
Groundmass or clast supported?	Variable, clast to groundmass supported	Groundmass supported	Groundmass supported
Clast size range	300 μm to 1 cm	<5 μm to 4 mm	<25 cm to 5 m
Groundmass Composition	calcite, Mg-rich clay minerals, anhydrite-gypsum	silicate (clay minerals)	microcrystalline calcite, silicate glass, anhydrite
Groundmass Proportion	20–65%	20–30%	50–60%
Clast Proportion	35–80%	70–80%	40–50%
Mineral and Lithic Clasts Present (vol %):			
Limestone (or calcite grains)	up to 20	up to 50	up to 6
Dolomite	None	up to 25	10–45
Gneiss (incl. quartz, feldspar)	up to 60	up to 10	up to 2–8
Mafic clasts, diopside marble	up to 15	up to 5	na
Silicate glass	None	None	up to 10
Sandstone and shale	None	None	up to 1-2
Anhydrite, gypsum	**up to 5	None	up to 9
Other minerals (incl. sulfides, titanite, zircon, apatite, celestite, barite)	< 1	up to 1	up to 5

* na = not available **likely replacement
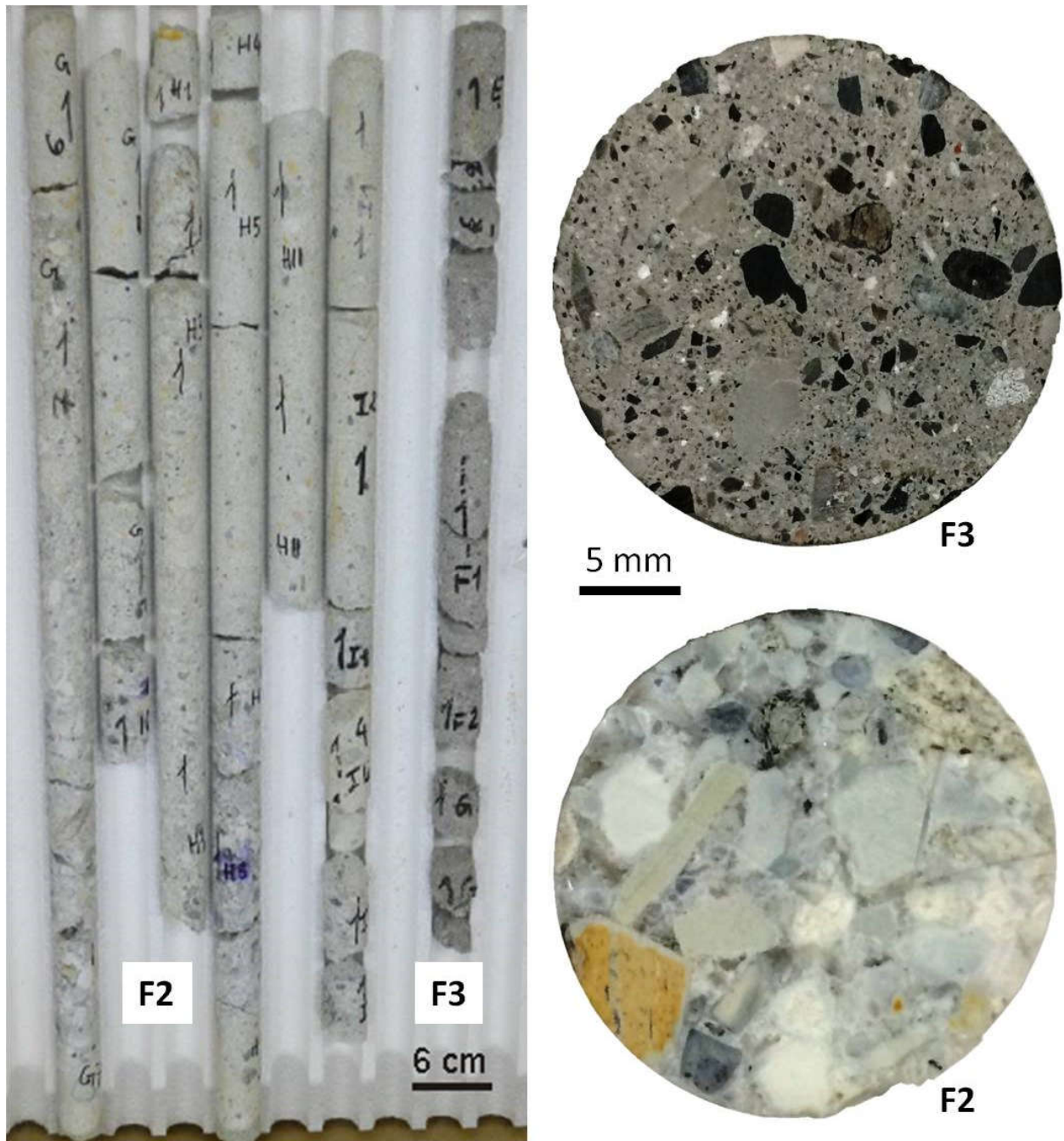
Figure 3.2 Left: F2 and F3 cores in core box (modified from Zylberman, 2014). Right: cross sections of F2 and F3 cores. Note the difference in colour, texture and clasts populations between cores. F3 is more representative of the particulate impact melt at Haughton. Cross section of each core is approximately 2.5 cm.
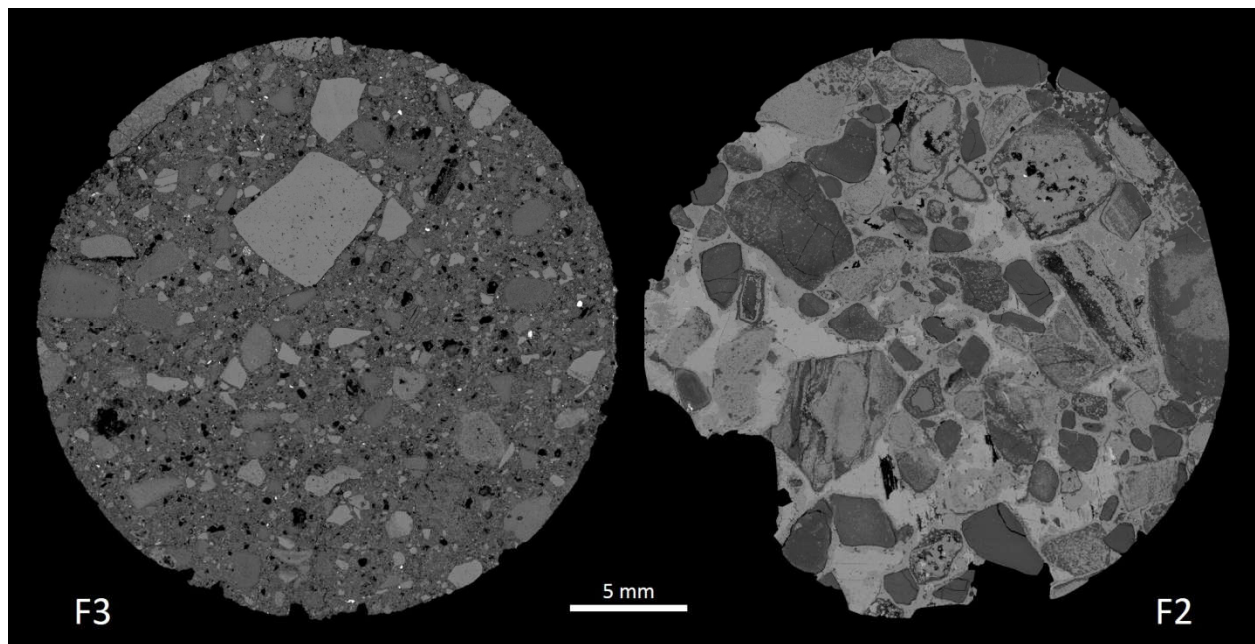
Figure 3.3 Backscattered electron maps of HAUF3C (left) and HAUF2G7uwo2 (right), representative sections of the F3 and F2 cores.

3.4.1 F3 Core

The F3 core is a medium to dark grey, clast-rich polymict impactite. The general texture of the rock is consistent throughout the core. On the macro-scale, it is very similar in appearance to the clast-rich impact melt rocks that comprise the bulk of the crater-fill at Haughton (Osinski et al. 2005c). The F3 core is groundmass-supported, fragmental and poorly-sorted (Figs. 3.4 A-B). Examination using a petrographic microscope is quite difficult as the groundmass is a friable grey to brown and clasts are poorly recognizable. BSE imagery analysis indicates that the groundmass consists of a fine-grained fibrous clay mineral (Figs. 3.4 C-D). Within the groundmass, there is a generally high concentration of micrometre-scale fragments or grains, dominantly of calcite. The groundmass proportion ranges from 20 to 30 vol%; therefore, the rock consists of up to 80% clasts. The overall clast size varies from < 5 µm to > 4 mm, but the vast majority are 10 to 100 µm in width.

Most clasts in the F3 core are mineral or lithic fragments with preserved internal textures. The clast population consists of angular, sub-rounded to irregular fragments of all target lithologies except for sulfates (Figs. 3.5 A-F). Clasts consist of both lithic and individual mineral clasts that originated from disaggregated target rocks. Lithic clasts consist of limestone (Fig. 3.5A), dolomite (Fig. 3.5B), gneiss, metagranite, diopside, diopside marble (Fig. 3.5C) and diabase. Mineral clasts include quartz (Fig. 3.5D), K-feldspar (Fig. 3.5E), plagioclase, biotite (Fig. 3.5F), clinopyroxene, magnetite, titanomagnetite, apatite, celestite, barite and zircon. Anhydrite and gypsum were not observed in the groundmass or as clasts. Shock metamorphic features observed include kink-banding in biotite (Fig. 3.5F) as well as planar fractures and planar deformation features (PDFs) in quartz (Fig. 3.5D). Partially digested and relict clasts are common (Fig. 3.5D); clast coronas are present but very thin (< 100 μm), visible only in BSE images. These partially digested clasts show more evidence of alteration, with potassium feldspar having been particularly susceptible (Fig. 3.5D). Figure 3.5A shows a silicate groundmass that intruded into a limestone clast. BSE and EDS analysis show that the intrusion is of a slightly different composition and has fewer and smaller clasts than the groundmass surrounding the clast. Most silicate clasts consist of clay minerals and/or are partially replaced by calcite. No veins or vugs were observed.

Two thin sections of the F3 core were analyzed by microprobe to determine silicate groundmass composition (Table 3-2). The groundmass compositions range from: 33.81 to 55.38 wt% SiO_2; 17.62 to 25.55 wt% MgO; 2.78 to 12.75 wt% Al_2O_3; 1.14 to 16.06 wt% CaO; and 1.11 to 3.12 wt% FeO. K_2O, Na_2O, and TiO_2 are present only in trace amounts. The low totals (73-94%) and overall composition is consistent with a spectrum of Mg-rich clay minerals. Clay minerals are also consistent with the morphology and grain size observed (Fid. 3.4D). Compositions generally do not have ideal clay mineral stoichiometry (Appendix C) and are examined in more detail below.

Reflectance spectra of the F3 and F2 cores (UV-vis-NIR range of 350–2500 nm) show absorption features of hydrous minerals including OH stretching overtones near 1400 nm, HOH stretching overtones at 1410 nm, HOH combination stretching and bending vibrations at 1910 nm, and OH-metal bands between 2200 –2400 nm (Fig. 3.6). The metal-OH bands can be diagnostic for clay mineral identification (Clark et al., 2007, 1990). It is important to note,

however, that each reflectance spectra represent a combination of both the groundmass and clasts of the cores given the spot size so are representative of multiple of minerals.

The spectra for F3 show, with one exception, absorption bands at 610 and 711 nm, which are likely due to the presence of Fe-oxide. The F3 spectra have a doublet at the 1400 nm and an absorption at 1900 nm with a shoulder at 1950 nm. There are 3 diagnostic absorption features, at 2315 nm (strong), 2294 nm (weak) and 2392 nm (weak). There is also an unidentified weak feature at 2347 nm. The Mg-OH band at 2315 nm is somewhat sharp and symmetrical. Representative spectra of both cores are plotted with spectra of phases known to be present through petrographic and Raman analyses (calcite and gypsum), as well as a range of Mg-rich clay mineral spectra that are potentially present, based on the silicate groundmass geochemistry and spectral analysis (Fig. 3.18). The best spectral fit to the 2310 μm band and to the overall spectra is saponite. However, it is not an exact match. Talc also matches quite well and there is a subtle 2243 nm feature present in F3 and talc but missing from the saponite spectra.

Table 3-2 Average WDS analyses of the F3 core silicate groundmass.

Sample Name	HAUF3C n=10	SD	HAUF3F1B n=9	SD	Average All F3 n=19	SD
SiO_2	42.78	4.08	46.57	4.51	44.57	4.60
Al_2O_3	5.40	1.05	5.65	2.90	5.52	2.07
Na2O	0.05	0.03	0.04	0.02	0.05	0.02
MgO	20.92	1.64	21.94	2.30	21.40	1.99
F	0.21	0.07	0.16	0.08	0.18	0.08
TiO_2	0.36	0.65	0.03	0.02	0.21	0.49
CaO	5.39	4.93	4.70	3.33	5.06	4.15
P_2O_5	0.03	0.04	0.02	0.01	0.02	0.03
FeO	1.87	0.66	1.40	0.14	1.65	0.53
MnO	0.02	0.01	0.02	0.01	0.02	0.01
Cr_2O_3	BDL		BDL		BDL	0.01
K_2O	0.75	0.84	1.09	1.52	0.91	1.19
Cl	0.09	0.03	0.08	0.03	0.09	0.03
SO_3	0.18	0.10	0.16	0.22	0.17	0.17
Total	78.04		81.85		79.84	

Values are in weight percent; n=number of probe spots. BDL = below detection limit.
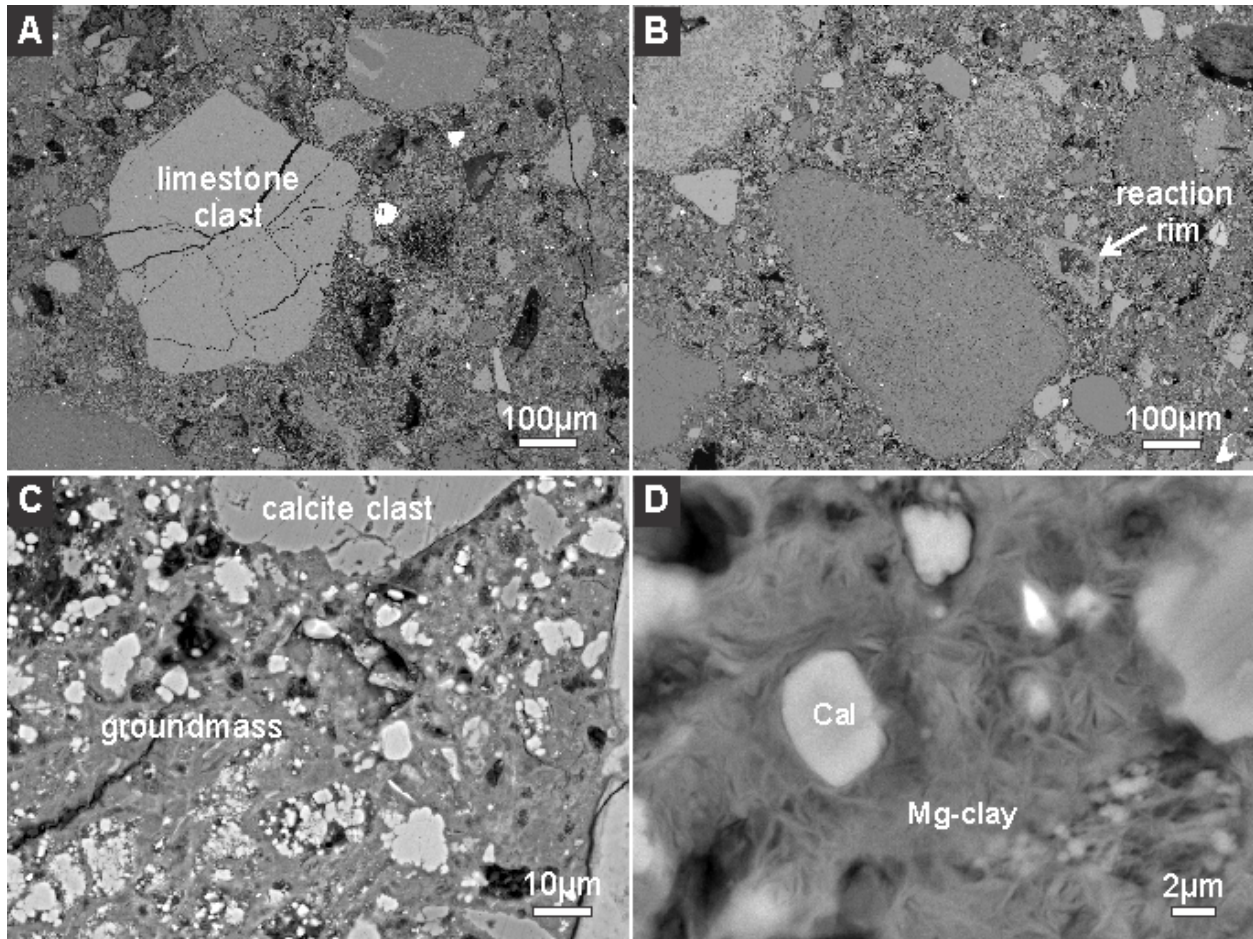
Figure 3.4 BSE photomicrographs of the F3 core illustrating the groundmass at various magnifications: A) and B) show a poorly sorted impactite with a variety of clasts. The largest left of centre in A is a limestone clast. Note the reaction rim in B; C) 1100X magnification, showing interclast texture of the silicate groundmass; D) 8500X magnification showing silicate groundmass cementing micrometre-scale clasts. Cal = calcite.
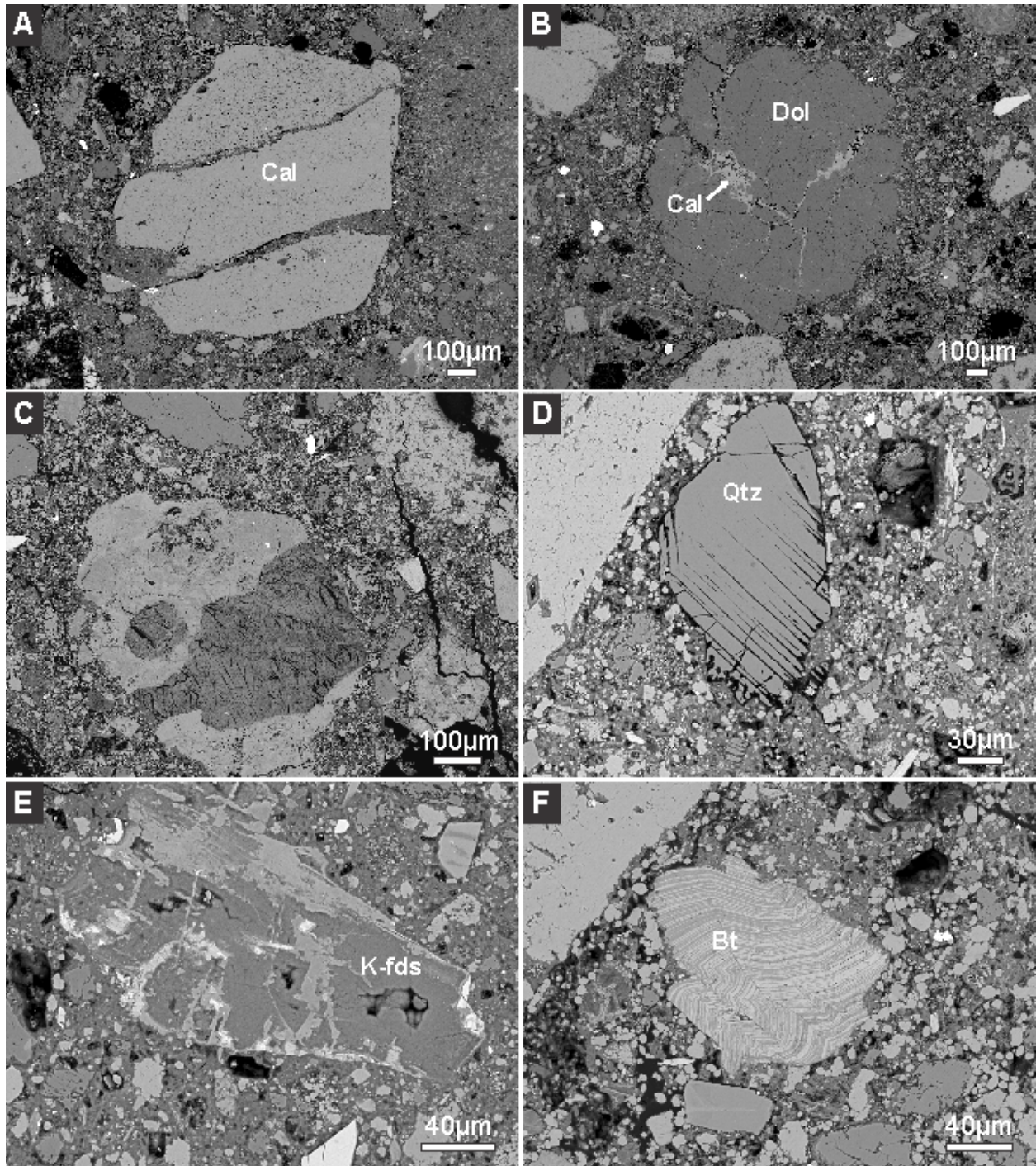
Figure 3.5 BSE photomicrographs of the F3 core: A) limestone clast with two groundmass intrusions; B) dolomite clast with calcite along fractures; C) diopside-K-feldspar marble clast; D) quartz clast with planar fractures E) altered potassium feldspar; F) kink-banding in biotite.
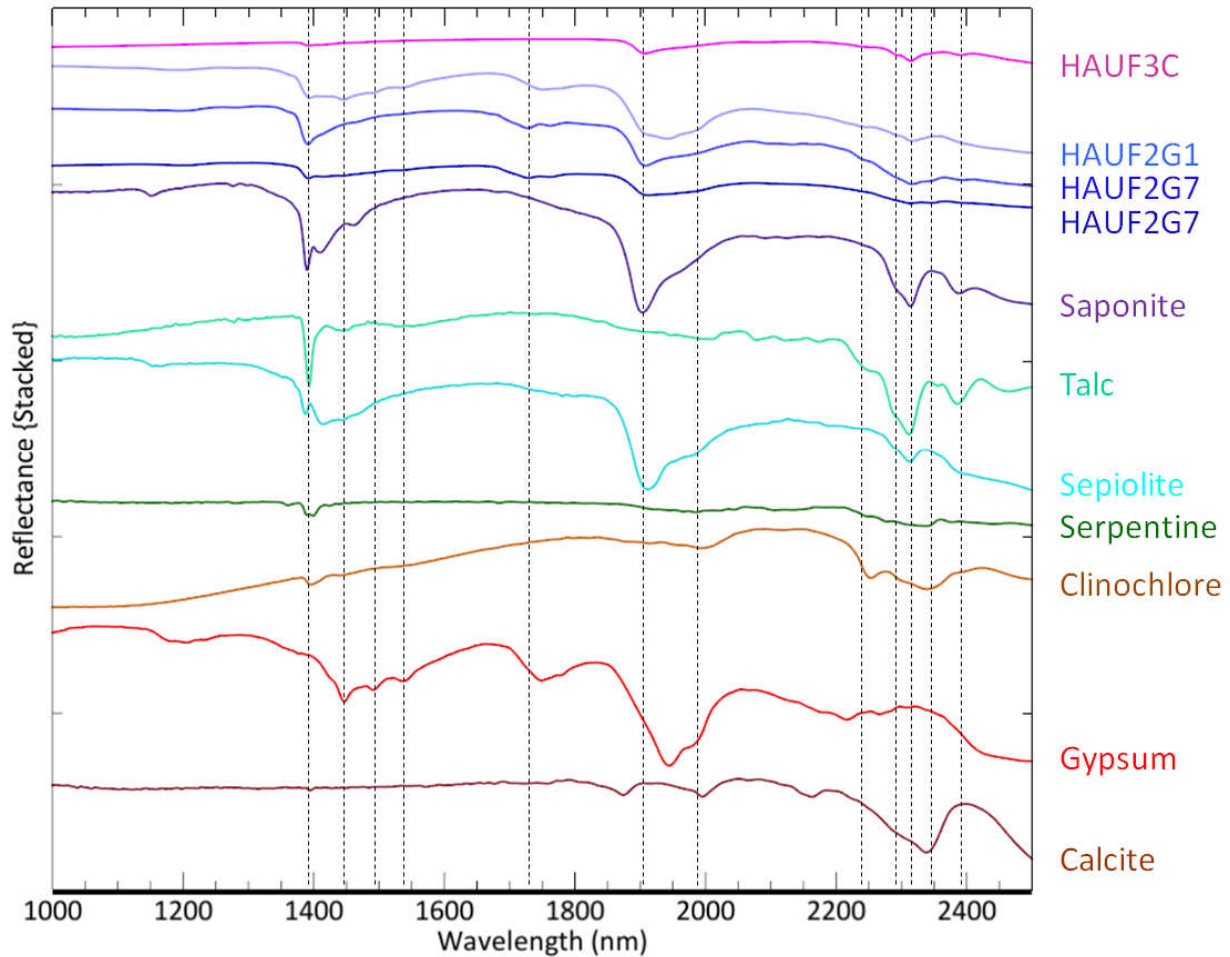
Figure 3.6 Comparison of representative core spectra from the F2 and F3 cores (HAUF#) with Mg-rich clay minerals, gypsum and calcite from 1000 to 2500 nm. Reference mineral spectra are from the USGS Beckman Mineral 3375 database including saponite (SapCa-1.AcB), talc (HS21.3B), sepiolite (SepNev-1), serpentine (HS318.4B), clinochlore (GDS158 Flagst), gypsum (SU2202) and calcite (HS48.3B). All spectra are available in Appendix D.

3.4.2 F2 core

The F2 core is both compositionally and texturally heterogeneous. The core stratigraphy is depicted in Figure 6 of Zylberman et al. (2017). It is a white to pale green clast-rich polymict impactite, with a lower density and higher natural remanent magnetization (NRM) than the F3 (Zylberman, 2014). Basic descriptions of groundmass mineralogy and igneous textures were

59

presented in Chapter 2. Here we present more detailed textural and chemical descriptions including quantified proportions and breakdown of groundmass into subtypes.

Groundmass proportion varies widely from 20 to 65%, consisting of 3 different but intermingling compositional types: 1) calcite; 2) anhydrite-gypsum; and 3) clay minerals. This lithology is largely clast-supported. Quantitative abundances obtained with Image J analysis of a single representative thin section of F2 are 12 vol% sulfate groundmass; 26 vol% carbonate groundmass; 1 vol% silicate groundmass and 61 vol% clasts (see Appendix H). Clast proportion ranges from 35 to 80% where most clasts are >300 µm to <1 cm, rounded, zoned and/or intensely altered. The largest clasts are most common in the carbonate groundmass, whereas smaller clasts are more common within the silicate-rich groundmass. Clast lithologies are dominated by silicate rock fragments of gneiss and diabase from the crystalline basement. Carbonate clasts are common but largely appear to be replacement of silicates. Sandstone, shale and dolomite clasts were not observed, and anhydrite is rare. Hydrothermal alteration is pervasive throughout the core, including silicate alteration to clay minerals, calcite and gypsum replacement, as well as centimetre-scale selenite veins. Each groundmass type is described in detail below.

3.4.2.1 *Calcite groundmass*

Calcite is present in the F2 core as a groundmass phase in a variety of compositional and textural forms (Table 3-3). Previous work did not divide the calcite into types. Optical microscopy as well as EPMA-BSE-CL-WDS mapping were combined to investigate calcite variability (e.g. Fig. 3.7). Six main types of calcite (A, B, C, D, E and F) are distinguished, based on composition and texture. Representative microprobe compositions are given for each type in Table 3-4 (see Appendix C for all microprobe analyses of carbonates). The largest variations in calcite chemistry are of MgO, SO_3, SiO_2 and Al_2O_3. All other measured oxides have values in trace amounts or below detection limits.

Type A calcite is an optically pure, colourless sparry calcite, which generally occurs as cement that has infilled interclast and intraclast space (Fig. 3.8A). Type A is the most abundant form of calcite observed in the F2 core. Grain size ranges from 5 to 300 µm and it generally lacks any internal structure or inclusions. Calcite also occurs as acicular to radial clusters (see

Chapter 2), which may or may not have a silicate corona (Fig 3.8B). Type A commonly surrounds, or has infiltrated or is present adjacent to other types of calcite, particularly Type B.

Types B and C are silica-rich calcite. Type B is irregularly shaped and contains silicate inclusions <20 μm across that are distributed throughout the crystals which give it a 'dirty' appearance in this section (Fig. 3.7). Microprobe spot analyses of Type B calcite show elevated silica abundances, with an average of 1.87 wt% SiO_2 (Table 3-4). Type C is also silica-rich with acicular silicate inclusions wherein it commonly occurs as sparry calcite that is intergrown with acicular to spherulitic silicate (Figs. 3.8C-D). The intergrowths are observed both wholly within a calcite grain (Fig. 3.8D) as well as across calcite grain boundaries (Fig. 3.8C). The acicular inclusions are ≤5 μm in width and range in length from 1 to 80 μm, are pleochroic (colourless to a faint green to gray), and highly birefringent. The abundance of the inclusions is the reason the calcite is so silica-rich; the microprobe beam size was reduced to 1-2 μm, but inclusions were inevitably incorporated into the analysis (Table 3-4). Figure 3.8E shows a single calcite grain with an inclusion-rich core and growth zone, with sparry calcite in between. There is a core rim that is interfingered with the outer rim calcite that may be fluid related.

Type D calcite is sulfur-rich (up to 5 wt% SO_3), non-porous and generally occurs as rims around clasts (Fig. 3.8F) displaying low cathodoluminescence (Figs. 3.9 and 3.10). It is commonly overgrown by a sulfur-poor calcite and/or partially replaced by Type D calcite.

Types E and F calcite are porous with an abundance of voids less than 5 μm and has a composition that is sulfur-rich to sulfur-poor. Type E has irregularly-shaped voids. This type has previously been interpreted as replacement calcite (Chapter 2) because of its wispy terminations (Fig. 3.9). Type F has spherical voids, or vesicles, which have previously been interpreted as a primary igneous texture (Chapter 2). Both types E and F may be filled with sulfate inclusions identified by EDS spot analyses and can occur as single grains or be concentrated in the core of a grain (Fig. 3.8E). Globule-shaped, porous to sulfur-rich regions of the calcite groundmass are common adjacent to acicular calcite.

Table 3-3 Relationship between chemistry and texture of calcite in the groundmass of the F2 core.

Type	Texture								Occurrence	
	Sparry calcite	Aci. to spherulitic calcite	Porous	Sulfate incl.	Irr. silica incl.	Aci. silica incl.	pseudo-morphic	Over-growth	Inter-clast	Intra-clast
A: clean	Y	Y	N	N	N	N	Y	Y	Y	Y
B: silica-rich	N	N	N	N	Y	N	N	N	Y	N
C: silica-rich	N	N	N	N	Y	Y	N	N	Y	Y
D: sulfur-rich	Y	N	Y	N	N	N	N	Y	Y	N
E: clean to S-rich	N	N	Y	Y	N	N	N	Y	Y	N
F: clean to S-rich	N	N	Y	Y	N	N	N	Y	Y	N

Incl. = inclusions; Aci = acicular; Irr = irregular.

Table 3-4 Representative WDS analysis of calcite types in the F2 core.

Calcite Type	Sparry		Silica-rich		Silica-rich Aci.		Sulfur-rich		Porous		Porous sph.	
	A	S.D.	B	S.D.	C	S.D.	D	S.D.	E	S.D.	F	S.D.
	n=17		n=5		n=6		n=6		n=2		n=2	
SiO_2	0.10	0.07	1.87	1.71	8.48	3.98	0.02	0.03	0.10	0.02	0.07	0.02
Al_2O_3	0.03	0.04	0.16	0.09	0.40	0.14	nd	nd	nd		0.04	0.02
MgO	0.06	0.05	0.93	0.87	4.63	2.23	0.11	0.13	0.07	0.02	0.15	0.00
F	0.17	0.09	0.23	0.04	0.15	0.14	0.12	0.10	0.20	0.17	0.37	0.40
CaO	57.47	0.52	55.11	1.49	47.39	3.84	57.27	0.66	56.75	0.28	55.28	0.48
FeO	0.02	0.01	0.02	0.02	0.04	0.01	0.02	0.00	nd	nd	0.03	0.01
MnO	0.02	0.01	0.01	0.00	0.02	0.01	0.02	0.01	nd	nd	nd	nd
Cl	nd	nd	0.02	0.02	0.02	0.01	nd	nd	nd	nd	nd	nd
SO_3	1.22	0.83	1.24	0.69	0.75	0.19	3.26	1.13	0.77	0.20	4.59	0.32
BaO	0.05	0.04	0.03	0.02	0.06	0.03	0.03	0.01	0.06	0.02	nd	nd
SrO	0.36	0.18	0.14	0.10	0.11	0.06	0.28	0.10	0.12	0.07	0.68	0.06
Total	59.49		59.78		62.05		61.15		58.07		61.21	

All values are in wt%. n = number of analyses; nd = not detected, detection limits of major element oxides ~200-500 ppm; ~200-800 ppm for minor element oxides; Aci = acicular; sph = spherical.
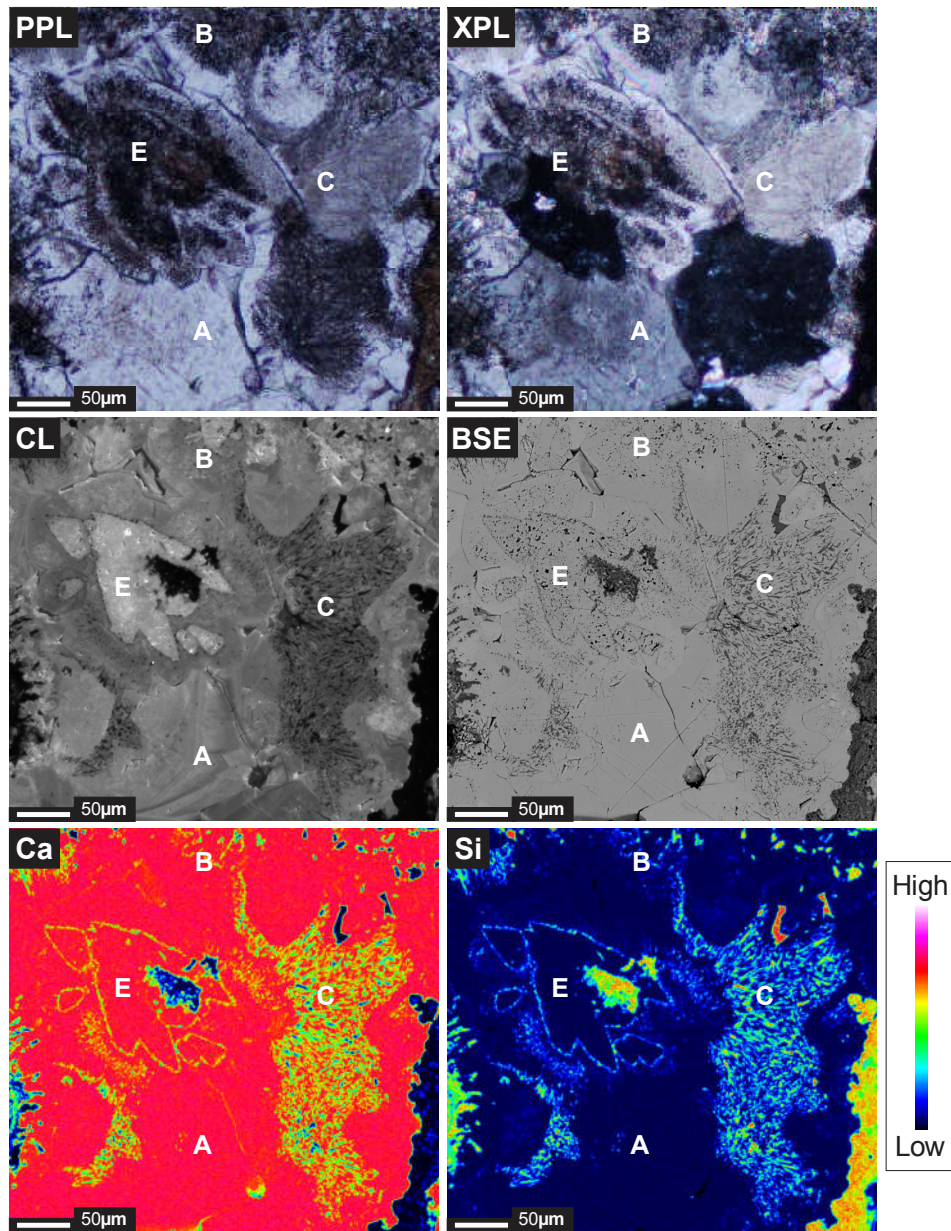
Figure 3.7 Optical photomicrographs in plane-polarized (PPL) and crossed-polarized light (CPL) as well as BSE-CL-WDS maps of a region of the F2 core rich in calcite illustrating calcite types A, B, C and E in the groundmass and the benefit of utilizing all the above visual data combined. Compare grain boundaries and zoning in plane light and CL, in particular. Note that porous calcite shows up as very bright in CL.
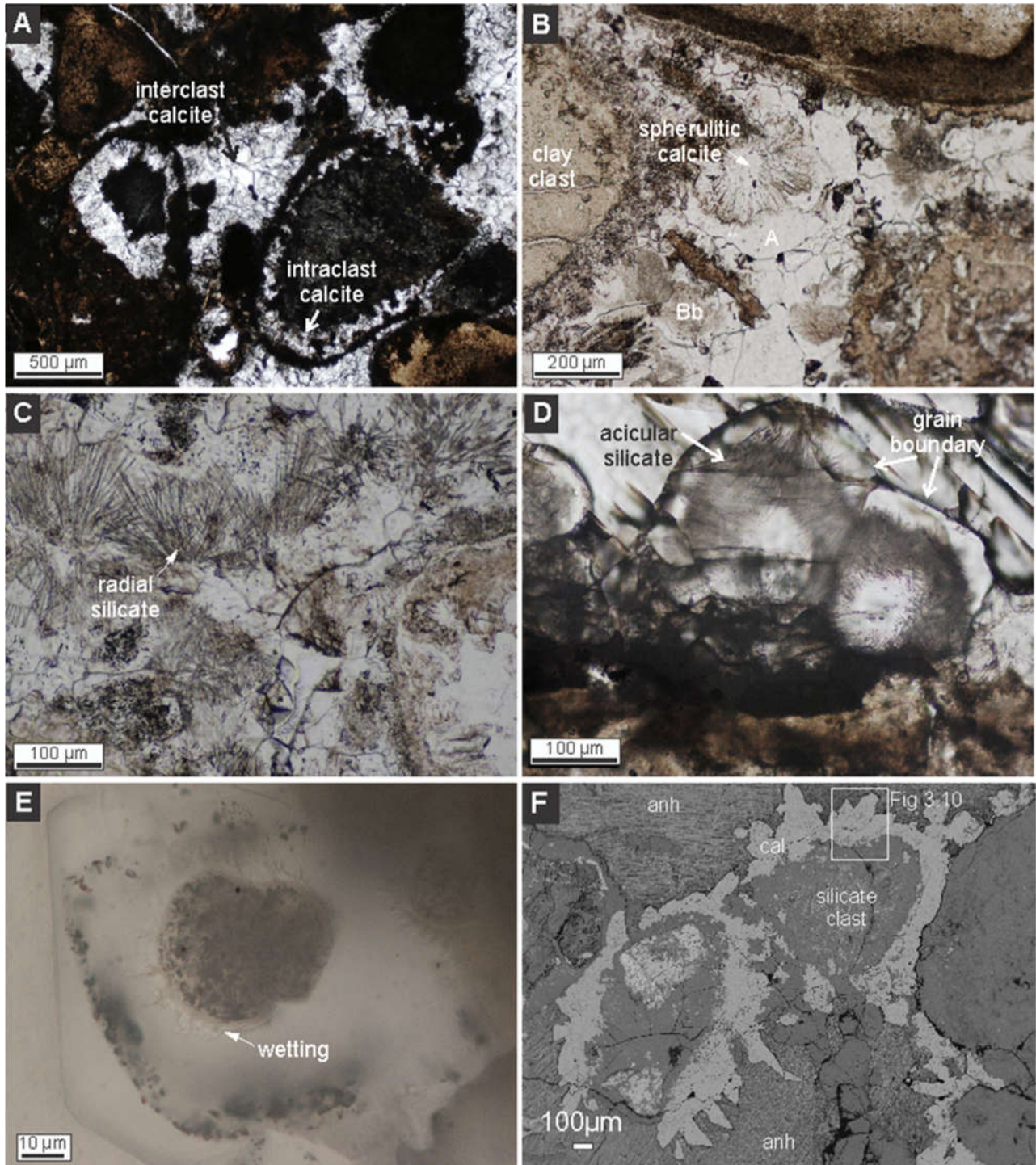
Figure 3.8 Plane-polarized optical photomicrographs of calcite A-E showing: A) intraclast and interclast occurrences of Type A calcite; B) Spherulitic calcite with silicate corona, surrounded by calcite cement, Type A; C) Type Bb acicular to radial silicate inclusions in calcite groundmass; D) Type Bb in thick section showing another calcite grain with

acicular to radial silicate needles with inward radial growth; E) Single calcite grain with inclusion-rich core; note the wetting contact between the core and centre grain, and a second zone of dark inclusions; and F) BSE image of calcite corona around clasts, hosted by anhydrite groundmass. White box in context contour for Figure 3.10.
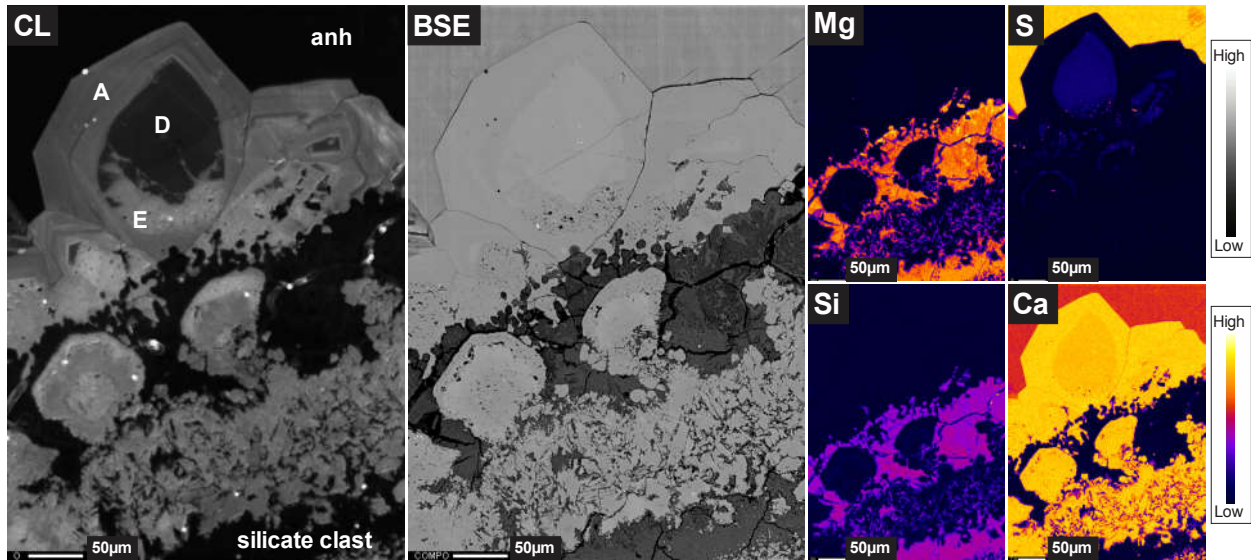
Figure 3.9 BSE-CL-WDS maps of the edge of a clast in the F2 core showing a variety of textures including wormy to vermicular texture between silicate and calcite and calcite overgrowths with S-rich Type D calcite, S-poor Type A calcite, and Type E altered porous calcite with sulfate-filled voids. Note that porous calcite shows up as very bright in CL.
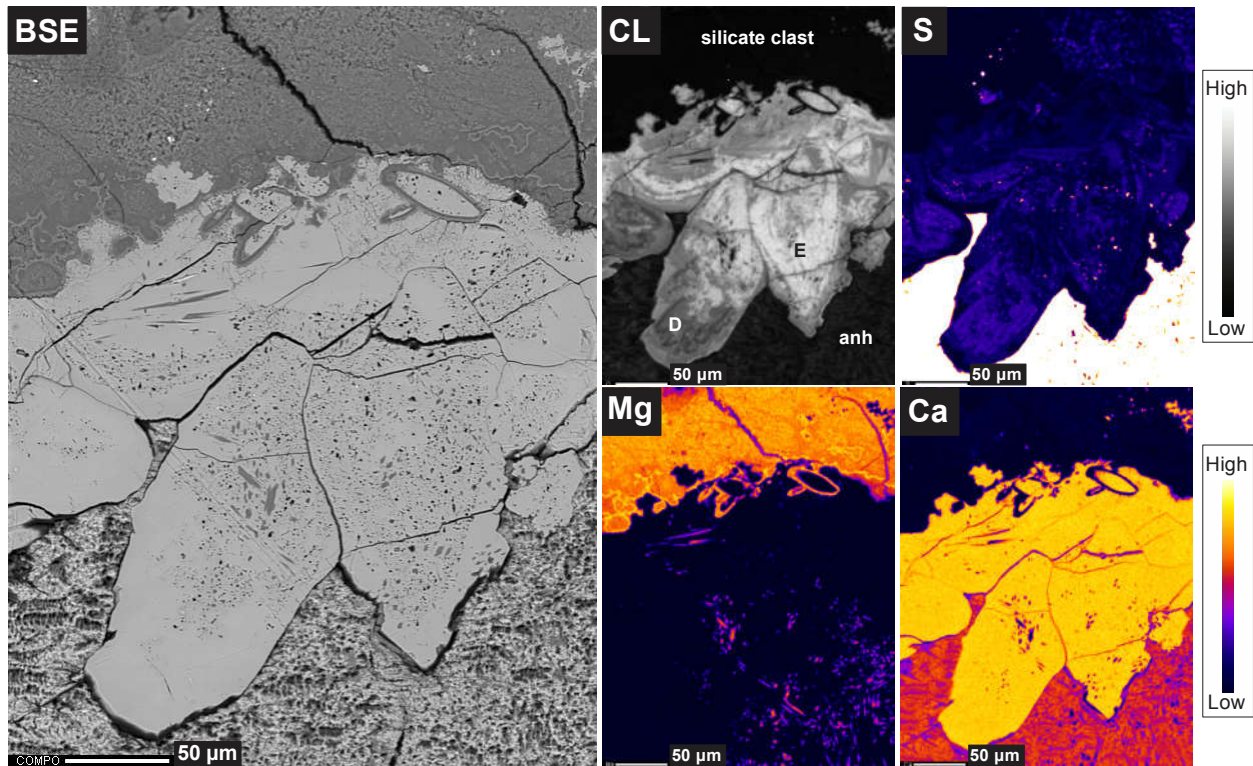
Figure 3.10. BSE-CL-WDS maps of the edge of a calcite corona on silicate clast in the F2 core. Note calcite types D and E identified in the CL map. The porous calcite shows up as very bright in CL; sulfate inclusions present in type E shown by the sulfur map; and Mg-silicate inclusions in the sulfate groundmass shown in the Mg map.

3.4.2.2 Silicate groundmass

The silicate groundmass in the F2 core displays a variety of textures (e.g., see Chapter 2) and compositions. There are two primary types of silicate groundmass. The first, Type 1, is the most abundant (Fig 3.11A). The groundmass has a porphyritic texture, is very fine grained (< 5 μm) and light brown in plain-polarized light; groundmass and clasts are not always distinguishable. There are fewer and generally much smaller clasts relative to the carbonate groundmass. Within these silicate regions, clasts are not as heavily altered or mantled as they are in the carbonate groundmass; some are recognizable fragments of the Precambrian target rocks, particularly refractory mineral clasts like zircon, titanite and garnet. Feldspars and other less resistant minerals are partially digested (Fig. 3.11B) or replaced by clay minerals. Grain size and

morphology in addition to the low wt% oxides totals show the silicate groundmass dominantly consists of clay minerals.

Three textural and compositional types of clay minerals are present in the Type 1 groundmass (Fig. 3.11C and Table 3-5). Two of the three clay minerals are dominated by SiO_2 and MgO with minor to trace amounts of Al_2O_3 and CaO. The first clay mineral is dark grey in BSE, has a low relief and a platy to fibrous morphology. It is the dominant clay phase and has a molar Mg:Si ratio of 3:4. The second clay mineral is light grey in BSE, has a higher relief and forms clusters or nodular aggregates. It has a molar Mg:Si ratio of 3:2. The light nodular clay mineral is richer in MgO, and slightly richer in Al_2O_3, whereas the dark phase is richer in SiO_2. The third type is coarser grained (5 to 15 µm), bladed, Al-rich and most commonly is present filling larger voids. Although only a single WDS analysis of this type was acquired, several EDS analyses show that the composition is consistent. The F3 groundmass composition is like the F2 dark clay mineral groundmass where the molar Mg:Si ratio is 3:4.

A separate and different region of clay mineral groundmass, Type 2, was only observed in one thin section (HAUF2G7uwo2) and is distinctive by its pseudomorphic acicular texture (Fig. 3.11 D-E). Although the pseudomorphs are completely replaced by a dark Mg-rich clay mineral (≤ 2 µm), the relict grains show normal zoning, that is reflected by subtle changes in clay mineral composition (Table 3-5) and lower brightness in BSE along the edges. This enables relict grain boundaries to be distinguished. The darker inner relict acicular grain is depleted in MgO and richer in Al_2O_3. The same region also shows evidence of fluid interaction in the form of ghost clasts and fluid pathways (Fig. 3.11F) where the acicular texture is cut by a finer grained clay mineral that lack the acicular texture. Some of the groundmass has been partially replaced by calcite adjacent these interaction zones. The composition of the Type 2 silicate groundmass is similar to that of the F2 dark (T1) groundmass, which consist dominantly of hydrated Mg-rich silicates, based on WDS spot analyses, discussed below. The regions with evidence of fluid interactions as well as the edges of the replaced acicular grains are slightly depleted in silica with respect to the regions without. Additional silicates within the F2 core groundmass occur as acicular inclusions within both the carbonate and sulfate groundmass as well as zoned skeletal grains hosted in the sulfate groundmass, described in Chapter 2. These silicate inclusions consist primarily of Mg-rich clay minerals but have a much broader composition (Table 3-6).

67

Figure 3.12 shows the compositions of all the silicate groundmass types, the composition of selected altered silicate clasts and the acicular silicate inclusions within the calcite groundmass. The F3 groundmass, and the F2 T1 dark groundmass plot broadly between the saponite and talc compositions; by comparison, F2 T2 acicular groundmass plots in the region of an Al-bearing talc, with some mixing towards the saponite and chlorite compositions. The F2 T1 light groundmass plots between serpentine and clinochlore (chlorite) compositions. Stoichiometric calculations support these findings (See Appendix C), however XRD analyses are required to confirm mineralogy. F2 T1 bladed groundmass is quite different; it plots close to Al-rich chlorite but on a tie line towards montmorillonite. The geochemistry of the skeletal silicates represents a series of transects from core to edge of the zoned crystals described in Chapter 2. These skeletal silicates show a large range in composition but plot broadly between the compositions of talc and chlorite and between the compositions of serpentine and chlorite. Some of the acicular inclusions plot close to talc and trend towards the silica apex; the latter are likely the result of incorporation of the host calcite in the analysis as the inclusions are only a few micrometres larger than the microprobe beam. All remaining F2 silicate analyses, such as alteration halos, coronas etc. which were omitted from the ternary diagram for the purpose of clarity, plot within the region of tie lines between talc, saponite, and chlorite compositions.

Visible to near infrared reflectance spectra of the F2 core are more complex than the F3 spectra as there is more variation amongst the analyses. In general, the main absorptions are the same between analyses, but the strength and width of the absorptions vary. The strongest OH and HOH bands as well as the 2310 nm band are in the same position as the bands in the F3 spectra, but the bands are broader. The same clay mineral that matched best with saponite and talc spectra observed in F3 is present. The broad absorption band centered at 2310 nm, however, tends towards shorter wavelengths representative of a shift towards the Al-OH band from the Mg-OH. This is consistent with the microprobe analysis (Table 3-5) discussed above showing that the nodular clay mineral has more Al. The slanted 'V' shape of the absorption is similar to that of the serpentine spectra. Although serpentine is not a simple match, ENVI's Spectral Analyst tool continuously returned a favorable match to serpentine. There is also a subtle 2360 nm absorption present in some but not all F2 analyses, which is consistent with the dominant absorption of clinochlore. In accordance with the WDS analysis and stoichiometry, this suggests

that the second groundmass clay mineral in F2 is a mixed layer serpentine-clinochlore. The magnesian clay sepiolite is also plotted in Figure 3.6, as it has a fibrous texture, but its 1400 nm band does not match that of the cores.
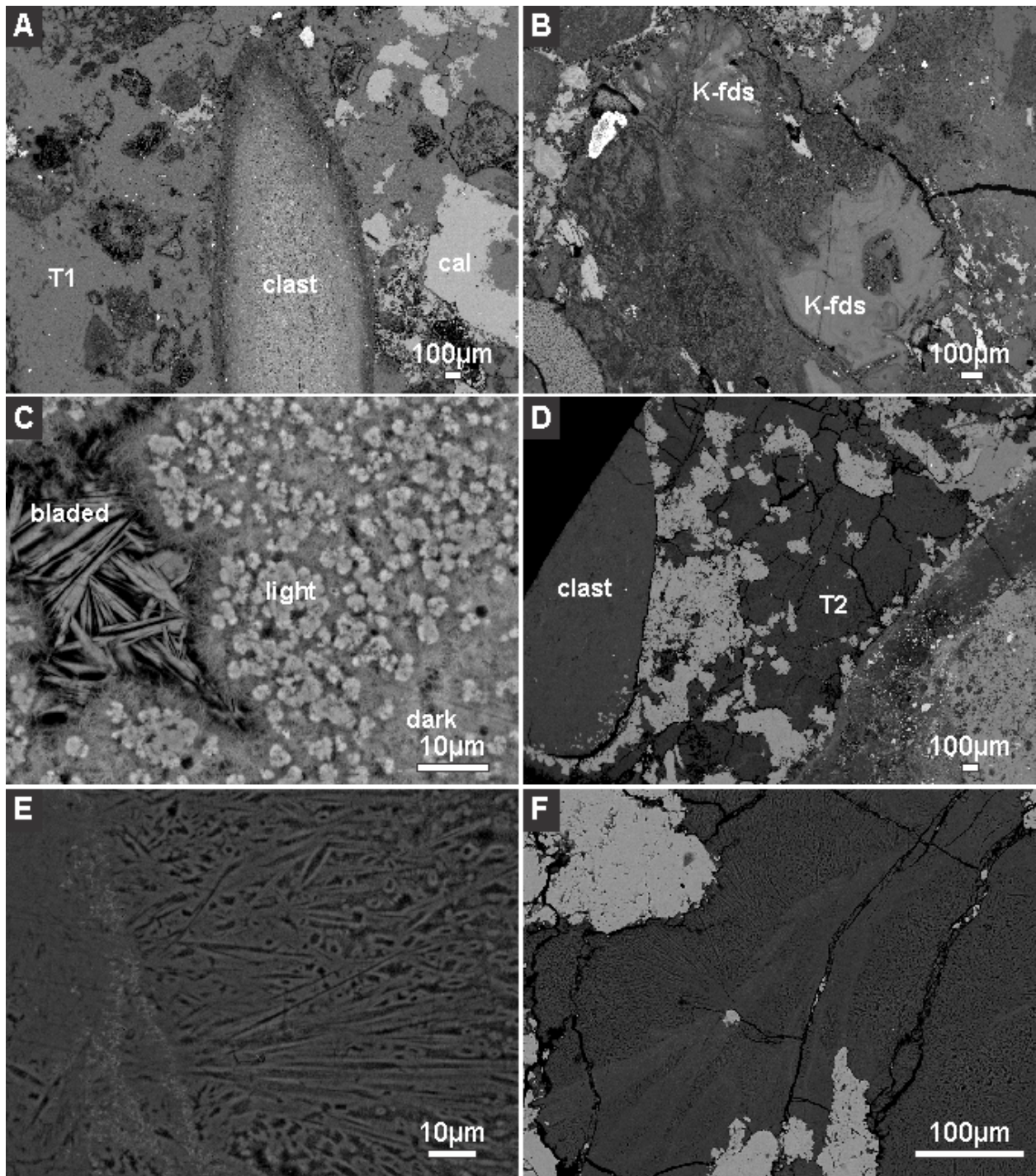
Figure 3.11 Silicate groundmass in the F2 core. A) Type 1 (T1) clay mineral groundmass; B) partially digested potassium feldspar clasts in Type 1 groundmass; C) clay mineral groundmass at high magnification; note three different textures: dark platelet to fibrous, light nodular clay mineral and a coarser bladed void-filling clay mineral; D) Type 2 silicate

groundmass with some replacement by calcite; E) Type 2 groundmass displaying acicular texture; and F) Fluid pathways within the Type 2 acicular groundmass.

Table 3-5 Microprobe analyses of the F2 core Type 1 silicate groundmass.

	TYPE 1						TYPE 2	
	Dark		**Light**		**Bladed**		**Acicular**	
	Average	S.D.	Average	S.D.			Average	S.D.
	n=20		n=9		n=1		n=15	
SiO_2	46.50	2.07	37.79	1.32	38.14		46.48	2.76
Al_2O_3	4.96	1.35	7.84	2.00	19.02		2.76	1.09
Na2O	0.06	0.02	0.02	0.01	0.05		0.04	0.01
MgO	24.89	1.86	36.92	1.02	14.88		24.22	3.24
F	0.12	0.07	0.04	0.06	0.00		0.22	0.06
TiO_2	0.08	0.03	0.01	0.01	0.01		0.02	0.01
CaO	1.36	0.32	0.25	0.07	1.18		0.79	0.13
P_2O_5	0.01	0.02	0.00	0.01	0.05		0.01	0.01
FeO	1.85	0.60	0.72	0.19	0.41		0.29	0.15
MnO	0.03	0.01	0.03	0.01	0.01		0.03	0.01
Cr_2O_3	0.01	0.01	0.01	0.01	0.01		0.01	0.01
K_2O	0.11	0.03	0.01	0.01	0.04		0.10	0.03
Cl	0.05	0.02	0.05	0.06	0.10		0.02	0.01
SO_3	0.12	0.05	0.07	0.02	0.35		0.08	0.02
Total	80.15		83.77		74.06		75.06	

Values are in weight percent

To illustrate the alteration trends of the silicates discussed above, the Chemical Index of Alteration [CIA= $Al_2O_3/(Al_2O_3+Na_2O+K_2O+CaO)$ in molecular proportions] (Nesbitt and Young, 1982) is plotted against a Pearce element ratio; where Mg is the mobile element, and Al is the immobile element (Figure 3.13). The composition of talc and serpentine would plot far off the chart to the right, as they typically contain little to no Al; however, compositions of a 5:1 mix of talc:chlorite and serpentine:chlorite are shown as red circles. The serpentinization arrow points in the direction of both the talc and serpentine compositions while the chloritization arrow points towards an increase in chlorite proportion. Chloritization and Si loss are the dominant

alteration processes occurring in the F2 core groundmass. The F3 core shows additional alkali loss and/or sericitization.

The F2 T1 dark groundmass and the F3 groundmass have Mg# ($100*Mg/(Mg+Fe)$ molar) between 93-97 whereas the F2 T1 light groundmass and F2 T2 acicular groundmass, acicular inclusions and skeletal silicate grains all have Mg# 98-100. Therefore, there is very little Fe in the groundmass, relative to Mg. This may be a result of low Fe in the target rocks (e.g. carbonates, felsic gneisses), and high Fe mobility and leaching from hydrothermal fluids to form sulfides. Iron sulfides are present in the alteration coronas around rare mafic clasts where leached Fe reacted with S-rich fluids (Zylberman et al., 2017).
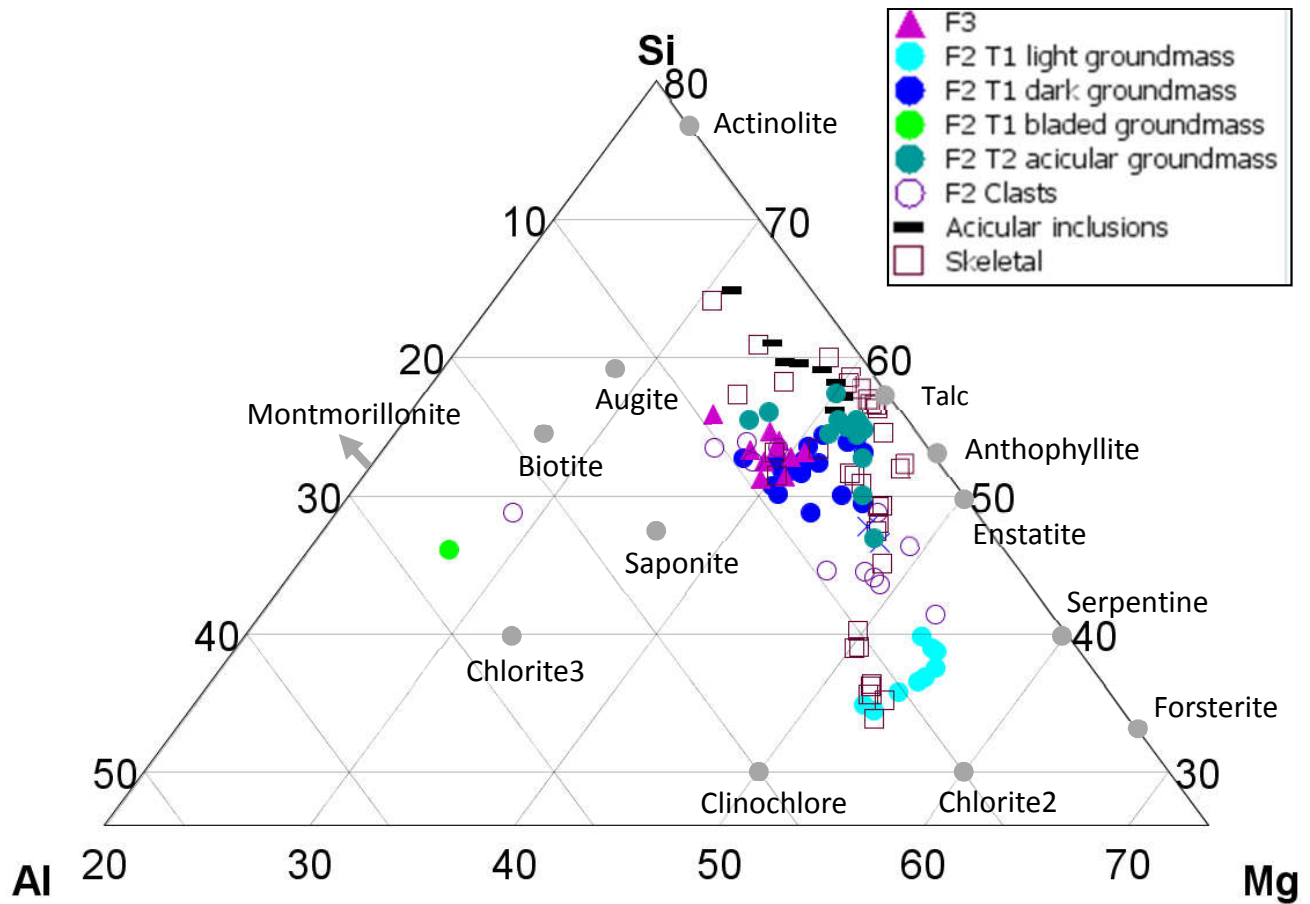
Figure 3.12 Ternary diagram illustrating F2 and F3 core silicate analysis of groundmass types, clasts, skeletal grains and acicular inclusions plotted as molar Si-Mg-Al. Note reference mineral nodes in light grey for common phyllosilicate and mafic mineral phases. Among those are 3 chlorite compositions: clinochlore $Mg_5Al_2Si_3O_{10}(OH)_8$; chlorite3 $Fe_{2.5}Mg_{2.5}Al2Si_3O_{10}(OH)_8$; and chlorite2 $Mg_6AlSi_3O_{10}(OH)_8$ as chlorite has a wide compositional range. The skeletal grains represent a series of transects through the zoned crystals. Note the scale bars as the diagram is a magnified region of a full ternary diagram.
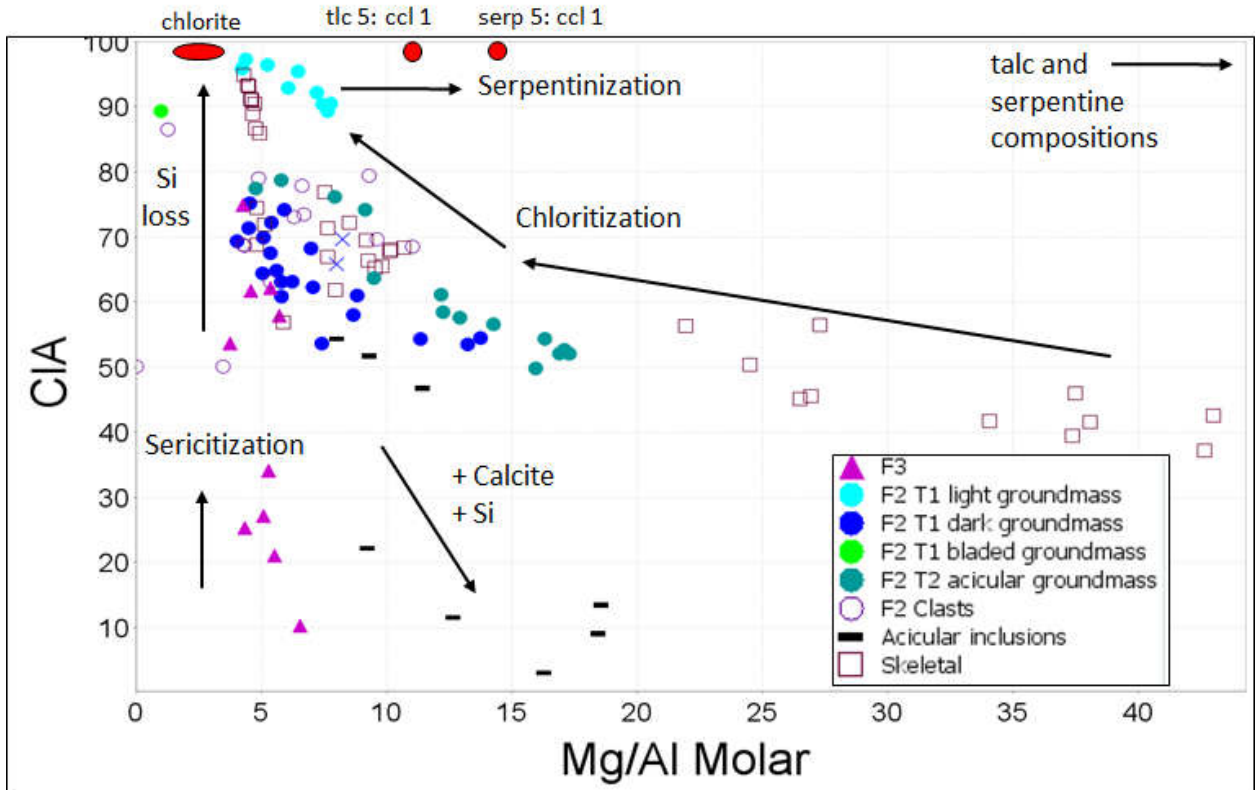
Figure 3.13 Alteration trends for the F2 and F3 cores silicate microprobe analyses of groundmass types, clasts, skeletal grains and calcite hosted acicular inclusions. The Chemical Index of Alteration, CIA= $Al_2O_3/(Al_2O_3+Na_2O+K_2O+CaO * 100)$ in molecular proportions is after Nesbitt and Young (1982) plotted against the Pearce element ratio of Mg/Al molar. Note the dominant chloritization and Si loss trends. The chlorite compositional range, as well as 5:1 mixes of talc:clinochlore and serpentine:clinochlore, are illustrated by red circles for reference.

3.4.2.3 Sulfates

The sulfate groundmass consists of tabular to lath-shaped anhydrite (Fig. 3.14A) grains ranging from 25 μm to 1 mm long. The anhydrite dominantly fills interclast space (i.e., between clasts) but is also observed as having filled intraclast space (i.e., within the clast). Anhydrite surrounds both acicular and skeletal Mg-silicate crystals (Figs. 3.14A-B), identified in Chapter 2 as igneous intergrowth textures, the latter in the form pseudomorphs after olivine. Most clasts within the groundmass are rounded, but some angular clasts comprise silicate-carbonate fragments as well as clasts that appear to fit like a puzzle piece into the nearby calcite groundmass (Fig. 3.14C). Anhydrite also occurs as a replacement of silicate and carbonate clasts and coronas around clasts (Fig. 3.14D). Late-stage replacement of anhydrite by the selenite form of gypsum is common, as well as mm- to cm-scale selenite veins (Fig. 3.14E). Barite and celestite clusters are observed along silicate clast boundaries (Fig. 3.14F), within clast coronas as well as inclusions within calcite, sulfate and silicate in the groundmass.

Microprobe analyses (Table 3-6), microXRD (Appendix B) and Raman analysis (Appendix G) confirm that the sulfate groundmass ranges from anhydrite to bassanite to gypsum, which is a common transition of sulfate minerals during heating through thin section processing (Pichler and Schmitt-Riegraf, 1997), epoxy impregnation (Flemming and Léveillé, 2007), microprobe analysis or hydration from alteration or weathering. The sulfate contains trace amounts of other components, on the order of 0.01 to 0.19 wt% MgO, up to 0.28 wt% SiO_2, up to 0.08 wt% BaO, 0.01 to 0.40 wt% SrO, 0.02 to 0.14 wt% PbO and 0.02 to 0.14 wt% Cl. Trace amounts of these elements are common in sedimentary sulfates and have a wide range depending on the setting (Lu et al., 1997). The abundance of each sulfate as groundmass is highly variable. Petrographically, the gypsum is easily distinguished from anhydrite and bassanite, but the latter two are indistinguishable from each other.

Gypsum is also identified in the F2 Vis-NIR reflectance spectra by the 1450 nm, 1490 nm and 1540 nm triplet and broad 1900 – 2000 nm HOH band in HAUF2G1 (Fig. 3.6). Although other phases such calcite are abundant, the absorptions of these minerals are hidden by the more reflective clay minerals. Talc reflectance for example, obscures carbonate signatures (Brown et al., 2010).

Table 3-6 EPMA-WDS analyses of F2 core sulfates in the groundmass.

Sample ID							HAUF2G7uwo									
Spot #	A01	A02	A03	A04	A05	A06	A07	A08	A09	A10	A11	A12	A13	A14	A15	A16
SiO_2	0.12	0.06	0.09	0.02	0.01	0.02	0.01	0.01	0.02	0.01	0.07	0.08	0.02	0.01	0.02	5.68
MgO	0.08	0.03	0.06	0.02	0.02	0.01	0.01	n.d.	0.01	0.02	0.04	0.06	0.01	0.01	0.02	1.87
CaO	37.77	36.25	37.19	38.29	40.43	40.62	40.56	39.20	38.70	40.97	37.03	39.67	37.44	37.68	38.73	0.58
FeO	0.01	n.d.	n.d.	n.d.	0.01	n.d.	0.01	0.01	0.00	n.d.	0.01	0.01	n.d.	n.d.	0.02	1.21
BaO	0.03	0.02	0.00	0.05	n.d.	0.02	0.03	n.d.	0.03	0.02	n.d.	n.d.	0.03	n.d.	0.04	41.71
SrO	0.16	0.14	0.13	0.20	0.26	0.03	0.40	0.14	0.17	0.38	0.01	0.07	0.02	0.08	0.10	10.83
SO_3	56.07	53.55	54.52	55.53	60.34	59.14	60.12	57.71	57.34	59.47	54.63	56.76	54.63	55.96	57.47	31.03
F	n.d.	n.d.	n.d.	0.01	n.d.	n.d.	n.d.	n.d.	n.d.	n.d.	n.d.	n.d.	n.d.	n.d.	n.d.	n.d.
Cl	0.08	0.11	0.10	0.09	0.01	0.01	0.01	0.12	0.08	0.00	0.13	0.08	0.14	0.11	0.08	n.d.
PbO	0.05	0.08	0.06	0.10	0.04	0.10	0.11	0.03	0.02	0.06	0.06	0.06	0.05	0.10	0.07	0.06
Total	94.37	90.24	92.16	94.30	101.11	99.95	101.26	97.23	96.38	100.93	91.98	96.79	92.34	93.94	96.55	92.96

Sample ID		HAUF2G2uwo							HAUF2G8uwo						
Spot #	A17	A18	B19	B20	B21	B22	A23	A24	A25	A26	A27	B28	B29	B30	B31	B32
SiO_2	0.07	0.06	0.02	0.00	0.21	0.17	0.02	0.10	0.16	0.28	0.27	0.01	0.01	0.02	0.26	0.15
MgO	0.04	0.05	0.04	0.01	0.08	0.02	n.d.	0.07	0.10	0.15	0.19	0.02	0.03	0.01	0.15	0.09
CaO	39.42	40.16	39.51	39.49	40.74	40.17	39.60	39.13	40.05	33.54	34.26	39.57	40.08	39.52	36.52	36.66
FeO	0.02	0.02	n.d.	0.00	0.00	0.02	0.00	0.02	0.01	0.03	0.02	0.02	n.d.	0.00	0.02	0.03
BaO	0.07	0.06	0.02	0.06	0.02	0.08	n.d.	0.02	0.01	0.04	n.d.	n.d.	0.01	n.d.	0.01	n.d.
SrO	0.22	0.05	0.17	0.04	0.11	n.d.	n.d.	0.33	0.18	0.03	0.10	0.29	0.14	0.31	0.27	0.22
SO_3	57.01	57.21	58.03	56.89	59.17	57.89	57.46	57.15	58.44	50.35	49.88	55.85	57.71	55.81	53.16	53.70
F	n.d.	n.d.	n.d.	n.d.	n.d.	n.d.	n.d.	0.01	0.01	n.d.	n.d.	n.d.	n.d.	n.d.	n.d.	n.d.
Cl	0.00	0.00	n.d.	0.00	0.01	n.d.	0.00	0.00	0.01	0.19	0.18	0.00	0.00	n.d.	0.15	0.13
PbO	0.07	0.09	0.08	0.06	0.03	0.09	0.07	0.08	0.03	0.06	0.13	0.03	0.07	0.14	n.d.	0.09
Total	96.90	97.70	97.86	96.55	100.36	98.43	97.15	96.90	98.99	84.66	85.03	95.79	98.06	95.80	90.55	91.06

Values are in weight percent; n=number of probe spots, note A16 is a barite composition, n.d.=not detected.
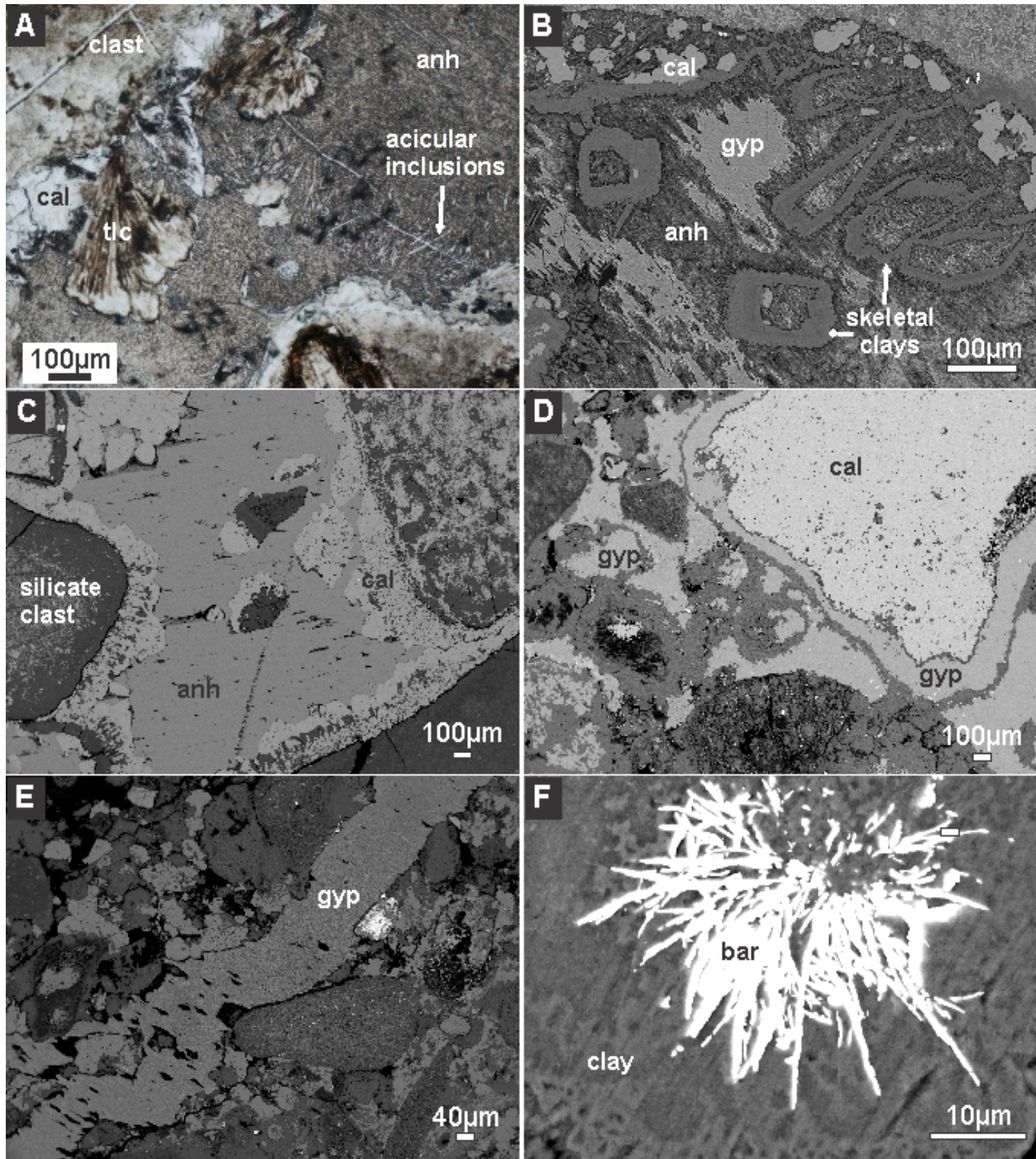
Figure 3.14 Plane light photomicrograph (A) and backscattered electron images of sulfate occurrences in the F2 core: A) Acicular silicate inclusions hosted in anhydrite. Note also the fan-shaped Mg-silicate occurrence growing out from the edge of a clast into the groundmass; B) Skeletal Mg-silicate crystals hosted in anhydrite-gypsum; C) Rip-up clasts hosted in anhydrite-gypsum, note the calcite lining the edge of the clasts; D) Gypsum

replacement of silicate corona around a carbonate clast; E) Gypsum vein cross-cutting F2 core; F) Radial cluster of barite hosted in a clay mineral clast corona.

3.4.2.4   Silicate-carbonate clasts

The original mineralogy of the majority of clasts within the F2 core is altered beyond recognition; however, most can be categorized as silicate or carbonate based on relict textures observed in BSE, and composition based on EDS analyses. An assortment of clasts are presented in Figure 3.15A-F. Those clasts that contain recognizable primary mineralogy are partially digested and/or replaced by clay minerals (Figs. 3.15A-B), calcite and to a lesser extent, gypsum. Many clasts have a complex formation and alteration history. For example, Figure 3.15C shows a silicate clast that was partially replaced by calcite. The inner silicate corona is preserved as well as the textures between the silicate and carbonate that surrounded it. Chapter 2 interprets this as emulsion textures between the silicate and calcite melts, and a series of calcite overgrowths around the clast, as well as a later porous replacement calcite filled with gypsum inclusions. Figure 3.17D is a curious example of a mostly preserved K-feldspar-apatite-pyroxene clast with a silicate corona that is likely a remnant of the preserved silicate groundmass that previously hosted the clast. Mg-rich clay mineral clasts are observed with a calcite rim (Fig. 3.15E). Crystalline calcite also fills some of the voids within the clast. Figure 3.15F shows a garnet mineral clast with a thin silicate rim hosted in calcite. In the carbonate groundmass, silicate coronas are filled by carbonate groundmass rather than a clast, and fragments of coronas or reaction rims are locally present. Some clast coronas are nearly completely replaced by gypsum (Fig. 3.15D). In previous studies, zoned clasts were observed in the core hand sample (Zylberman, 2014) in which clasts are light green in the centre with an orange rim. BSE imaging, EDS and WDS analyses show that these result from an increase in Al and Ca, and a decrease in Fe in the rim of the clast.
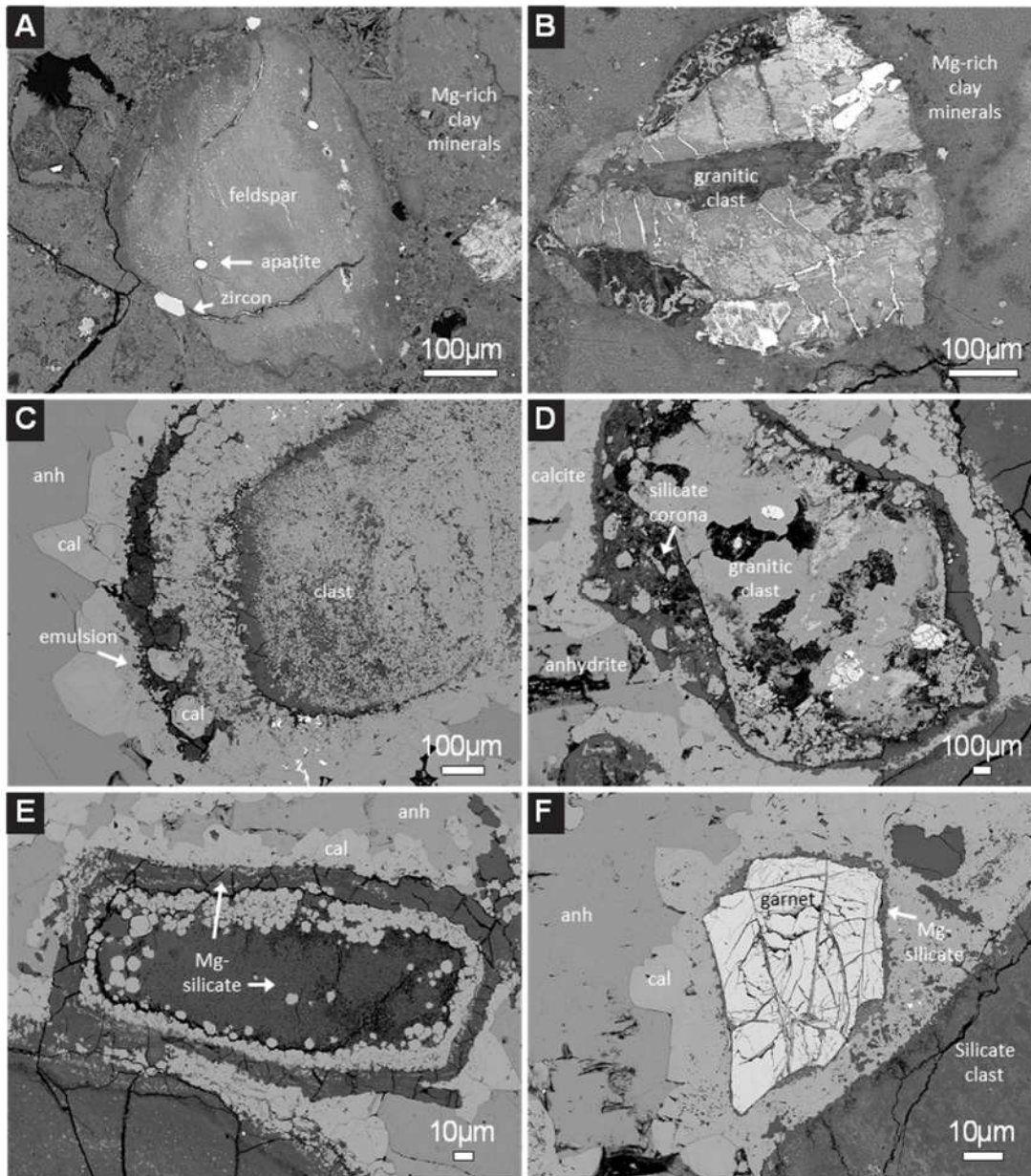
Figure 3.15 Backscattered electron photomicrographs of clasts in the F2 core. A) Altered feldspar clast in silicate groundmass with unaltered apatite and zircon inclusions; B) Preserved granitic clast without corona hosted in silicate groundmass, veining is pre-impact; C) Silicate-calcite clast hosted in calcite-sulfate groundmass; note the layered zones of silicate to calcite from the centre to the rim of the grain (context image for Figure 3.9 map); D) Partially altered granitic clast with irregular silicate corona, within which are calcite grains or fragments; E) Silicate clast with partial replacement by calcite, hosted in

calcite-sulfate groundmass; F) Garnet clast with thin silicate clay mineral rim hosted in calcite groundmass.

3.5 Discussion

This Chapter in addition to Chapter 2 present textural and compositional evidence that suggests that the F2 and F3 cores are hydrothermally altered impact melt rocks. The origins of each groundmass type, the differences between the F2 and F3 cores, the textural evidence for carbonate and sulfate melting, immiscibility of silicate-carbonate melts and heterogenous melting, hydrothermal alteration and paragenesis, and, implications for the study of Mars are discussed below.

3.5.1 Origin of the silicate groundmass in F3 and F2

The best spectral matches for the F3 groundmass are saponite and talc. The variation in some of the reflectance OH-HOH band positions in F3 (see Fig. 3.6), may be explained by: 1) the presence of calcite and other minerals in the sample that are generally hidden by the clay minerals; 2) ion substitution; and/or 3) the possibility that the F3 clays are mixed-layered clay minerals, such as a combination of talc and Mg-saponite. The latter is supported by the geochemical results, which suggest a single dominant type of clay mineral in the F3 silicate groundmass plotted between the compositions of both saponite and talc (Fig. 3.12). Therefore, we infer that the F3 core groundmass comprises a mixture of talc and saponite with a variable alkali content and an abundance of micrometre-scale clasts, predominantly calcite. Evidence for this includes the preserved porphyritic texture common in impact melt rocks (Dressler and Reimold, 2001; Osinski et al., 2018), and partially assimilated clasts and clast coronas. In contrast with the previously described, similar-looking particulate impact melt rock at Haughton (Osinski et al., 2005c), the F3 impact melt rock is distinguished by its hydrated silicate groundmass and lack of appreciable quantities of sulfate in the groundmass or clasts.

The F2 core silicate groundmass comprises several Mg-series clay minerals including an Al-rich talc, and a series of clay mixtures or interlayered clay minerals consisting of talc and saponite, talc and chlorite and serpentine and chlorite, as principal groundmass components. These clay minerals were determined using textural and compositional data; however, precise

80

amounts of interlayering and/or substitution can only be confirmed using XRD analyses. Nevertheless, the narrow range in silicate groundmass chemistry presented in this study; consisting dominantly of MgO, SiO$_2$ and minor Al$_2$O$_3$ with only trace amounts or values below detection limits of CaO, K$_2$O, FeO, Na$_2$O, eliminates all but a few magnesian clay mineral species. Thus, these mineral phases are interpreted with a good degree of confidence.

As with the F3 silicate groundmass, the clay minerals are interpreted to represent replacement of impact melt products. Textural evidence to support an impact melt origin includes the presence of a variety of preserved igneous textures described here and in Chapter 2 such as porphyritic, acicular, dendritic and skeletal textures. In addition to evidence of intergrowth and emulsion textures that occur between what is now calcite and clay phases, and the presence of clay mineral globules and clast coronas. The Type 2 groundmass undoubtedly represents the groundmass of an aphanitic acicular impact melt rock as shown by the pseudomorphic acicular texture. The skeletal silicate which plots as a mixture of serpentine and chlorite (or Al-rich serpentine, Chapter 2) is interpreted as a pseudomorph after olivine (Chapter 2). The inferred presence of multiple clay minerals in Type 1 silicate groundmass suggests there may have been multiple primary phases, such as olivine, pyroxene and minor plagioclase. The formation of the ultramafic minerals olivine and pyroxene in impact melt generated from mixed silicate, dolostone, limestone target rocks is supported by similar observations of impact melt at Meteor Crater (Hörz et al., 2002; Osinski et al., 2015, 2003). To date Meteor Crater and Haughton are the only terrestrial impact structures with suspected ultramafic melts rocks (Hörz et al., 2002; Osinski et al., 2015) but these may be common on other planetary bodies such as the Moon and Mars.

Clay minerals are common secondary phases of impact melt rocks and glasses from impact-generated hydrothermal systems (Naumov, 2005), particularly where primary minerals include silicates. Although there are no primary silicates preserved in the F3 and F2 groundmasses, there are preserved silicate clasts, particularly in F3, from Haughton target rocks from which we may infer a silicate protolith. These clast lithologies include diabase and orthogneiss; however, based on their abundance and mineralogy, they would not supply enough Mg to form the suggested mafic to ultramafic protolith for the current Mg-rich clay minerals. It is, therefore, assumed that a large portion of the Mg came from melting a large volume of the dolomite target as suggested in

previous studies (Osinski et al., 2005c; Osinski and Spray, 2001) or extensive alteration by dolomite-derived Mg-saturated fluids. However, hydrothermal dolomite has not been documented at Haughton. Complete melting of dolomite is also supported by the lack of dolomite clasts in F2, despite the abundance of this rock type in the target stratigraphy (Fig. 3.1). There is one known exception, small, relict rhombs were observed in BSE within the microtexture of a large clast in the F2 core. The clast was identified and confirmed in Chapter 2 as diopside, using microXRD. This suggests that some dolomite may have metamorphosed to diopside in the early post-impact hydrothermal stage.

The silicate glasses in the groundmass of the impact melt rocks exposed on the surface presented by Osinski et al. (2005c) also have low totals (65 wt% in G1 type and 80–95 wt% G2 type glasses), which indicate hydrated phases. Among which, the MgO-rich G2 Type glasses fit well within the compositional range of the F3 silicate groundmass. This compositional overlap would suggest that some of the exposed melt rocks may also contain clay minerals. Consequently, the F3 hydrated silicate groundmass likely represents altered MgO-rich silicate glass, common throughout the crater-fill rocks. Alteration of the F2 and F3 cores will be discussed further in section 3.6.7.

3.5.2 Origin of the carbonate groundmass in F2.

Differentiating between different calcite origins is a challenge, particularly as hydrothermal calcite and calcite crystallization from a melt commonly occur together, or textures may have more than one plausible interpretation. The combined methods of EPMA-BSE-CL-WDS-EDS mapping and optical petrography of thin and thick sections were essential to make these distinctions, although the origin of some calcites remain undetermined. Cathodoluminescence greatly contributed to determining the order of calcite crystallization by revealing zoning patterns and textures not resolved using traditional optical techniques. Evidence presented here and in Chapter 2 demonstrates that there is calcite in the F2 core formed by both primary crystallization from impact-induced melting (types C, D and F); and secondary mineralization through hydrothermal precipitation and/or replacement (types A, B, E). This interpretation is outlined below.

It is proposed that Type A calcite was formed by hydrothermal alteration, as it occurs as cement that has filled voids between and within clasts and has a homogeneous near end-member chemistry typical of hydrothermal calcite. It also occurs as replacement of silicate clast coronas, which indicates it post-dates the impact melt emplacement (e.g., Fig. 3.8A). This is also consistent with the sparry hydrothermal calcite observed as veins and vugs within the exposed faulted blocks and crater-fill impactites at Haughton (Osinski et al., 2005a). Type B calcite may be just a variation of Type A calcite enriched in SiO_2 and MgO due to entrained silicate inclusions from primary silicate clasts or groundmass. Enrichments of SiO_2 and MgO in the Type C calcite are also due to silicate inclusions; however, they have a different origin. The presence of intergrowths of acicular and radial silicates within Type C calcite indicates that these phases must have been coeval, therefore, the calcite and silicate inclusions crystallized from a melt (Chapter 2). This is not a novel observation as cotectic crystallization of calcite and silicate such as olivine occurs in calcite carbonatites (Chakhmouradian et al., 2016; Sharygin and Doroshkevich, 2017).

Type D calcite is interpreted as having crystallized from a melt and is easily distinguished from other calcite types in CL and sulfur maps as it has a distinct enrichment in sulfur. This sulfur is likely contained within the crystal lattice however, TEM observations are required to confirm this interpretation. This sulfur-rich calcite occurs as the earliest growth phase of a series of calcite overgrowths on the edge of clasts. The conditions in which sulfur would be taken up into calcite are not well-constrained; however, combined carbonate-sulfate melts have been made experimentally (Martin et al., 2012; Veksler et al., 2012). The experiment by Martin et al. (2012) consisted of 70% basalt + 15% carbonate + 15% sulfate, which produced two melts upon heating: a basaltic silicate melt, which was immiscible with a carbonate-sulfate melt. Upon cooling, the carbonate-sulfate melt crystallized and anhydrite and calcite dendrites formed rather than a single combined type D calcite phase (Martin et al., 2012). However, the proportions of anhydrite and calcite were approximately equal, and more experimental work is necessary to better understand the relationship between these two melted phases in different proportions.

Type D calcite is the dominant calcite type that was replaced by Type E calcite. Type E calcite has irregularly distributed porosity with wispy terminations (Fig. 3.9), and based on textures described in Putnis (2009), is interpreted as a late stage hydrothermal replacement. It

pre-dates the late-stage gypsum mineralization, as the irregularly shaped pores are commonly filled by gypsum. The late sulfate-poor calcite overgrowth over Type D is of secondary origin and coeval with the fluids responsible for Type E replacement, so we have grouped it with type A.

Type F calcite is a vesicular calcite, that contains tiny spherical voids that are commonly formed by trapped gases during rapid crystallization from a melt (Chapter 2). Vesicular calcite can also be generated by decarbonation reactions, wherein lithic limestone clasts are entrained in hot breccias or melt, or through rapid back-reaction of CO_2 and CaO to form calcite (Hamann et al., 2018a).

3.5.3 Origin of the sulfate groundmass in F2.

Gypsum is a late-stage hydrothermal precipitation product, shown by having filled cavities and cross-cutting vein relationships with all other phases (Fig. 3.14D-E), in agreement with the previous work of Osinski et al., (2001) and Osinski and Spray (2003). Gypsum is also the product of hydration of anhydrite and replacement of calcite and clay minerals in the groundmass, coronas and clasts. Moreover, Osinski and Spray (2003) observed that gypsum cross-cuts the anhydrite groundmass.

Primary magmatic anhydrite was first recognized in the volcanic setting at El Chichón, Mexico, where it occurs as inclusions within phenocrysts, and has similarly been documented at Mount Pinatubo, Philippines (Luhr, 2008). Various sulfates have been documented in carbonatites including anhydrite, barite and celestite as magmatic phenocrysts, exsolution structures and inclusions in minerals as well as in hydrothermal assemblages (Bolonin and Nikiforov, 2014; Gomide et al., 2013). The presence of sulfates in a melt indicates high oxygen fugacity and high sulfur content (Luhr 2008). It is difficult to differentiate between magmatic and hydrothermal sulfates in carbonatites without S-O isotope data or melt inclusions (A. Chakhmouradian, pers. comm.), as the liquid phase of the lavas can persist down to hydrothermal temperatures (e.g., 400-500°C; Gomide et al., 2013 and references therein). Hydrothermal sulfates are common in a variety of settings from epithermal porphyry deposits to seafloor hydrothermal systems (Pirajno, 2009). In impact structures, hydrothermal anhydrite is observed at depth within the fractured and brecciated rocks of the central uplift, such as at the

Puchezh-Katunki structure in Russia, within the chlorite-anhydrite alteration zone (Naumov, 2005).

Sulfates in the groundmass in the F2 core may have originated from primary crystallization from an impact-induced melt or from secondary mineralization through hydrothermal precipitation and/or replacement. Primary sulfate has been suggested at Haughton within the crater-fill impactites where liquid immiscibility textures as well as quench and flow textures were observed (Osinski and Spray, 2003). Primary anhydrite contains high SiO_2 (up to 2 wt%) contents, whereas in the present study SiO_2 ranges between 0.02 to 0.16 wt% (Table 3-6). These values are still higher than the anhydrite in the unshocked target rocks with SiO_2 values below detection levels (Osinski and Spray, 2003, Table 2). Key evidence in the F2 core for primary anhydrite rests on its intergrowth with acicular and skeletal silicate phases (Figs. 3.14A,B). These textures are unlikely to have formed if the anhydrite were hydrothermal (Chapter 2).

Barite and celestite are present in the target rocks and have also been observed as hydrothermal phases at Haughton, in the form of isolated euhedral to irregularly-shaped grains associated with calcite in the crater-fill impactites (Osinski et al., 2005a). In this study, the radial to spherulitic habit of barite and celestite hosted within silicate groundmass, as well as within quenched silicate clast coronas, suggests that it was produced by rapid crystallization from a melt. Barite interpreted to have crystallized from a melt based on occurrence and texture has also been identified.at the Steen River impact in Alberta, Canada in clasts within breccia (Walton et al., 2019).

3.5.4 Differences between F2 and F3

The hydrothermally altered impact melt rocks of the F3 and F2 cores were collected in the same central setting only 12 metres apart, with a difference in depth of ~3 m (Zylberman et al., 2017). Yet, they have significant textural and chemical differences, such as groundmass type(s), clast size, shape, and distribution, and extent of hydrothermal alteration. Why are they so different despite being so close together? These distinctions illustrate the heterogeneity of the melt rocks, and how emplacement and modification conditions may change based on unknown, unexposed factors. Basement topography, for example, may play a big role in pooling impact melt. Drill cores in the central uplift of the Manicouagan structure, Québec for example, show

significant changes in the thickness and chemistry of the impact melt sheet on very short lateral distances as a result of large displacement fault systems in the crater floor, in other words, a variable basement topography (Spray and Thompson, 2008).

The high concentration of crystalline basement clasts within F2 core may be explained by its presumed proximity to the most uplifted crystalline target lithology at the centre of the structure. Precambrian crystalline target rocks are locally abundant in the surrounding particulate melt rocks at the surface, as shocked clasts and melt fragments (Grieve, 1988; Metzler et al., 1988), except the Precambrian-age crystalline basement does not outcrop in the vicinity of the impact structure. The crystalline, silicate clasts may be particularly abundant due to their proximity to the target source rocks, as very clast-rich melt rocks are typically found close to the contact with the underlying brecciated target rocks of the central uplift (Osinski et al., 2008a). The contrast in silicate clast abundance with F3 may be explained again by unknown topography and unexposed contacts with the underlying fractured central uplift. In impact structures where the basement-breccia-melt contacts are exposed, the transition from breccia to melt can occur over as little as a metre (e.g., Mistastin impact structure, Labrador; Mader and Osinski, 2018). Based on geophysical surveys, Zylberman et al. (2017) proposed the F2 core was more intensely altered due to the formation of a topographic low as a result of glaciation which exposed it to gypsum-forming, sulfate-rich fluids. At a minimum, it is apparent that the F2 core was much more permeable than F3 at the time of gypsum precipitation because of its higher degree of alteration, and therefore fluid infiltration.

The alternating mineralogical and textural zoning of the F2 groundmass may be the result of melting of different target rock of widely varying compositions, which leads to poor melt mixing. The variety of textures in F2 suggest variable degrees of undercooling. Skeletal and acicular textures for example, indicate rapid cooling and crystallization (Chapter 2), which may also have prevented melt mixing. The differences in clast abundance, size, and roundness in the two cores (Table 3-1), are likely a function of proximity to the underlying contact with the central uplift, variable amounts of assimilation of a wide range of target rock compositions and temperature of the melt. The F3 core lacks preserved pseudomorphs in the silicate groundmass and very few clast reaction rims, suggesting there was little time for chemical interaction between groundmass and clast, whereas F2 has both abundant reactions rims and rounded clasts due to partial assimilation. It follows then that the F2 melt may have remained hotter for longer

and so may have been thicker. It is postulated here that the variation in clast abundance is likely due to viscosity, e.g. carbonate melt is of very low viscosity (Dobson et al., 1996), as observed in carbonatite lava. A carbonate melt would assimilate a much higher quantity of clasts than a silicate melt. The high rate of clast assimilation would cause significant undercooling, resulting in a combination of quenching and intergrowth textures resulting in a very clast-rich, heterogeneous impact melt rock.

It is understood that heterogeneous targets form heterogeneous impactite deposits. Numerous impact structures have been studied in detail, based exclusively on drill core (e.g., Chicxulub (Nelson et al., 2012), Manson (Hartung et al., 1990), Kärdla (Versh et al., 2005), etc.). It should be noted then that studies of representative core samples present only a pinhole view of complex depositional processes and products.

3.5.5 Silicate-carbonate Immiscibility

Generally, the process of impact melting is set apart from magmatic melting in that it results from whole rock melting and mixing rather than partial melting and differentiation (Osinski et al., 2018), except in the case of very thick impact melt sheets (>1 km) where differentiation can occur (Lightfoot, 2017; Therriault et al., 2002). The Haughton impact resulted in the melting of felsic metamorphic rocks, minor mafic dykes, carbonates, sulfates, and other sedimentary rocks. We suggest that these texturally heterogeneous melt rocks reflect heterogeneous crystallization conditions on a scale of a thin section or smaller. Conditions that may vary dramatically include the composition of the melt, nucleation sites, temperature or degree of undercooling andcooling rate. Textural evidence in the F2 core supports both the presence of 1) a single chemically heterogeneous melt (e.g., carbonate-silicate intergrowths); and 2) immiscible melts (e.g., emulsion textures). The dynamic and turbulent nature of impact melting, clast assimilation and differential movement may result in a broad range of conditions from a small to large scale.

Recent studies have shown that liquid immiscibility in impact melts is not uncommon, and the melts of variable composition may readily unmix during cooling (e.g., Dence et al., 1974; Masaitis et al., 1980; Hamann et al., 2018b; Stöffler et al., 2018). Immiscibility textures between primary calcite and silicate glass have been documented at Haughton in the crater-fill deposits shown by intermingling silicate-carbonate, carbonate globules and irregular blebs within silicate

glasses (Osinski and Spray, 2001). The emulsion textures observed between silicate and carbonate in this study occur between Type D S-rich calcite, which is partially to completely replaced by Type E calcite, and Mg-rich clay minerals. These observations agree with the experimental work of Martin et al. (2012) who demonstrated that a sulfate-carbonate melt separates from the basaltic melt. The principal difference between the experiment and the emulsion texture represented in Figure 3.9 are the proportions of melted sulfate and carbonate. In the experiment, equal parts carbonate and sulfate were melted; whereas at Haughton the melt would have consisted primarily of carbonate and a maximum of 5 wt% sulfate. Unfortunately, experimental studies on sulfate solubility in a carbonate melt are limited because of the low temperature of disassociation.

Phase relationships between various silicate and carbonate melt compositions have been experimentally determined, wherein the miscibility gap is present and decreases with increasing Al/Si ratio, decreasing pressure or increasing Mg/Ca (Thompson et al., 2007). Experimental studies showing evidence of carbonate-silicate immiscibility mainly include high pressure conditions and a significant amount of sodium and/or chlorine in the melt (Brooker and Kjarsgaard, 2011; Lee and Wyllie, 1998; Safonov et al., 2011), such as those suggested to explain the formation of carbonatite magmas. The impactites studied here, however, have negligible amounts of both alkalis and chlorine. If mixing and subsequent unmixing of silicate and carbonate occurred, it may be strictly the result of high pressure. It is more likely that the emulsion textures observed in the F2 core are the result of incomplete mixing of compositionally different melts. The emulsion textures occur predominantly around clast boundaries, where localized melt of the clast rims do not mix with the host melt. In this case where the melt did not have the opportunity to mix, the abundance of sodium or chlorine in the melt would be inconsequential.

Impact melting temperatures in impact structures can reach upwards of 2300°C (Timms et al., 2017), well above the liquidus temperature for all target rocks. The intergrowth of acicular and skeletal silicate crystals hosted by carbonate or sulfate groundmass are evidence for coeval crystallization from a single melt (Chapter 2), consistent with a melt where mixing of heterogeneous target rocks was successful. The textures suggest the high-temperature Mg-silicate minerals crystallized first, followed by calcite or anhydrite. The abundance of Mg in the

clay minerals suggest dolomite contributed to the melt, as mentioned above. In an analogous case of carbonatite formation through ascension of a dolomite-enstatite melt, Moore and Wood (1998) explain that as pressure decreases in the CaO-MgO-SiO_2-CO_2 system, forsterite, diopside, Ca-rich carbonate melt + carbon dioxide would be produced. This is consistent with partition coefficients calculated by Veksler et al. (2012) wherein a mixed silicate-carbonate melt, Mg would partition ($D < 1$) into the silicate phase, whereas Ca partitions largely into the carbonate and sulfate melts. The decomposition and partitioning of Mg into the silicate melt has previously been proposed by Osinski and Spray (2001), but in that case dolomite was commonly a clast within the melt. It has also been suggested, most recently in the case of Meteor Crater, that the products of devolatilization of dolomite, MgO and CaO are dissolved into the SiO_2-rich melt (Hörz et al., 2015; Kieffer and Simonds, 1980). The vesicular calcite is cited as evidence for the presence of CO_2 in the gas phase, as it likely represented CO_2 bubbles. Although some devolatization of carbonates may have occurred at Haughton (Martinez et al., 1994), the presence of carbonate impact melt rocks are evidence that a significant volume of carbonate also melted.

3.5.6 Hydrothermal alteration

3.5.6.1 *Mineral assemblages*

It was thought that Haughton differed from other similar sized impacts into mixed silicate-carbonate targets such as the Ries impact structure, Germany, as it lacked clay-zeolite-feldspar assemblages (Osinski et al., 2001). The current study confirms that carbonate, sulfate and sulfide mineralization occur in the F2 core within the central crater-fill impactites at Haughton in addition to abundant and pervasive alteration to Mg-series clay minerals: talc, chlorite, saponite, and serpentine, although quartz was not identified in the cores. The lack of clay minerals and zeolites elsewhere in the structure is likely due to the prevalence of carbonate and sulfate target rocks relative to silicates (Osinski et al., 2001). There is also evidence for localized sericitization of feldspar clasts, however, as with all silicates within the cores, it is overprinted by Mg-rich clay minerals. Carbonate, sulfate and sulfide alteration phases are absent in F3 but pervasive silicate alteration to Mg-rich clays is common, and some sericitization of primary feldspars is locally present in the groundmass. This study is the first to observe talc and serpentine as secondary minerals in terrestrial impact melt rocks, but as stated previously, only a handful of impact

structures have ben studies in detail in terms of their post-impact hydrothermal systems. Serpentine has been observed as a secondary mineral at the Lonar crater, but solely within the altered target rocks (Osae et al., 2005). There are only a handful of terrestrial impact structures into predominantly mafic to ultramafic targets. Of these, only Lonar has been examined for hydrothermal alteration, and yields common secondary mineral assemblages for silicate targets: smectite, zeolites and calcite (Hagerty and Newsom, 2003).

Clay alteration minerals have been identified in more than 80% of impact structures that have been explored for hydrothermal minerals (Naumov, 2005). Talc and serpentine are formed by 1) hydrothermal alteration and/or retrograde metamorphism through hydration and/or carbonation reactions with Mg-rich minerals olivine, pyroxene, amphibole such as in ultramafic rocks (e.g. Allen et al., 1996); or 2) through metamorphism of siliceous dolomite (Deer et al., 1992). A hydration reaction with forsterite would form brucite and serpentine; whereas a carbonation/hydration reaction would produce magnesite and serpentine, or magnesite and talc (Kelemen and Hirth, 2012). With increasing CO_2, more talc would be formed. To date, magnesite and brucite have not been observed in the cores, but magnesite was identified in the F2 core in several UV-visible-NIR spectra by the spectrometer's automatic indexer. These missing mineral products (magnesite, brucite) must have been removed from the system, altered, or could not be identified petrographically. Similar reactions with fayalite or Fe-rich minerals would produce magnetite but there is very little Fe in the target rocks or clay minerals, therefore, the absence of magnetite is not surprising. In the latter case, any precursor dolomite that survived impact melting and disassociation has likely been altered/metamorphosed to talc. A common skarnification reaction for instance is the addition of dolomite, silica and water to form calcite, talc and CO_2, which may occur at $\leq 400°C$ (Winter, 2001). Given the occurrence of carbonate and products of carbonation in the core, it is likely CO_2 had an active role in these reactions; however, fluid inclusion analyses of glasses within impact breccia and hydrothermal phases show no evidence of CO_2 (Bain and Kissin, 1988; Osinski et al., 2005a).

The interstratification of clay minerals is a normal stage when one clay mineral has been altered to another; saponite to chlorite for example, is very common during the process of chloritization (Beaufort et al., 2015). Chloritization is very common in impact hydrothermal systems (Naumov, 2005). Smectite (saponite) and chlorite (clinochlore) can occur as both a

retrograde metamorphic alteration of magnesian minerals and/or as a metasomatic product via addition of Mg to the rock (Beaufort et al., 2015). These minerals are favoured when Al is present. Although the crystalline basement rocks are dominantly felsic, it is interesting that all the resulting clay phases are alkali-poor. Naumov (2005) explains that this is a common chemical trend within the central area of impact structures, wherein there is addition Mg and Ca and depletion of Si and Al. Some cations such as K and Na are removed from the system which is consistent with Haughton as the alkalies must have been transported elsewhere during incorporation of Ca into carbonates.

3.5.6.2   *Mineralization in the centre of the structure*

Intense alteration in the central part of an impact structure is expected. Based on numerical modeling of large impact structures (e.g., Sudbury and Chicxulub) the thermal field in an impact-induced hydrothermal system is hottest and longest-lived at the crater centre (e.g. Abramov and Kring, 2007) enabling more intense alteration. The central uplift acts as a conduit enabling fluid flowing toward the structure's centre and upwards (Jõeleht et al., 2005). As the impact melt cools, initial temperatures at the centre of an impact structure may have exceeded 500-600°C, enabling thermal metamorphism and metasomatism of impactites (Kirsimäe and Osinski, 2013).

3.5.6.3   *Paragenesis*

In both the F2 and F3 cores, pervasive replacement of the silicate groundmass to clay minerals suggests high water to rock ratios and/or high CO_2 activity in the fluid. The water to rock ratio is particularly significant in the case of the F2 core, which was subjected to silicate alteration followed by carbonate and sulfate alteration and/or replacement. The F2 core alteration is consistent with the thermochemical model for Mars where ultramafic host rock were pervasively altered to chlorite, talc, serpentine and smectite (saponite) in a convecting hydrothermal system within the central uplift (Schwenzer and Kring, 2013). Similar to Haughton, lateral zonation of hydrothermal mineral assemblages in the central uplifts has been documented in other impact structures (e.g., Kärdla) where the main features comprise a transition from smectite to chlorite followed by replacement of calcite by anhydrite (Naumov, 2005). The following alteration sequence is proposed for the cores based on petrographic relationships in this study and other constraints reported by Osinski et al. (2005a). The earliest hydrothermal event is a high temperature (>200°C) stage where retrograde metamorphism of

mafic to ultramafic impact melt in the presence of H_2O and CO_2-rich fluids resulting in metasomatism via serpentinization of silicate phases, i.e., the breakdown of silicates and formation of serpentine and talc. Both these minerals may be formed at high temperature but are stable over a wide range: talc from 150 to 650 °C and serpentine from 200 to 500°C, depending on the polymorph and pressure (Evans and Guggenheim, 1988; Majumdar et al., 2016; Winter, 2001). Of the surviving phases, talc would be the first to form. In addition to temperature stability, an increase in the SiO_2 activity and high water:rock ratio favoured the formation of talc in place of serpentine (Bach et al., 2012). As temperature decreased, the system evolved to a main stage (200–80°C) where chloritization accompanied by Si loss resulted in mixed clay minerals between talc and saponite, talc and chlorite and serpentine and chlorite. This mineral assemblage also follows modeled trends for decreasing water to rock ratio resulting in alteration of talc to smectite to chlorite (Schwenzer and Kring, 2013) suggesting that as the system evolved, fluids were progressively less available. Calcite, celestite/barite and anhydrite would also have precipitated during this stage. Calcite precipitation can result from boiling and increase in pH (Osinski et al., 2005a). The range of types of hydrothermal calcite, including overgrowths and later replacement suggest carbonate alteration may have been long-lasting. Finally, continued gypsum precipitation and replacement occurred in the last low temperature (<80°C) stage.

3.5.7 Implications for hydrothermal mineralization on Mars

Hydrothermal systems on Noachian to Hesperian Mars are thought to have been common and are proposed to have formed in a variety of settings, including both volcanic and impact-related (Schulze-Makuch et al., 2007). Evidence for impact-induced hydrothermal alteration on Mars was first identified through orbital remote sensing by Marzo et al. (2010), in which hydrated phases were identified within the central uplift and crater floor of the Toro crater, and it was concluded that phyllosilicate formation spanned from the Noachian to Hesperian eras. This study was followed by a decade of orbital observations by CRISM and OMEGA imaging spectrometers of hydrated minerals (Carter et al., 2013; Michalski et al., 2015) in impact structures and elsewhere. Ordered most to least abundant, they include Fe/Mg phyllosilicates, chlorites/corrensites, Al-smectites and micas, opaline silica, zeolites and sulfates, Al-Kaolins, serpentinites and carbonates, prehnite and epidote (Carter et al., 2013).

A wide range of analogue studies have been completed at the Haughton impact structure (e.g., Greenberger et al., 2016; Lee and Osinski, 2005; Osinski et al., 2013; Parnell et al., 2004; Pontefract et al., 2012; Tornabene et al., 2005). As a result of the newly identified hydrothermal mineral assemblages (talc, serpentine, saponite, chlorite, calcite and sulfate) in the F2 core, Haughton may present a potential analogue for a range of Martian rocks. Many studies have been completed to interpret the complex environments where clay minerals, sulfates and carbonates co-exist on Mars (Brown et al., 2010; Cloutis et al., 2006; Ehlmann et al., 2009; Poulet et al., 2005). Interstratified or mixed layering of talc and saponite, similar those in the F2 core, are currently being investigated through orbital observations on Mars (Michalski et al., 2015). Thermochemical modeling, thermal evolution models as well as terrestrial observations show the hydrous phases serpentine, chlorite and other clay minerals would result from hydrothermally altered mafic Martian crust in large impact structures in Noachian terrains on Mars (Abramov and Kring, 2005; GR Osinski et al., 2013; Schwenzer and Kring, 2009). Serpentine as well as chlorite and Fe/Mg smectites have been identified in some of the southern highland Noachian craters on Mars, with highest concentrations in the central peak region (Ehlmann et al., 2010). Serpentinization and carbonation were common processes forming talc/saponite in the Nili Fossae region of Mars (Amador et al., 2018). Finally, nakhlite meteorites are basaltic clinopyroxenites that have been hydrothermally altered and host secondary mineral assemblages that are similar to the F2 core. The secondary phases are generally located within fractures and veins and include: ferric saponite and Al-rich ferric serpentine, amorphous silicate gel of saponitic composition, halite, Ca-sulfates and carbonate (calcite, dolomite and ankerite) (Bridges et al., 2018; Hicks et al., 2014). Hence, these impact melt rock cores from Haughton's central uplift may be used to evaluate both orbital and rover observations of calculated assemblages for hydrothermal mineralization on Mars.

Serpentinization is important for habitability as it can produce both H_2 and methane, increases porosity of the rock (Mccollom and Bach, 2009; Tutolo et al., 2016) and is an exothermic reaction i.e., produces heat (Fyfe, 1974). Serpentinization processes may also be related to submarine ultramafic rocks in Hadean Earth, a potential site for the first living cells giving the abundance of microbial life that currently lives at the Lost City hydrothermal vent

(Müntener, 2010). Consequently, serpentine-rich hydrothermal environments on Mars should be in the top candidates for future Martian exploration.

3.6 Conclusions

In closing, although Haughton has been studied for over 40 years, there is still more that can be learned from subsurface deposits as the impactites exposed at surface only tell a part of the story. This study identifies new lithologies and mineralogy at Haughton which enable a better understanding of the heterogeneity of impact melt and hydrothermal alteration of mixed silicate, carbonate and sulfate target rocks at the centre of the Haughton impact structure. By characterizing these new impact melt rocks in drill cores at the centre of the Haughton impact structure, we conclude:

1) Haughton's impact melt is far more heterogeneous than previously thought. The melt rocks consists of the previously documented clast-rich particulate impact melt with a groundmass of microcrystalline calcite, glass and anhydrite (Osinski et al., 2005c); a clast-rich crystalline Mg-rich silicate-carbonate-sulfate impact melt rock (represented by the F2 core); and a clast-rich silicate impact melt rock dominated by Mg-rich clay mineral groundmass (represented by the F3 core).

2) The cores support the melting of carbonates and sulfates in response to hypervelocity impact. Although challenging, we show that in many cases it is possible to differentiate between these impact melt products and the products of hydrothermal replacement using a combination of micro-analyses.

3) The presence of Mg-rich clay minerals which we interpret as a mixture or interlayering of talc, saponite, serpentine and chlorite, at the centre of the Haughton structure are new to Haughton. Talc and serpentine in particular, are novel hydrothermal phases in terrestrial craters. Future studies should include detailed XRD to confirm these phases, but if this interpretation is correct, then their presence suggests the precursor melt may have been of an ultramafic composition.

4) Hydrothermal alteration is the most intense and decreases outwards from the centre of the structure. The hydrothermal model for the centre of the Haughton structure should be

updated. In addition to quartz (Osinski et al., 2001), it should include the above mentioned clay minerals, calcite, anhydrite and gypsum.

3.7 References

Abramov, O., Kring, D. a., 2005. Impact-induced hydrothermal activity on early Mars. J. Geophys. Res. 110, E12S09. https://doi.org/10.1029/2005JE002453

Abramov, O., Kring, D.A., 2007. Numerical modeling of impact-induced hydrothermal activity at the Chicxulub crater. Meteorit. Planet. Sci. 42, 93–112. https://doi.org/10.1111/j.1945-5100.2007.tb00220.x

Agrinier, P., Deutsch, A., Schärer, U., Martinez, I., 2001. Fast back-reactions of shock-released CO2 from carbonates: An experimental approach. Geochim. Cosmochim. Acta 65, 2615–2632. https://doi.org/10.1016/S0016-7037(01)00617-2

Allen, R.L., Barrett, T.J., Browne, P.R.L., Clemson, J.E., Dunne, K.P.E., Ettlinger, A.D., Gibson, H.L., Groat, L.A., Hannington, M.D., Hawke, M.M., Jowett, E.C., Lang, J.R., Leitch, C.H.B., Lentz, D.R., Macdonald, A.J., McLeod, M., Martin, R.F., Murray, J., Pan, Y., Paradis, S., Peterson, E.U., Ray, G.E., Reardon, N.C., Rhys, D.A., Santaguida, F., Sherlock, R.L., Serbert, C., Simandl, G.J., Simmons, S.F., Taner, M.F., Thompson, A.J.B., Thompson, J.F.H., Turner, R.J.W., Wilson, G.C., Wolfson, I., Ziegler, J.F., 1996. Atlas of Alteration. Geological Association of Canada Mineral Deposits Division, St. John's.

Amador, E.S., Bandfield, J.L., Thomas, N.H., 2018. A search for minerals associated with serpentinization across Mars using CRISM spectral data. Icarus 311, 113–134. https://doi.org/10.1016/j.icarus.2018.03.021

Artemieva, N., Morgan, J., 2017. Quantifying the Release of Climate-Active Gases by Large Meteorite Impacts With a Case Study of Chicxulub. Geophys. Res. Lett. 1–9. https://doi.org/10.1002/2017GL074879

Bach, W., Jöns, B., Klein, F., 2012. Metasomatism within the ocean crust, in: Harlov, D.E., Austrheim, H. (Eds.), Metasomatism and the Chemical Transformation of Rock, Lecture

Notes in Earth System Sciences. Springer-Verlag Berlin Heidelberg, pp. 253–288.

Bain, J.G., Kissin, S.A., 1988. A preliminary study of fluid inclusions in shock-metamorphosed sediments at the Haughton Impact Structure, Devon Island, Canada., in: 51st Annual Meeting of the Meteoritical Society. Fayetteville, AR, United States (USA), p. 256.

Beaufort, D., Rigault, C., Billon, S., Billault, V., Inoue, A., Inoue, S., Patrier, P., 2015. Chlorite and chloritization processes through mixed-layer mineral series in low-temperature geological systems – a review. Clay Miner. 50, 497–523. https://doi.org/10.1180/claymin.2015.050.4.06

Bell, M.S., 2016. CO2 release due to impact devolatilization of carbonate: Results of shock experiments. Meteorit. Planet. Sci. 51, 619–646. https://doi.org/10.1111/maps.12613

Bolonin, A. V., Nikiforov, A. V., 2014. Intermediate sulfates in barite-celestite isomorphic series: Composition and mode of occurrence. Geol. Ore Depos. 56, 302–314. https://doi.org/10.1134/S1075701514040023

Bridges, J.C., Hicks, L.J., Treiman, A.H., 2018. Carbonates on Mars, in: Filiberto, J., Schwenzer, S.P. (Eds.), Volatiles in the Martian Crust. Elsevier, Cambridge, US, p. 427.

Brooker, R.A., Kjarsgaard, B.A., 2011. Silicate-carbonate liquid immiscibility and phase relations in the system SiO2-Na2O-Al2O3-Cao-Co2 at 0·1-2·5 GPa with applications to carbonatite genesis. J. Petrol. 52, 1281–1305. https://doi.org/10.1093/petrology/egq081

Brown, A.J., Hook, S.J., Baldridge, A.M., Crowley, J.K., Bridges, N.T., Thomson, B.J., Marion, G.M., de Souza Filho, C.R., Bishop, J.L., 2010. Hydrothermal formation of Clay-Carbonate alteration assemblages in the Nili Fossae region of Mars. Earth Planet. Sci. Lett. 297, 174–182. https://doi.org/10.1016/j.epsl.2010.06.018

Carter, J., Poulet, F., Bibring, J.P., Mangold, N., Murchie, S., 2013. Hydrous minerals on Mars as seen by the CRISM and OMEGA imaging spectrometers: Updated global view. J. Geophys. Res. E Planets 118, 831–858. https://doi.org/10.1029/2012JE004145

Chakhmouradian, A.R., Reguir, E.P., Zaitsev, A.N., 2016. Calcite and dolomite in intrusive

carbonatites. I. Textural variations. Mineral. Petrol. 110, 333–360.
https://doi.org/10.1007/s00710-015-0390-6

Clark, R.N., King, T.V. V, Klejwa, M., Swayze, G.A., Vergo, N., 1990. High Spectral
Resolution Reflectance Spectroscopy of Minerals. J. Geophys. Res. 95, 12653–12680.

Clark, R.N., Swayze, G.A., Wise, R.A., Livo, K.E., Hoefen, T.M., Kokaly, R.F., Sutley, S.J.,
2007. USGS Digital Spectral Library splib06a, Data Series. Reston, VA.
https://doi.org/10.3133/ds231

Cloutis, E.A., Hawthorne, F.C., Mertzman, S.A., Krenn, K., Craig, M.A., Marcino, D., Methot,
M., Strong, J., Mustard, J.F., Blaney, D.L., Bell, J.F., Vilas, F., 2006. Detection and
discrimination of sulfate minerals using reflectance spectroscopy. Icarus 184, 121–157.
https://doi.org/10.1016/j.icarus.2006.04.003

Deer, W.A., Howe, R.A., Zussman, J., 1992. An introduction to the rock-forming minerals (2nd
edition), 2nd editio. ed. Pearson Prentice Hall, Harlow, England.

Dence, M.R., 1972. The nature and significance of terrestrial impact structures, in: 15th
International Geological Congress. pp. 77–89.

Dence, M.R., W. von Engelhardt, Plant, A.G., Walter, L.S., 1974. Indications of fluid
immiscibility in glass from West Clearwater Lake impact crater, Quebec, Canada. Contrib.
to Mineral. Petrol. 46, 81–97.

Dobson, D.P., Jones, A.P., Rabe, R., Sekine, T., Kurita, K., Taniguchi, T., Kondo, T., Kato, T.,
Shimomura, O., Urakawa, S., 1996. In-situ measurement of viscosity and density of
carbonate melts at high pressure. Earth Planet. Sci. Lett. 143, 207–215.
https://doi.org/10.1016/0012-821x(96)00139-2

Dressler, B.O., Reimold, W.U., 2001. Terrestrial impact melt rocks and glasses, in: Earth-
Science Reviews. Elsevier, Amsterdam, pp. 205–284.
https://doi.org/http://dx.doi.org/10.1016/S0012-8252(01)00064-2

Ehlmann, B.L., Mustard, J.F., Murchie, S.L., 2010. Geologic setting of serpentine deposits on

Mars. Geophys. Res. Lett. 37, 1–5. https://doi.org/10.1029/2010GL042596

Ehlmann, B.L., Mustard, J.F., Swayze, G.A., Clark, R.N., Bishop, J.L., Poulet, F., Des Marais, D.J., Roach, L.H., Milliken, R.E., Wray, J.J., Barnouin-Jha, O., Murchie, S.L., 2009. Identification of hydrated silicate minerals on Mars using MRO-CRISM: Geologic context near Nili Fossae and implications for aqueous alteration. J. Geophys. Res. E Planets 114, 1–33. https://doi.org/10.1029/2009JE003339

Evans, B.W., Guggenheim, S., 1988. Talc, pyrophyllite and related minerals, in: Hydrous Phyllosilicates, Reviews in Mineralogy 19. Mineralogical Society of America, Washington D.C., pp. 225–293. https://doi.org/10.1016/B978-0-12-397220-0.00008-8

Flemming, R.L., Léveillé, R., 2007. A cautionary tale of section preparation altering mineralogy prior to examination, in: GAC-MAC Annual Meeting Abstract Volume 32. Geological Association of Canada, Yellowknife, Canada, p. 28.

Frisch, T., Thorsteinsson, R., 1978. Haughton astrobleme: a mid-Cenozoic impact, Devon Island, Canadian Arctic Archipelago. Arctic 31, 108–124.

Frisch, T., Trettin, H.P., 1991. Precambrian Successions in the Northermost Part of the Canadian Shield, in: Geology of the Inuitian Orogen and Arctic Platform of Canada and Greenland. Geological Survey of Canada, Ottawa, pp. 103–108.

Gomide, C.S., Brod, J.A., Junqueira-Brod, T.C., Buhn, B.M., Santos, R.V., Barbosa, E.S.R., Cordeiro, P.F.O., Palmieri, M., Grasso, C.B., Torres, M.G., 2013. Sulfur isotopes from Brazilian alkaline carbonatite complexes. Chem. Geol. 341, 38–49. https://doi.org/10.1016/j.chemgeo.2013.01.006

Graup, G., 1999. Carbonate-silicate liquid immiscibility upon impact melting: Ries Crater, Germany. Meteorit. Planet. Sci. 34, 425–438.

Greenberger, R.N., Mustard, J.F., Osinski, G.R., Tornabene, L.L., Pontefract, A.J., Marion, C.L., Flemming, R.L., Wilson, J.H., Cloutis, E.A., 2016. Hyperspectral mapping of alteration assemblages within a hydrothermal vug at the Haughton impact structure, Canada. Meteorit.

{&} Planet. Sci. 51, 2274–2292. https://doi.org/http://dx.doi.org/10.1111/maps.12716

Grieve, R.A.F., 1988. The Haughton impact structure: summary and synthesis of the results of the HISS project. Meteoritics 23, 249–254.

Hagerty, J.J., Newsom, H.E., 2003. Hydrothermal alteration at the Lonar Lake impact structure, India: Implications for impact cratering on Mars. Meteorit. Planet. Sci. 38, 365–381. https://doi.org/10.1111/j.1945-5100.2003.tb00272.x

Hamann, C., Bläsing, S., Hecht, L., Schäffer, S., Deutsch, A., Osterholz, J., Lexow, B., 2018a. The reaction of carbonates in contact with laser-generated, superheated silicate melts: Constraining impact metamorphism of carbonate-bearing target rocks. Meteorit. Planet. Sci. 43. https://doi.org/10.1111/maps.13133

Hamann, C., Fazio, A., Ebert, M., Hecht, L., Wirth, R., Folco, L., Deutsch, A., Reimold, W.U., 2018b. Silicate liquid immiscibility in impact melts. Meteorit. Planet. Sci. 53, 1594–1632. https://doi.org/10.1111/maps.12907

Hartung, J.B., Kunk, M.J., Anderson, R.R., 1990. Geology, geophysics, and geochronology of the Manson impact structure, in: Sharpton, V.L., Ward, P.D. (Eds.), GLOBAL CATASTROPHES IN EARTH HISTORY : AN INTERDISCIPLINARY CONFERENCE ON IMPACTS, VOLCANISM, AND MASS MORTALITY Special Paper 247. Geological Society of America, pp. 207–221.

Hicks, L.J., Bridges, J.C., Gurman, S.J., 2014. Ferric saponite and serpentine in the nakhlite martian meteorites. Geochim. Cosmochim. Acta 136, 194–210. https://doi.org/10.1016/j.gca.2014.04.010

Hörz, F., Archer, P.D., Niles, P.B., Zolensky, M.E., Evans, M., 2015. Devolatilization or melting of carbonates at Meteor Crater, AZ? Meteorit. Planet. Sci. 50, 1050–1070. https://doi.org/10.1111/maps.12453

Hörz, F., Mittlefehldt, D.W., See, T.H., Galindo, C., 2002. Petrographic studies of the impact melts from Meteor Crater, Arizona, USA. Meteorit. Planet. Sci. 37, 501–531.

Ivanov, B. a, Deutsch, A., 2002. The phase diagram of CaCO3 in relation to shock compression and decomposition. Phys. Earth Planet. Inter. 129, 131–143. https://doi.org/10.1016/S0031-9201(01)00268-0

Izawa, M.R.M., Banerjee, N.R., Osinski, G.R., Flemming, R.L., Parnell, J., Cockell, C.S., 2011. Weathering of Post-Impact Hydrothermal Deposits from the Haughton Impact Structure: Implications for Microbial Colonization and Biosignature Preservation. Astrobiology 11, 537–550. https://doi.org/10.1089/ast.2011.0612

Jessberger, E., 1988. 40Ar-39Ar Dating of the Haughton Impact Structure. Meteoritics 23, 233–234.

Jõeleht, A., Kirsimae, K., Plado, J., Versh, E., Ivanov, B., 2005. Cooling of the Kärdla impact crater : II . Impact and geothermal modeling. Meteorit. Planet. Sci. 40, 21–33.

Kelemen, P.B., Hirth, G., 2012. Reaction-driven cracking during retrograde metamorphism: Olivine hydration and carbonation. Earth Planet. Sci. Lett. 345–348, 81–89. https://doi.org/10.1016/j.epsl.2012.06.018

Kieffer, S.W., Simonds, C.H., 1980. The role of volatiles and lithology in the impact cratering process. Rev. Geophys. 18, 143–181. https://doi.org/10.1029/RG018i001p00143

Kirsimäe, K., Osinski, G.R., 2013. Impact-induced hydrothermal activity, in: Osinski, G.R., Pierazzo, E. (Eds.), Impact Cratering Processes and Products. Wiley-Blackwell, p. 316.

Langenhorst, F., Deutsch, A., 2012. Shock Metamorphism in Minerals. Elements 8, 31–36.

Lee, P., Osinski, G.R., 2005. The Haughton-Mars Project: Overview of science investigations at the Haughton impact structure and surrounding terrains, and relevance to planetary studies. Meteorit. Planet. Sci. 40, 1755–1758. https://doi.org/10.1111/j.1945-5100.2005.tb00144.x

Lee, W.J., Wyllie, P.J., 1998. Petrogenesis of carbonatite magmas from mantle to crust, constrained by the system CaO-(MgO + FeO*)-(Na2O + K2O)-(SiO2+ Al2O3+ TiO2)-CO2. J. Petrol. 39, 495–517. https://doi.org/10.1093/petroj/39.3.495

Lightfoot, P.C., 2017. Nickle Sulfide Ores and Impact Melts Origin of the Sudury Igneous
Complex. Elsevier Inc.

Lu, F.H., Meyers, W.J., Schoonen, M.A.A., 1997. Minor and trace element analyses on gypsum :
an experimental study 142.

Luhr, J.F., 2008. Primary igneous anhydrite: Progress since its recognition in the 1982 El
Chichón trachyandesite. J. Volcanol. Geotherm. Res. 175, 394–407.
https://doi.org/10.1016/j.jvolgeores.2008.02.016

Mader, M.M., Osinski, G.R., 2018. Impactites of the Mistastin Lake impact structure: Insights
into impact ejecta emplacement. Meteorit. Planet. Sci. 27.
https://doi.org/10.1111/maps.13173

Majumdar, A.S., Hövelmann, J., Mondal, S.K., Putnis, A., 2016. The role of reacting solution
and temperature on compositional evolution during harzburgite alteration: Constraints from
the Mesoarchean Nuasahi Massif (eastern India). Lithos 256–257, 228–242.
https://doi.org/10.1016/j.lithos.2016.04.016

Martin, A.M., Righter, K., Treiman, A.H., 2012. Experimental constraints on the destabilization
of basalt+calcite+anhydrite at high pressure-high temperature and implications for
meteoroid impact modeling. Earth Planet. Sci. Lett. 331–332, 291–304.
https://doi.org/10.1016/j.epsl.2012.03.026

Martinez, I., Agrinier, P., Schaerer, U., Javoy, M., 1994. A SEM-ATEM and stable isotope study
of carbonates from the Haughton impact crater, Canada. Earth Planet. Sci. Lett. 121, 559–
574.

Marzo, G.A., Davila, A.F., Tornabene, L.L., Dohm, J.M., Fairén, A.G., Gross, C., Kneissl, T.,
Bishop, J.L., Roush, T.L., McKay, C.P., 2010. Evidence for Hesperian impact-induced
hydrothermalism on Mars. Icarus 208, 667–683.
https://doi.org/10.1016/j.icarus.2010.03.013

Masaitis, V.L., Raikhlin, A.I., Mashchak, M.S., 1980. Immiscibility of impact melts, in: Lunar

and Planetary Science Conference XI. pp. 677–679.

Mccollom, T.M., Bach, W., 2009. Thermodynamic constraints on hydrogen generation during serpentinization of ultramafic rocks. Geochim. Cosmochim. Acta 73, 856–875. https://doi.org/10.1016/j.gca.2008.10.032

Metzler, A., Ostertag, R., Redeker, H.J., Stöffler, D., 1988. Composition of the Crystalline Basement and Shock Metamorphism of Crystalline and Sedimentary Target Rocks at teh Haughton Impact Crater, Devon Island, Canada. Meteoritcs 23, 197–207. https://doi.org/10.1017/CBO9781107415324.004

Michalski, J.R., Cuadros, J., Bishop, J.L., Darby Dyar, M., Dekov, V., Fiore, S., 2015. Constraints on the crystal-chemistry of Fe/Mg-rich smectitic clays on Mars and links to global alteration trends. Earth Planet. Sci. Lett. 427, 215–225. https://doi.org/10.1016/j.epsl.2015.06.020

Moore, K.R., Wood, B.J., 1998. The Transition from Carbonate to Silicate Melts in the CaO-MgO-SiO2-CO2 System. J. Petrol. 39, 1943–1951. https://doi.org/10.1093/petroj/39.11-12.1943

Müntener, O., 2010. Serpentine and serpentinization: A link between planet formation and life. Geology 38, 959–960. https://doi.org/10.1130/focus102010.1

Naumov, M.V., 2005. Principal features of impact-generated hydrothermal circulation systems: mineralogical and geochemical evidence. Geofluids 5, 165–184.

Nelson, M.J., Newsom, H.E., Spilde, M.N., Salge, T., 2012. Petrographic investigation of melt and matrix relationships in Chicxulub Crater Yaxcopoil-1 brecciated melt rock and melt rock-bearing suevite (846-885 m, units 4 and 5). Geochim. Cosmochim. Acta 86, 1–20. https://doi.org/http://dx.doi.org/10.1016/j.gca.2012.02.022

Nesbitt, H.W., Young, G.M., 1982. Early Proterozoic climates and plate motions inferred from major element chemistry of lutites. Nature 299, 715–717.

O'Keefe, J.D., Ahrens, T.J., 1989. Impact production of CO2 by the Cretaceous/Tertiary

extinction bolide and the resultant heating of the Earth. Nature.
https://doi.org/10.1038/338247a0

Osae, S., Misra, S., Koeberl, C., Sengupta, D., Ghosh, S., 2005. Target rocks, impact glasses, and
melt rocks from the Lonar impact crater, India: Petrography and geochemistry. Meteorit.
Planet. Sci. 40, 1473–1492. https://doi.org/10.1111/j.1945-5100.2005.tb00413.x

Osinski, G., Tornabene, L.L., Banerjee, N.R., Cockell, C.S., Flemming, R., Izawa, M.R.,
McCutcheon, J., Parnell, J., Preston, L.J., Pickersgill, A.E., Pontefract, A., Sapers, H.M.,
Southam, G., 2013. Impact-generated hydrothermal systems on Earth and Mars. Icarus 224,
347–363. https://doi.org/10.1016/j.icarus.2012.08.030

Osinski, G.R., Bunch, T.E., Flemming, R.L., Buitenhuis, E., Wittke, J.H., 2015. Impact melt-
and projectile-bearing ejecta at Barringer Crater, Arizona. Earth Planet. Sci. Lett. 432, 283–
292. https://doi.org/10.1016/j.epsl.2015.10.021

Osinski, G.R., Bunch, T.E., Witte, J., 2003. Evidence for the shock melting of carbonates from
meteor crater, Arizona, in: 66th Annual Meteoritical Society Meeting. p. abstract #5070.

Osinski, G.R., Grieve, R.A.F., Bleacher, J.E., Neish, C.D., Pilles, E.A., Tornabene, L.L., 2018.
Igneous rocks formed by hypervelocity impact. J. Volcanol. Geotherm. Res. 353, 25–54.
https://doi.org/10.1016/j.jvolgeores.2018.01.015

Osinski, G.R., Grieve, R.A.F., Collins, G.S., Marion, C., Sylvester, P., 2008a. The effect of
target lithology on the products of impact melting. Meteorit. Planet. Sci. 43, 1939–1954.
https://doi.org/10.1111/j.1945-5100.2008.tb00654.x

Osinski, G.R., Lee, P., Parnell, J., Spray, J.G., Baron, M., 2005a. A case study of impact-induced
hydrothermal activity: The Haughton impact structure, Devon Island, Canadian High
Arctic. Meteorit. Planet. Sci. 40, 1859–1877. https://doi.org/10.1111/j.1945-
5100.2005.tb00150.x

Osinski, G.R., Lee, P., Spray, J.G., Parnell, J., Lim, D.S.S., Bunch, T.E., Cockell, C.S., Glass, B.,
2005b. Geological overview and cratering model for the Haughton impact structure, Devon

Island, Canadian High Arctic. Meteorit. Planet. Sci. 40, 1759–1776.
https://doi.org/10.1111/j.1945-5100.2005.tb00145.x

Osinski, G.R., Spray, J.G., 2005. Tectonics of complex crater formation as revealed by the
Haughton impact structure, Devon Island, Canadian High Arctic. Meteorit. Planet. Sci. 40,
1813–1834. https://doi.org/10.1111/j.1945-5100.2005.tb00148.x

Osinski, G.R., Spray, J.G., 2003. Evidence for the shock melting of sulfates from the Haughton
impact structure, Arctic Canada. Earth Planet. Sci. Lett. 215, 357–370.
https://doi.org/10.1016/S0012-821X(03)00420-5

Osinski, G.R., Spray, J.G., 2001. Impact-generated carbonate melts: evidence from the Haughton
structure, Canada. Earth Planet. Sci. Lett. 194, 17–29. https://doi.org/10.1016/S0012-
821X(01)00558-1

Osinski, G.R., Spray, J.G., Grieve, R.A.F., 2008b. Impact melting in sedimentary target rocks:
An assessment, in: Evans, K.R., Horton, J.W., King, J.D.T., Morrow J.R. (Eds.), The
Sedimentary Record of Meteorite Impacts, Geological Society of America Special
Publication 437. Geological Society of America, Boulder, pp. 1–18.
https://doi.org/10.1130/2008.2437(01).For

Osinski, G.R., Spray, J.G., Lee, P., 2005c. Impactites of the Haughton impact structure, Devon
Island, Canadian High Arctic. Meteorit. Planet. Sci. 40, 1789–1812.
https://doi.org/10.1111/j.1945-5100.2005.tb00147.x

Osinski, G.R., Spray, J.G., Lee, P., 2001. Impact-induced hydrothermal activity within the
Haughton impact structure, arctic Canada: Generation of a transient, warm, wet oasis.
Meteorit. Planet. Sci. 36, 731–745. https://doi.org/10.1111/j.1945-5100.2001.tb01910.x

Parnell, J., Lee, P., Cockell, C.S., Osinski, G.R., 2004. Microbial colonization in impact-
generated hydrothermal sulphate deposits, Haughton impact structure, and implications for
sulphates on Mars. Int. J. Astrobiol. 3, 247–256.
https://doi.org/10.1017/S1473550404001995

Pichler, H., Schmitt-Riegraf, C., 1997. Rock-forming Minerals in Thin Section. Chapman and Hall.

Pirajno, F., 2009. Hydrothermal Processes and Mineral Systems. Springer, Geological Survey of Western Australia, Berlin. https://doi.org/http://dx.doi.org/10.1007/978-1-4020-8613-7

Pohl, J., Eckstaller, A., Robertson, R.B., 1988. Gravity and magnetic investigations in the Haughton impact structure, Devon Island, Canada. Meteoritcs 23, 235–238.

Pontefract, A., Osinski, G.R., Lindgren, P., Parnell, J., Cockell, C.S., Southam, G., 2012. The effects of meteorite impacts on the availability of bioessential elements for endolithic organisms. Meteorit. Planet. Sci. 47, 1681–1691. https://doi.org/http://dx.doi.org/10.1111/maps.12004

Pope, K.O., Baines, K.H., Ocampo, A.C., Ivanov, B.A., 1994. Impact winter and the Cretaceous/Tertiary extinctions; results of a Chicxulub asteroid impact model. Earth Planet. Sci. Lett. 128, 719–725. https://doi.org/http://dx.doi.org/10.1016/0012-821X(94)90186-4

Poulet, F., Bibring, J.-P., Mustard, J.F., Gendrin, A., Mangold, N., Langevin, Y., Arvidson, R.E., Gondet, B., Gomez, C., Team, T.O., Berthé, M., Bibring, J.-P., Langevin, Y., Erard, S., Forni, O., Gendrin, A., Gondet, B., Manaud, N., Poulet, F., Poulleau, G., Soufflot, A., Combes, M., Drossart, P., Encrenaz, T., Fouchet, T., Melchiorri, R., Bellucci, G., Altieri, F., Formisano, V., Fonti, S., Capaccioni, F., Cerroni, P., Coradini, A., Korablev, O., Kottsov, V., Ignatiev, N., Titov, D., Zasova, L., Mangold, N., Pinet, P., Schmitt, B., Sotin, C., Hauber, E., Hoffmann, H., Jaumann, R., Keller, U., Arvidson, R., Mustard, J., Forget, F., 2005. Phyllosilicates on Mars and implications for early martian climate. Nature 438, 623.

Putnis, A., 2009. Mineral Replacement Reactions. Rev. Mineral. Geochemistry 70, 87–124. https://doi.org/10.2138/rmg.2009.70.3

Quesnel, Y., Gattacceca, J., Osinski, G.R., Rochette, P., 2013. Origin of the central magnetic anomaly at the Haughton impact structure, Canada. Earth Planet. Sci. Lett. 367, 116–122. https://doi.org/10.1016/j.epsl.2013.02.032

Redeker, H.-J., Stöffler, D., 1988. The allochthonous polymict breccia layer of the Haughton
impact crater, Devon Island, Canada. Meteoritics 23, 185–196.

Redeker, H.J., Stöffler, D., 1988. The Allochtonous Polymict Breccia Layer of the Haughton
Impact Crater, Devon Island, Canada. Meteoritics 23, 185–196.

Reimold, W., Koeberl, C., Gibson, R., Dressler, B., 2005. Economic mineral deposits in impact
structures: a review. Impact tectonics 479–552.

Robertson, P.B., 1988. The Haughton impact structure, Devon Island, Canada: Setting and
History of investigations. Meteoritics 23, 181–184.

Robertson, P.B., Mason, G.D., 1975. Shatter cones from Haughton Dome, Devon Island,
Canada. Nature 255, 393–394.

Robertson, P.B., Plant, A.G., 1981. Shock Metamorphism in sillimanite from the Haughton
impact structure, Devon Island, Canada. Contrib. to Mineral. Petrol. 78, 12–20.

Safonov, O.G., Kamenetsky, V.S., Perchuk, L.L., 2011. Links between carbonatite and
kimberlite melts in chloride-carbonate-silicate systems: Experiments and application to
natural assemblages. J. Petrol. 52, 1307–1331. https://doi.org/10.1093/petrology/egq034

Schulze-Makuch, D., Dohm, J.M., Fan, C., Fairén, A.G., Rodriguez, J.A.P., Baker, V.R., Fink,
W., 2007. Exploration of hydrothermal targets on Mars. Icarus 189, 308–324.
https://doi.org/10.1016/j.icarus.2007.02.007

Schwenzer, S.P., Kring, D. a., 2013. Alteration minerals in impact-generated hydrothermal
systems – Exploring host rock variability. Icarus 226, 487–496.
https://doi.org/10.1016/j.icarus.2013.06.003

Schwenzer, S.P., Kring, D. a., 2009. Impact-generated hydrothermal systems capable of forming
phyllosilicates on Noachian Mars. Geology 37, 1091–1094.
https://doi.org/10.1130/G30340A.1

Sharygin, V. V, Doroshkevich, A.G., 2017. Mineralogy of Secondary Olivine-hosted Inclusions

in Calcite Carbonatites of the Belaya Zima Alkaline Complex , Eastern Sayan , Russia : Evidence for Late-magmatic Na-Ca-rich Carbonate Composition 90, 524–530.

Sherlock, S., Kelley, S., 2005. Re   evaluating the age of the Haughton impact event. … Planet. Sci. 40, 1777–1787. https://doi.org/10.1111/j.1945-5100.2005.tb00146.x

Singleton, A.C., Osinski, G.R., McCausland, P.J.A., Moser, D.E., 2011. Shock-induced changes in density and porosity in shock-metamorphosed crystalline rocks, Haughton impact structure, Canada. Meteorit. Planet. Sci. 46, 1774–1786. https://doi.org/http://dx.doi.org/10.1111/j.1945-5100.2011.01290.x

Spray, J.G., Thompson, L.M., 2008. Constraints on central uplift structure from the Manicouagan impact crater. Meteorit. Planet. Sci. 43, 2049–2057. https://doi.org/10.1111/j.1945-5100.2008.tb00660.x

Stöffler, D., Hamann, C., Metzler, K., 2018. Shock metamorphism of planetary silicate rocks and sediments: Proposal for an updated classification system. Meteorit. Planet. Sci. 53, 5–49. https://doi.org/10.1111/maps.12912

Therriault, A.M., Fowler, A.D., Grieve, R.A.F., 2002. The Sudbury Igneous Complex : A Differentiated Impact Melt Sheet *. Econ. Geol. 97, 1521–1540.

Thompson, A.B., Aerts, M., Hack, A.C., 2007. Liquid Immiscibility in Silicate Melts and Related Systems. Rev. Mineral. Geochemistry 65, 99–127. https://doi.org/10.2138/rmg.2007.65.4

Thorsteinsson, R., Mayr, U., 1987. The sedimentary rocks of Devon Island, Canadian Arctic Archipelago. Geological Survey of Canada Memoir 411, Ottawa, Canada.

Timms, N.E., Erickson, T.M., Zanetti, M.R., Pearce, M.A., Cayron, C., Cavosie, A.J., Reddy, S.M., Wittmann, A., Carpenter, P.K., 2017. Cubic zirconia in >2370 °C impact melt records Earth's hottest crust. Earth Planet. Sci. Lett. 477, 52–58. https://doi.org/10.1016/j.epsl.2017.08.012

Tornabene, L.L., Moersch, J.E., Osinski, G.R., Lee, P., Wright, S.P., 2005. Spaceborne visible

and thermal infrared lithologic mapping of impact-exposed subsurface lithologies at the Haughton impact structure, Devon Island, Canadian High Arctic; applications to Mars. Meteorit. Planet. Sci. 40, 1835–1858.

Tutolo, B.M., Mildner, D.F.R., Gagnon, C.V.L., Saar, M.O., Seyfried, W.E., 2016. Nanoscale contraints on porosity generation and fluid flow during serpentinization. Geology 44, 103–106.

Veksler, I. V., Dorfman, A.M., Dulski, P., Kamenetsky, V.S., Danyushevsky, L. V., Jeffries, T., Dingwell, D.B., 2012. Partitioning of elements between silicate melt and immiscible fluoride, chloride, carbonate, phosphate and sulfate melts, with implications to the origin of natrocarbonatite. Geochim. Cosmochim. Acta 79, 20–40. https://doi.org/10.1016/j.gca.2011.11.035

Versh, E., Kirsimäe, K., Jõeleht, A., Plado, J., 2005. Cooling of the Kärdla impact crater: I. The mineral paragenetic sequence observation. Meteorit. Planet. Sci. 40, 3–19. https://doi.org/10.1111/j.1945-5100.2005.tb00361.x

Walton, E.L., Timms, N.E., Hauck, T.E., Maclagan, E.A., Herd, C.D.K., 2019. Evidence of impact melting and post-impact decomposition of sedimentary target rocks from the Steen River impact structure ,. Earth Planet. Sci. Lett. 515, 173–186. https://doi.org/10.1016/j.epsl.2019.03.015

Winter, J.D., 2001. An introduction to igneous and metamorphic petrology. Prentice Hall, New Jersey.

Young, K.E., van Soest, M.C., Hodges, K. V., Watson, E.B., Adams, B. a., Lee, P., 2013. Impact thermochronology and the age of Haughton impact structure, Canada. Geophys. Res. Lett. 40, 3836–3840. https://doi.org/10.1002/grl.50745

Zylberman, W., 2014. Magnetometry and petrography of a core from the Haughton impact structure, Nunavut, Canadian High Arctic.

Zylberman, W., Quesnel, Y., Rochette, P., Osinski, G.R., Marion, C., Gattacceca, J., 2017.

Hydrothermally enhanced magnetization at the center of the Haughton impact structure? Meteorit. Planet. Sci. 52, 2147–2165. https://doi.org/10.1111/maps.12917

Chapter 4

4 An in-depth analysis of the impact-generated hydrothermal system at the centre of the Haughton impact structure, Devon Island, Canada.

4.1 Introduction

The formation of hydrothermal systems have only recently been recognized as a common process generated by hypervelocity impact on Earth and Mars, and have been suggested as possibly having been present elsewhere in the solar system (Marzo et al., 2010; Osinski et al., 2013; Schulze-Makuch et al., 2007). The formation of a hydrothermal system requires a heat source, fluid, and a permeable zone of rock through which the fluid can flow. Following an impact event, the initially superheated impact melt and breccias, the elevated geothermal gradient in the central uplift, and remaining heat from the shock wave, induce fluid flow in the newly fractured and brecciated target rocks (Abramov, 2004; Abramov and Kring, 2007; Kirsimäe and Osinski, 2013; McCarville and Crossey, 1996). Alteration of impact melt rocks and breccias also occurs, but only after they have cooled sufficiently to become permeable (Abramov and Kring, 2007). Minerals from the target rocks are dissolved into the hydrothermal fluids, transported along fluid pathways and precipitate new minerals and/or existing minerals are altered upon cooling. Impact-generated hydrothermal systems on Earth and on other planetary bodies such as Mars may provide a potentially warm, wet, nutrient-rich habitat for extremophiles, in addition to the formation of secondary minerals which can act as geochemical catalysts for the origins of life (Cockell, 2006; Cockell and Lee, 2002; Osinski et al., 2001; Parnell et al., 2010b). As a result, impact-generated hydrothermal systems on Mars should be principal targets to study and explore for Martian life (Osinski et al., 2013). Furthermore, syngenetic to epigenetic deposits resulting from impact-induced hydrothermal systems have produced economically viable natural resources, e.g., Zn-Cu-Pb deposits at the Sudbury impact structure and Pb-Zn deposits at the Siljan impact structures (Grieve, 2005; Reimold et al., 2005).

110

Understanding the processes and products of hydrothermal systems is important given the economical and astrobiological implications. Despite these facts, only about half of the ~40% of craters with evidence of impact inducted hydrothermal activity on Earth have been examined in detail (Osinski et al., 2013).

In the 23-km diameter Haughton impact structure on Devon Island in the Canadian High Arctic, hydrothermal circulation is thought to have begun soon after the impact, as the structure lacks large amounts of impermeable silicate impact melt rock. Previous studies have shown that mineralization at this site is concentrated in and around the central uplift and in the faulted crater rim region (Osinski et al., 2001, 2005a,). The Haughton impact event occurred in the late Paleogene, with Ar-Ar and (U-Th)/He ages of ~23 Ma (Jessberger, 1988; Young et al., 2013, respectively) and an Ar-Ar age of 39 Ma (Sherlock and Kelley, 2005). A ~1880 m thick sequence of Paleozoic sedimentary rocks of the Arctic Platform that included limestones, dolostones, evaporites and minor shale and sandstone underlain by the Precambrian crystalline basement was impacted (Metzler et al., 1988; Thorsteinsson and Mayr, 1987) (Figs. 4.1 and 4.2). Exposed faulted blocks of target lithologies become younger towards the rim of the structure and occur primarily in the periphery of the central uplift. The crater-fill consists of grey clast-supported lithic breccias and grey particulate impact melt rocks, which contain clasts from all known target rocks (Osinski et al., 2005c, 2005b). The groundmass of the melt rocks consists of microcrystalline calcite, silicate glass and anhydrite. In addition, Chapter 3 presents evidence for silicate impact melt rocks and silicate-carbonate-sulfate melt rocks in the centre of the central uplift. The central uplift at Haughton lacks a central peak, which is thought to have collapsed in the final stages of crater formation due to weak strength of the layered sedimentary target rocks (Osinski and Spray, 2005).

The hydrothermal system at Haughton is one of the few that have been characterized in any detail (Osinski et al., 2005a, 2001; Zylberman et al., 2017, Chapter 3 this document). The dominant mineralization styles are veins and vugs of marcasite, calcite, selenite and quartz. Mg-rich clay minerals have recently been detected for the first time (Chapter 2, 3). Mineralization occurs in four distinct locations within the impact structure: 1) within the crater-fill melt rocks and breccias; 2) as cement in the exposed brecciated target rocks in the central uplift; 3) as veins within the faulted target rock blocks around the outer margin of the eastern and southern parts of

the central uplift; and 4) as hydrothermal pipe structures along faults and fractures in the crater rim (Osinski et al., 2005a). To date, clay mineralization has been identified exclusively within the silicate melt rocks in the central uplift (Chapter 3), which also host hydrothermal Fe-oxides, such as magnetite and sulfide mineralization in clast coronas as the result of leaching from the host mafic clasts (Zylberman et al., 2017). The hydrothermal system at Haughton has been previously divided into three main stages based on mineralogy and fluid inclusion studies: early, main and late (Osinski et al., 2001). The early stage is a high temperature (>200 °C), vapour-dominated phase represented by quartz mineralization and potential serpentinization in the central uplift. The main stage is characterized by fluid inclusions that are dominated by liquid-vapour inclusions (80-200 °C) and are associated with calcite and marcasite in the central uplift periphery and chloritization of the silicate melt rocks at the centre of the structure. Finally the late stage is characterized by low temperature, liquid-only fluid inclusions (< 80 °C) dominated by sulfate mineralization (Osinski et al., 2001; Chapter 3). Some occurrences are partially overprinted by iron oxides and sulfates as a result of weathering (Greenberger et al., 2016; Izawa et al., 2011). Although no economic deposits have been identified at Haughton, there have been a series of fruitful in situ astrobiological studies completed that suggest the Haughton impactites and/or hydrothermal system could have hosted microbial life (Parnell et al., 2010b, 2010a, 2004; Pontefract et al., 2012).

The objective of this study is to evaluate and better constrain the hydrothermal system within the centre and periphery of the central uplift at the Haughton impact structure by providing new constraints from recently acquired samples and a systematic microanalytical approach including cathodoluminescence and fluid inclusion studies of the different target rocks and allochthonous impactites. Cathodoluminescence has been applied to study the impactites at Haughton for the first time and yields important insights into the identification and differentiation of different generations of calcite. Furthermore, carbonate mineralization within carbonate target rocks presents the challenge of distinguishing between diagenetic and potentially multiple generations of hydrothermal calcite. Carbonate precipitation commonly persists through the life of these hydrothermal systems (Osinski et al., 2005a). New fluid inclusion data including phases within the newly acquired drill core at the centre of the Haughton structure (Chapter 2 and 3), is also presented and will expand the known composition and hydrothermal temperature profile.

Collectively, this study, along with Chapter 3 and previous works, will enable an improved model of the mineralization at the centre of the Haughton structure.
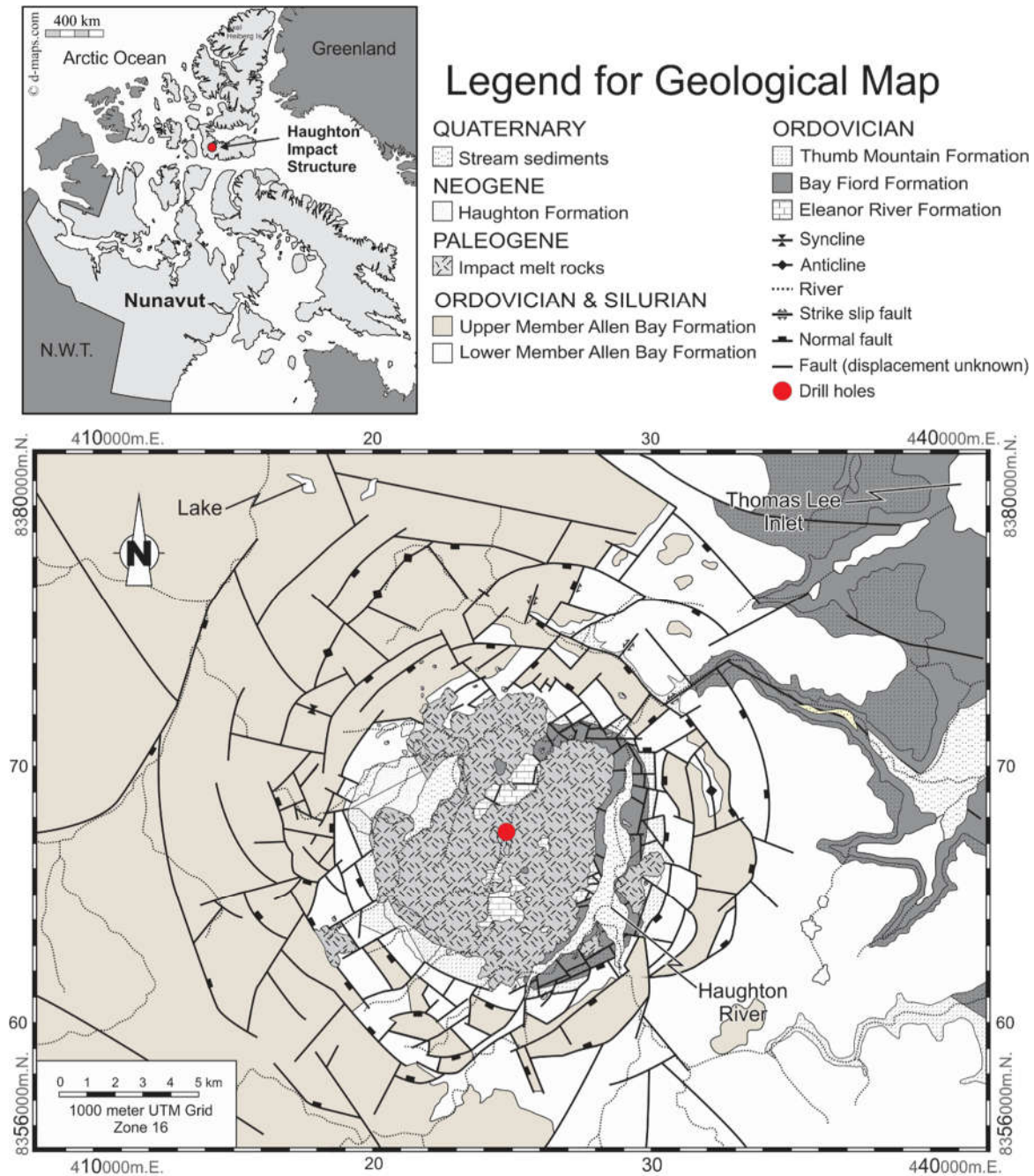
Figure 4.1 Location and geologic map of the Haughton impact structure, on Devon Island in Nunavut, Canada, modified from Osinski et al. (2005c).

4.2 Analytical Methods

4.2.1 Sampling

Samples used in this study were collected during the 2013 field season (CM-#). Samples from previous expeditions were also used (HMP-#, SA, HTS-#). All samples were collected within the central region to the central uplift periphery of the Haughton impact structure, largely within the Haughton River Valley. Samples consist of veins, vugs and cement within each lithology of the target rock, as well as impactites with evidence of alteration. Polished thin sections of representative samples of each type of mineralization in each type of the exposed target rock formations as well as within the impact melt rocks were prepared in the Thin Section Lab at the Department of Earth Sciences at Western University. Unshocked and shocked host samples were also collected or re-examined as reference materials.

4.2.2 Petrography

Forty-three polished thin sections were examined with a Nikon LV100POL petrographic microscope to identify and evaluate hydrothermal phases, of which a sub-selection of 25 were chosen for further analysis. Carbonate and quartz samples were analyzed by optical cathodoluminescence (CL) on a Reliotron microscope stage-mounted CL instrument in the Department of Earth Sciences, Western University. The optical-CL is connected to a high-sensitivity CCD camera on the third ocular of the microscope and is operated through use of Act 1 software. Exposure times range from 10 - 60 s. The beam is focused on the sample by manual placement of two small magnets. Beam conditions are maintained at ~ 600 µA and ~15 kV. Optical-CL has the advantage of being able to switch easily between transmitted light to polarized light to CL imaging mode although it has limited magnification and resolution compared to electron microprobe analysis (EPMA)-CL. Optical-CL is also limited to the visible part of the electromagnetic spectrum, whereas EPMA-CL can detect the near-infrared, visible and ultra-violet range, which can result in differing CL results for the same sample. Carbonate host rocks were also examined in CL and compared to vugs and veins.

For quartz samples, wavelength dispersive spectroscopy (WDS) was used to map Si, Fe, Al and K, and energy dispersive spectroscopy (EDS) was used to map Ti, S, Ca, C, F, Mg and Mn.

Quantitative WDS analysis for all silicates, including clay minerals and quartz were collected for Si, Ti, Cr, Al, Mg, Mn, Fe, Ca, Na, K, P, Cl, F and S, with standards enstatite, rutile, chromite, albite, enstatite, rhodonite, hematite, diopside, albite, orthoclase, apatite, sodalite, fluorite and anhydrite, respectively. The probe accelerating voltage and current was set to 15 kV and 20 nA, respectively, with a 5 μm spot size. The beam width was reduced to 2 μm where appropriate, to avoid inclusions and adjacent phases.

Carbonate-sulfide regions were mapped using WDS for Mg, Ca, Mn, Fe, Al, K, S and Cl, and EDS for C, F, Na, Sr, Si, Ba, Ti and P. Quantitative WDS point analyses of calcite were collected for Ca, Mg, Fe, Mn, Sr, Ba, Si, S, Cl, F, Al, and Ce, with standards calcite, dolomite, siderite, siderite, strontianite, barite, quartz, anhydrite, sodalite, fluorite, corundum and cerium phosphate, respectively. For calcite, the probe accelerating voltage and current was set to 15 kV and 5 nA, respectively, with a 25 μm spot size. Sulfides were mapped using WDS for Fe, S, Pb, Zn and Cu, and EDS for Ca, Si, and Mg. Quantitative WDS point analyses of sulfides were collected for As, Fe, Co, Cu, Au, Ni, V, Zn, S, Pb, and Te, with standards arsenopyrite, pyrite, pure cobalt, chalcopyrite, pure Au, millerite, pure V, sphalerite, pyrite, galena and pure Te, respectively. The detection limits for WDS analyses range from 100 to 500 ppm for major element oxides, and from 200 to 1100 ppm for minor element oxides.

4.2.3 Mineral Identification

Laser Raman spectroscopy was used to identify and distinguish mineralogy of hydrothermal phases, particularly sulfates and sulfides such as polymorphs of FeS_2, pyrite and marcasite. Analyses were completed on a Renishaw InVia Reflex Raman spectrometer at Surface Science Western. Samples were viewed using an optical microscope integrated with the Raman. Three lasers, 785, 633 and 514 nm wavelengths, respectively, were equipped with a polarizer and half waveplate and two gratings, 1800 and 1200 1/m, with a spot size of 1-2 μm. Most spectra were collected with a spectral range of 50 to 1250 cm^{-1}. Laser wavelengths were changed as needed to obtain the best Raman spectra for the intended mineral. Data was evaluated using the Renishaw Wire 4.2 software and/or Crystal Sleuth software and compared to the RRUFF sample database of Raman spectra. Powder X-ray diffraction (PXRD) was used to identify mineral phases present within carbonate veins. Preparation included use of a micro-drill or dremel to extract vein material from the host rock then ground with a pestle and mortar. Samples were mounted in an

aluminum backpack holder and analyzed at the LSIS laboratory, Western University using a
Rigaku RU-200BVH rotating anode diffractometer operating at 45 kV and 160 mA with a Co Kα
anode source. Data were collected with a step size of 0.02° and scanned from 2° to 82° 2θ with a
scanning speed of 10° 2θ/min. Mineralogy was assessed by manually linking 2θ peaks with their
representative d-spacing and comparing to various mineral databases. Selected diffraction
patterns were also interpreted using Bruker AXS EVA software package and compared to the
International Centre for Diffraction Database (ICDD) PDF-4 database. Most veins consisted
dominantly of calcite, with minimal contamination of dolomite and quartz from the host rocks.

4.2.4 Fluid Inclusions

Fluid inclusion petrography was completed on 20 thin and 6 doubly-polished thick sections.
This consisted of searching for inclusions and if found, distinguish and characterize each fluid
inclusion assemblage. Fluid inclusion microthermometry and analysis were carried out on a
Linkham THMSG600 heating-freezing stage mounted on an Olympus BX53F microscope on
doubly polished ≥100 μm thick section chips. The heating-freezing stage was calibrated using
synthetic inclusions of pure H_2O [Tm(ice) = 0 °C] and H_2O–CO_2 inclusions [$T_m(CO_2)$ =
-56.6 °C] entrapped in quartz, with an error of +/- 0.1°C. Last ice melting (T_m(ice)) and the
temperature of homogenization (T_h) were measured in two-phase (liquid-vapour) inclusions
hosted in calcite, quartz, anhydrite and gypsum. Aqueous fluid salinities were calculated using
Tm(ice) and the equations after (Bodnar, 1993).

4.2.5 Gas Analysis

Quantitative analysis of fluid inclusion volatiles was completed on one sample of quartz
cement (HMP99-063) in the Eleanor River Formation breccia from the central uplift periphery
using the methodology described by Blamey (2012). Sample preparation was completed in the
high temperature geochemistry laboratory at Western University. A doubly polished section of
the sample was separated from the slide using an acetone bath, followed by manual separation of
the quartz from the host carbonate with the use of tweezers. The quartz chips were then double
washed in HCl and rinsed, then triple washed with distilled water and KOH to remove any
organic matter and/or remaining carbonate. Approximately 25 mg of sample was sent to the
Fluid Inclusion Gas Laboratory at New Mexico Institute of Mining and Technology where it was

dried below 100°C for 2-4 hours. The sample was crushed incrementally under a vacuum of ~10^{-8} Torr, yielding 4 bursts but only 3 yielded reasonable results. The crushing may open a single inclusion or multiple inclusions. Data acquisition was accomplished using a Pfeiffer Prisma quadrupole mass spectrometer operating in the fast-scan, peak-hopping mode. Gases measured were H_2, He, CH_4, N_2, O_2, Ar and CO_2 as well as H_2O. Calibration was completed using Scott Gas minimax commercial gas mixtures and 3 in-house fluid inclusion gas standards. Quantitative analysis of each of the gas species was provided via proprietary software. Unfortunately, the small sample size led to limited results.

4.3 Host stratigraphic target units

Though the clast population within the crater fill impactites is believed to represent all sedimentary strata identified in Figure 4.2, as well as the Precambrian basement in the central region of Devon Island, there are limited exposures of intact strata older than the Eleanor River Formation within the Haughton structure. Neither the older sedimentary units, including the Cape Clay, Cass Fjord, Rabbit Point, and Bear Point Formations, nor the crystalline basement, occur as outcrops. A small shocked sandstone outcrop is exposed in the central uplift and is interpreted as part of the Blanley Bay Formation (newly referred to as the Christian Elv Formation (Dewing and Nowlan, 2012)). The Neogene-aged Haughton Formation is also present within the Haughton structure, but its deposition post-dates the impact event and related hydrothermal activity.

Each mineralized unit present within the structure is described below, from the oldest to the youngest exposed target rocks, followed by the impact melt rocks. A large portion of the sedimentary rock descriptions are sourced from Thorsteinsson and Mayr (1987a) and references therein, with minor additions of local observations by this author's field work.

4.3.1 Eleanor River Formation

Faulted blocks of the Eleanor River Formation outcrop near the centre of the crater, as well as in the southeastern central uplift periphery. It is easily identifiable, resistant, grey to brown limestone that is in striking contrast with the surrounding grey melt rocks (Fig. 4.2D). Outside the crater, the Eleanor River Formation has a sharp lower contact to the Blanley Bay Formation

and an unconformable contact with the overlying Bay Fiord Formation. The unit is divided into 4 members in ascending order A, B, C and D, each of which represent shallowing upward carbonate sequences. Members A and C are medium bedded to massive strata whereas Members B and D are laminated to thinly bedded and recessive (Thorsteinsson and Mayr, 1987). The units range from dominantly lime mudstone with mottled dolomite to wackestone, packstone, grainstone and stromatolitic boundstone beds. Dolomite, sulfates and chert nodules are rare to absent in the lower members but common to abundant in the upper members (Thorsteinsson and Mayr, 1987).

4.3.2 Bay Fiord Formation

The Bay Fiord Formation is an evaporite-rich carbonate unit that sharply overlies the Eleanor River Formation. It is divided into A through D members. The basal member A is recessive and consists of crystalline to laminated anhydrite with some gypsum replacement in the form of nodules and increasing dolomite laminations to beds up stratigraphy. Member B consists on planar, thinly bedded dolomitic siltstone and shale with minor gypsum laminations at the base and minor interbeds of intraclasts and pellets. Member C consists of bioturbated and burrowed medium to thick bedded dolostone with some lime mudstone to skeletal wackestone and an abundance of fragments of corals, brachiopods, bryozoans and echinoderms. Member D is an non-fossiliferous finely crystalline, thinly bedded dolostone (Thorsteinsson and Mayr, 1987).

4.3.3 Thumb Mountain Formation

The Thumb Mountain Formation lies conformably on the Bay Fiord Formation. It is a light grey to brown fossiliferous calcareous dolostone to dolomitic limestone. Bed thicknesses vary from thin to thick and bedded to massive; beds are thickest at the top of the section. The unit ranges from mudstone to skeletal packstone with labyrinth mottling. The limestone is lime mudstone whereas the dolomite is fine to medium crystalline. A distinctive characteristic of the Thumb Mountain Formation is the abundance of megafossils, particularly up section, which comprise corals, bryozoans, brachiopods, gastropods, cephalopods, trilobites and ostracodes (Thorsteinsson and Mayr, 1987). An example of Thumb Mountain's packstone cemented by diagenetic calcite is illustrated in Figures 4.3A and B.

4.3.4 Irene Bay Formation

Together, the Bay Fiord, Thumb Mountain and Irene Bay Formations make up the Cornwallis Group. The Irene Bay Formation is a thin unit, 40 to 80 m thick of recessive, green argillaceous limestone and minor shale that overlies the Thumb Mountain Formation (Kerr, 1967). Although it was probably present pre-impact, to date no outcrops have been identified within the Haughton structure.

4.3.5 Allen Bay Formation

The Allen Bay Formation conformably overlies the Irene Bay Formation. It consists of 3 members; the lower member consists of medium bedded to massive limestone comprised of lime mudstone to skeletal-wackestone and packstone. The limestone may have grey shale and limestone nodules and a few megafossils. The middle and upper members consist primarily of dolostone. The middle member consists of two facies, a light-coloured thin to medium-bedded dolomite and a second dark coloured massive dolomite. The light facies consists of fine to medium crystalline dolomite, with algal wavy laminations to stromatolite hemispheres. There is also minor anhydrite, conglomerate and solution breccia (Thorsteinsson and Mayr, 1987). The dark facies consist of thin to thick bedded limestone and dolomite. Dolostone is predominant upwards in this Member with textures ranging from mudstone, wackestone to dominantly grainstone with skeletal fragments, and mudlumps (Figs. 4.3C-D). The dolomite is medium crystalline and porous. The upper member Allen Bay consists of interbedded laminated detrital dolomite with micrite pellets and thin- to thick-bedded limestone to dolomite. Originally interpreted as a grainstone, it is near-completely replaced by dolomitization (Thorsteinsson and Mayr, 1987). This unit is commonly identified by its abundance of sparite vugs.
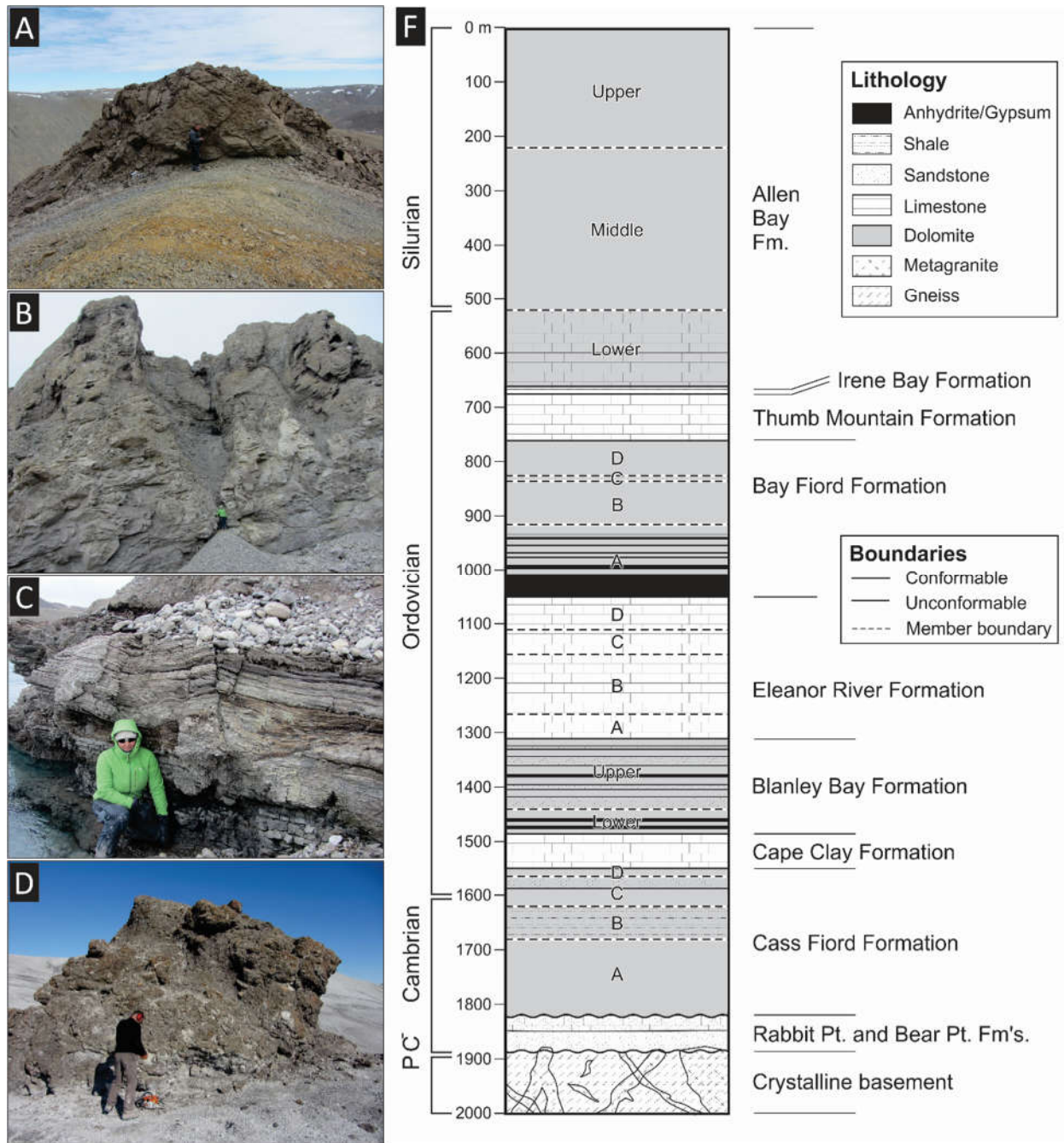
Figure 4.2 Example outcrops of the exposed target units in the form of faulted and brecciated blocks in the central uplift and central uplift periphery at Haughton: A) Middle Allen Bay Formation; B) Thumb Mountain Formation; C) Member A of the Bay Fiord Formation; and D) Eleanor River Formation. Person (~175 cm tall) for scale in each field photo. F) Stratigraphic column showing the pre-impact target stratigraphy at Haughton (from Osinski et al. (2005c), compiled with data from Thorsteinsson and Mayr (1987).
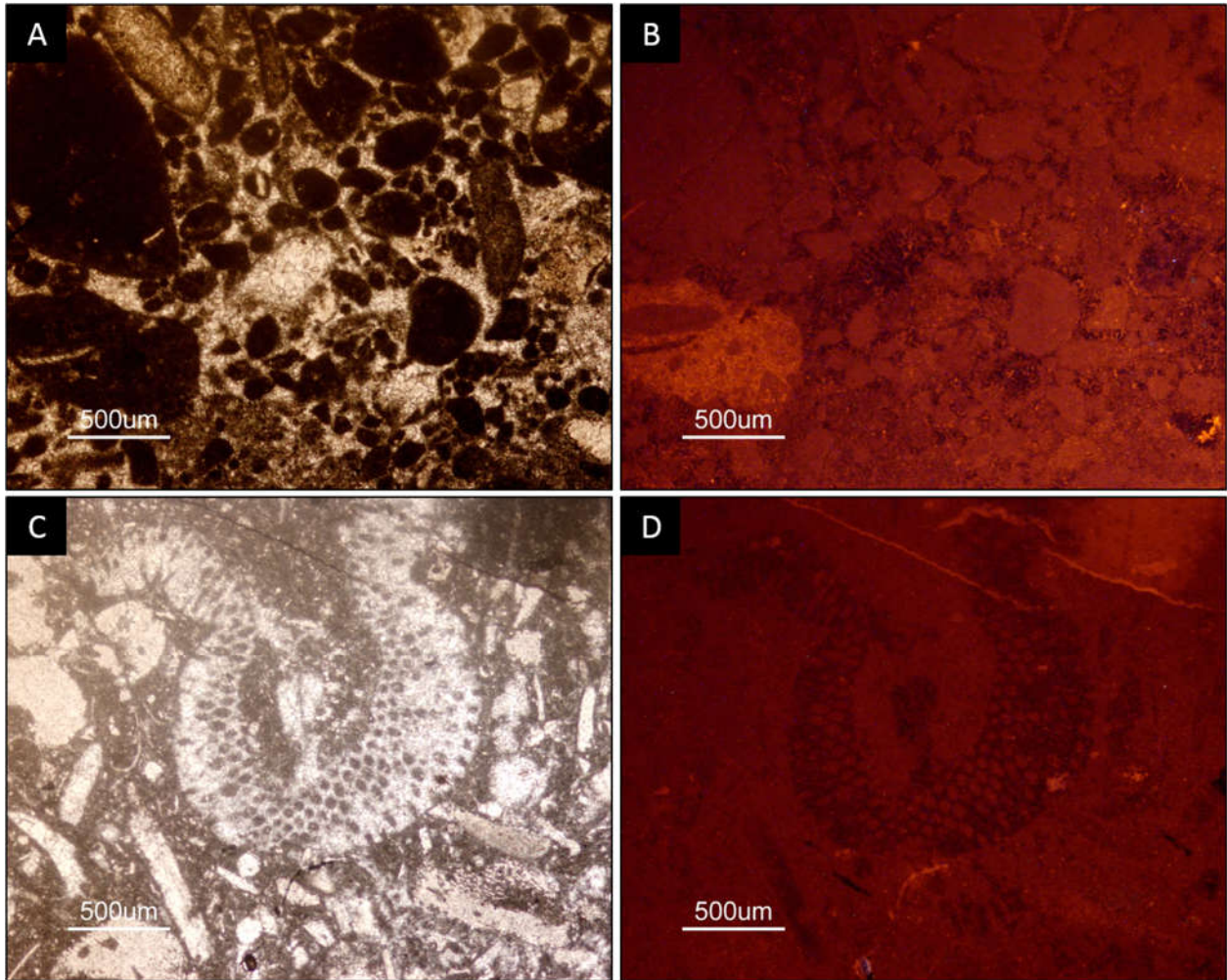
Figure 4.3 A) Plane-polarized light photomicrograph; and B) Optical cathodoluminescence image of the Thumb Mountain Formation showing a packstone cemented by diagenetic calcite, where the cement has little to no luminescence; C) Plane-polarized light photomicrograph; and D) optical cathodoluminescence photomicrograph of the Allen Bay Formation. Note the diagenetic intraclast calcite within the coral is non-luminescent.
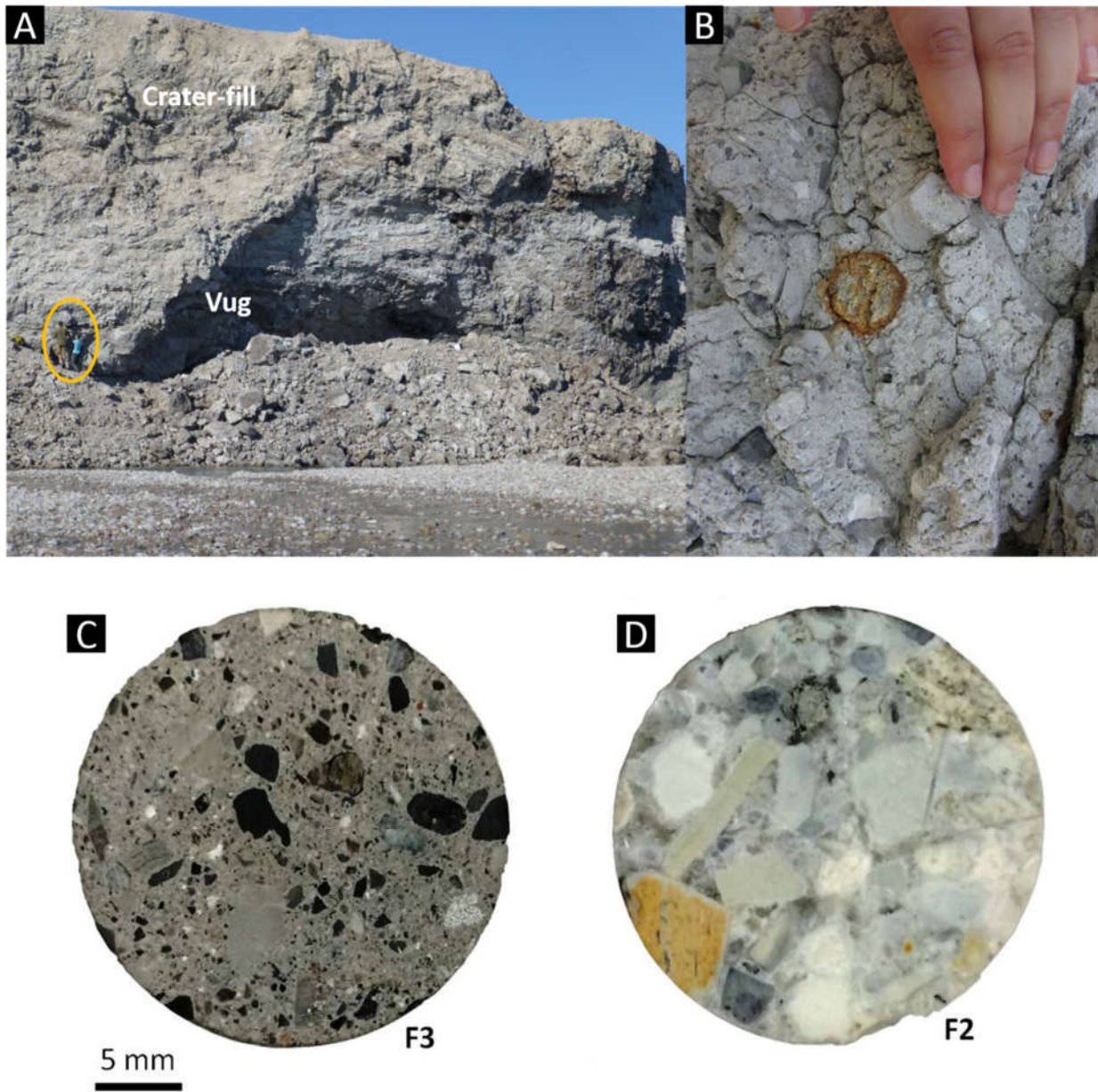
Figure 4.4 Crater-fill impact melt rocks: A) particulate impact melt rocks described in Osinski et al. (2005); people for scale; B) close-up view of the particulate impact melt rocks centered on an altered gneiss clast; C) F3 core silicate impact melt rock; and D) F2 core carbonate-silicate-sulfate impact melt rock described in Chapters 2 and 3.

4.4 Crater-fill impact melt rocks

There are 3 different varieties of impact melt rocks at Haughton (Fig. 4.4). The most common impact melt rock type makes up most of the exposed grey crater-fill. It is a light grey, clast-rich, particulate impact melt rock with a groundmass of microcrystalline calcite, anhydrite and silicate glass, with clasts consisting of all target rock lithologies (Osinski et al., 2005c). Hydrothermal mineralization previously identified in this unit consist of a variety of vugs composed of calcite, marcasite, gypsum and minor quartz, pyrite and fluorite (Osinski et al., 2005a; Osinski and Spray, 2001).

The second and third types of melt rocks originate from two cores collected at the centre of the structure, which were first described by Zylberman et al. (2017) and characterized and classified as melt rocks in Chapters 2 and 3. The F2 core melt rock is a light green, clast-rich sulfate-carbonate-silicate crystalline melt rock dominated by silicate clasts >300 µm in size, and the presence of a series of hydrothermal phases. These hydrothermal phases include a range of Mg-rich clay minerals (saponite, talc, serpentine and chlorite, inferred by compositional data in Chapter 3) that have replaced nearly all silicate phases, as well as calcite, anhydrite, and gypsum in the form of intraclast and interclast cement. The F3 melt rock is similar in appearance and clast population to the first type of impact melt but has a clay mineral rich groundmass interpreted as of talc and /or saponite (Chapter 3).

4.5 Mineralization

The veins and vugs hosted within the Haughton impact structure are, with the exception of much older diagenetic carbonate and Paleozoic Mississippi Valley type mineralization (Mitchell et al., 2004), formed by the impact (see below). Haughton is a relatively young impact (23 – 39 Ma discussed above), and no other heating events have occurred since. Each type of mineralization in the target rocks and impact melt rocks of the central uplift and periphery is described below, with the exception of clay minerals that are described in detail in Chapter 3.

4.5.1 Quartz Mineralization

The Eleanor River Formation within the central uplift comprises intrasparite limestone with sparry brown calcite cement. Quartz is the principal type of mineralization observed within the Eleanor River Formation, previously identified but not examined in detail by Osinski et al. (2005a). Quartz occurs as a microcrystalline quartz cement within a fragment-supported monomict breccia (Fig. 4.5). The quartz-cemented breccia occurs in most of the exposed Eleanor River outcrops in the central uplift. Breccia fragments are angular to sub-rounded. Backscattered electron and cathodoluminescence imaging reveal a minimum of four alternating layers of microcrystalline prismatic quartz and colloform quartz (Fig. 4.5). The latter are continuous rounded or botryoidal bands of fibrous microcrystalline quartz, with undulose to radial extinction. The colloform quartz has a slightly elevated proportion of alkalies and P_2O_5 relative to the prismatic quartz; the prismatic quartz has up 230 ppm TiO_2 (close to the detection limit), whereas the TiO_2 in the colloform quartz is all below detection limits (Table 4-1). Otherwise, there are no detectable chemical differences from measured WDS analyses. It should be noted however, that to obtain reliable trace element values, e.g. Ti, future work should consist of laser-ablation inductively coupled plasma mass spectrometry. Unfortunately, no measurable fluid inclusions could be identified in thin or doubly-polished sections of the quartz cement; however, previous studies identified 2 primary fluid inclusion assemblages (FIAs), one single liquid-only and one 2-phase liquid-vapour assemblage with homogenization temperatures ranging from 84.3 to 249.8 °C (Osinski et al., 2005a). Quantitative analysis of fluid inclusion volatiles within the cement, that is the combined prismatic and colloform cement, show that the fluid source(s) had slightly elevated N_2/Ar values (87.4 ±15.6 mol%) with respect to meteoric water (38 mol%; (Blamey, 2012)) (Table 4-2).
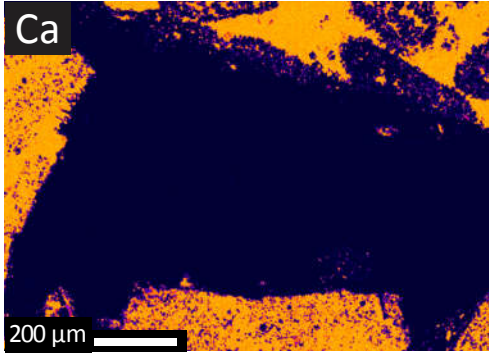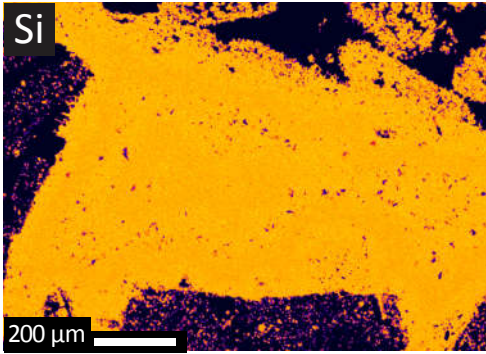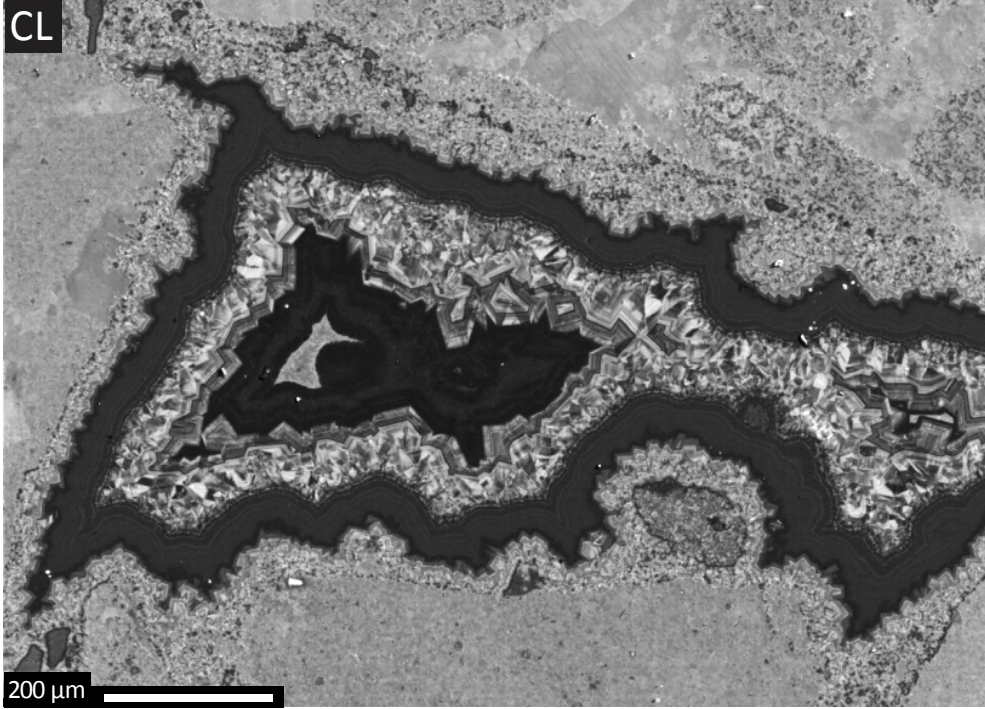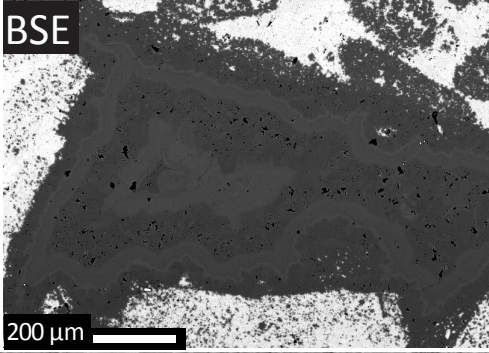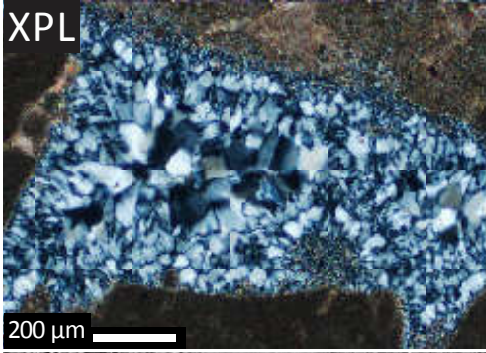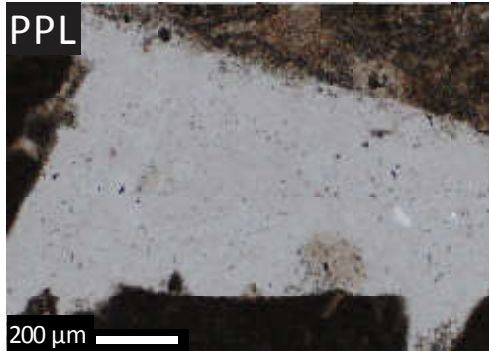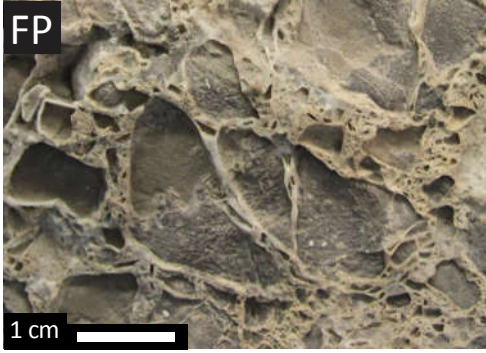
Figure 4.5 Field photographs (FP) and plane-polarized light (PPL), cross-polarized light (XPL), backscattered electron (BSE), cathodoluminescence (CL) photomicrographs, and silica and calcium EDS maps showing microcrystalline prismatic and colloform quartz within Eleanor River Formation.

Table 4-1 Microprobe analyses of hydrothermal quartz cement in the Eleanor River Formation.

	G1 Quartz	G1 Quartz	G2 Colloform	G2 Colloform	G2 Colloform	G3 Quartz	G3 Quartz	G3 Quartz
SiO_2	97.34	96.58	94.94	95.58	96.92	97.38	97.84	99.45
Al_2O_3	BDL	0.11	BDL	BDL	BDL	BDL	BDL	BDL
Na_2O	BDL	BDL	0.03	BDL	BDL	BDL	BDL	BDL
MgO	BDL	BDL	BDL	BDL	BDL	BDL	BDL	BDL
F	BDL	BDL	0.03	BDL	0.06	BDL	0.08	BDL
TiO_2	BDL	BDL	BDL	BDL	BDL	BDL	BDL	0.02
CaO	0.02	0.02	0.03	0.04	0.07	0.02	BDL	0.02
P_2O_5	BDL	BDL	BDL	BDL	BDL	BDL	BDL	BDL
FeO	0.15	0.13	0.11	0.11	0.08	0.08	0.10	BDL
MnO	BDL	BDL	BDL	BDL	BDL	BDL	BDL	BDL
Cr_2O_3	BDL	BDL	BDL	BDL	BDL	BDL	BDL	BDL
K_2O	BDL	0.02	0.02	0.02	0.03	BDL	BDL	BDL
Cl	BDL	BDL	BDL	BDL	BDL	BDL	BDL	BDL
SO_3	BDL	BDL	BDL	0.02	BDL	BDL	BDL	BDL
Total	97.29	96.56	95.03	95.69	97.21	97.37	97.86	99.34

Values are in wt.%. G1 = Qtz generation in contact with the host rock; G2 = Qtz generation at the centre. BDL = below detection limits

Table 4-2 Quantitative analysis of fluid inclusion volatiles in quartz cement within the Eleanor River Formation

Gas (mol %)	Analysis Bursts	
	1	2
H_2	0.00	0.00
He	0.00	0.00
CH_4	0.23	0.27
H2O	95.11	96.40
N_2	2.06	1.62
O_2	0.08	0.06
Ar	0.02	0.02
CO_2	2.50	1.62
Moles Gas (non-aqueous)	0.00	0.00
N_2/Ar	103.85	72.84
CO_2/CH_4	11.04	6.01
CO_2/N_2	1.22	1.00

Analyses are from sample HMP99-063. Water values are too low for reliable watergas ratio.

4.5.2 Carbonate Mineralization

Calcite veins and vugs are the most common type of mineralization at Haughton. These veins and vugs occur in all but the Eleanor River Formation. In outcrop, most calcite is white, but may be translucent to brownish, the latter where associated with marcasite. Within the target lithologies, calcite veins are typically thin, mm- to cm-scale and may occur parallel to bedding, but more commonly they cross-cut bedding. Thicker veins tend to be planar, whereas the very thin veins may be sinuous. Below, the carbonate veins in the host rocks are described.

The Bay Fiord Formation has abundant calcite veins (with minor marcasite). The calcite veins are mm- to cm-scale and cross-cut bedding. They are dominantly observed in the dolostone members, although extensive gypsum replacement is most prevalent in the lower member A. In a

representative section (HMP02-053), a single vein appears to consist of a single generation of prismatic, euhedral, brownish cleaved calcite. However, optical cathodoluminescence shows that there are in fact two main generations within the vein (Fig. 4.6): one with normally zoned, low luminescence calcite, and a second, later infilling of subhedral calcite with notably abundant cleavage planes that luminesces brighter than the first. Microprobe analyses show the calcite to be chemically very pure. The first dark generation is Fe-rich (up to 0.1 wt% FeO) with below detection limit amount of MnO, whereas the lightly luminescent calcite has up to 0.05 wt% MnO and FeO at or below the detection limit (<200 ppm). Cyclic MgO zoning (from 0.05−0.43 wt%) occurs in the first generation but does not exactly match the zoning shown in CL; however, there is a correlation between higher MgO values and brighter luminescence. A third generation of calcite is present in the same sample (not shown), in which the first and second generation have been partially replaced by pure and clear, low luminescent fine-grained calcite cement. It is both elevated in MnO (0.05−0.08 wt%) and FeO (up to 0.15 wt%) than the previous two generations. For all carbonate chemistry, see Appendix C Table C-2.

The same three calcite types identified in the Bay Fiord Formation occur in the Thumb Mountain Formation, but with a different textural relationship. In the case of sample SA08-13, the first dark, cleavage plane-rich luminescent calcite occurs only in the cores, overgrown by the second brightly luminescent thick rim. Overall, the calcite vein is a combination of comb, rhombic and zonal calcite, all of which are then replaced at the vein-host margin by the fine-grained, fresh, clear, non-luminescent third generation calcite. However, in a different sample of the Thumb Mountain Formation (CMDI13-11), there is a calcite vein with up to 5 generations of calcite mineralization (Fig. 4.7). There is a low luminescent comb calcite, although brighter than the host calcite, which is overgrown by three generations of alternating thin, very brightly luminescent calcite and a dark poorly-luminescent calcite. The last generation is a brightly luminescent, void-filling, massive and fine-grained calcite. The calcite veins in the Thumb Mountain Formation show the most chemical and textural variation from one vein to the next.

Similar calcite generations are observed in the Allen Bay Formation as well. There are two key differences: the first generation of calcite crystallized along the vein-host boundary is the bright luminescent, fine-grained calcite (sample CMDI13-19); and the darker, coarser-grained calcite overgrowths have irregular, discontinuous zoning, particularly in the core (Fig. 4.8).

Separate vugs of massive, low-luminescent, fine-grained calcite with 3-8 μm liquid-only fluid inclusions were also observed.

Calcite within the type 1 impact melt rocks can occur as monomineralic veins and vugs and as calcite-marcasite vugs. Most single generation calcite veins occur within this unit as homogeneous, sparry calcite that cross-cuts both the melt groundmass and clasts (sample HMP02-087, Fig. 4.9). Calcite-marcasite mineralization occurs in abundance in a multi-metre sized vug in the impact melt rocks of the central uplift periphery shown in Figure 4.4A. The same vug is also host to other minor minerals such as sphalerite and celestite, carbonate flowstone, and a variety of low temperature weathering products (Izawa et al., 2011). In some cases, there is a single calcite generation that has grown over the marcasite (HMP99-131). In others, a void-filling, normally zoned calcite with euhedral grains occurs with a darkly luminescent core, a moderately luminescent centre and slightly brighter outer edge (HMP99-137). This multi-generation calcite has a much greater range in chemistry. For example, MgO ranges from 0.03 to 0.63 wt%, compared to the single generation calcite (0.12-0.36 wt%), or the adjacent host carbonate (Appendix C).

Hydrothermal calcite in the F2 core silicate-carbonate-sulfate impact melt, as determined in Chapter 3, occurs primarily as a recrystallization or replacement of calcite and other phases forming both interclast or intraclast cement. There is no evidence of a brown calcite, nor any calcite with abundant cleavage planes, such as those previously described in the target units. The hydrothermal calcite occurs as sparry void-filling calcite, and may be massive to coarse grained, anhedral to subhedral. There is a very wide range in chemistry within each sample and from one to the next. There are particularly high SrO values, up to 0.94 wt%, whereas most other veins have less than 0.1 wt% (Appendix C). It should be noted that these samples represent several metres of core within a very heterogeneous melt rock unit. Calcite in the melt rocks is much clearer, there are no visible brown tints. Calcite textures range from massive, rhombic to zonal. Calcite replacement in the F3 core samples is very rare, but it occurs under similar conditions to F2.

A comparison of calcite compositions for each stratigraphic host unit and representative veins are shown in Figure 4.10. MgO is the dominant substitution element. In addition, all the

single generation veins (e.g., HMP02-087) have a narrow range of calcite compositions; whereas those veins with multiple generations show a wider compositional range, such as an increase in FeO, SrO and MnO above detection limits. The host rocks have a narrower chemistry than the vein in both the Bay Fiord and the Thumb Mountain Formations, but the opposite is true for the Allen Bay Formation. The Allen Bay host carbonate has the higher MgO values, whereas an Allen Bay calcite vein has the highest and widest range of FeO values (0.06 – 0.70 wt%). Calcite in the F2 melt rock has the widest compositional range; however, it is very challenging to differentiate between primary igneous calcite and hydrothermal calcite (Chapter 3).
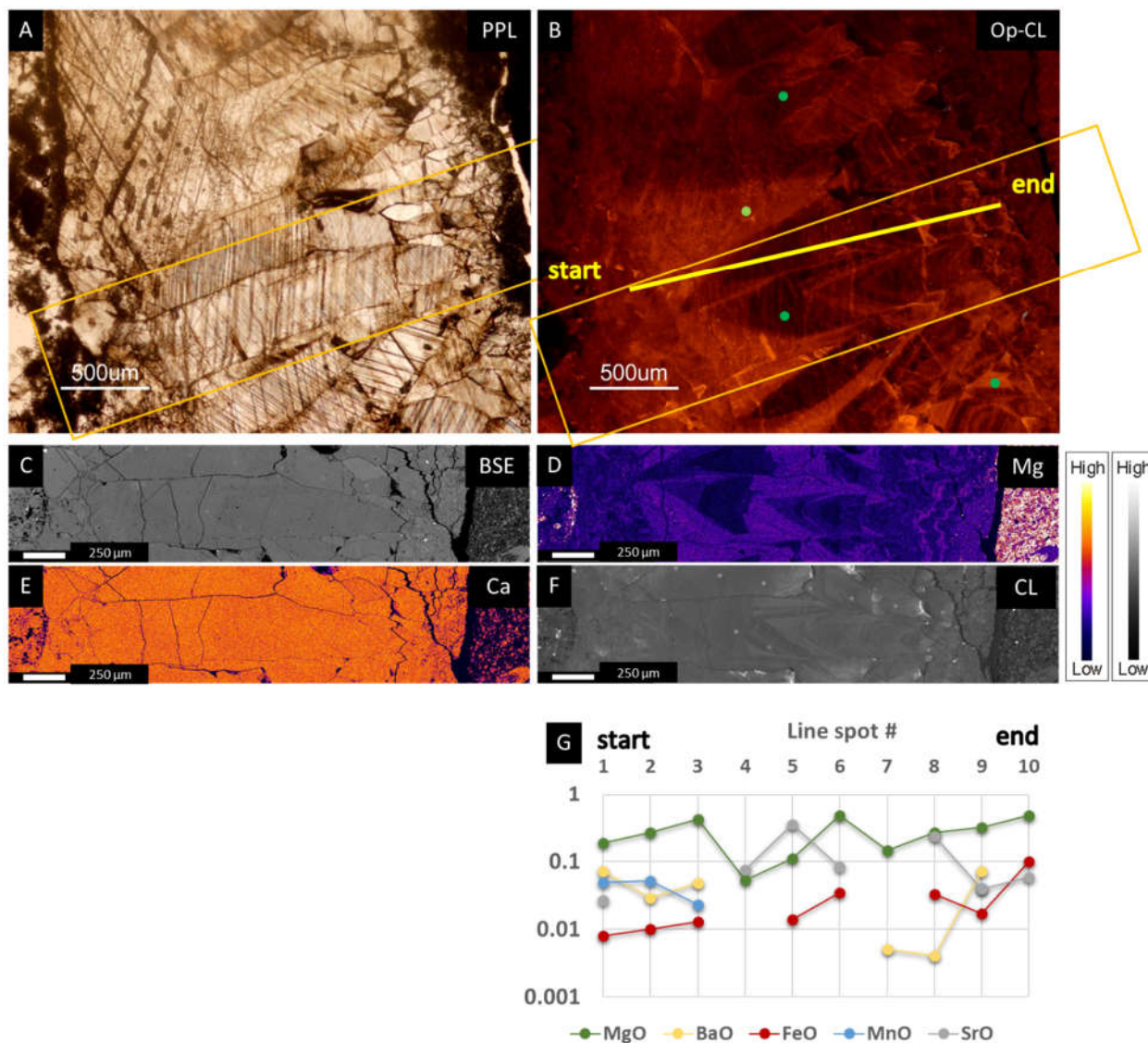
Figure 4.6 Calcite vein in the Bay Fiord Formation in A) plane-polarized light (PPL); B) optical cathodoluminescence (Op-CL) photomicrographs with a region outlined by an orange rectangle. The associated inset region is shown as C) BSE image; D) and E) are WDS element maps for Mg and Ca, respectively; F) an EPMA CL map; and G) is a plot that represents the line of microprobe analyses collected from 'start' to 'end', identified in the B. Green dots in B represent additional analyses not shown on plot. Spot analyses below detection limits for individual analyses are not included. Note 3σ detection limits are ~200-600 ppm.
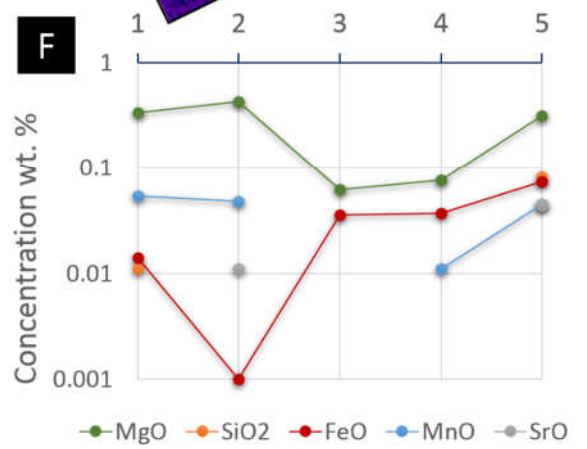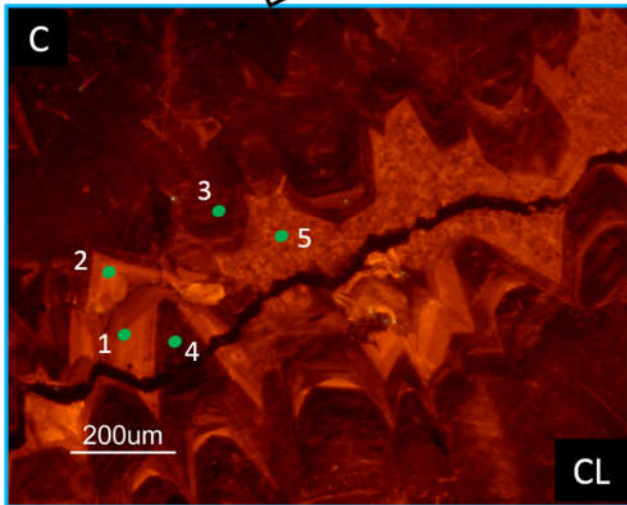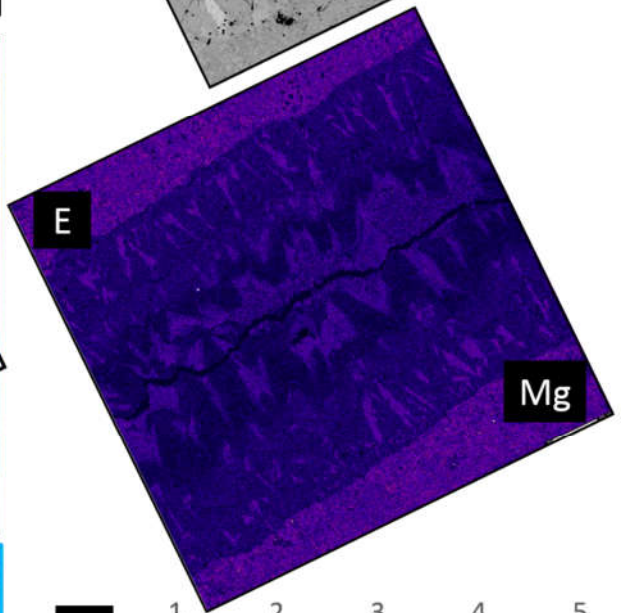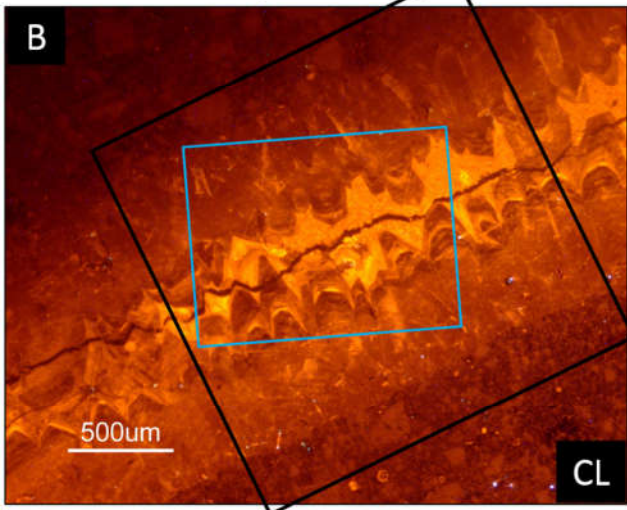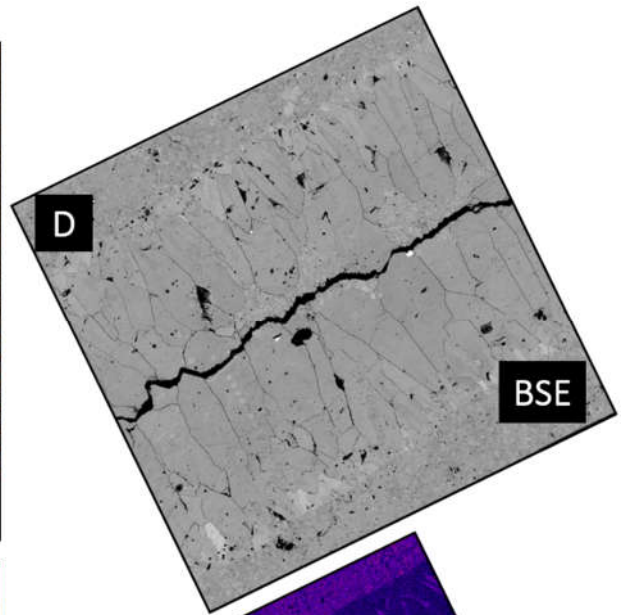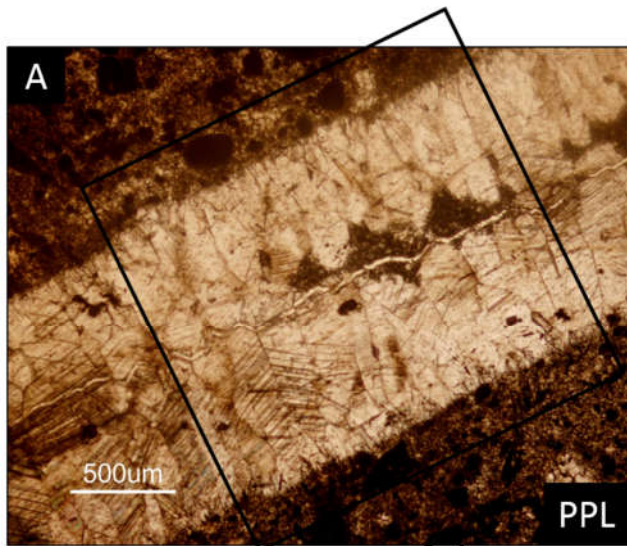
Figure 4.7 Multi-generation calcite vein within the Thumb Mountain Formation (sample CMDI13-11): A) plane-polarized light photomicrograph (PPL); B) optical cathodoluminescence photomicrograph; C) magnified inset in B with green points identifying microprobe spot analysis; D) backscattered electron image; E) WDS element map showing variation in Mg (higher concentrations are magenta, lower concentrations are dark purple); F) element oxide concentrations in the 5 spots identified in C. Low luminescent zones are Mg-poor and Fe-rich, whereas bright luminescent zones are Mg- and Mn-rich. Spot analyses below detection limits for individual analyses are not included. Note 3σ EPMA detection limits are ~200-600 ppm.
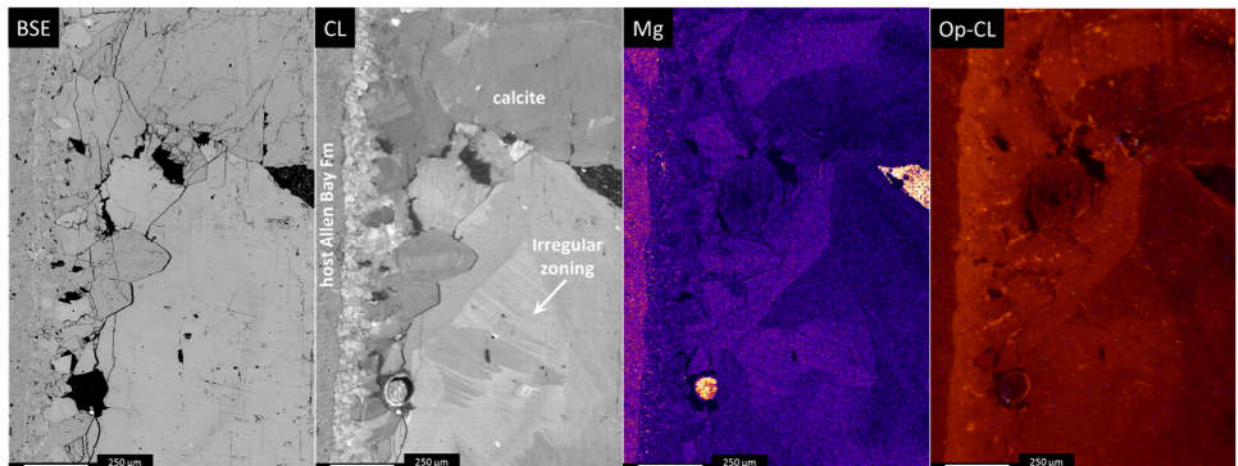
Figure 4.8 Backscattered electron photomicrograph, EPMA-cathodoluminescence, WDS-Mg, and optical cathodoluminescence maps of an Allen Bay Formation calcite vein. The host carbonate is on the far left and the contact with the vein is vertical in the image. Note the 'wispy' irregular zoning in CL.
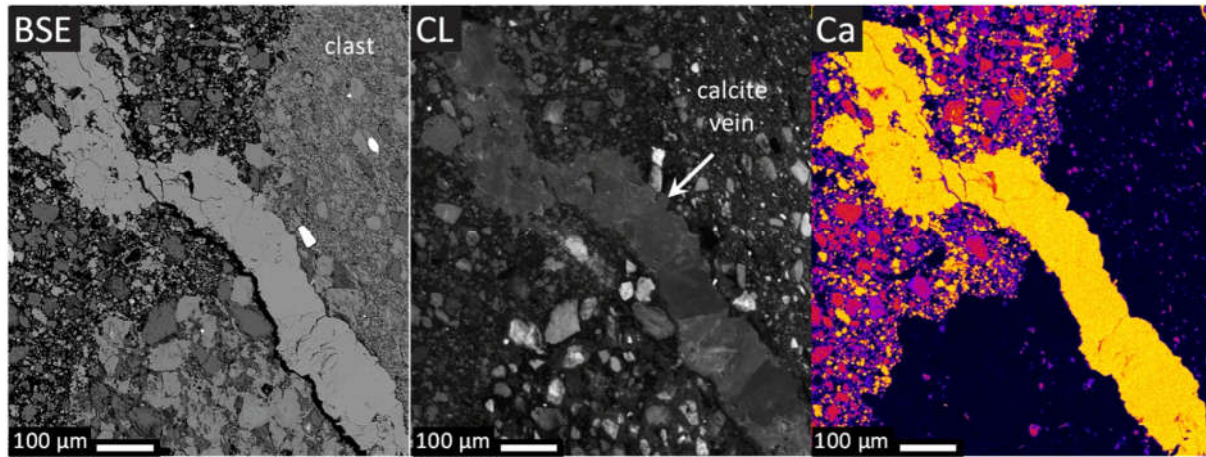
Figure 4.9 Backscattered electron (BSE), cathodoluminescence (CL) and WDS calcium element map (Ca) of a single generation calcite vein hosted within the breccia. Note the vein cross-cuts both the breccia groundmass and that of a large clast.
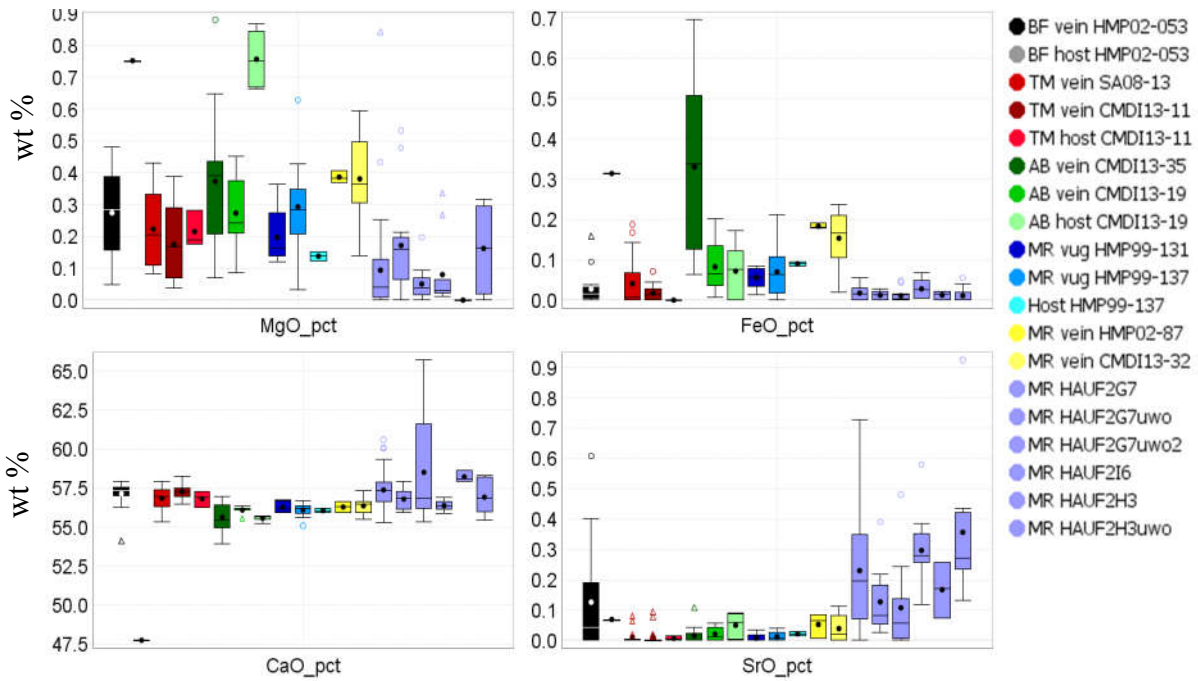
Figure 4.10 Box and whisker plots showing the variation in calcite compositions in host carbonate units and calcite veins within them and the melt rocks. BF = Bay Fiord; TM = Thumb Mountain; AB = Allen Bay; MR = melt rock. Mauve data come from various depths within the F2 core. Note: the MR is represented by only a single generation vein HMP02-87. The BF host rock is represented by only a single analysis and may not be representative of the average host composition. 3σ EPMA detection limits are ~100-1100 ppm depending on the day and settings.

4.5.3 Sulfide Mineralization

Sulfide mineralization occurs in the Eleanor River Formation, the Bay Fiord Formation and in the impact melt rocks. In the upper member of the Eleanor River Formation, a small marcasite-only vug occurs as an open fracture in a single outcrop in the Haughton River Valley, along the central uplift periphery. The marcasite occurs as a thin layer and covers an area approximately 30 cm across. Marcasite in the Bay Fiord Formation is associated with thin 1-2 mm calcite-marcasite veins, where it both completely fills in the thin vein and is bounded by calcite at the ends, or occurs as nodules within the centre of multi-generation calcite veins (Fig. 4.11). In the latter case, there is a calcite grain completely enclosed within a marcasite grain and the same marcasite grain is completely enclosed by the surrounding calcite (Figs. 4.11A–C). There is an increase in FeO along the grain boundaries.

In the type 1 melt rock, botryoidal marcasite forms a crust of radial grains on the host melt rock and is overgrown with polyhedral to elongated rhombohedral translucent calcite (Figs. 4.12A–I). Osinski et al. (2001) also identified marcasite as individual tetragonal octahedra in micro-cavities and as euhedral grains within a groundmass of hydrothermal calcite. Marcasite chemistry varies very little from one occurrence to the next, regardless of host unit (Table 4-3). Euhedral to subhedral, 10–20 µm large pyrite grains occur around the margins of mafic clasts, and are associated or overgrown by magnetite (see Fig. 7 in Zylberman et al. (2017)). Sphalerite is observed, for the first time at Haughton, as ~50 µm inclusions within the marcasite hosted by impact melt rocks in the central uplift periphery (Figs. 4.12J–M).
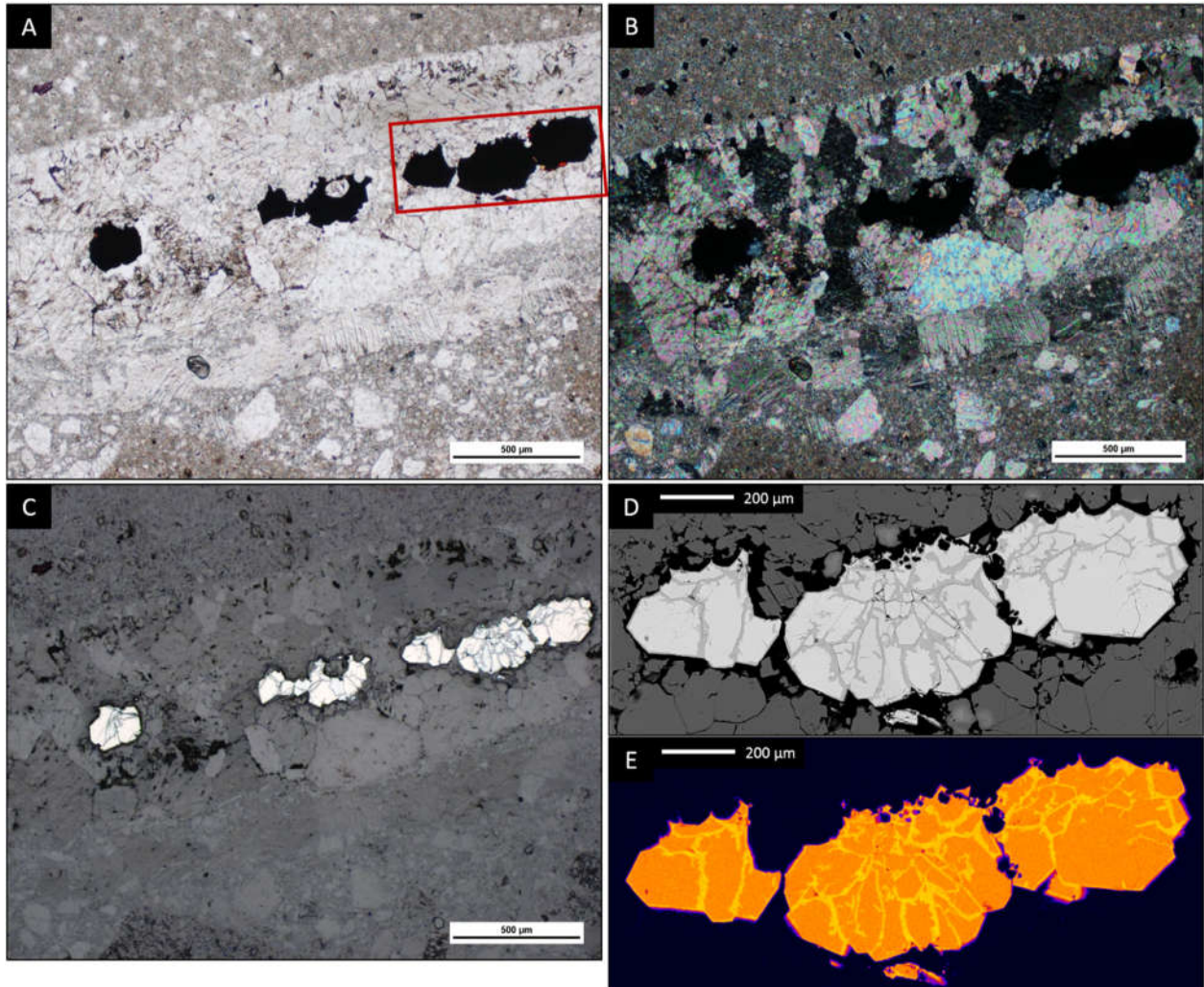
Figure 4.11 Nodular marcasite-calcite vein in the Bay Fiord Formation, central uplift periphery. A) plane-polarized light; B) crossed-polarized light; C) reflected light photomicrographs; D) backscattered electron image of the red box region in A; E) a WDS Fe map of D. Note the first generation of calcite formed before the marcasite, while the second formed after the marcasite.
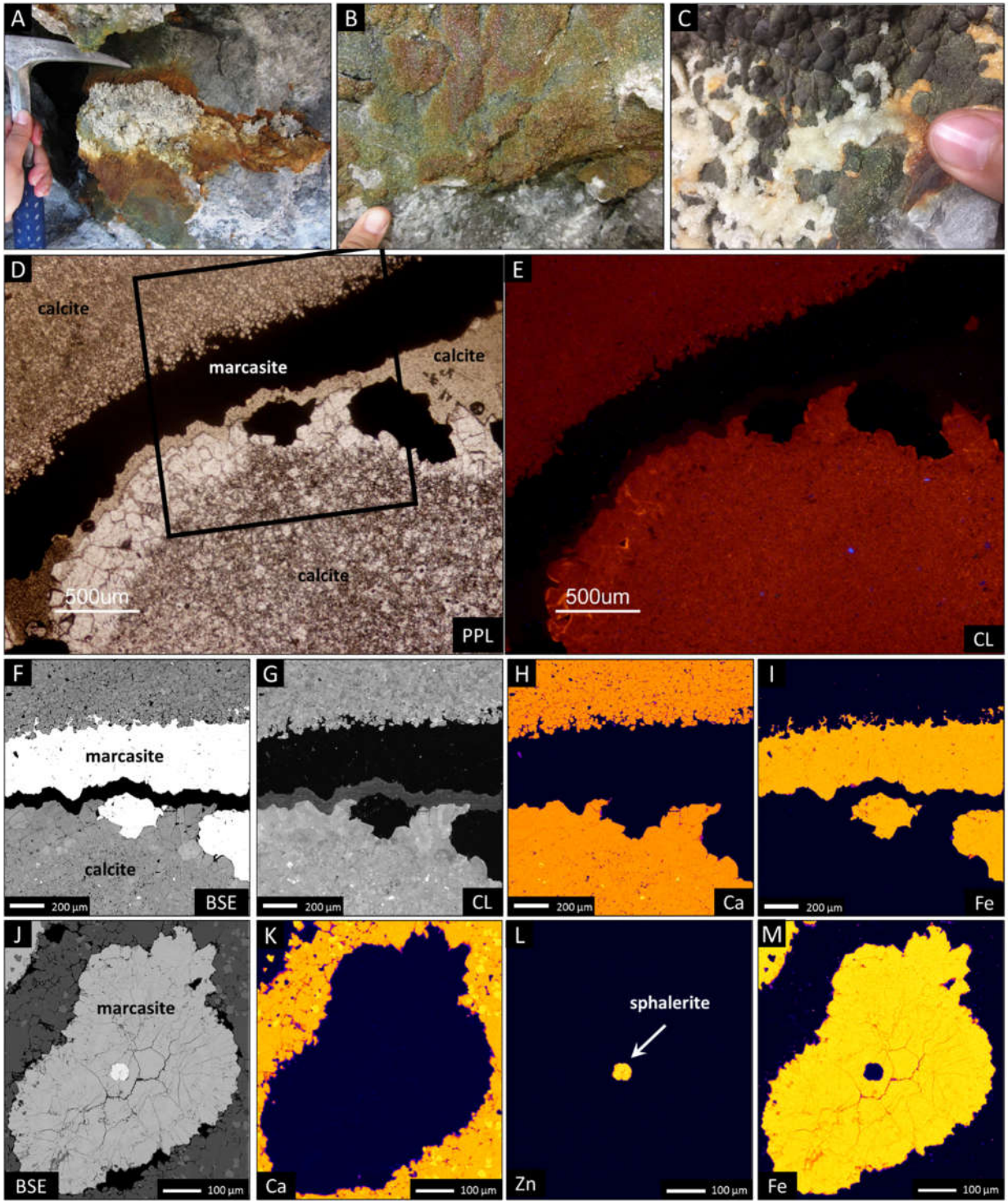
Figure 4.12 A-I Marcasite-calcite vugs in the central uplift periphery, illustrated in Fig.4.4A, sample HMP99-131, note multiple generations of calcite; A, B, C are field photographs, D is a plane-polarized light (PPL) photomicrograph, E is an optical cathodoluminescence photomicrograph, F and J are backscattered electron images, G is an EMPA-cathodoluminescence map, and H, I, K, L and M are element maps. J-M shows that there is no chemical zoning discernable within the marcasite and shows a ~50 μm inclusion of sphalerite in the centre of a marcasite nodule. A sulfur map, not shown here confirms presence of sphalerite.

Table 4-3 Microprobe analyses of hydrothermal marcasite.

Host rock	Crater-fill melt rocks						Bay Fiord	
sample ID	99-131	SD	99-137	SD	CMDI13-02	SD	CMDI13-38	SD
	n=11		n=8		n=9		n=12	
As	0.03	0.02	BDL		0.04	0.02	0.03	0.01
Fe	46.01	0.19	46.30	0.25	46.24	0.57	46.27	0.29
Co	0.03	0.01	0.03	0.01	0.03	0.01	0.03	0.01
Cu	BDL		BDL		BDL		BDL	
Au	BDL		BDL		BDL		BDL	
Ni	BDL		BDL		BDL		BDL	
V	BDL		BDL		BDL		BDL	
Zn	BDL		BDL		BDL		BDL	
S	52.99	0.38	53.09	0.19	52.46	0.43	53.36	0.28
Pb	BDL		BDL		BDL		BDL	
Te	BDL		BDL		BDL		BDL	
Total	99.05		99.42		98.80		99.69	

All values are in weight %. SD = standard deviation; BDL = below detection limits, detection limits ranged from 50-200 ppm.

4.5.4 Sulfate Mineralization

Sulfate mineralization at Haughton occurs in the form of anhydrite, bassanite and gypsum with minor barite, celestite and fibroferrite. The latter three minerals occur in vugs in the melt rocks or in hydrothermal pipe structures as described previously (Osinski et al., 2005a, 2001).

In the faulted blocks of the Bay Fiord Formation in the central uplift periphery, there is abundant replacement of selenite-type gypsum as well as abundant gypsum veins, particularly in the anhydrite-rich lower member. Massive selenite, with grains up to 50 cm across also occur within the Type 1 impact melt rocks on the periphery of the central uplift. Gypsum also occurs as replacement of a series of minerals within the type 2, F2 core melt rock, particularly in clast coronas (Fig. 4.13A). Gypsum veins up to 500 μm thick also cross-cut the groundmass and clasts. Results from fluid inclusion petrography show that all selenite have single phase, liquid-only fluid inclusions (Fig. 4.13A inset). The selenite is transparent and always coarse to very coarse-grained, with the exception of the <5 μm gypsum inclusions in altered calcite in the F2 core (Fig. 4.13B).

Anhydrite occurs within the F2 core melt rock as well as a void-filling, groundmass cement (Fig. 4.13C). Note we refer to both bassanite and anhydrite as anhydrite for simplicity, as a wide range of sulfate compositions are present (see Chapter 3). There are incidences where calcite (possibly primary) or a radial, bladed Mg-rich clay mineral line the boundaries of clasts where the anhydrite is present as cement. Fluid inclusion petrography of the anhydrite shows some unidentified solid inclusions, as well as an abundant 2-phase primary fluid inclusion assemblage with consistent liquid-vapour ratios. The majority of inclusions are less than 3 μm across and very difficult to see. However, larger ~5-8 μm inclusions occur in clusters, are regularly shapedround, and consist of a vapour proportion on the order of 70% (Fig. 4.13C inset). Heating of this assemblage was completed first, as anhydrite is a soft mineral and the priority was to ascertain a temperature of homogenization. Upon heating, the liquid to vapour ratio was reduced to ~40% vapour, but the inclusions began to decrepitate at ~250°C. The entire chip was 'cooked', so unfortunately further measurements would not have been reliable.

4.5.5 Oxide Mineralization

To date, hydrothermal magnetite has only been observed in limited abundance lining the edges of mafic clasts in the F2 impact melt core (Fig. 4.13D). The magnetite occurs as 5-50 µm porous and non-porous grains. The porous grains may be associated with fine-grained pyrite, or a second non-porous generation of magnetite. Zylberman et al. (2017) noted that these magnetites have a near end-member Fe_3O_4 composition compared to primary magnetite from the source clasts, which have higher levels of Ti and Mn.
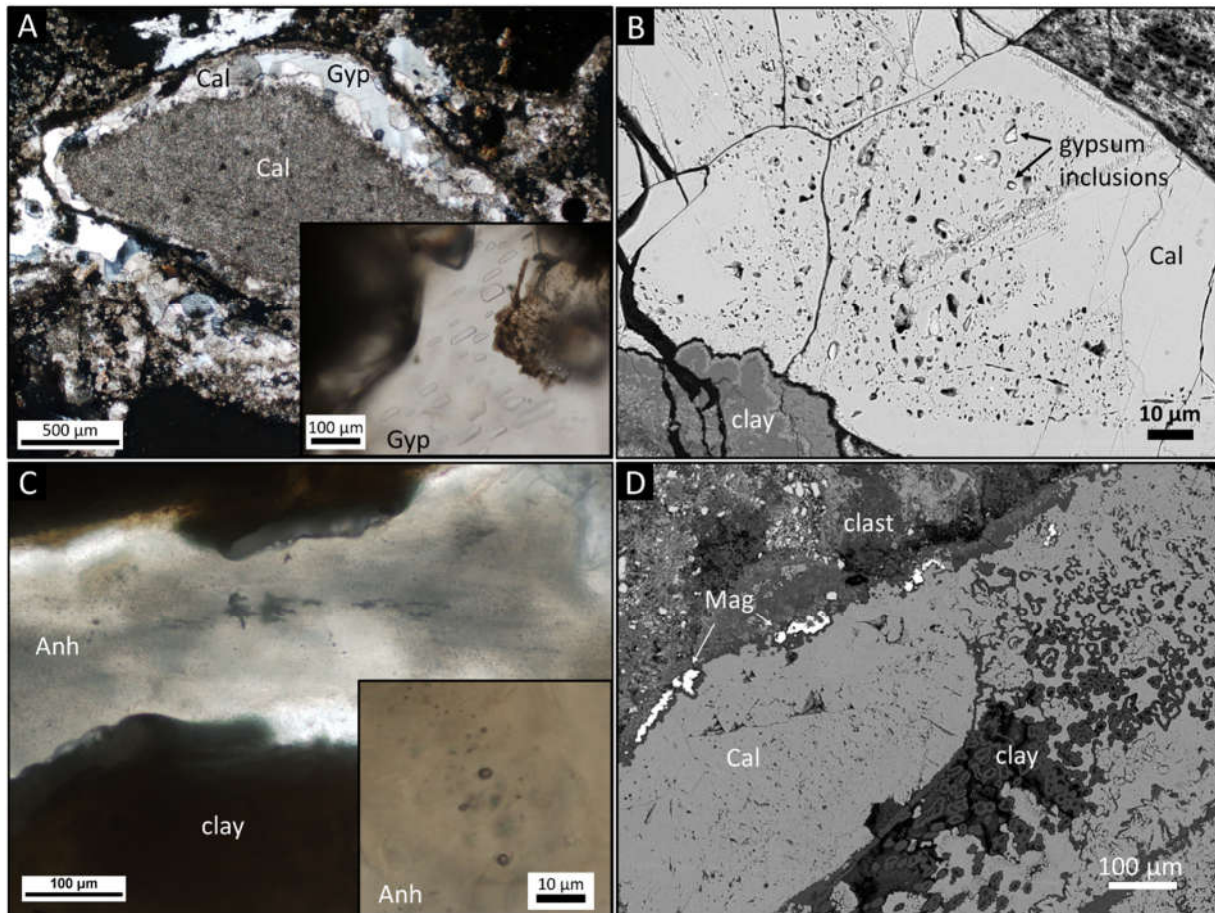
Figure 4.13 Mineralization in the F2 core. A) Plane polarized light of gypsum replacement of clast corona. Inset showing liquid-only fluid inclusions; B) Gypsum inclusions in irregularly porous calcite; C) anhydrite hosting abundant primary liquid-vapour fluid inclusions. Inset showing a primary liquid-vapour fluid inclusion assemblage; D) Mineralization of magnetite along the edge of a clast.

4.6 Updated hydrothermal model

Based on the petrographic and fluid inclusion results of this study, combined with those from previous studies (Chapters 3, this document; Osinski et al., 2005a, 2001; Zylberman et al., 2017), an updated paragenetic sequence and hydrothermal model for Haughton is presented in Figure 4.14. Mineralization is divided by the host unit as well as the location within the impact structure, that is in the centre or around the periphery of the central uplift. The model proposes that the mineralization can be split into: early (>200°C), main (~80–200°C) and late (<80 °C) stages. Included in the paragenetic sequence are several newly identified hydrothermal mineral phases described above, including anhydrite, magnetite and sphalerite, as well as the series of Mg-rich clay minerals described in Chapter 3: talc, serpentine, chlorite, and saponite. The model does not include phases related to weathering processes, identified in previous studies, such as jarosite, copiapite, rozenite, melanterite and szomolnokite (Greenberger et al., 2016; Izawa et al., 2011). It should be noted that the model is not a complete representation of the variation of mineralization with depth in the crater centre, as the drill cores did not reach the basal contact of the melt rocks. In the following discussion, we address the origin of the main mineral phases, how to distinguish between hydrothermal and pre-impact carbonate mineralization, mineral paragenesis, comparative mineralization at other impact structures and the life of the hydrothermal system.
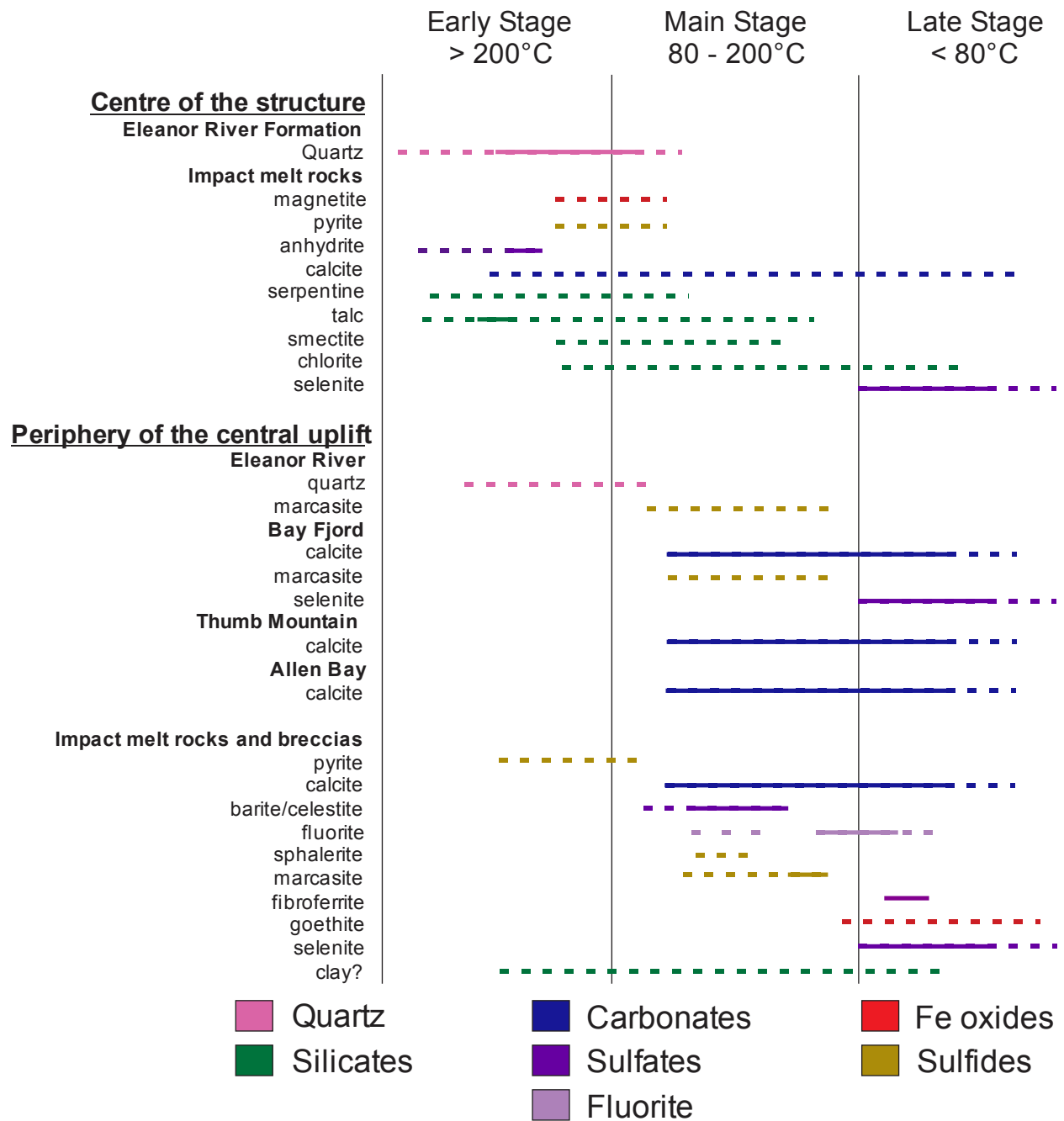
Figure 4.14 Updated model of hydrothermal mineralization sequence on the central uplift and central uplift periphery at the Haughton impact structure. Data compiled from the previous model by Osinski et al. (2001, 2005) with incorporation of results from this work, and Chapter 3. Solid lines represent constrained timing from fluid inclusion studies, phase relationships and petrography, whereas hatched lines indicate approximations based solely on petrography.

4.7 Discussion

4.7.1 Hydrothermal mineralization at Haughton

It is well established that an impact-generated hydrothermal system formed at Haughton (Osinski et al., 2005a, 2001, Chapter 3), wherein mineralization occurred as vugs and veins within the impact melt rocks and in the faulted and fractured blocks around the periphery of the central uplift, as cement in the centre of the structure, and as hydrothermal pipe structures in the faulted crater rim (Osinski et al., 2005a). The latter case excluded, this study confirms mineralization within these settings and further describes the relationships between mineralization and the host rock through field observations, and petrographic and micro-analytical results.

Deep fluid circulation through the porous and permeable impact melt rocks and breccias in the crater centre, as well as transport along the faulted and brecciated blocks of the central uplift periphery allowed for fluid flow and a hydrothermal system to form. Rock-fluid reactions were mainly responsible for the composition of the geothermal fluids and therefore mineralogy. Similar to many impact-generated hydrothermal systems in mixed targets (Naumov, 2002, 2005), the hydrothermal fluids at Haughton consisted of aqueous, low salinity, near pH-neutral fluids (Osinski et al., 2005a), initially silica-supersaturated, which evolved to be rich in SO_4^{2-} and CO_3^{2-}, and mineralized carbonates, sulfides and sulfates in an overall retrograde (cooling) system (Fig. 4.14).

4.7.2 Origin and implication of hydrothermal quartz

The microcrystalline prismatic and colloform quartz that cements the Eleanor River Formation-hosted breccia is proposed to be part of the early phase of impact-generated hydrothermal mineralization at Haughton. Evidence for this interpretation includes the observation that both colloform and fine zonal prismatic quartz are common primary growth textures in epithermal quartz veins (e.g., Moncada et al., 2012). One of the most common features of hydrothermal activity is the precipitation and redistribution of silica (Pirajno, 2009). There are several nearby sources of silica to form the cement, including the most likely source: the Eleanor River Formation chert, and/or the underlying sandstone in the Blanley Bay Formation.

The formation of colloform quartz first requires the presence of amorphous silica from silica-supersaturated fluids, which generally represents rapid changes in the physical and chemical nature of the fluid (Fournier, 1985a). The state of supersaturation may have been the result of rapid cooling through boiling, mixing of different fluid sources, changes in pH, contact with organic material (Fournier, 1985a) or reactions with silicate impact melt rock or glass. In this case, it is more likely that silica supersaturation was achieved through rapid cooling and boiling as the host rock is a carbonate and the other processes typically involve more acidic or more alkaline fluids. High temperature, an increase in pH or salinity, time or addition of Mg in solution may enable the transformation of amorphous silica to quartz (or chalcedony) with either poorly crystalline cristobalite or opal CT as an intermediate phase (Fournier, 1985b and references therein). The variety of silica that precipitates is dependent on the hydrothermal conditions (Fournier, 1985b): both microcrystalline quartz and colloform quartz can form through moderate to intense boiling (Fournier, 1985a; Shimizu, 2014). A boiling water table at Haughton has previously been proposed and discussed by Osinski et al. (2001), yet this study presents the best evidence thus far. The relationship between boiling and the alternating quartz textures suggests the intensity of the boiling of silica supersaturated fluid fluctuated over time. In general, the higher temperatures of transition from amorphous silica to quartz result in coarser grained quartz, and high degrees of silica supersaturation result in rapid nucleation and precipitation (Fournier, 1985a; Shimizu, 2014). Fluctuations may be due to changes in the volume or concentration of silica in the fluid or in temperature. These fluctuations in deposition may also be responsible for the range in fluid inclusion results in previous studies (Osinski et al., 2005a).

Silica can be used as a geothermometer, as the solubilities for various types of silica are well understood. In hydrothermal fluids above ~180°C, silica solubility is controlled by quartz; at lower temperature, particularly below 140 °C, chalcedony controls solubility. Therefore, precipitation above 180 °C is likely to form quartz, whereas below 180 °C may precipitate chalcedony, or colloform quartz (Fournier, 1985b; Henley et al., 1984). There are conditions at which quartz can be formed at lower temperature, such as in the presence of organics or volcanic glass, but these conditions are unlikely in this case. It may be that the fluctuating conditions of the precipitation of the quartz cement were that of temperature rising above and below 180 °C.

Most forms of silica that precipitate during boiling do not trap useful fluid inclusions (Moncada et al., 2012), and unfortunately we could not identify useful inclusions in the quartz. Bulk gas analysis of inclusions within the quartz cement confirm the fluids were not magmatic; however, the gas contents were elevated with respect to meteoric water, which indicates some fluid evolution occurred. Finally, the quartz cement appears to have completely sealed the rock, after which no other fluids could have mineralized the Eleanor River Formation. Collectively, this supports the view that the quartz cement mineralized in the early phase of the hydrothermal system, as later fluids could not penetrate the rock.

4.7.3 Distinguishing between different carbonate generations

Distinguishing between different generations of carbonates is a major challenge, particularly where the carbonate has multiple possible genetic sources. Here, we are reasonably confident in differentiating these calcite occurrences due primarily to thorough systematic petrographic macro and microanalysis, including the indispensable application of cathodoluminescence imaging.

The first step in distinguishing diagenetic and impact hydrothermal calcites was to evaluate the host rocks and veins on the outcrop scale for diagenetic features both in situ and in the literature, such as cementation, veining and vugs. In the case of Haughton, pre-impact millimetre-scale calcite and gypsum veins are present in the target rocks, which are cemented and sealed desiccation or synaeresis cracks (Thorsteinsson and Mayr, 1987). These were surficial cracks that occur as a result of subaerial drying out of the sediment or subaqueous shrinkage of hardened crusts, respectively (Moore and Wade, 2013). In outcrop, the diagenetic calcite veins can be differentiated from impact-generated veins, as they are typically U- or V- shaped, form networks, are filled with sediments from later deposited layers, have limited lateral and vertical extents and are commonly capped by an overlying layer. Hydrothermal veins tend to be thicker and longer, and cross-cut bedding. Calcite veins may cross-cut the impactite deposits or cement an impact melt rock or breccia not present pre-impact, such as in the F2 core. Fenestral vugs, like those in the Eleanor River Formation can also be distinguished from the typical hydrothermal vugs, as they occur parallel to laminations. Similarly, in thin section, characterization of the host groundmass textures such as interparticle, intercrystal or intraparticle cement, e.g. interparticle cement of the Thumb Mountain Formation (Figs. 4.3A-B); the intraparticle calcite in the Allen Bay Formation (Fig 4.3C), will help distinguish them from hydrothermal calcite. Fortunately, the

breccias and melt rocks have not undergone any lithification, due to burial diagenesis. The challenges in these samples lie more in differentiating the hydrothermal calcite from calcite crystallized from an impact melt (Chapter 3).

Basic optical microscopy and micro-imaging was essential in identifying different generations based on morphology, texture, distribution, cross-cutting or paragenetic relationships, and zoning through extinction patterns, etc. Cathodoluminescence proved extremely useful in differentiating the various carbonate generations by revealing patterns and chemical zoning not visible using other techniques. Cathodoluminescence in carbonate is controlled primarily by the balance of $[Mn^{+2}]$ and $[Fe^{+2}]$; these ions can substitute for Ca^{+2} in calcite or Mg^{+2} in dolomite (Hiatt and Pufahl, 2014). Mn^{+2} is the dominant luminescence activator in calcite i.e., produces luminescence, while Fe^{+2} is the dominant quencher, i.e., inhibits luminescence. It is worth noting that additional intrinsic and extrinsic factors also contribute to CL in carbonate (e.g., growth rate, Pb, Ni, rare earth elements (REEs), structural defects, etc.) but none so much as Mn^{+2} and Fe^{+2}. Cathodoluminescence in carbonate is a representation of the relative concentrations of these ions, from which textural evolution and geochemistry can be inferred, in addition to potential redox conditions at the time of formation. All of the carbonate we have interpreted as diagenetic at Haughton is dull to darkly luminescent (Fig. 4.3), which is typical of early diagenesis and may indicate an oxygen-rich environment in which the calcite was formed (Hiatt and Pufahl, 2014, Table 5-2).

In the multi-generation hydrothermal veins such as those in the Bay Fiord, Thumb Mountain and Allen Bay Formations (Figs. 4.6–4.8), a combination of the petrography, CL and element mapping was used. Cathodoluminescence was most useful to show zoning and chemical changes not visible in backscattered electron or element mapping. As chemical zoning is still evident in CL even when concentrations of Fe and Mn are below EPMA detection limits. As little as 25 ppm Mn can cause luminescence, provided that Fe concentrations are lower than 200 ppm (Budd et al., 2000 and refs therein), and as little as 100 ppm Fe can cause quenching (Mason, 1987). Zoning style and textures in CL may also indicate how conditions change from one generation to the next. Sharp boundaries may represent sharp changes in precipitation (Bechberger and Coulson, 2014). In the hydrothermal calcite occurrences in the impact melt rocks, a combination of optical extinction patterns and CL zoning was applied to determine grain boundaries, as well

as generations. Distribution coefficients for Fe^{2+} and Mn^{2+} incorporation increase with increasing temperature or decreasing precipitation rate (Dromgoole and Walter, 1990). In general the distribution coefficient for Mn in calcite is greater than that for iron, and it would require approximately 1000-fold change in precipitation rate or increase in temperature of at least 25°C to significantly change Mn^{2+}/Fe^{2+} (Dromgoole and Walter, 1990). This relationship suggests that the more luminescent calcite generations were precipitated at a different rate relative to the darker generations, or at higher temperature. Alternatively, they may result from fluid mixing.

4.7.4 The evolution of calcite mineralization

As mentioned, the diagenetic calcite in the Paleozoic rocks is poorly luminescent, and representative of the pre-impact setting and burial conditions. It is evident that many generations of impact-generated hydrothermal carbonate precipitated in the Haughton impactites throughout the life of the hydrothermal system. Precipitation of calcite can occur as a result of loss of vapour phase, i.e., the decrease in P_{CO2}, an increase in pH, an increase in temperature or increase in salinity (Fournier, 1985; Nicholson, 1993; Segnit et al., 1962). Heating of carbonate-rich fluids can cause calcite to precipitate, whereas cooling without boiling will cause them to dissolve (Fournier, 1985).

The brown-coloured calcite in plane-polarized light is interpreted as an older phase than the transparent to translucent clear calcite, based on cross-cutting relationships. Previous workers suggested the carbonate precipitation was long-lived (Osinski et al., 2005a, 2001). This research demonstrates, through cathodoluminescence zoning textures, that changes in fluid composition and temperature were indeed common. In the case of the Thumb Mountain Formation, for example, the first generation of comb calcite grew up to 800 µm long crystals, whereas every subsequent generation grew no more than 150 µm before being overgrown or replaced by a new generation. These observations indicate that the system was not only dynamic but that the more abrupt changes likely occurred later in the evolution of the system.

The rhombic, zonal and comb textures of the calcite are evidence of non-boiling (Moncada et al., 2012), which is supported by fluid inclusion studies previously completed on Haughton carbonates, indicating carbonate did not form within the vapour-dominated stage of the hydrothermal system (Osinski et al., 2005a). The irregular, discontinuous zoning in calcite in the

Allen Bay Formation is probably the result of truncated deformation twinning (Burkhard, 1993). This suggests a strained environment during formation or a period of increased temperature (Burkhard, 1993).

The overall calcite vein chemistry within the target strata is generally homogeneous, however, the few occurrences that differ may be explained. Meteoric water can cause Mg loss in calcite or aragonite and recrystallization of calcite in as little as 1000 years (Budd and Hiatt, 1993). Subtle but alternating magnesium zoning resolved in WDS maps of calcite showed the crystallization history was complex (e.g. Fig. 4.7). Although the CL maps did not match the chemical zoning exactly (Fig. 4.7), they were likely related to the fact that Mg^{2+}, along with Mn^{2+} and Fe^{2+} substitute for the same Ca^{2+} site in the calcite crystal structure. The relative increase in FeO in the Allen Bay Formation vein (sample CMDI13-35) may be due to the presence of tiny sulfide inclusions within calcite that went undetected. The increase in MgO in the Allen Bay host rock may be that that sample is particularly dolomite-rich.

The brown calcite was abundant in host rock veins but lacking within the core impact melt rocks, showing variation in associated mineral phases in the different locations. Although carbonate-rich fluids were plentiful within the Haughton structure, fluids from the centre of the structure may not have mixed with those at the periphery or the fluid composition was actively modified during transport from one location within the structure to the next. The latter is more likely the case, as carbonate veins were commonly chemically linked to their host rocks.

4.7.5 Implications for sulfate mineralization

Anhydrite, bassanite and gypsum are all present at Haughton, indicating that sulfate mineralization occurred at various temperatures and stages of hydration and oxidation. The presence of sulfates is not a surprise, as the Bay Fiord Formation provided a sulfate-rich source rock. Anhydrite, like calcite and fluorite, has a retrograde solubility in low salinity fluids. In high salinity fluids, it becomes prograde. For a review on sulfate solubility, transition temperatures and phase relations, see Van Driessche et al. (2017). All of the above minerals may hydrate or dehydrate, i.e. transform into one another, under the right conditions. Anhydrite may alter to gypsum, for example, provided ample water and lower temperature (<60 °C). At Haughton,

sulfate solubility would mainly be controlled by temperature, as all fluids are low salinity, and near-neutral pH (Section 4.7.1.).

Hydrothermal anhydrite is common in a variety of settings but more common in seafloor hydrothermal vents (e.g., Ramboz et al., 1988). Anhydrite is present as a hydrothermal mineral at several impact structures (e.g., Ries, Boltysh, Puchezh-Katunki; Naumov, 2005). In each of these cases, it is present in fractured crystalline basement rocks. Anhydrite precipitation at the Chicxulub impact structure is interpreted to have been driven by the boiling of sea water, or melt-seawater interaction, based on the presence of heterogeneous fluid inclusion assemblages (Gonzalez-Partida et al., 2000).

The most notable sulfate discovery in this study is that liquid-vapour fluid inclusions in hydrothermal anhydrite in the core have a minimum homogenization temperature of 250 °C. This is a very conservative minimum as at the point of decrepitation, ~40% of the volume of the inclusion was vapour. This suggests that the true homogenization temperature was substantially higher $\geq 300°C$. Furthermore, anhydrite is known to precipitate from hydrothermal fluids above 300°C, e.g. in porphyry Cu systems (Allen et al., 1996). The previous highest recorded temperature at Haughton was 249.8°C in quartz cement, where the represented range may be a heterogeneous fluid inclusion assemblage (84.3–249.8°C). The highest recorded fluid inclusion temperatures in any impact hydrothermal system is ~440°C in quartz at the Kärdla impact structure, Estonia (Kirsimäe et al., 2002b). Still, this temperature does provide new constraints for the hydrothermal system. It is not clear if this 'hot' anhydrite was the result of recrystallization of sulfate impact melt, or a void-filling cement. Based on the textural evidence, we believe both may be present in the melt rock cores.

Given its presence within vugs in the impact melt rocks both around the periphery of the central uplift as well as the cores collected in the centre of the structure, selenite (gypsum) mineralization/replacement was abundant and dominated the final low temperature stage of mineralization. The presence of gypsum solely within host rocks rich in sulfate, indicates that the sulfate-rich fluids did not travel far, or fluid compositions changed significantly and quickly as a function of the host rock-fluid interaction.

4.7.6 Paragenesis and comparisons with other impacts

In the centre of the central uplift, quartz is the earliest high temperature mineral to have formed within the Eleanor River Formation. Within the impact melt rocks, anhydrite, pyrite and magnetite were the earliest hydrothermal phases, in addition to serpentinization and formation of talc as replacement of the silicates in the F2 impact melt (Chapter 3). Anhydrite was observed around radial talc in the F2 impact melt rock, which indicates at least some talc formed earlier than anhydrite (e.g., Fig. 3.14A, Chapter 3). However, the paragenetic timing of most of the clay minerals is ambiguous (e.g., Fig 4.13). At the end of the early stage and throughout the main stage, calcite formed as cement and as a replacement of a wide variety of melt rock and clast phases. In addition, silicate groundmass and clast alteration to talc-saponite in F3 and F2 impact melt rocks occured, as well as chloritization in F2 impact melt rock. Mineral assemblages in F2 impact melt rock suggest that it was subjected to higher temperatures than the F3 impact melt rock. At some point during clay mineral formation, pervasive metasomatism removed nearly all alkalis from the silicates in the impact melt rock cores. It is notable that no marcasite was identified in either of the core impact melt rocks, suggesting that Fe was in short supply and the little Fe present had already precipitated in the form of pyrite or magnetite at higher temperatures. Pyrite forms at temperatures above 180°C, depending on the right pH conditions, below which marcasite may form (Nicholson, 1993). Finally, during the late stage of the system, interaction with carbonate and sulfate-rich fluids resulted in pervasive low temperature replacement by both calcite and gypsum.

Around the periphery of the central uplift, quartz and pyrite were the dominant early phase minerals. We suspect that clay minerals are present in the exposed impact melt rocks within the periphery based on similarities in geochemistry with previous studies, as discussed in Chapter 3. However, this interpretation has yet to be confirmed, and therefore is indicated with a question mark in the model (Fig. 4.14). Temperature decrease paired with cooling or boiling is effective in precipitating sulfides (Reed and Palandri, 2006). Marcasite formation followed at temperatures <180°C and many generations of carbonate precipitation and replacement, as well as other minor minerals: barite, celestite and fluorite (Osinski et al., 2005a). Unfortunately we were unsuccessful in acquiring new calcite thermometry, but we know from Osinski et al. (2005a), that the calcite in the central uplift periphery formed between 150°C to less than 60°C. The late

stage, and likely the longest-lasting stage is dominated by a series of calcite and gypsum replacement, similar to the mineralization at the centre of the structure. The gypsum occurs solely within the impact melt rocks and the Bay Fiord Formation. The gypsum was accompanied by the formation of goethite and fibroferrite, followed by later weathering phases.

Both vertical and horizontal zonation of hydrothermal mineral assemblages commonly occur in the central area of an impact structure. Deep drilling (~400 to over 1000 m) at the centre of other craters (e.g., Ries, Siljan, Puchezh-Katunki, Boltysh) show a common transition of smectite to chlorite and substitution of calcite by anhydrite with depth (Naumov, 2005 and references therein). By the same token, chlorite increases with increasing temperature and depth in geothermal field deposits, and smectite remains a lower temperature phase (Papapanagiotou et al., 1995). A principal difference at Haughton is not only that the clay minerals are Mg-rich, but they are very likely mixed layers of talc and saponite that are stable at much higher temperature (Meunier, 2005). This is consistent with carbonate-dominated target rocks at Haughton, whereas the impacts listed above are dominated by their silicate targets.

The drill cores at Haughton are too shallow (~15 m) to draw parallel transition zones, but we can compare the mineralization in F2 and F3 impact melt rock cores to the impact melt rocks that outcrop within the interior of the crater and around the periphery of the central uplift. If the same transition zones are present at Haughton, then the cores may represent the transition between the two zones, as both smectite and chlorite (inferred in Chapter 3), calcite and anhydrite are present in abundance.

The Ries and Chicxulub impacts are the best comparable craters to Haughton in terms of target rocks, as they occurred into mixed carbonate-sulfate-silicate targets; however the proportion of impacted carbonates relative to the silicates at Haughton would have been much higher. Ries and Chicxulub both show early stage hydrothermal quartz, and abundant fracture-filling calcite veins (Arp et al., 2013; Osinski, 2005). However, the hydrothermal mineralogy there also contains K-metasomatism and Fe- and K-rich clay minerals (Lüders and Rickers, 2004; Muttik et al., 2008; Osinski, 2005; Simpson et al., 2019). Differences in the hydrothermal mineralogy at Haughton are a result of the more dominant carbonate source rocks and ion

distribution upon formation of impact melts, followed by leaching of Fe and alkalies and their transport elsewhere.

Another interesting note is the pervasive nature of the alteration at the centre of the Haughton structure. Prior to this thesis, the mineralization at Haughton was reported to occur mainly as veins and vugs filling fractures and faults (Osinski et al., 2005a, 2001). Pervasive mineralization at the centre of the Ries and Chicxulub structures was thought to be the result of large water to rock ratios, resulting from a syn- to post-impact lake, and seawater, respectively (Lüders and Rickers, 2004; Osinski, 2005; Osinski et al., 2019). There is no evidence for seawater interaction at Haughton, and the post-impact lake sediments in the centre of the structure, that is the Haughton Formation, is far younger than the impact. Perhaps, like the Ries impact, there was a syn to -post-impact lake or another process at work to increase the water to rock ratios needed for the intensity of alteration observed.

4.7.7 The lifetime of the hydrothermal system

There are very few geochronological tools that can be applied to date the duration of the hydrothermal system at Haughton. With the present data, the lifetime of the hydrothermal system can only be surmised through numerical models or comparison to numerical modeling of similar-sized craters in similar target rocks. Osinski et al. (2005a) pointed out that the model for the comparable Ries impact structure showed it may last many thousands of years (Pohl et al., 1977); however, this model assumed the crater-fill to consist primarily of lithic breccias, rather than melt-bearing breccias. Chapters 2 and 3 show that not only did Haughton host particulate melt rocks, but crystalline silicate melt rocks as well. Thus, because the main heat source for the hydrothermal system at Haughton was the melt rocks, it would have taken longer to cool relative to the model proposed for the similar sized Ries. By comparison, the hydrothermal system of the much smaller 4-km diameter Kärdla impact structure, with comparable target rocks, was estimated to have lasted up to 10,000 years (Jõeleht et al., 2005). A recent study by Schmieder and Jourdan (2013) that used Ar-Ar techniques to investigate the crystalline Lappajärvi impact, Finland, suggest that the lifetime of impact-generated hydrothermal systems in medium-sized craters may be an order of magnitude longer than previously thought (600 ka to 1.6 Ma).

Our results show that cooling at the early and perhaps even the main stage of the hydrothermal system at Haughton was relatively short. The presence of colloform quartz and botryoidal marcasite are indicative of rapid crystal growth. Moreover, the pervasive alteration described above and in Chapter 3 in the crater centre suggests convective or advective fluid flow, which is far more efficient than conductive heat flow. This interpretation is in agreement with previous models that show the first stage of cooling was rapid, due to latent heat of vapourization (Jõeleht et al., 2005). It follows that in an environment where a melt cools and the host rocks have a high permeability, gases will escape, and early cooling of the hydrothermal system will be relatively rapid, similar to a closed epithermal system.

4.8 Conclusions

By combining the field and systematic laboratory observations of hydrothermal mineralization at Haughton from this study with previous observations, this study has been able to generate a more comprehensive model for mineralization in impacts into carbonate and sulfate-rich mixed targets. Primary conclusions of the study are:

1. Multiple diagenetic and impact-induced hydrothermal calcite generations are present at Haughton and can be distinguished using a petrographic-microanalytical-cathodoluminescence approach.

2. Calcite mineralization is very long-lived in all the host strata and impact melt rocks, except the Eleanor River Formation.

3. In the early to main stages of the hydrothermal system, there is evidence of mild to moderate boiling and fluctuating fluid conditions. For example, temperature may have fluctuated up and down as opposed to a simple slow decrease in temperature over time. Fluctuating conditions are also supported by the multitude of calcite generations and their sharp transitions.

4. The hydrothermal system at Haughton lasted longer than previously thought, but the initial stage of the system was relatively rapid. Colloform and botryoidal mineral textures in quartz and marcasite are not only evidence of rapid growth, but that rapid mineralization is common through space and time in the hydrothermal system at Haughton.

5. We present an updated hydrothermal model including a series of new phases outlined using location, relative time, temperature and host rock.

6. In addition to the distribution of mineralization within structural localities, we recognize the impact that host lithologies have on the distribution of mineralization is equally important.

4.9 References

Abramov, O., 2004. Numerical modeling of an impact-induced hydrothermal system at the Sudbury crater. J. Geophys. Res. 109, E10007. https://doi.org/10.1029/2003JE002213

Abramov, O., Kring, D.A., 2007. Numerical modeling of impact-induced hydrothermal activity at the Chicxulub crater. Meteorit. Planet. Sci. 42, 93–112. https://doi.org/10.1111/j.1945-5100.2007.tb00220.x

Allen, R.L., Barrett, T.J., Browne, P.R.L., Clemson, J.E., Dunne, K.P.E., Ettlinger, A.D., Gibson, H.L., Groat, L.A., Hannington, M.D., Hawke, M.M., Jowett, E.C., Lang, J.R., Leitch, C.H.B., Lentz, D.R., Macdonald, A.J., McLeod, M., Martin, R.F., Murray, J., Pan, Y., Paradis, S., Peterson, E.U., Ray, G.E., Reardon, N.C., Rhys, D.A., Santaguida, F., Sherlock, R.L., Serbert, C., Simandl, G.J., Simmons, S.F., Taner, M.F., Thompson, A.J.B., Thompson, J.F.H., Turner, R.J.W., Wilson, G.C., Wolfson, I., Ziegler, J.F., 1996. Atlas of Alteration. Geological Association of Canada Mineral Deposits Division, St. John's.

Arp, G., Kolepka, C., Simon, K., Karius, V., Nolte, N., Hansen, B.T., 2013. New evidence for persistent impact-generated hydrothermal activity in the Miocene Ries impact structure, Germany. Meteorit. Planet. Sci. 48, 2491–2516. https://doi.org/10.1111/maps.12235

Bechberger, M., Coulson, I.M., 2014. Applications of cathodoluminescence imaging to sedimentary rocks, in: Coulson, I.M. (Ed.), Cathodoluminescence and Its Application to Geoscience. Mineralogical Association of Canada Short Course Series 45, Fredericton, NB, pp. 47–74.

Blamey, N.J.F., 2012. Composition and evolution of crustal, geothermal and hydrothermal fluids interpreted using quantitative fluid inclusion gas analysis. J. Geochemical Explor. 116–117,

17–27. https://doi.org/10.1016/j.gexplo.2012.03.001

Bodnar, R.J., 1993. Revised equation and table for determining the freezing point depression of H2O-NaCl solutions. Geochim. Cosmochim. Acta 57, 683–684.

Budd, D.A., Hammes, U., Ward, W.B., 2000. Cathodoluminescence in calcite cements: new insights on Pb and Zn sensitizing, Mn activation and Fe quenching at low trace-element concentrations. J. Sediment. Res. 70, 217–226.

Budd, D.A., Hiatt, E.E., 1993. Mineralogical Stabilization of High-Magnesium Calcite: Geochmical Evidence for Intracrystal Recrystallization within Holocene Porcellaneous Foraminifera FORAMINIFERA 1 Porcellaneous foraminifera are a unique type of high-Mg calcite (HMC) bioclast in th. J. Sediment. Petrol. 63, 261–274.

Burkhard, M., 1993. Calcite twins, their geometry, appearance and significance as stress-strain markers and indicators of tectonic regime: a review. J. Struct. Geol. 15, 351–368. https://doi.org/10.1016/0191-8141(93)90132-T

Cockell, C.S., 2006. The origin and emergence of life under impact bombardment. Philos. Trans. R. Soc. Lond. B. Biol. Sci. 361, 1845–55; discussion 1856. https://doi.org/10.1098/rstb.2006.1908

Cockell, C.S., Lee, P., 2002. The biology of impact craters - A review. Biol. Rev. Camb. Philos. Soc. 77, 279–310. https://doi.org/10.1017/S146479310100584X

Dewing, K., Nowlan, G., 2012. The Lower Cambrian to Lower Ordovician carbonate platform and shelf margin, Canadian Arctic Islands, in: Derby, J., Fritz, R., Longacre, S., Morgan, W., Sternbach, C. (Eds.), The Great American Carbonate Bank: The Geology and Economic Resources of the Cambrian-Ordovician Sauk Megasequence of Laurentia, AAPG Memoir 98. Shell and the American Association of Petroleum Geologists, pp. 627–647. https://doi.org/10.1306/13331510M983509

Dromgoole, E.L., Walter, L.M., 1990. Iron and manganese incorporation into calcite: Effects of growth kinetics, temperature and solution chemistry. Chem. Geol. 81, 311–336.

https://doi.org/10.1016/0009-2541(90)90053-A

Fournier, R.O., 1985a. The behavior of silica in hydrothermal solutions, in: B.R.Berger, P.M.Bethke (Eds.), Geology, Geochemistry of Epithermal Systems, Reviews in Economic Geology Volume 2. Society of Economic Geologists, pp. 45–61.

Fournier, R.O., 1985b. Silica minerals as indicators of conditions during gold deposition, in: Tooker, E. (Ed.), Geologic Characteristics of Sediment- and Volcanic-Hosted Disseminated Gold Deposits - Search for an Occurrence Model, U.S. Geological Survey Bulletin 1646. U.S. Government Printing Office, USA, pp. 15–26.

Fournier, R. O., 1985. Carbonate transport and deposition in the epithermal environment, in: Berger, B.R., Bethke, P.M. (Eds.), Geology and Geochemisty of Epithermal Deposits, Reviews in Economic Geology. Society of Economic Geologists, pp. 63–72.

Gonzalez-Partida, E., Carillo-Chavez, A., Martinez-Ibarra, R., 2000. Fluid inclusions from anhydrite related to the Chicxulub Crater impact breccias, Yucatan, Mexico; preliminary report. Int. Geol. Rev. 42, 279–288.

Greenberger, R.N., Mustard, J.F., Osinski, G.R., Tornabene, L.L., Pontefract, A.J., Marion, C.L., Flemming, R.L., Wilson, J.H., Cloutis, E.A., 2016. Hyperspectral mapping of alteration assemblages within a hydrothermal vug at the Haughton impact structure, Canada. Meteorit. {&} Planet. Sci. 51, 2274–2292. https://doi.org/http://dx.doi.org/10.1111/maps.12716

Grieve, R.A.F., 2005. Economic natural resource deposits at terrestrial impact structures, in: McDonald, I., Boyce, A.J., Butler, I.B., Herrington, R.J., Polya, D.A. (Eds.), Mineral Deposits and Earth Evolution, Geological Society, London Special Publications 248. Geological Society of London, London, pp. 1–29. https://doi.org/10.1144/gsl.sp.2005.248.01.01

Henley, R.W., Truesdell, A.H., Barton Jr., P.B., J.A., W., 1984. Fluid-mineral equilibria in hydrothermal systems. Reviews in Economic Geology Volume 1, Society of economic geologists.

Hiatt, E.E., Pufahl, P.K., 2014. Cathodoluminescence petrography of carbonate rocks: a review of applications for understanding diagenesis, reservoir quality, and pore system evolution, in: Coulson, I.M. (Ed.), Cathodoluminescence and Its Applications to Geoscience. Mineralogical Association of Canada, Fredericton, NB, pp. 75–96.

Izawa, M.R.M., Banerjee, N.R., Osinski, G.R., Flemming, R.L., Parnell, J., Cockell, C.S., 2011. Weathering of Post-Impact Hydrothermal Deposits from the Haughton Impact Structure: Implications for Microbial Colonization and Biosignature Preservation. Astrobiology 11, 537–550. https://doi.org/10.1089/ast.2011.0612

Jessberger, E., 1988. 40Ar-39Ar Dating of the Haughton Impact Structure. Meteoritics 23, 233–234.

Jõeleht, A., Kirsimae, K., Plado, J., Versh, E., Ivanov, B., 2005. Cooling of the Kärdla impact crater : II . Impact and geothermal modeling. Meteorit. Planet. Sci. 40, 21–33.

Kerr, J.W., 1967. New nomenclature for Ordivician rock unites of the eastern and southern Queen Elizabeth Islands, Arctic Canada. Bull. Can. Pet. Geol. 15, 91–113.

Kirsimäe, K., Osinski, G.R., 2013. Impact-induced hydrothermal activity, in: Osinski, G.R., Pierazzo, E. (Eds.), Impact Cratering Processes and Products. Wiley-Blackwell, p. 316.

Kirsimäe, K., Suuroja, S., Kirs, J., 2002. Hornblende alteration and fluid inclusions in Kärdla impact crater, Estonia: Evidence for impact-induced hydrothermal activity. … Planet. Sci. 37, 449–457.

Lüders, V., Rickers, K., 2004. Fluid inclusion evidence for impact-related hydrothermal fluid and hydrocarbon migration in Creataceous sediments of the ICDP-Chicxulub drill core Yax-1. Meteorit. Planet. Sci. 39, 1187–1197. https://doi.org/10.1111/j.1945-5100.2004.tb01136.x

Marzo, G.A., Davila, A.F., Tornabene, L.L., Dohm, J.M., Fairén, A.G., Gross, C., Kneissl, T., Bishop, J.L., Roush, T.L., McKay, C.P., 2010. Evidence for Hesperian impact-induced hydrothermalism on Mars. Icarus 208, 667–683.

https://doi.org/10.1016/j.icarus.2010.03.013

Mason, R.A., 1987. Ion microprobe analysis of trace elements in calcite with an application to the cathodoluminescence zonation of limestone cements from the Lower Carboniferous of South Wales, U.K. Chem. Geol. 64, 209–224. https://doi.org/10.1016/0009-2541(87)90003-9

McCarville, P., Crossey, L.J., 1996. Post-impact hydrothermal alteration of the Manson impact structure., in: Koeberl, C., Anderson, R.R. (Eds.), The Manson Impact Structure, Iowa: Anatomy of an Impact Crater Special Paper #302. Geological Society of America, Boulder, CO, United States (USA), pp. 347–376.

Metzler, A., Ostertag, R., Redeker, H.J., Stöffler, D., 1988. Composition of the Crystalline Basement and Shock Metamorphism of Crystalline and Sedimentary Target Rocks at teh Haughton Impact Crater, Devon Island, Canada. Meteoritcs 23, 197–207. https://doi.org/10.1017/CBO9781107415324.004

Meunier, A., 2005. Clays. Springer-Verlag Berlin Heidelberg, Germany.

Mitchell, I., Linnen, R.L., Creaser, R.A., 2004. The setting and age of the Bermuda Zn-Pb showing, Grinnell Peninsula, Devon Island: Implications for MVT mineralization in the Canadian Arctic. Explor. Min. Geol. 13, 109–118. https://doi.org/10.2113/13.1-4.109

Moncada, D., Mutchler, S., Nieto, A., Reynolds, T.J., Rimstidt, J.D., Bodnar, R.J., 2012. Mineral textures and fluid inclusion petrography of the epithermal Ag-Au deposits at Guanajuato, Mexico: Application to exploration. J. Geochemical Explor. 114, 20–35. https://doi.org/10.1016/j.gexplo.2011.12.001

Moore, C.H., Wade, W.J., 2013. Chapter 11 Natural Fracturing in Carbonate Reservoirs. Dev. Sedimentol. 67, 285–300.

Muttik, N., Kirsimäe, K., Somelar, P., Osinski, G.R., 2008. Post-impact alteration of surficial suevites in Ries crater, Germany: Hydrothermal modification or weathering processes? Meteorit. Planet. Sci. 43, 1827–1840. https://doi.org/10.1111/j.1945-5100.2008.tb00646.x

Naumov, M., 2002. Impact-generated hydrothermal systems: Data from Popigai, Kara, and Puchezh-Katunki impact structures, in: Plado, J., Pesonen, L.J. (Eds.), Impacts in Precambrian Shields. Springer-Verlag, Berlin, pp. 117–171.

Naumov, M.V., 2005. Principal features of impact-generated hydrothermal circulation systems: mineralogical and geochemical evidence. Geofluids 5, 165–184.

Nicholson, K., 1993. Geothermal Fluids: Chemistry and Exploration Techniques. Springer-Verlag, Berlin, Germany.

Osinski, G., 2005. Hydrothermal activity associated with the Ries impact event, Germany. Geofluids 5, 202–220.

Osinski, G., Tornabene, L.L., Banerjee, N.R., Cockell, C.S., Flemming, R., Izawa, M.R., McCutcheon, J., Parnell, J., Preston, L.J., Pickersgill, A.E., Pontefract, A., Sapers, H.M., Southam, G., 2013. Impact-generated hydrothermal systems on Earth and Mars. Icarus 224, 347–363. https://doi.org/10.1016/j.icarus.2012.08.030

Osinski, G.R., Grieve, R.A.F., Hill, P.J.A., Simpson, S.L., Cockell, C., Christeson, G.L., Ebert, M., Gulick, S., Melosh, H.J., Riller, U., Tikoo, S.M., Wittmann, A., 2019. Explosive interaction of impact melt and seawater following the Chicxulub impact event. Geology 48, 108–112. https://doi.org/10.1130/g46783.1

Osinski, G.R., Lee, P., Parnell, J., Spray, J.G., Baron, M., 2005a. A case study of impact-induced hydrothermal activity: The Haughton impact structure, Devon Island, Canadian High Arctic. Meteorit. Planet. Sci. 40, 1859–1877. https://doi.org/10.1111/j.1945-5100.2005.tb00150.x

Osinski, G.R., Lee, P., Spray, J.G., Parnell, J., Lim, D.S.S., Bunch, T.E., Cockell, C.S., Glass, B., 2005b. Geological overview and cratering model for the Haughton impact structure, Devon Island, Canadian High Arctic. Meteorit. Planet. Sci. 40, 1759–1776. https://doi.org/10.1111/j.1945-5100.2005.tb00145.x

Osinski, G.R., Spray, J.G., 2005. Tectonics of complex crater formation as revealed by the

Haughton impact structure, Devon Island, Canadian High Arctic. Meteorit. Planet. Sci. 40, 1813–1834. https://doi.org/10.1111/j.1945-5100.2005.tb00148.x

Osinski, G.R., Spray, J.G., 2001. Impact-generated carbonate melts: evidence from the Haughton structure, Canada. Earth Planet. Sci. Lett. 194, 17–29. https://doi.org/10.1016/S0012-821X(01)00558-1

Osinski, G.R., Spray, J.G., Lee, P., 2005c. Impactites of the Haughton impact structure, Devon Island, Canadian High Arctic. Meteorit. Planet. Sci. 40, 1789–1812. https://doi.org/10.1111/j.1945-5100.2005.tb00147.x

Osinski, G.R., Spray, J.G., Lee, P., 2001. Impact-induced hydrothermal activity within the Haughton impact structure, arctic Canada: Generation of a transient, warm, wet oasis. Meteorit. Planet. Sci. 36, 731–745. https://doi.org/10.1111/j.1945-5100.2001.tb01910.x

Papapanagiotou, P., Patner, P., Beaufort, D., Fouillac, A.-M., Rojas, J., 1995. Occurrence of smectites and smectite-rich mixed layers at high temperature within reservoirs of active geothermal fields. Proc. World Geotherm. Congr. 2, 1071–1076.

Parnell, J., Boyce, A., Thackrey, S., Muirhead, D., Lindgren, P., Mason, C., Taylor, C., Still, J., Bowden, S., Osinski, G.R., Lee, P., 2010a. Sulfur isotope signatures for rapid colonization of an impact crater by thermophilic microbes. Geol. 38, 271–274. https://doi.org/http://dx.doi.org/10.1130/G30615.1

Parnell, J., Lee, P., Cockell, C.S., Osinski, G.R., 2004. Microbial colonization in impact-generated hydrothermal sulphate deposits, Haughton impact structure, and implications for sulphates on Mars. Int. J. Astrobiol. 3, 247–256. https://doi.org/10.1017/S1473550404001995

Parnell, J., Taylor, C.W., Thackrey, S., Osinski, G.R., Lee, P., 2010b. Permeability data for impact breccias imply focussed hydrothermal fluid flow. J. Geochemical Explor. 106, 171–175. https://doi.org/10.1016/j.gexplo.2009.12.002

Pirajno, F., 2009. Hydrothermal Processes and Mineral Systems. Springer, Geological Survey of

Western Australia, Berlin. https://doi.org/http://dx.doi.org/10.1007/978-1-4020-8613-7

Pohl, J., Stöffler, D., Gall, H., Ernstson, K., 1977. The Ries impact crater, in: Roddy, D.J., Pepin, R.O., Merrill, R.B. (Eds.), Impact and Explosion Cratering. Pergamon Press, New York, N.Y., New York, pp. 343–403.

Pontefract, A., Osinski, G.R., Lindgren, P., Parnell, J., Cockell, C.S., Southam, G., 2012. The effects of meteorite impacts on the availability of bioessential elements for endolithic organisms. Meteorit. Planet. Sci. 47, 1681–1691. https://doi.org/http://dx.doi.org/10.1111/maps.12004

Ramboz, C., Oudin, E., Thisse, Y., 1988. Geyser-type discharge in Atlantis II Deep, Red Sea: evidence of boiling from fluid inclusions in epigenetic anhydrite. Can. Mineral. 26 pt 3, 765–786.

Reed, M.H., Palandri, J., 2006. Sulfide Mineral Precipitation from Hydrothermal Fluids. Rev. Mineral. Geochemistry 61, 609–631. https://doi.org/10.2138/rmg.2006.61.11

Reimold, W., Koeberl, C., Gibson, R., Dressler, B., 2005. Economic mineral deposits in impact structures: a review. Impact tectonics 479–552.

Schmieder, M., Jourdan, F., 2013. The Lappajarvi impact structure (Finland); age, duration of crater cooling, and implications for early life. Geochim. Cosmochim. Acta 112, 321–339. https://doi.org/http://dx.doi.org/10.1016/j.gca.2013.02.015

Schulze-Makuch, D., Dohm, J.M., Fan, C., Fairén, A.G., Rodriguez, J.A.P., Baker, V.R., Fink, W., 2007. Exploration of hydrothermal targets on Mars. Icarus 189, 308–324. https://doi.org/10.1016/j.icarus.2007.02.007

Segnit, E.R., Holland, H.D., Biscardi, C.J., 1962. The solubility of calcite in aqueous solutions - I the solubility of calcite in water between 75° and 200° at CO2 pressures up to 60 atm. Geochim. Cosmochim. Acta 26, 1301–1331.

Sherlock, S., Kelley, S., 2005. Re evaluating the age of the Haughton impact event. … Planet. Sci. 40, 1777–1787. https://doi.org/10.1111/j.1945-5100.2005.tb00146.x

Shimizu, T., 2014. Reinterpretation of Quartz in terms of hydrothermal fluid evolution at the Koryu Ai-Ag deposit, Japan. Econ. Geol. 109, 2051–2065.

Simpson, S.L., Osinski, G.R., Longstaffe, F., 2019. Clay mineral diversity through the Chicxulub peak-ring: a comparison of microtextural, X-ray diffraction and spectral datasets, in: Lunar and Planetary Science Conference XXXXX. LPI, Houston Texas.

Thorsteinsson, R., Mayr, U., 1987. The sedimentary rocks of Devon Island, Canadian Arctic Archipelago. Geological Survey of Canada Memoir 411, Ottawa, Canada.

Van Driessche, A.E.S., Stawski, T.M., Benning, L.G., 2017. New Perspectives on Mineral Nucleation and Growth, in: New Perspectives on Mineral Nucleation and Growth. Springer International Publishing, Switzerland, pp. 227–256. https://doi.org/10.1007/978-3-319-45669-0

Young, K.E., van Soest, M.C., Hodges, K. V., Watson, E.B., Adams, B. a., Lee, P., 2013. Impact thermochronology and the age of Haughton impact structure, Canada. Geophys. Res. Lett. 40, 3836–3840. https://doi.org/10.1002/grl.50745

Zylberman, W., Quesnel, Y., Rochette, P., Osinski, G.R., Marion, C., Gattacceca, J., 2017. Hydrothermally enhanced magnetization at the center of the Haughton impact structure? Meteorit. Planet. Sci. 52, 2147–2165. https://doi.org/10.1111/maps.12917

Chapter 5

5   Summary and Implications

5.1   Introduction

Prior to this study, knowledge of impacts into calcareous sedimentary target rocks was much less than for impacts into crystalline targets (Osinski et al., 2008b, 2008a; Stöffler et al., 2018a). This is due in part to the difficulty to distinguish the variety of carbonate and sulfate impactite products as well as the discrepancy of fewer studies completed at impacts into calcareous targets. The overarching objective of this thesis was to better understand the response of carbonate- and sulfate-rich target rocks to meteorite impact. This was accomplished by characterizing the products of the impact (Chapters 2 and 3) and the impact-generated hydrothermal system (Chapter 4) at the centre of the carbonate-rich Haughton impact structure, Canada. Below, we synthesize the new state of knowledge of impactites and hydrothermal mineralization at Haughton, their implications, the potential for economic deposits at Haughton and recommendations for future work.

5.2   New Haughton Overview

The description and understanding of impactites at Haughton have greatly evolved in the forty plus years since it was first confirmed as an impact. For many years it was thought that the dominantly carbonate target at Haughton produced a single principal impactite lithology of allochthonous lithic breccias with 'rare silicate melt particles' (H.-J. Redeker and Stöffler, 1988; Robertson and Sweeney, 1983). The impactites were later re-interpreted as a series of lithic monomict breccias, allochthonous lithic polymict breccias and pale grey particulate impact melt rocks (Osinski et al., 2008b, 2005c). The latter is the volumetrically dominant crater-fill lithology (Osinski et al., 2005b). The groundmass of these melt rocks, exposed at the surface, consists of microcrystalline calcite, silicate glass and anhydrite, all of which were interpreted to have crystallized from the melt. The melt rocks could only be differentiated from the lithic polymict breccias through microanalytical techniques. Textural evidence consisted of calcite spherules and irregularly-shaped globules of calcite intermingling with or hosted within silicate

glass (Osinski and Spray, 2001), and a variety of carbonate-sulfate-silicate immiscibility textures as well as sulfate flow and quench textures (Osinski and Spray, 2003). Though these studies presented convincing evidence, greater detail is provided in this study, wherein two new types of impact melt rocks from shallow cores in the crater centre are described (Chapter 2 and 3). The first core presents strong textural evidence for a clast-rich, crystalline carbonate-sulfate-silicate impact melt rock that shows classic igneous textures, including acicular to spherulitic calcite and silicate, calcite-silicate and sulfate-silicate intergrowths and skeletal silicates hosted within sulfate groundmass (Chapter 2). The second core intersected a new type of melt rock at Haughton that has an exclusively silicate groundmass, which consists of Mg-rich clay minerals (Chapter 3).

Previous hydrothermal investigations at Haughton presented a preliminary hydrothermal model which described a 3-stage moderate to low temperature system dominated by calcite-sulfide-sulfate mineralization. Mineralization was described as cavity- and fracture-filling vugs and veins within the crater-fill and faulted target blocks around the central uplift periphery, as hydrothermal pipes within the faulted blocks in the crater rim region and quartz cement in the centre of the structure (Osinski et al., 2005a, 2001). In this study, two new crater-fill lithologies have been identified in the crater centre with not only void-filling mineralization but intense pervasive alteration of the entire rock and new mineral phases (Chapter 3). A detailed micro-analytical cathodoluminescence approach has been applied here to all the previously described mineralization and shows that the carbonates in the periphery of the central uplift and the quartz cement in the crater centre both represent multiple generations of mineralization (Chapter 4). The same methodology was applied to the new impact melt lithologies and demonstrated pervasive alteration by Mg-rich clay minerals of the silicate melt rock, as well as intense alteration by calcite, anhydrite and gypsum in the carbonate-sulfate-silicate melt rock. The previous and current work on the hydrothermal mineralization (Chapters 2, 3, and 4; Osinski et al., 2005a, 2001) is synthesized in Chapter 4, which presents an updated hydrothermal model at the centre and periphery of the central uplift, including the introduction of many newly identified magnesian clay minerals (talc, serpentine, chlorite, Mg-saponite and/or their mixtures), calcite, gypsum, magnetite and high temperature anhydrite ($>>250$ °C) at the centre of the structure and sphalerite in the uplift periphery.

5.3 Implications

Previous studies of impacts into calcareous sedimentary target rocks generally lacked the characteristic igneous textures of impact melt rocks in crystalline targets (Kieffer and Simonds, 1980; Osinski et al., 2018). The results of this thesis show that this is not always the case (Chapter 2), and in fact, although the challenge remains, we have shown that distinguishing and thereby interpreting the diversity of carbonate impactites is achievable with the right set of microanalytical tools (Chapter 3 and 4). Consequently, Haughton now presents very strong evidence in support of carbonate and sulfate melting in response to impact. These observations should impact future modeling of post-impact climatic effects, i.e., if a substantial amount of carbonate has melted, as opposed to decomposed, less carbon dioxide would be released into the atmosphere.

The unearthing of Haughton's first silicate impact melt rock in particular and the Mg-rich clay minerals suggest that the primary silicate impact melt rocks formed at Haughton were ultramafic in composition, where magnesium was likely sourced from the dolomite target rocks Of the 198 impacts on Earth, this is similar only to Meteor Crater, which is also hosted in carbonate rocks (Hörz et al., 2015; Osinski et al., 2015).

The updated hydrothermal model at Haughton shows that alteration at the centre of the impact into calcareous targets is much more pervasive and complex than previously thought and is more in line with those observed at other mixed target impacts (e.g. Ries and Chicxulub). Both the impact melt and hydrothermal mineralization formed from and within Haughton's mixed target rocks are far more heterogeneous than previously thought. In addition to Haughton, there is evidence for carbonate impact melt products at the aforementioned Meteor Crater (Osinski et al., 2003), Chicxulub (Jones et al., 2000), Ries (Graup, 1999), Tenoumer (Pratesi et al., 2005) and more recently at Lockne (Sjöqvist et al., 2012), Steinheim (Anders et al., 2011) and Steen River (Walton et al., 2019) structures. Similarly, hydrothermal studies completed at impact structures into carbonate targets include Haughton (Osinski et al., 2001, 2005a; Chapter 4), Lockne (Sturkell et al., 1998), Ries (Muttik et al., 2008; Newsom et al., 1986; Osinski, 2005) and the Chicxulub (Abramov and Kring, 2007; Ames et al., 2004; Hecht et al., 2004; Zürcher and Kring, 2004) impact structures. Of these few exceptional impacts, totaling 8 including Haughton, the Haughton structure presents the best preserved and field accessible model to study and understand impactites and hydrothermal mineralization in impacts into calcareous targets.

166

5.4 Haughton as an economic deposit?

One of Haughton's principal target rocks, the Thumb Mountain Formation, extends to Little Cornwallis Island, which hosts a Zn-Pb Mississippi Valley type (MVT) deposit, the now closed Polaris Mine. Another MVT deposit, the Bermuda Zn-Pb Showing on the Grinnell Peninsula on Devon Island is hosted in the Blue Fiord Formation. Both of these deposits have been dated using the Rb-Sr method and are the same age within error (~357 Ma) and are related to saline fluids mobilized at the time of the Ellesmerian Orogeny (Mitchell et al., 2004). A third Arctic MVT deposit, the Nanisivik Zn-Pb MVT on Baffin Island, is hosted in the Bylot Supergroup and was mineralized much earlier ~461 Ma (Sherlock et al., 2004). All of these deposits thus formed long before the Haughton impact.

There is no current evidence to suggest Haughton may host economic deposits of any kind, including Zn-Pb deposits, either pre- or post-impact. This mineralization would consist of sphalerite and galena; only a minute abundance of sphalerite has been identified. The evidence for immiscible impact melts is promising but it does not include evidence for an immiscible sulfide melt nor a sufficient source of metals. Evidence of boiling of supersaturated fluids that deposited the hydrothermal quartz (Chapter 4) is a process commonly responsible for depositing precious metals like Au (R.O. Fournier, 1985b; Shimizu, 2014). Free gold was not observed, nor was gold detected in pyrite at the ppm detection limits of the microprobe. As Haughton's hydrothermal fluids were near-neutral pH and low salinity (Osinski et al., 2005a), they would have been poor agents for transport of Pb and Zn, which require high salinities and more acidic conditions. Although sphalerite was found in very small quantities at Haughton, it is unlikely that an economic deposit lies undiscovered. Impacts are known to host petroleum reservoirs (Grieve and Masaitis, 1994; Grieve, 2013), and although some petroleum-rich fluid inclusions were identified within the structure (Osinski et al., 2005a), no significant oil or gas deposit has been identified. Consequently, no further investigation into the economic potential at Haughton is expected. However, we do recommend the hydrothermal model at Haughton be used to investigate and understand deposits at other impact sites.

5.5 Recommended future work

Laser ablation inductively coupled plasma mass spectrometry (LA-ICPMS) could be applied to the hydrothermal quartz to determine 1) titanium concentrations for use as a geothermometer and 2) to look for potential precious metal concentrations. Moreover, LA-ICP-MS could be used to analyze trace elements in the carbonates, to better distinguish the various genetic (melted and hydrothermal) populations. In situ oxygen and carbon isotopic analyses using an ion microprobe would also be useful in distinguishing between carbonate derived from crystallization or hydrothermal precipitation. To obtain the formation temperature for the carbonates, clumped isotope analysis may also be an option, however, it may be difficult to accurately microdrill a sufficient amount of material for analysis.

Additional, deeper drilling at Haughton may reveal a more complete history of both the formation of impactites and hydrothermal mineralization at the centre of the structure. Clay phases are the most difficult to place within the timeline of the hydrothermal model, thus it would be beneficial to complete a detailed investigation of the clay minerals throughout the structure, including the exposed impact melt rocks at the surface. Future study should include morphology imaging on a lithographic SEM and clay separation and treatments for detailed XRD and micro-XRD to confirm and characterize clay phases present and their interlayered or intermixed structure. The XRD analyses could be accompanied by clay mineral isotope studies to determine fluid composition and formation temperatures, to provide an overall better understanding of paragenesis.

Finally, it may be worthwhile to complete a petrographic and fluid inclusion investigation of the anhydrite identified by Osinski and Spray (2003) to evaluate and compare it to the hydrothermal and melt-generated anhydrite in this study.

5.6 References

Abramov, O., Kring, D.A., 2007. Numerical modeling of impact-induced hydrothermal activity at the Chicxulub crater. Meteorit. Planet. Sci. 42, 93–112. https://doi.org/10.1111/j.1945-5100.2007.tb00220.x

Ames, D.E., Kjarsgaard, I.M., Pope, K.O., Dressler, B., Pilkington, M., 2004. Secondary alteration of the impactite and mineralization in the basal Tertiary sequence, Yaxcopoil-1,

Chicxulub impact crater, Mexico. Meteorit. Planet. Sci. 39, 1145–1167.
https://doi.org/10.1111/j.1945-5100.2004.tb01134.x

Anders, D., Kegler, P., Buchner, E., Schmieder, M., 2011. Carbonate melt lithologies from the
Steinheim impact crater (SW Germany), in: 42nd Lunar and Planetary Science Conference.
Houston Texas.

Fournier, R.O., 1985. Silica minerals as indicators of conditions during gold deposition, in:
Tooker, E. (Ed.), Geologic Characteristics of Sediment- and Volcanic-Hosted Disseminated
Gold Deposits - Search for an Occurrence Model, U.S. Geological Survey Bulletin 1646.
U.S. Government Printing Office, USA, pp. 15–26.

Graup, G., 1999. Carbonate-silicate liquid immiscibility upon impact melting: Ries Crater,
Germany. Meteorit. Planet. Sci. 34, 425–438.

Grieve, R.A.., Masaitis, V.L., 1994. The economic potential of terrestrial impact craters. Int.
Geol. Rev. 36, 105–151.

Grieve, R.A.F., 2013. Economic deposits at terrestrial impact structures, in: Osinski, G.,
Pierazzo, E. (Eds.), Impact Cratering Processes and Products. Wiley-Blackwell, pp. 177–
193.

Hecht, L., Wittmann, A., Schmitt, R.-T., Stoeffler, D., 2004. Composition of impact melt
particles and the effects of post-impact alteration in suevitic rocks at the Yaxcopoil-1 drill
core, Chicxulub Crater, Mexico. Meteorit. Planet. Sci. 39, 1169–1186.

Hörz, F., Archer, P.D., Niles, P.B., Zolensky, M.E., Evans, M., 2015. Devolatilization or melting
of carbonates at Meteor Crater, AZ? Meteorit. Planet. Sci. 50, 1050–1070.
https://doi.org/10.1111/maps.12453

Jones, A.P., Claeys, P., Heuschkel, S., 2000. Impact melting of carbonates from the Chicxulub
crater, in: Gilmour, I., Koeberl, C. (Eds.), Impacts and the Early Earth, Lecture Notes in
Earth Sciences, Vol 91. Springer, Springer-Verlag Berlin Heidelberg, pp. 343–361.

Kieffer, S.W., Simonds, C.H., 1980. The role of volatiles and lithology in the impact cratering

process. Rev. Geophys. 18, 143–181. https://doi.org/10.1029/RG018i001p00143

Mitchell, I., Linnen, R.L., Creaser, R.A., 2004. The setting and age of the Bermuda Zn-Pb showing, Grinnell Peninsula, Devon Island: Implications for MVT mineralization in the Canadian Arctic. Explor. Min. Geol. 13, 109–118. https://doi.org/10.2113/13.1-4.109

Muttik, N., Kirsimäe, K., Somelar, P., Osinski, G.R., 2008. Post-impact alteration of surficial suevites in Ries crater, Germany: Hydrothermal modification or weathering processes? Meteorit. Planet. Sci. 43, 1827–1840. https://doi.org/10.1111/j.1945-5100.2008.tb00646.x

Newsom, H., Graup, G., Sewards, T., Keil, K., 1986. Fluidization and hydrothermal alteration of the Suevite deposit at the Ries Crater, West Germany, and implications for Mars. J. Geophys. Res. 91, E239–E251. https://doi.org/http://dx.doi.org/10.1029/JB091iB13p0E239

Osinski, G., 2005. Hydrothermal activity associated with the Ries impact event, Germany. Geofluids 5, 202–220.

Osinski, G.R., Bunch, T.E., Flemming, R.L., Buitenhuis, E., Wittke, J.H., 2015. Impact melt- and projectile-bearing ejecta at Barringer Crater, Arizona. Earth Planet. Sci. Lett. 432, 283–292. https://doi.org/10.1016/j.epsl.2015.10.021

Osinski, G.R., Bunch, T.E., Witte, J., 2003. Evidence for the shock melting of carbonates from meteor crater, Arizona, in: 66th Annual Meteoritical Society Meeting. p. abstract #5070.

Osinski, G.R., Grieve, R.A.F., Bleacher, J.E., Neish, C.D., Pilles, E.A., Tornabene, L.L., 2018. Igneous rocks formed by hypervelocity impact. J. Volcanol. Geotherm. Res. 353, 25–54. https://doi.org/10.1016/j.jvolgeores.2018.01.015

Osinski, G.R., Grieve, R.A.F., Collins, G.S., Marion, C., Sylvester, P., 2008a. The effect of target lithology on the products of impact melting. Meteorit. Planet. Sci. 43, 1939–1954. https://doi.org/10.1111/j.1945-5100.2008.tb00654.x

Osinski, G.R., Lee, P., Parnell, J., Spray, J.G., Baron, M., 2005a. A case study of impact-induced hydrothermal activity: The Haughton impact structure, Devon Island, Canadian High Arctic. Meteorit. Planet. Sci. 40, 1859–1877. https://doi.org/10.1111/j.1945-

5100.2005.tb00150.x

Osinski, G.R., Lee, P., Spray, J.G., Parnell, J., Lim, D.S.S., Bunch, T.E., Cockell, C.S., Glass, B., 2005b. Geological overview and cratering model for the Haughton impact structure, Devon Island, Canadian High Arctic. Meteorit. Planet. Sci. 40, 1759–1776. https://doi.org/10.1111/j.1945-5100.2005.tb00145.x

Osinski, G.R., Spray, J.G., 2003. Evidence for the shock melting of sulfates from the Haughton impact structure, Arctic Canada. Earth Planet. Sci. Lett. 215, 357–370. https://doi.org/10.1016/S0012-821X(03)00420-5

Osinski, G.R., Spray, J.G., 2001. Impact-generated carbonate melts: evidence from the Haughton structure, Canada. Earth Planet. Sci. Lett. 194, 17–29. https://doi.org/10.1016/S0012-821X(01)00558-1

Osinski, G.R., Spray, J.G., Grieve, R.A.F., 2008b. Impact melting in sedimentary target rocks: An assessment, in: Evans, K.R., Horton, J.W., King, J.D.T., Morrow J.R. (Eds.), The Sedimentary Record of Meteorite Impacts, Geological Society of America Special Publication 437. Geological Society of America, Boulder, pp. 1–18. https://doi.org/10.1130/2008.2437(01).For

Osinski, G.R., Spray, J.G., Lee, P., 2005c. Impactites of the Haughton impact structure, Devon Island, Canadian High Arctic. Meteorit. Planet. Sci. 40, 1789–1812. https://doi.org/10.1111/j.1945-5100.2005.tb00147.x

Osinski, G.R., Spray, J.G., Lee, P., 2001. Impact-induced hydrothermal activity within the Haughton impact structure, arctic Canada: Generation of a transient, warm, wet oasis. Meteorit. Planet. Sci. 36, 731–745. https://doi.org/10.1111/j.1945-5100.2001.tb01910.x

Pratesi, G., Morelli, M., Rossi, A.P., Ori, G.G., 2005. Chemical compositions of impact melt breecias and target rocks from the Tenoumer impact crater, Mauritania. Meteorit. Planet. Sci. 40, 1653–1672.

Redeker, H.-J., Stöffler, D., 1988. The allochthonous polymict breccia layer of the Haughton

impact crater, Devon Island, Canada. Meteoritics 23, 185–196.

Robertson, P.B., Sweeney, J.F., 1983. Haughton impact structure: structural and morphological aspects. Can. J. Earth Sci. 20, 1134–1151.

Sherlock, R.L., Lee, J.K.W., Cousens, B.L., 2004. Geologic and geochronologic constraints on the timing of mineralization at the Nanisivik zinc-lead Mississippi Valley-type deposit, northern Baffin Island, Nunavut, Canada. Econ. Geol. 99, 279–293. https://doi.org/10.2113/gsecongeo.99.2.279

Shimizu, T., 2014. Reinterpretation of Quartz in terms of hydrothermal fluid evolution at the Koryu Ai-Ag deposit, Japan. Econ. Geol. 109, 2051–2065.

Sjöqvist, A., Lindgren, P., Mansfeld, J., Sturkell, E., 2012. Carbonate melt fragments in resurge deposits from the Lockne impact structure, Sweden, in: 43rd Lunar and Planetary Science Conference. Houston Texas.

Stöffler, D., Hamann, C., Metzler, K., 2018. Shock metamorphism of planetary silicate rocks and sediments: Proposal for an updated classification system. Meteorit. Planet. Sci. 53, 5–49. https://doi.org/10.1111/maps.12912

Sturkell, E.F.F., Broman, C., Forsberg, P., Torssander, P., 1998. Impact-related hydrothermal activity in the Lockne impact structure, Jamtland, Sweden. Eur. J. Mineral. 10, 589–606. https://doi.org/10.1127/ejm/10/3/0589

Walton, E.L., Timms, N.E., Hauck, T.E., Maclagan, E.A., Herd, C.D.K., 2019. Evidence of impact melting and post-impact decomposition of sedimentary target rocks from the Steen River impact structure ,. Earth Planet. Sci. Lett. 515, 173–186. https://doi.org/10.1016/j.epsl.2019.03.015

Zürcher, L., Kring, D. a., 2004. Hydrothermal alteration in the core of the Yaxcopoil-1 borehole, Chicxulub impact structure, Mexico. Meteorit. Planet. Sci. 39, 1199–1221. https://doi.org/10.1111/j.1945-5100.2004.tb01137.x

Appendix A
Chapter 2 Supplementary Data

A.1 Methodology

Drilling methods may be found in Zylberman et al. (2017). The F2 core is a nearly continuous core 4.2 m in length, beginning at a depth of 8.6 m.

A.1.1 EPMA-WDS-EDS-BSE-CL

Polished thin sections were made at several depth intervals for the F2 core at the University of Western Ontario and Aix-Marseille Université. The softness of the carbonate-sulfate rich samples often resulted in a rough or uneven polish. To confirm optical interpretations, investigate micro-features and collect geochemical data, electron probe micro-analyses (EPMA) were completed on polished thin sections. This work was completed at the University of Western Ontario's Earth and Planetary Materials Analysis Laboratory on the JEOL JXA-8530F Field Emission Electron Probe Microanalyzer. For silicates, wavelength dispersive spectrometry was collected for Si, Ti, Cr, Al, Mg, Mn, Fe, Ca, Na, K, P, Cl, F and S with standards enstatite, rutile, chromite, albite, enstatite, rhodonite, hematite, diopside, albite, orthoclase, apatite, sodalite, fluorite and anhydrite, respectively, at 15 kV, 20nA and 2 to 5 μm spot size. Microprobe detection limits range from 100 to 500 ppm for major element oxides, and from 200 to 800 ppm for minor element oxides. In the case of the silicates, stoichiometric calculations were completed to infer mineral phases from the WDS results.

Element maps were constructed with a step size of 0.26 μm and a dwell time of 10 ms. Wavelength dispersive spectrometry was used to map Mg, Ca, Mn, Fe, Al, K, S and Cl with standards enstatite, diopside, rhodonite, hematite, kaerstite, orthoclase, anhydrite and sodalite, respectively. Energy dispersive spectrometry (EDS) was used to map Si, C, F, Na, Sr and Ba. Element maps, spectrometry and associated backscatter electron (BSE) imaging were collected with the probe current set to 15 kV and 50 nA. EPMA-Cathodoluminescence mapping was completed simultaneously under the same conditions to produce greyscale panchromatic images.

A.1.2 Micro X-Ray Diffraction

Mineralogical investigations were completed on two F2 thin sections: HAUF2G7 and HAUF2G7uwo. Polished thin sections were analyzed using micro X-ray diffraction (μXRD) performed in the Department of Earth Sciences at the University of Western Ontario on a Bruker D8 Discover diffractometer with theta-theta instrument geometry as described by Flemming (2007). The Bruker has a sealed Cobalt source, a Gobel mirror parallel beam optics system with a pinhole collimator of 300 μm and a two-dimensional Vantec 500 general area detector with diffraction system software (GADDS). Thin sections were placed on an XYZ stage and monitored through an optical microscope and laser system. Omega scans were completed on sample HAUF2G7 whereby the X-ray source and detector are rotated concurrently clockwise through a specified number of degrees, or the Omega (ω) angle. The first GADDS frame ($\Theta_1 = 14.5$, $\Theta_2 = 16$, $\omega = 6°$) was collected in 30 minutes and the second GADDS frame was collected in 60 minutes ($\Theta_1 = 29.5$, $\Theta_2 = 49.5$ $\omega = 20°$). Coupled scans, wherein the source and detector are set at the same angle relative to the sample, were completed on sample HAUF2G7uwo. Frame 1 was collected at $\Theta_1 = 10$ and $\Theta_2 = 20.5$ and frame 2 at $\Theta_1 = 29.5$ and $\Theta_2 = 40$ with a frame width of 39 and collection time of 30 min. Diffraction patterns were processed and interpreted using Bruker AXS DiffracPLUS EVA software wherein patterns were examined and indexed using the mineral database included in the software.

A.1.3 Raman Spectroscopy

Skeletal silicate grains were examined by Laser Raman spectroscopy using a Renishaw InVia Reflex Raman spectrometer at Surface Science Western. Laser wavelengths used were 785, 633 and 514 nm, the 785nm most frequently, with two gratings 1800 and 1200 l/mm. Each laser is equipped with a polarizer and half waveplate. Spectra were collected with a spectral range of 50 to 1250 cm^{-1}. The data was processed using both Renishaw Wire 4.2 and CrystalSleuth software, and phases were identified using comparisons to Raman spectra from the RRUFF sample database (Appendix G).

A.2 Supplementary Figures

Figure A.1. Photographic cross sections of F2 and F3 cores. Note the difference in colour, texture and clast populations. F3 is more representative of the particulate impact melt at Haughton. Cross section of each core is approximately 2.5 cm.
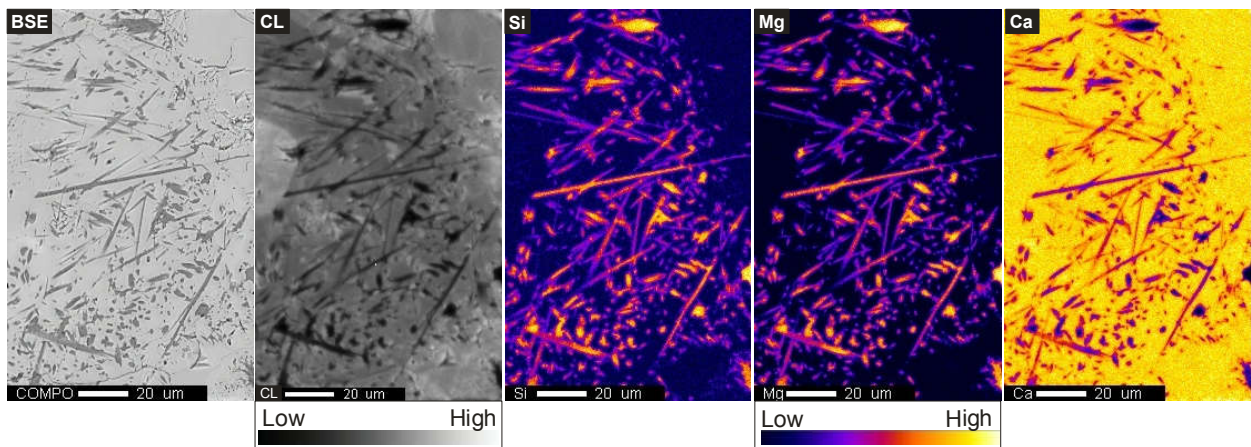
Figure A.2. BSE photomicrograph and CL-EDS-WDS element maps of acicular Mg-rich silicate hosted in calcite from inset in Figure 2.2D. Note the variation in CL intensity outside of the acicular zone.
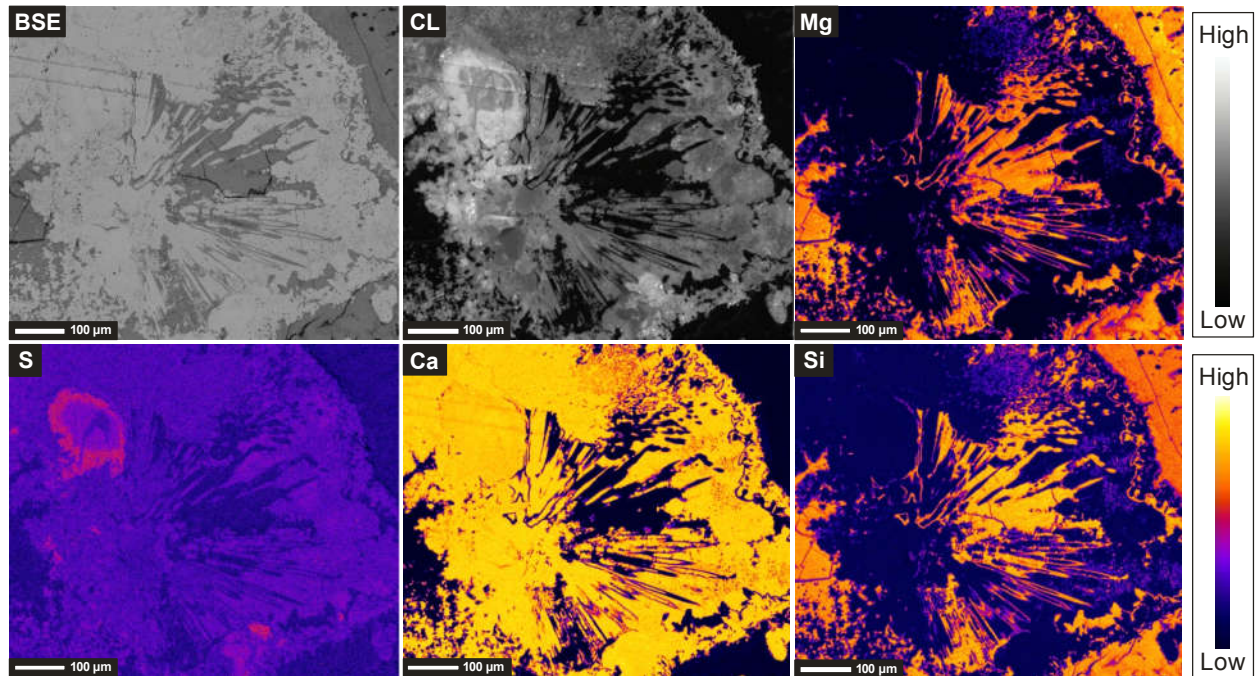
Figure A.3. BSE-WDS-EDS-CL element maps showing acicular calcite with mantled by Mg-rich silicate, hosted in calcite groundmass, expanded from Chapter 2 Figure 2.2G. Note also the sulfur-rich zone top left, upon closer inspection this is a vesicular zone within calcite with abundant sulfate amygdule; or inclusions.
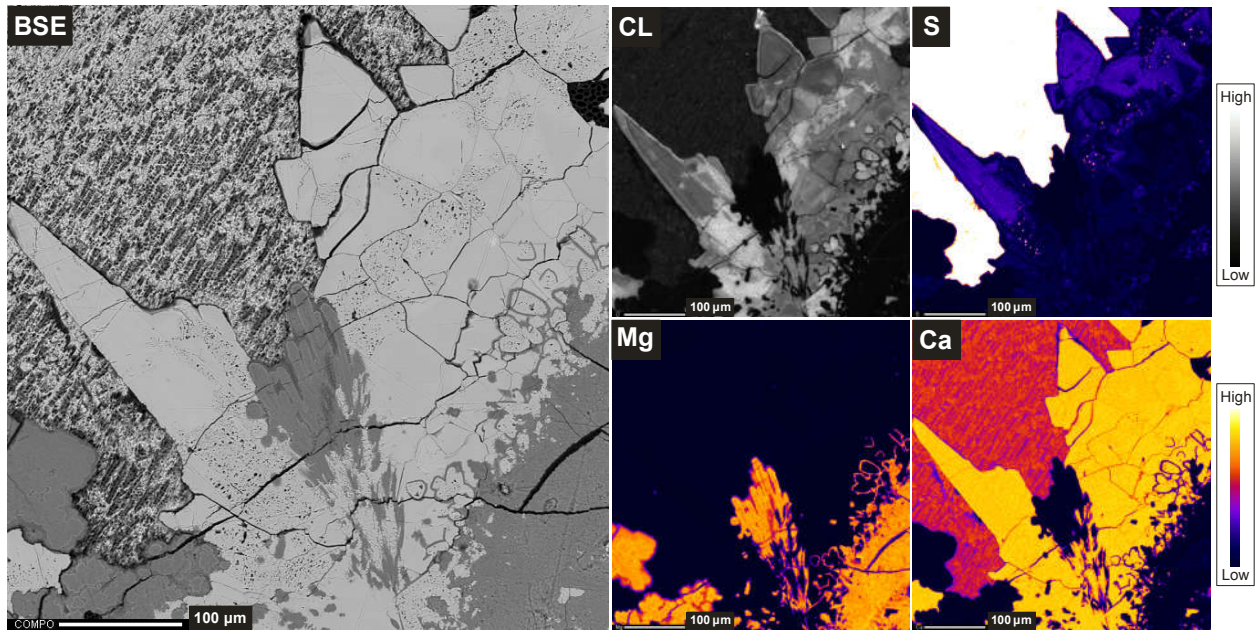
Figure A.4. Expanded from Chapter Figure 2.1K. BSE context image and WDS-EDS-CL element maps showing calcite growth on a silicate clast (lower right corner), including overgrowths of sulfur-poor calcite, vesicular calcite, sulfur-rich calcite and radial silicate hosted in anhydrite groundmass. The white region in the upper left of the sulfur map represents the anhydrite. Note the sharp contact between anhydrite, calcite and silicate.
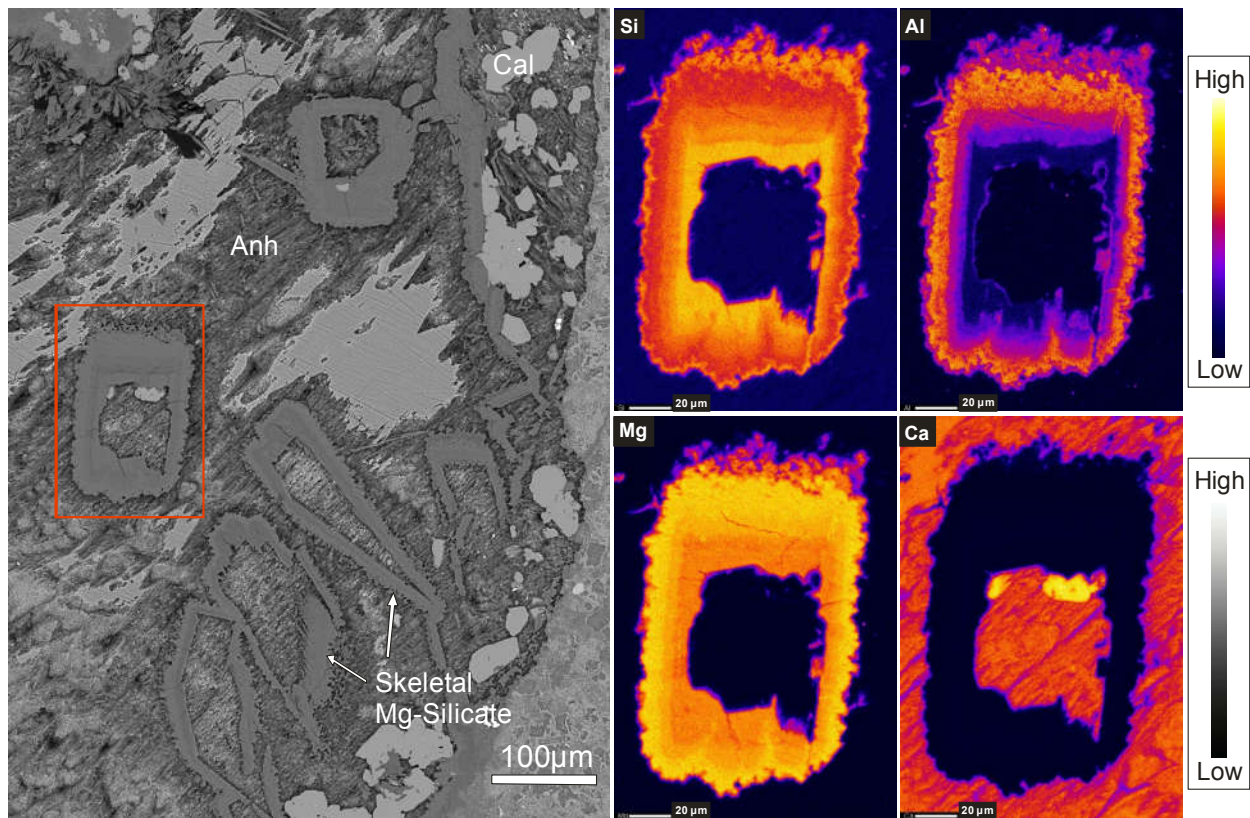
Figure A.5. BSE context image and WDS-EDS element maps showing detailed zoning of skeletal Si-Mg silicate grain hosted in anhydrite (bassanite) and gypsum groundmass. Note that the Al is progressively enriched from the centre towards the edge but decreases at the edge. Expanded from the Chapter 2 Figure 2.2L.
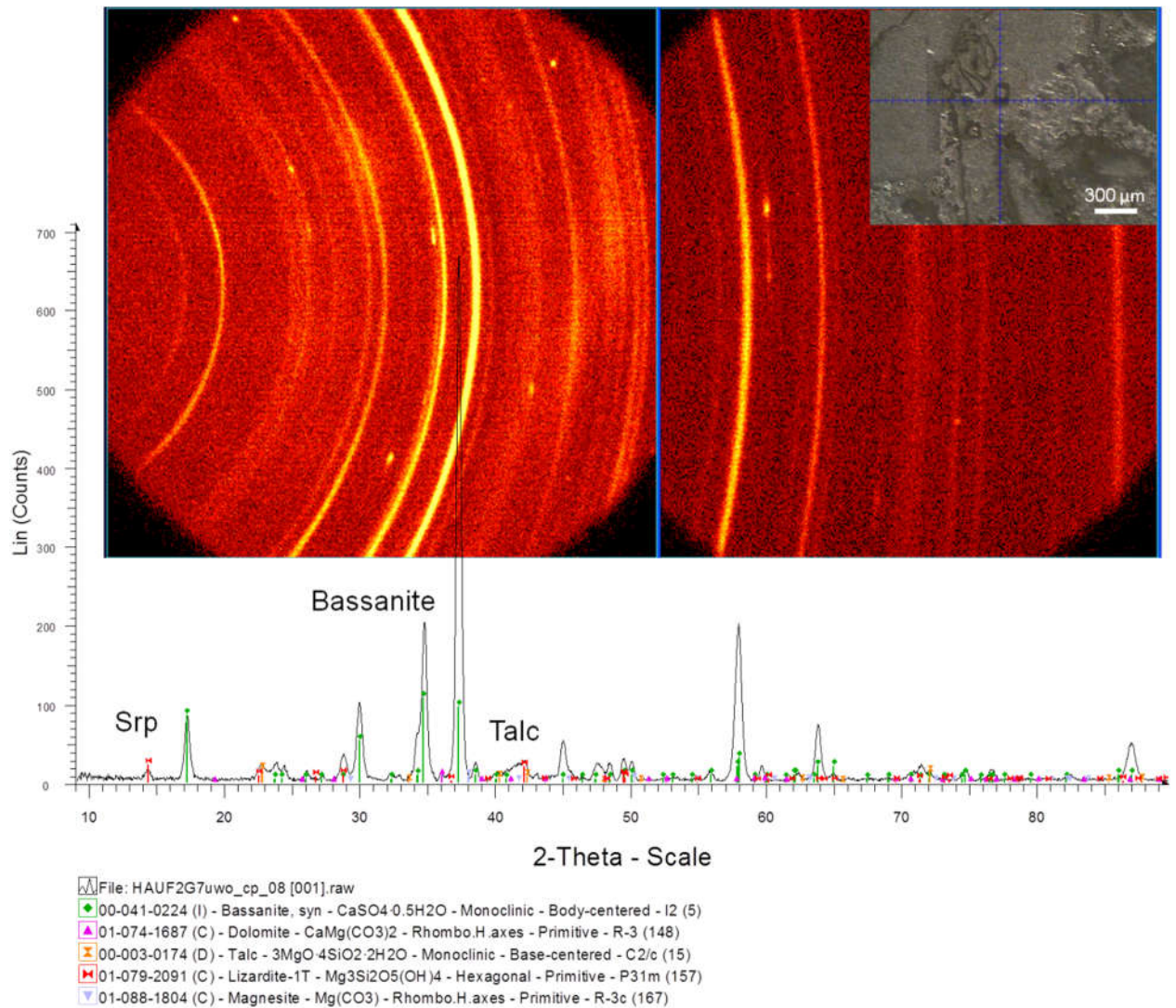
Figure A.6. Micro-X-ray Diffraction pattern and GADDS frames associated with a spot analysis centered on the HAUF2G7uwo skeletal grain from Figure 2.2L. Major phases include bassanite, talc and serpentine (Srp). The analysis spot size is 300 μm, so the silicate grain and surrounding sulfate groundmass are represented as well. The dolomite peaks are questionable and are likely to be a small clast as it was not observed petrographically.

180

Table A-1. Geochemistry and stoichiometry of skeletal silicates.												
	Line 1							Line 2				
Spot #	1	2	3	4	5	6	7	8	9	10	11	12
SiO$_2$	55.33	56.44	56.47	52.44	40.14	49.26	58.41	55.31	53.27	49.82	41.24	36.89
Al$_2$O$_3$	1.22	0.95	0.93	3.56	9.44	6.00	1.00	1.21	3.67	6.89	9.47	10.26
TiO$_2$	0.05	0.05	0.05	0.05	0.02	0.05	0.06	0.04	0.07	0.04	0.01	0.02
FeO*	0.17	0.17	0.16	0.51	0.29	0.52	0.16	0.18	0.57	0.56	0.47	0.23
MnO	0.03	0.02	0.01	0.02	0.01	0.01	BDL	BDL	BDL	BDL	BDL	BDL
MgO	23.72	28.17	27.85	22.39	34.63	24.34	26.88	25.70	17.08	26.10	35.61	36.57
CaO	0.50	0.45	0.54	1.07	0.60	1.16	0.58	0.56	1.27	1.13	0.74	0.39
Na$_2$O	0.06	0.06	0.08	0.07	0.03	0.07	0.08	0.12	0.12	0.10	0.04	0.02
K$_2$O	0.19	0.18	0.19	0.13	0.03	0.12	0.19	0.21	0.26	0.14	0.04	0.02
F	0.02	0.10	0.09	0.09	0.02	0.04	0.09	0.11	0.07	0.20	0.10	0.09
P$_2$O$_5$	0.11	0.01	0.05	0.40	0.32	0.92	0.02	0.07	1.34	1.07	0.48	0.15
Cl	0.04	0.04	0.03	0.05	0.04	0.06	0.04	0.05	0.06	0.05	0.06	0.03
SO$_3$	0.11	0.09	0.07	0.16	0.18	0.19	0.10	0.11	0.13	0.16	0.15	0.12
Cr$_2$O$_3$	0.01	BDL	0.01	BDL	BDL	0.00	BDL	BDL	BDL	BDL	BDL	BDL
Total	81.55	86.71	86.51	80.93	85.72	82.74	87.55	83.58	77.82	86.21	88.37	84.69
H20**	18.45	13.29	13.49	19.07	14.28	17.26	12.45	16.43	22.18	13.79	11.63	15.32
Number of ions on the basis of 7 oxygens												
Si	2.59	2.51	2.52	2.50	1.88	2.33	2.56	2.54	2.64	2.28	1.88	1.75
Al	0.07	0.05	0.05	0.20	0.52	0.34	0.05	0.07	0.21	0.37	0.51	0.58
Ti	0.00	0.00	0.00	0.00	0.00	0.00	0.00	0.00	0.00	0.00	0.00	0.00
Fe	0.01	0.01	0.01	0.02	0.01	0.02	0.01	0.01	0.02	0.02	0.02	0.01
Mn	0.00	0.00	0.00	0.00	0.00	0.00	0.00	0.00	0.00	0.00	0.00	0.00
Mg	1.66	1.87	1.85	1.59	2.41	1.72	1.76	1.76	1.26	1.78	2.41	2.59
Ca	0.02	0.02	0.03	0.05	0.03	0.06	0.03	0.03	0.07	0.06	0.04	0.02
Na	0.01	0.01	0.01	0.01	0.00	0.01	0.01	0.01	0.01	0.01	0.00	0.00
K	0.01	0.01	0.01	0.01	0.00	0.01	0.01	0.01	0.02	0.01	0.00	0.00
F	0.00	0.01	0.01	0.01	0.00	0.01	0.01	0.02	0.01	0.03	0.01	0.01
P	0.00	0.00	0.00	0.02	0.01	0.04	0.00	0.00	0.06	0.04	0.02	0.01
Cl	0.00	0.00	0.00	0.00	0.00	0.00	0.00	0.00	0.00	0.00	0.00	0.00
S	0.01	0.01	0.01	0.01	0.01	0.02	0.01	0.01	0.01	0.01	0.01	0.01
Cr	0.00	0.00	0.00	0.00	0.00	0.00	0.00	0.00	0.00	0.00	0.00	0.00
T site (Si+Al)	2.66	2.56	2.56	2.70	2.40	2.67	2.61	2.61	2.85	2.65	2.38	2.33
M site	1.69	1.89	1.88	1.67	2.45	1.80	1.79	1.80	1.35	1.86	2.47	2.62
Number of ions on the basis of 11 oxygens												
Si	4.08	3.94	3.95	3.93	2.95	3.67	4.02	4.00	4.15	3.58	2.95	2.76
Al	0.11	0.08	0.08	0.31	0.82	0.53	0.08	0.10	0.34	0.58	0.80	0.90
Ti	0.00	0.00	0.00	0.00	0.00	0.00	0.00	0.00	0.00	0.00	0.00	0.00
Fe	0.01	0.01	0.01	0.03	0.02	0.03	0.01	0.01	0.04	0.03	0.03	0.01
Mn	0.00	0.00	0.00	0.00	0.00	0.00	0.00	0.00	0.00	0.00	0.00	0.00
Mg	2.61	2.93	2.91	2.50	3.79	2.70	2.76	2.77	1.98	2.79	3.79	4.07
Ca	0.04	0.03	0.04	0.09	0.05	0.09	0.04	0.04	0.11	0.09	0.06	0.03
Na	0.01	0.01	0.01	0.01	0.00	0.01	0.01	0.02	0.02	0.01	0.01	0.00
K	0.02	0.02	0.02	0.01	0.00	0.01	0.02	0.02	0.03	0.01	0.00	0.00
F	0.00	0.02	0.02	0.02	0.00	0.01	0.02	0.02	0.02	0.04	0.02	0.02
P	0.01	0.00	0.00	0.03	0.02	0.06	0.00	0.00	0.09	0.07	0.03	0.01
Cl	0.00	0.00	0.00	0.00	0.00	0.00	0.00	0.00	0.00	0.00	0.00	0.00
S	0.01	0.01	0.01	0.02	0.02	0.02	0.01	0.01	0.02	0.02	0.02	0.02
Cr	0.00	0.00	0.00	0.00	0.00	0.00	0.00	0.00	0.00	0.00	0.00	0.00
T site (Si+Al)	4.18	4.02	4.03	4.25	3.77	4.19	4.10	4.10	4.48	4.16	3.75	3.66
M site	2.66	2.98	2.96	2.62	3.86	2.83	2.81	2.82	2.13	2.92	3.88	4.12

Note. Oxides are in wt%. Each 'Line' represents a series of spot analysis from core to rim of the skeletal grain. BDL = below detection limit. *All Fe is shown as FeO. ** H$_2$O is estimated by difference

Table A-1. Geochemistry and stoichiometry of skeletal silicates, continued.

		Line 3							Line 4					
Spot #	13	14	15	16	19	17	18	20	21	22	23	24	25	26
SiO_2	55.29	54.93	51.45	47.52	42.05	37.73	35.27	44.80	52.92	47.19	47.76	36.72	54.40	55.28
Al_2O_3	0.83	0.89	3.24	5.16	8.92	10.64	11.02	4.43	1.36	3.72	3.73	9.68	1.49	1.89
TiO_2	0.04	0.03	0.07	0.03	0.01	0.02	0.01	0.03	0.06	0.04	0.03	0.02	0.03	0.04
FeO*	0.13	0.14	0.51	0.62	0.57	0.24	0.13	0.42	0.20	0.48	0.45	0.28	0.17	0.16
MnO	BDL	BDL	0.02	BDL	BDL	BDL	BDL	BDL	BDL	BDL	BDL	BDL	BDL	BDL
MgO	28.04	26.27	19.54	19.62	34.83	37.35	37.58	29.74	28.49	29.79	30.03	35.44	32.09	32.75
CaO	0.52	0.56	0.68	1.12	0.74	0.40	0.31	0.76	0.71	0.82	0.83	0.50	0.47	0.55
Na_2O	0.15	0.09	0.10	0.08	0.04	0.01	0.02	0.13	0.15	0.10	0.08	0.02	0.10	0.19
K_2O	0.19	0.19	0.20	0.15	0.04	0.02	0.01	0.10	0.11	0.09	0.09	0.01	0.11	0.14
F	0.14	0.09	0.06	0.11	0.12	0.14	0.03	0.13	0.23	0.05	0.13	0.03	0.22	0.22
P_2O_5	0.00	0.01	0.30	0.96	0.38	0.14	0.08	0.13	0.02	0.04	0.03	0.03	0.03	0.01
Cl	0.04	0.06	0.09	0.04	0.06	0.03	0.02	0.02	0.01	0.02	0.01	0.02	0.02	0.03
SO_3	0.12	0.09	0.14	0.12	0.12	0.11	0.09	0.15	0.08	0.09	0.08	0.12	0.10	0.19
Cr_2O_3	BDL	BDL	BDL	BDL	0.02	BDL	BDL	BDL	BDL	BDL	BDL	BDL	BDL	BDL
Total	**85.32**	**83.29**	**76.37**	**75.52**	**87.88**	**86.78**	**84.57**	**80.83**	**84.22**	**82.26**	**83.01**	**82.46**	**88.84**	**91.01**
H20**	14.68	16.71	23.63	24.48	12.12	13.22	15.43	19.17	15.78	17.74	16.99	17.54	11.16	8.99
					Number of ions on the basis of 7 oxygens									
Si	2.50	2.53	2.53	2.45	1.92	1.75	1.68	2.19	2.44	2.25	2.25	1.78	2.38	2.36
Al	0.04	0.05	0.05	0.31	0.48	0.58	0.62	0.25	0.07	0.21	0.21	0.55	0.08	0.10
Ti	0.00	0.00	0.00	0.00	0.00	0.00	0.00	0.00	0.00	0.00	0.00	0.00	0.00	0.00
Fe	0.00	0.01	0.01	0.03	0.02	0.01	0.01	0.02	0.01	0.02	0.02	0.01	0.01	0.01
Mn	0.00	0.00	0.00	0.00	0.00	0.00	0.00	0.00	0.00	0.00	0.00	0.00	0.00	0.00
Mg	1.89	1.81	1.81	1.51	2.37	2.59	2.67	2.17	1.96	2.12	2.11	2.56	2.09	2.09
Ca	0.03	0.03	0.03	0.06	0.04	0.02	0.02	0.04	0.04	0.04	0.04	0.03	0.02	0.03
Na	0.01	0.01	0.01	0.01	0.00	0.00	0.00	0.01	0.01	0.01	0.01	0.00	0.01	0.02
K	0.01	0.01	0.01	0.01	0.00	0.00	0.00	0.01	0.01	0.01	0.01	0.00	0.01	0.01
F	0.02	0.01	0.01	0.02	0.02	0.02	0.00	0.02	0.03	0.01	0.02	0.00	0.03	0.03
P	0.00	0.00	0.00	0.04	0.01	0.01	0.00	0.01	0.00	0.00	0.00	0.00	0.00	0.00
Cl	0.00	0.00	0.00	0.00	0.00	0.00	0.00	0.00	0.00	0.00	0.00	0.00	0.00	0.00
S	0.01	0.01	0.01	0.01	0.01	0.01	0.01	0.01	0.01	0.01	0.01	0.01	0.01	0.01
Cr	0.00	0.00	0.00	0.00	0.00	0.00	0.00	0.00	0.00	0.00	0.00	0.00	0.00	0.00
T site (Si+Al)	2.54	2.58	2.58	2.76	2.40	2.33	2.30	2.44	2.51	2.46	2.46	2.34	2.45	2.46
M site	1.92	1.84	1.84	1.60	2.43	2.61	2.70	2.22	2.00	2.18	2.17	2.60	2.12	2.12
					Number of ions on the basis of 11 oxygens									
Si	3.93	3.98	3.98	3.85	3.01	2.75	2.65	3.44	3.83	3.53	3.54	2.80	3.74	3.71
Al	0.07	0.08	0.08	0.49	0.75	0.92	0.97	0.40	0.12	0.33	0.33	0.87	0.12	0.15
Ti	0.00	0.00	0.00	0.00	0.00	0.00	0.00	0.00	0.00	0.00	0.00	0.00	0.00	0.00
Fe	0.01	0.01	0.01	0.04	0.03	0.01	0.01	0.03	0.01	0.03	0.03	0.02	0.01	0.01
Mn	0.00	0.00	0.00	0.00	0.00	0.00	0.00	0.00	0.00	0.00	0.00	0.00	0.00	0.00
Mg	2.97	2.84	2.84	2.37	3.72	4.06	4.20	3.40	3.07	3.32	3.32	4.03	3.29	3.28
Ca	0.04	0.04	0.04	0.10	0.06	0.03	0.02	0.06	0.06	0.07	0.07	0.04	0.03	0.04
Na	0.02	0.01	0.01	0.01	0.01	0.00	0.00	0.02	0.02	0.01	0.01	0.00	0.01	0.02
K	0.02	0.02	0.02	0.02	0.00	0.00	0.00	0.01	0.01	0.01	0.01	0.00	0.01	0.01
F	0.03	0.02	0.02	0.03	0.03	0.03	0.01	0.03	0.05	0.01	0.03	0.01	0.05	0.05
P	0.00	0.00	0.00	0.07	0.02	0.01	0.01	0.01	0.00	0.00	0.00	0.00	0.00	0.00
Cl	0.00	0.00	0.00	0.00	0.00	0.00	0.00	0.00	0.00	0.00	0.00	0.00	0.00	0.00
S	0.01	0.01	0.01	0.02	0.01	0.01	0.01	0.02	0.01	0.01	0.01	0.02	0.01	0.02
Cr	0.00	0.00	0.00	0.00	0.00	0.00	0.00	0.00	0.00	0.00	0.00	0.00	0.00	0.00
T site (Si+Al)	4.00	4.06	4.06	4.34	3.77	3.67	3.62	3.84	3.95	3.86	3.87	3.67	3.86	3.86
M site	3.02	2.89	2.89	2.51	3.81	4.11	4.24	3.49	3.14	3.42	3.41	4.09	3.33	3.33

Note. Oxides are in wt%. Each 'Line' represents a series of spot analysis from core to rim of the skeletal grain. BDL = below detection limit. *All Fe is shown as FeO. ** H_2O is estimated by difference

References

Flemming, R.L., 2007. Micro X-ray diffraction (μXRD): a versatile technique for characterization of Earth and planetary materials. Can. J. Earth Sci. 44, 1333–1346. https://doi.org/10.1139/E07-020

Zylberman, W., Quesnel, Y., Rochette, P., Osinski, G.R., Marion, C., Gattacceca, J., 2017. Hydrothermally enhanced magnetization at the center of the Haughton impact structure? Meteorit. Planet. Sci. 52, 2147–2165. https://doi.org/10.1111/maps.12917

Appendix B   Micro X-ray Diffraction

MicroXRD was used to identify a variety of phases in two thin sections of the F2 core: HAUF2G7 and HAUF2G7uwo. Below are some representative results.
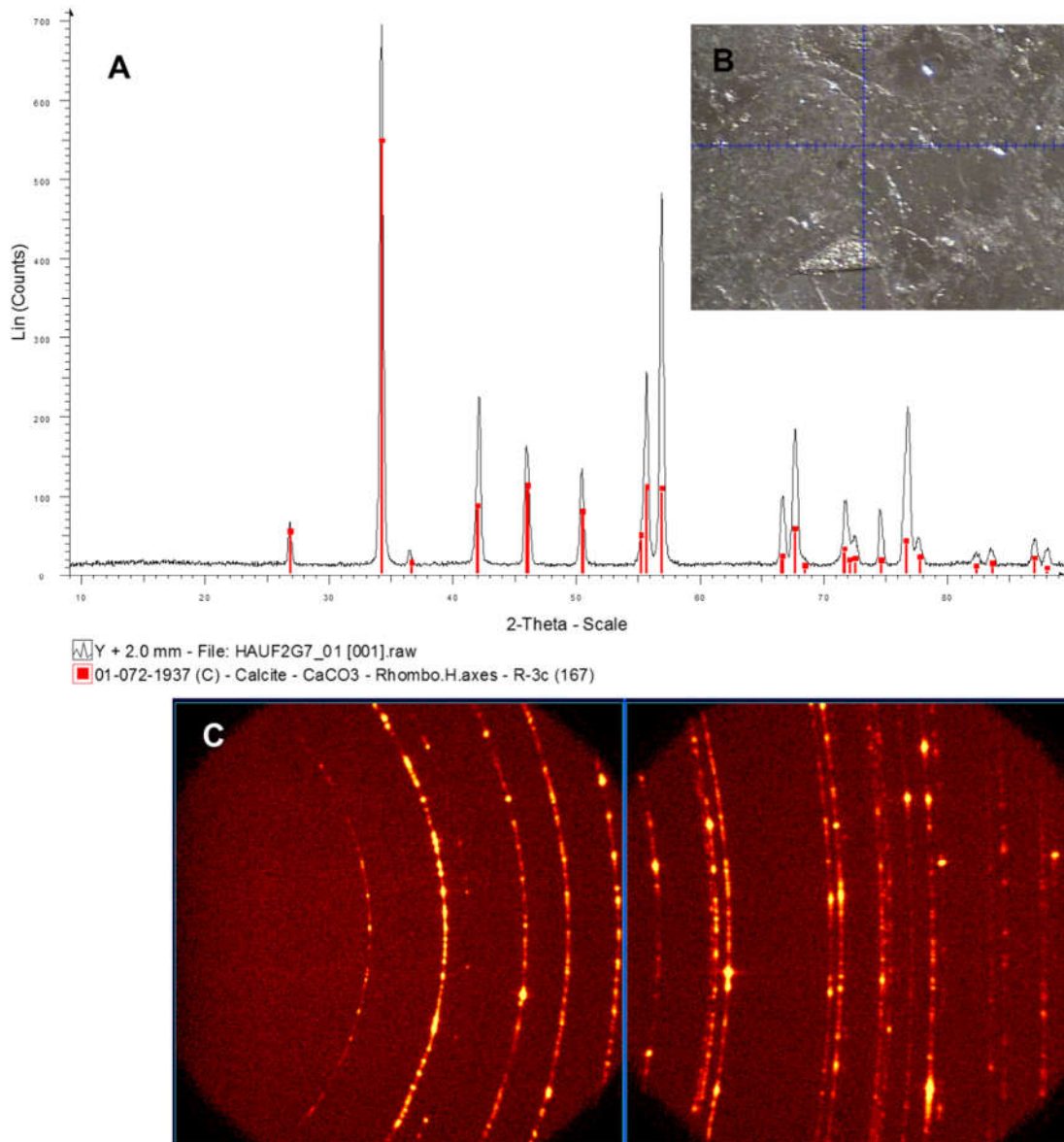
Figure B.1. A) Micro-X-ray diffractometer data for calcite clast with silicate mantle in sample HAUF2G7. Note no silicate was detected; B) Inset of spot identified in reflected light, each tick mark interval represents 50 µm; C) Associated GADDS images.
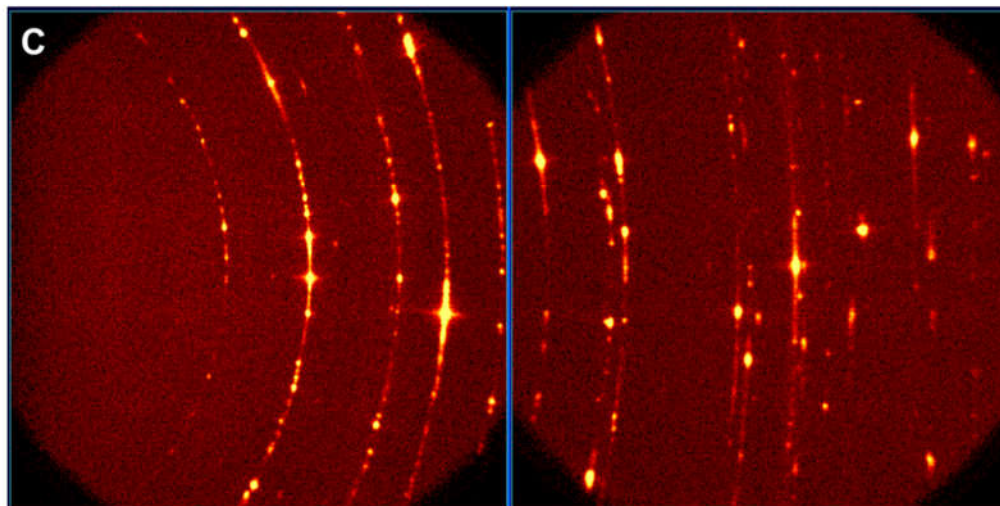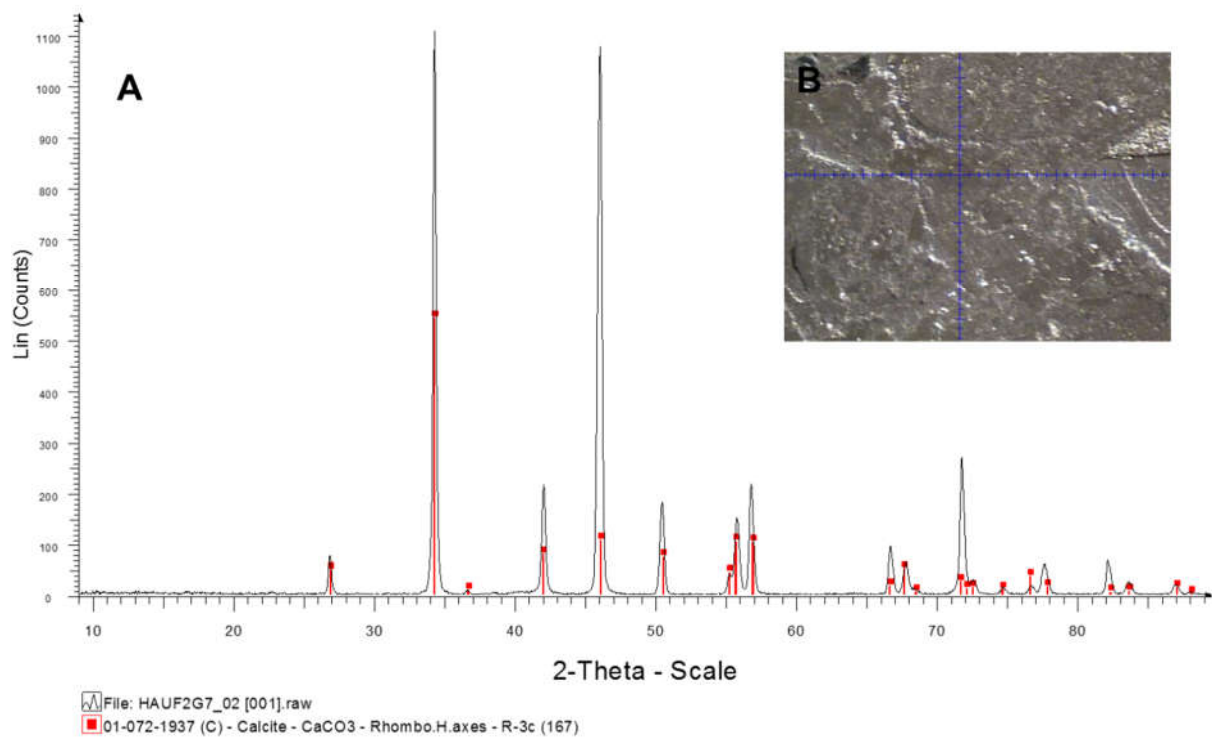
Figure B.2. A) Micro-X-ray diffractometer data for acicular silicate hosted in calcite in sample HAUF2G7. Note no silicate is detected; B) Inset of spot identified in reflected light, each tick mark interval represents 50 μm; C) Associated GADDS images.

185
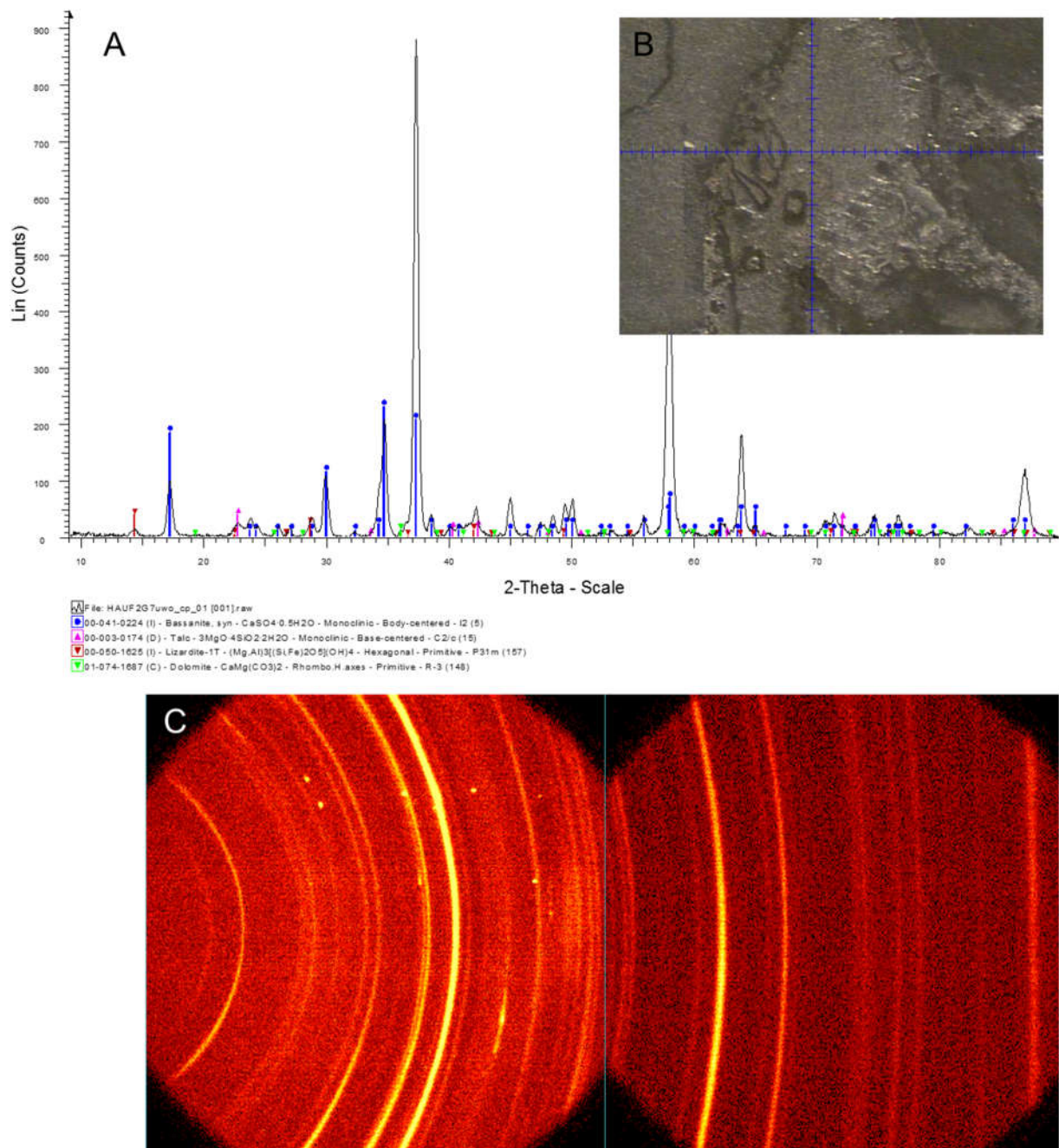
Figure B.3. A) Micro-X-ray diffractometer data for bassanite groundmass in sample HAUF2G7uwo. The bassanite dominates the pattern but adjacent skeletal silicates, serpentine and talc are also observed; B) Inset of spot identified in reflected light, each tick mark interval represents 50 μm; C) Associated GADDS images.

186
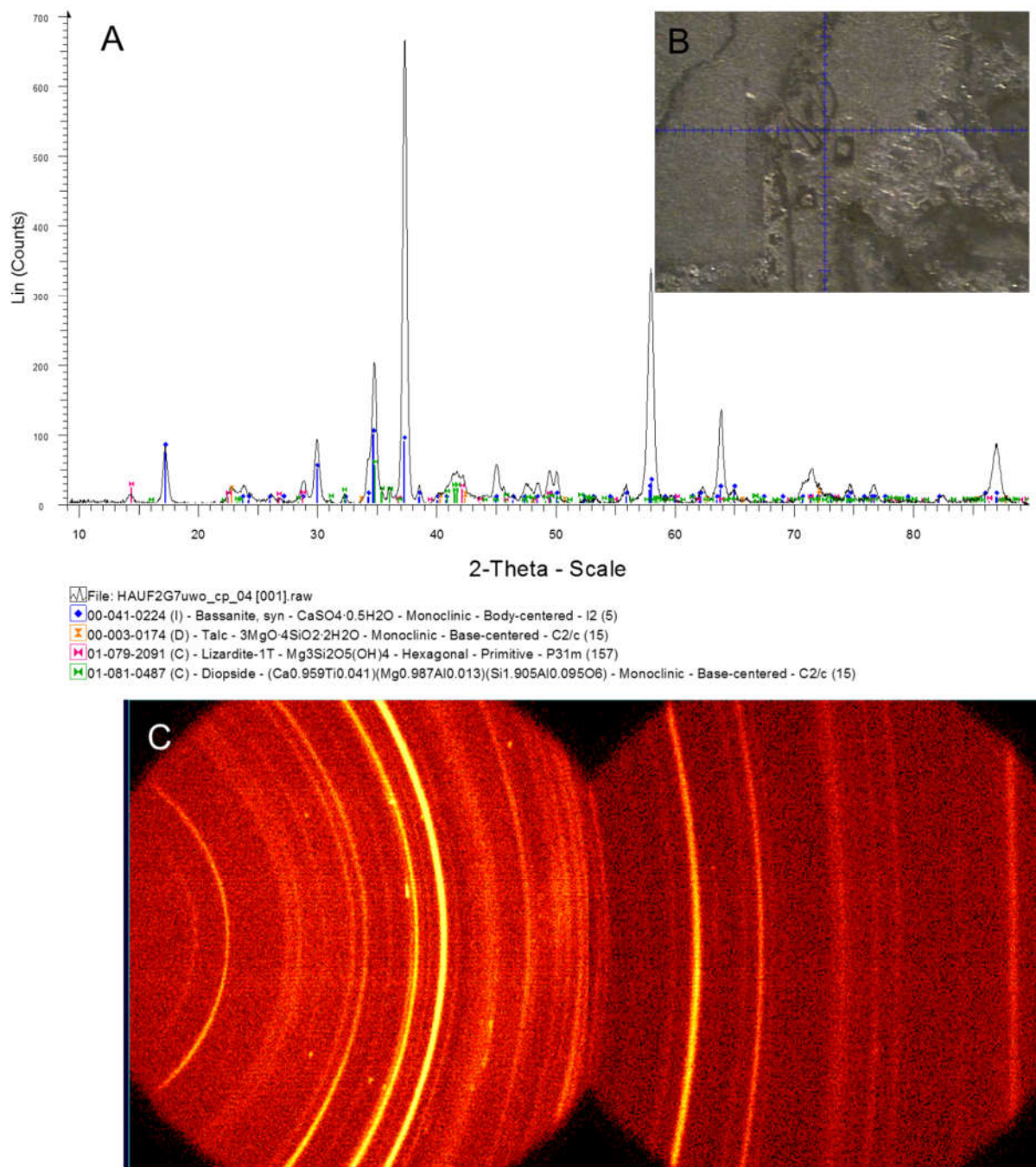
Figure B.4. A) Micro-X-ray diffractometer data for skeletal silicate hosted in bassanite groundmass in sample HAUF2G7uwo. The bassanite dominates the pattern, and silicates serpentine and talc are identified along with diopside. Note the large clast adjacent has been confirmed as diopside (Fig. B.5); B) Inset of spot identified in reflected light, each tick mark interval represents 50 μm; C) Associated GADDS images.
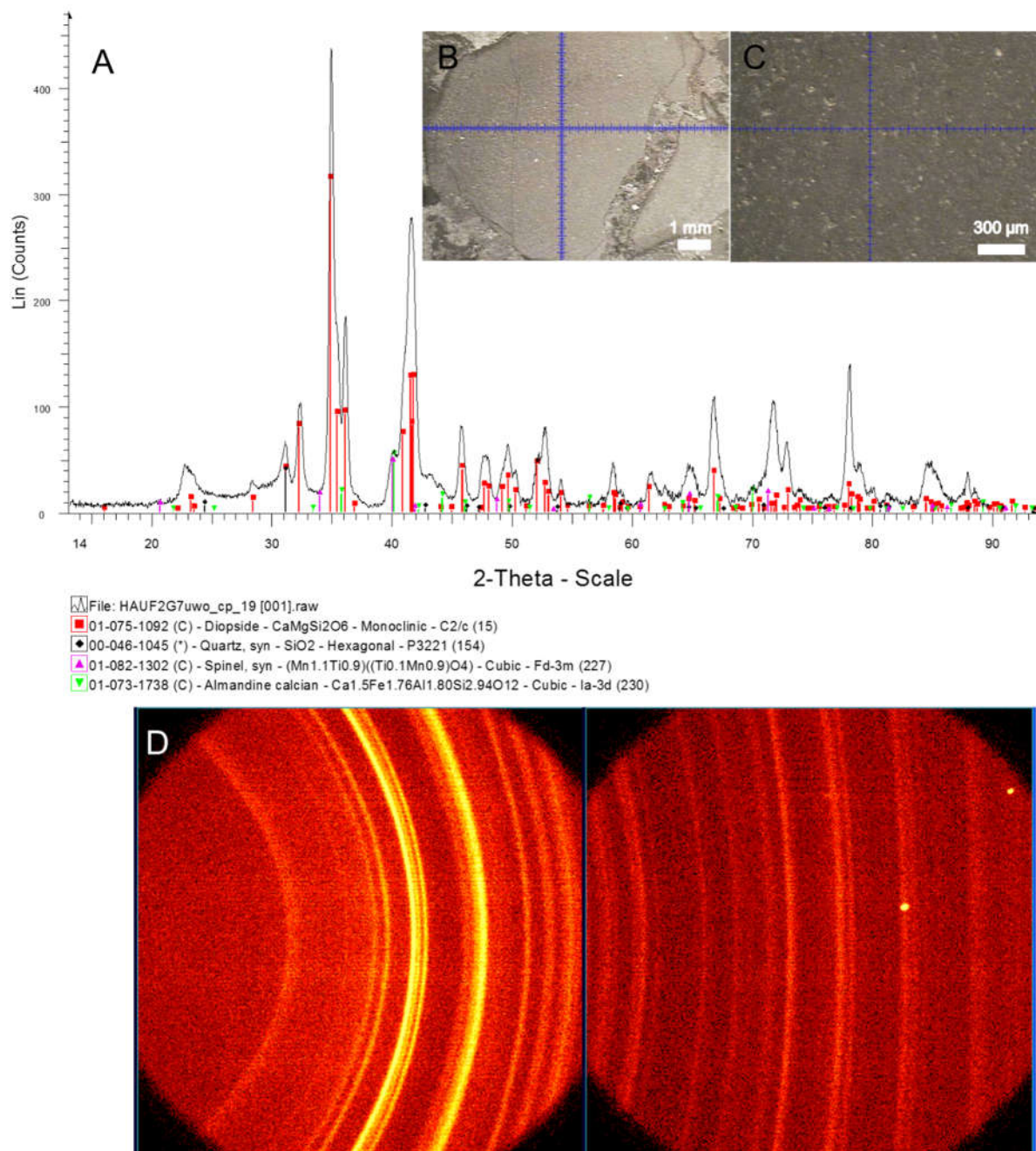
Figure B.5. A) Micro-X-ray diffractometer data for the centre of a large clast adjacent the skeletal silicates (Figs. D.3 and D.4) in HAUF2G7uwo. Diopside is the dominant pattern, accompanied by minor quartz. The matches to spinel and garnet are not reliable as the diopside peaks overprint everything; B) Inset of context image; C) Inset magnified context image in reflected light; D) Associated GADDS images.

Appendix C   Microprobe Data

Appendix C is available in the digital repository as an excel file. Tables provided as separate tabs include:

Table C-1. All silicates in Haughton's F2 and F3 cores; stoichiometry; molar values.

Table C-2. All carbonate WDS microprobe analyses.

Table C-3 Analyses of quartz in the Eleanor River Formation.

Table C-4. All sulfate WDS microprobe analyses.

Table C-5. All sulfide WDS microprobe analyses.

Appendix D   Reflectance Spectroscopy
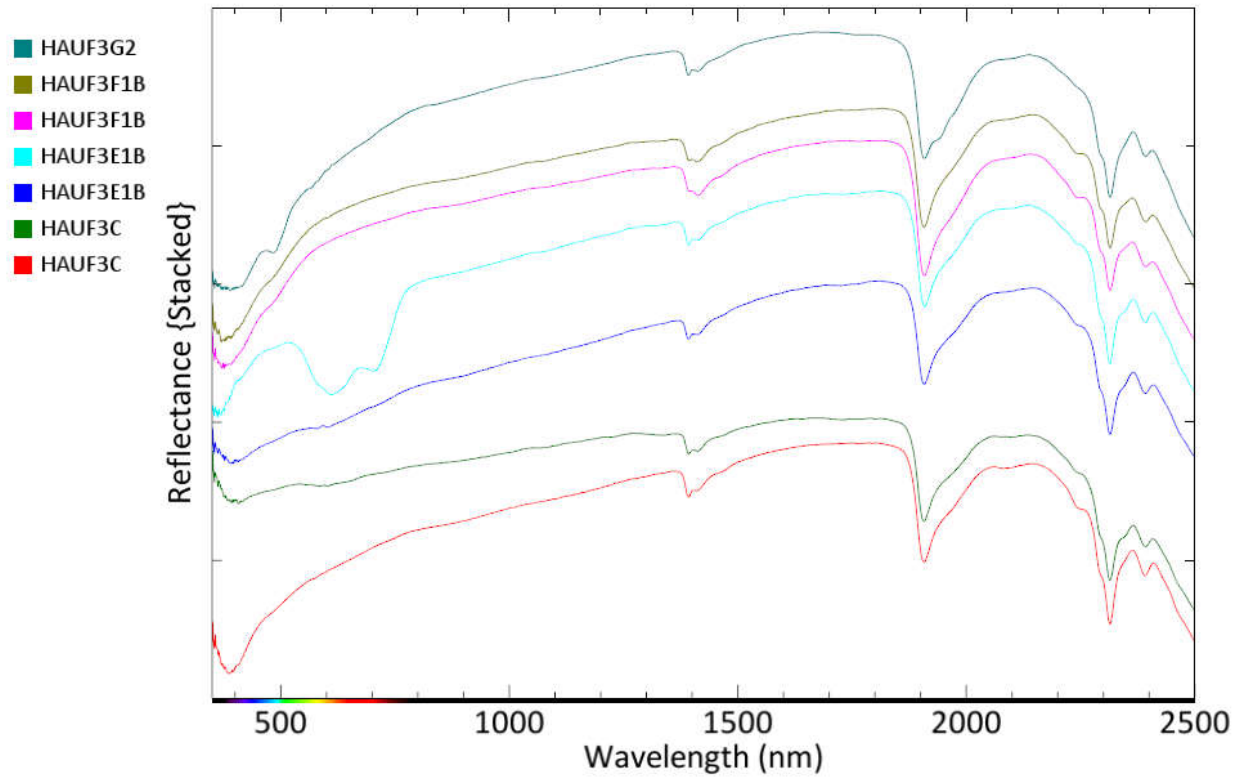
Figure D.1 Visible to near-infrared reflectance spectroscopy of the F3 core samples.
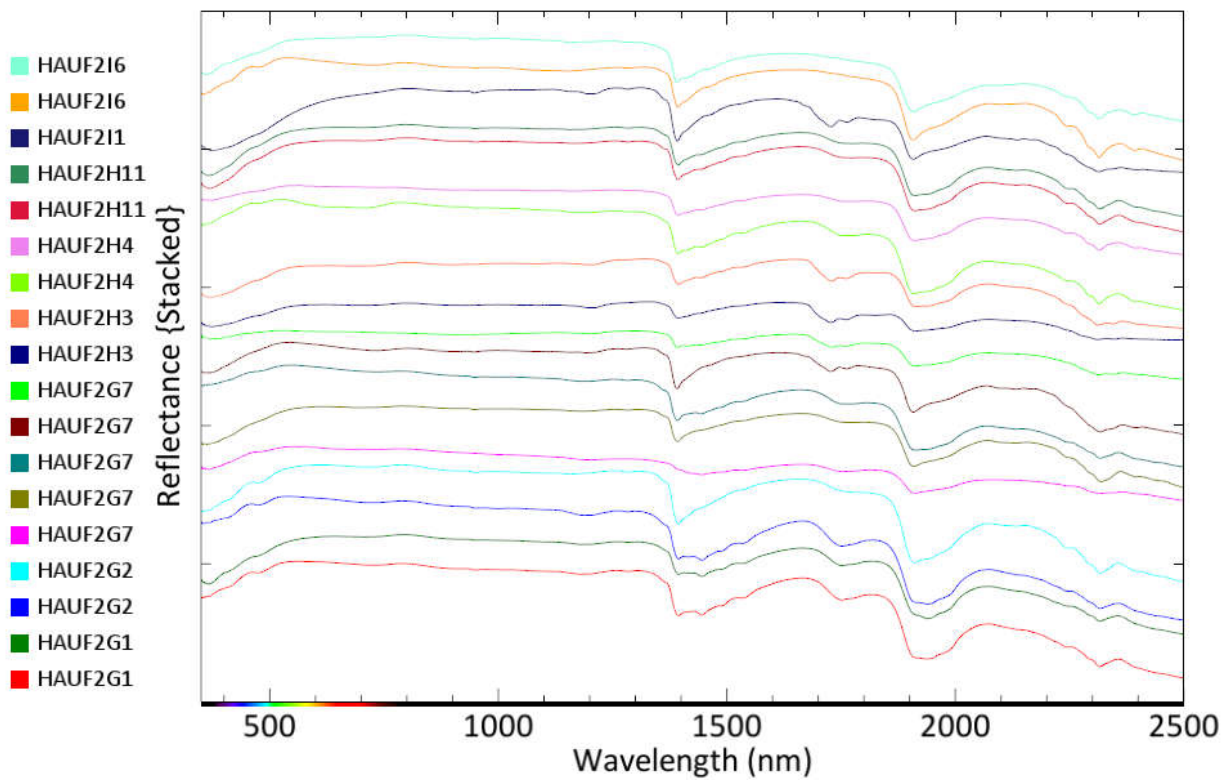
Figure D.2 Visible to near-infrared reflectance spectroscopy of the F2 core samples.

Appendix E   Chapter 3 Additional Figures
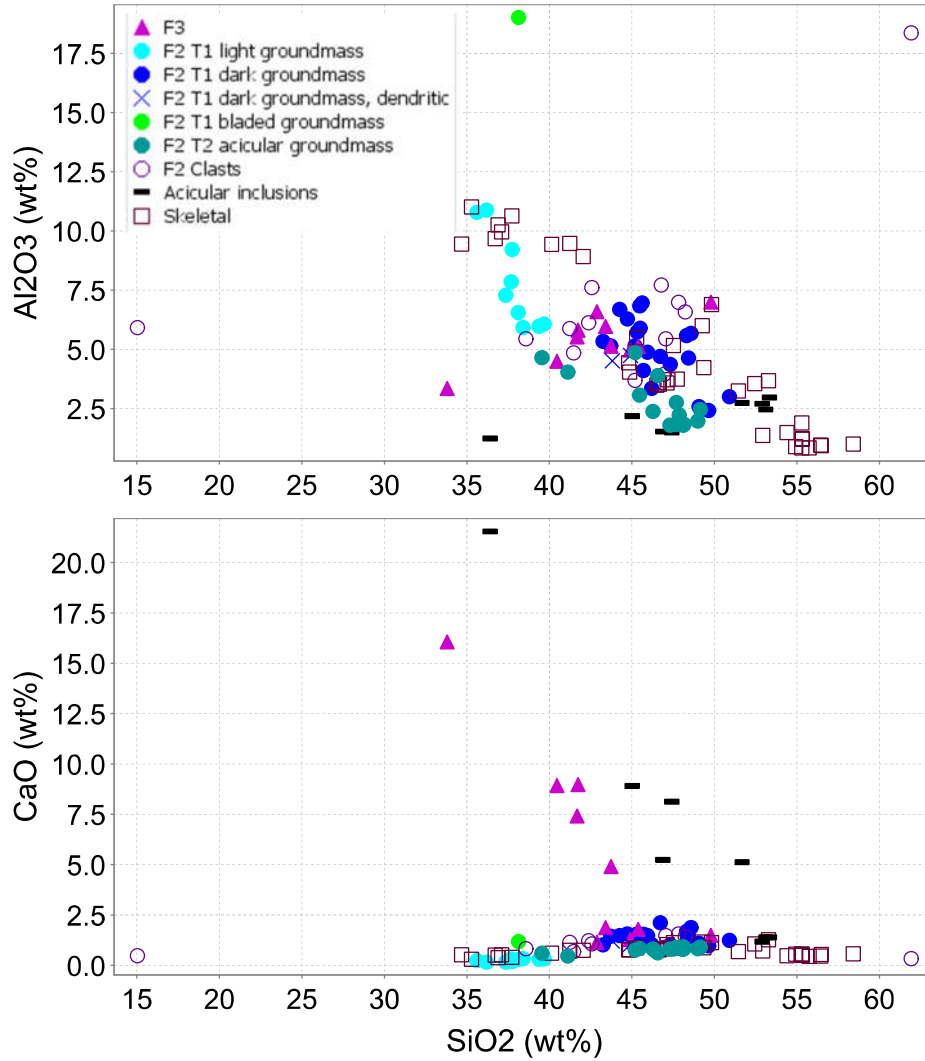
Figure E.1 Harker diagrams of Al₂O₃ as a function of SiO₂ for all the silicates in the F2 and F3 cores.
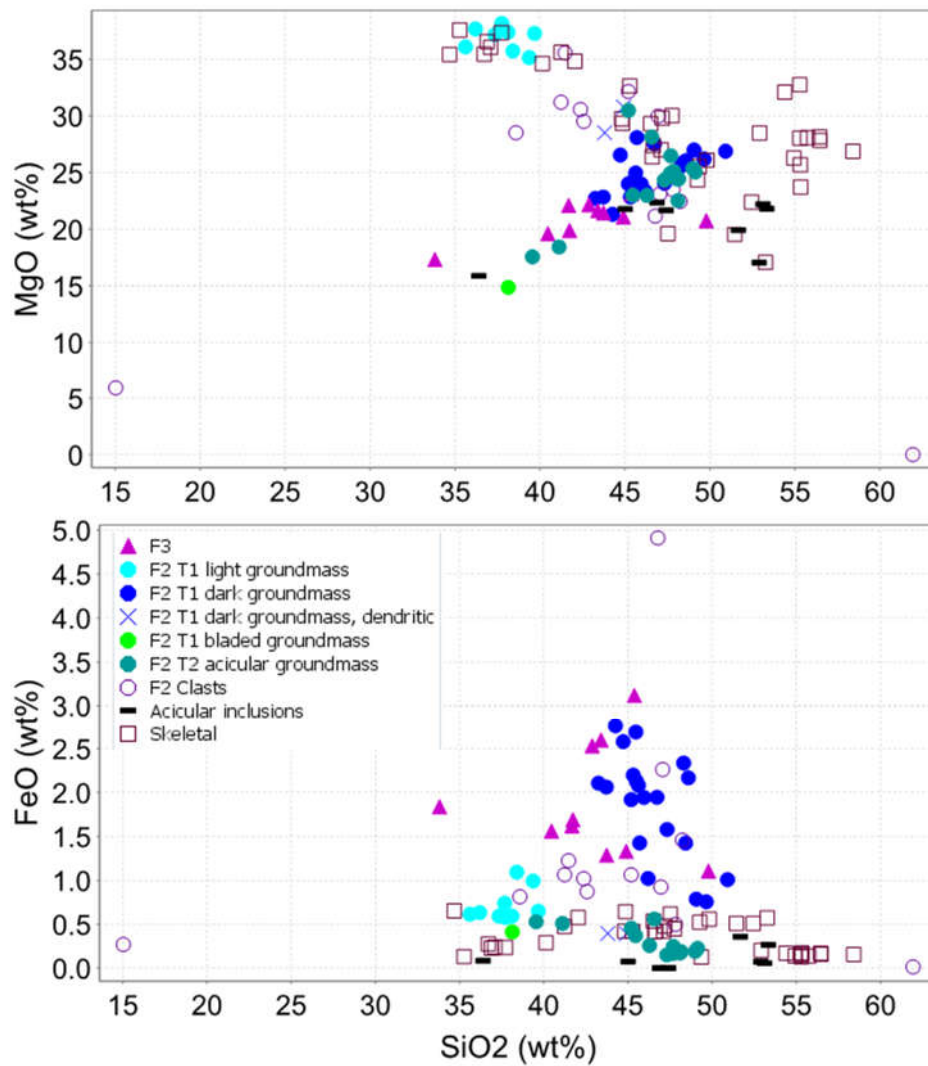
Figure E.2 Harker diagrams for MgO and FeO as a function of SiO₂ for all silicates in the F2 and F3 cores.

Appendix F   Additional Optical Cathodoluminescence Petrography

Optical Cathodoluminescence photomicrographs were collected using a Reliotron microscope stage-mounted CL instrument in the Department of Earth Sciences, Western University. The optical-CL is connected to a high-sensitivity CCD camera on the third ocular of the microscope and is operated through use of Act 1 software. The beam is focused on the sample by manual placement of two small magnets. Beam conditions were maintained at ~ 600 µA and ~15 kV. Exposure times range from 10 - 60 s (Chapter 4).

In the examples below, each region depicts an optical cathodoluminescence image (left) and a plane polarized light image (right). Annotations indicate WDS microprobe spots identified with green dots or yellow lines as well as probe map areas indicated by boxes.

HMP02-053 MAP 1
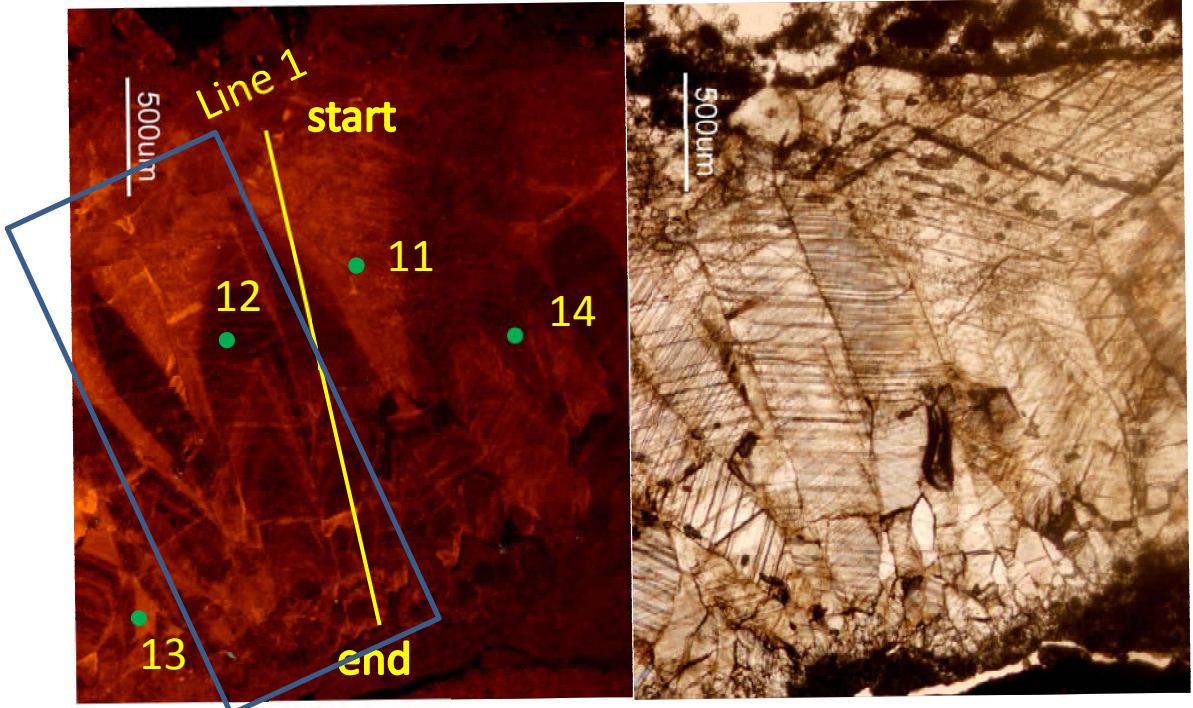
Probe area 1

HMP02-053 MAP 2
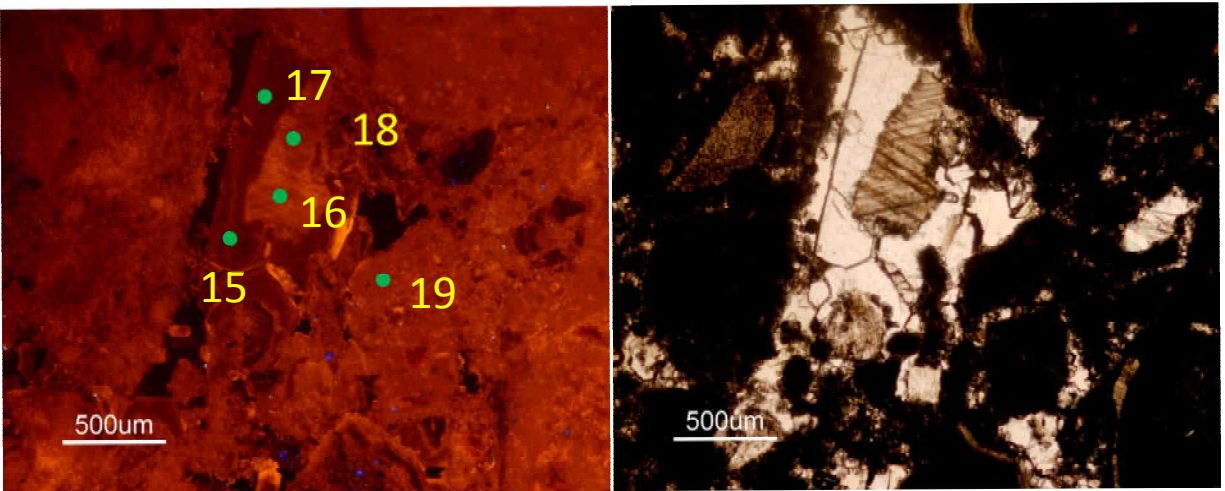
SA08-13 MAP 1
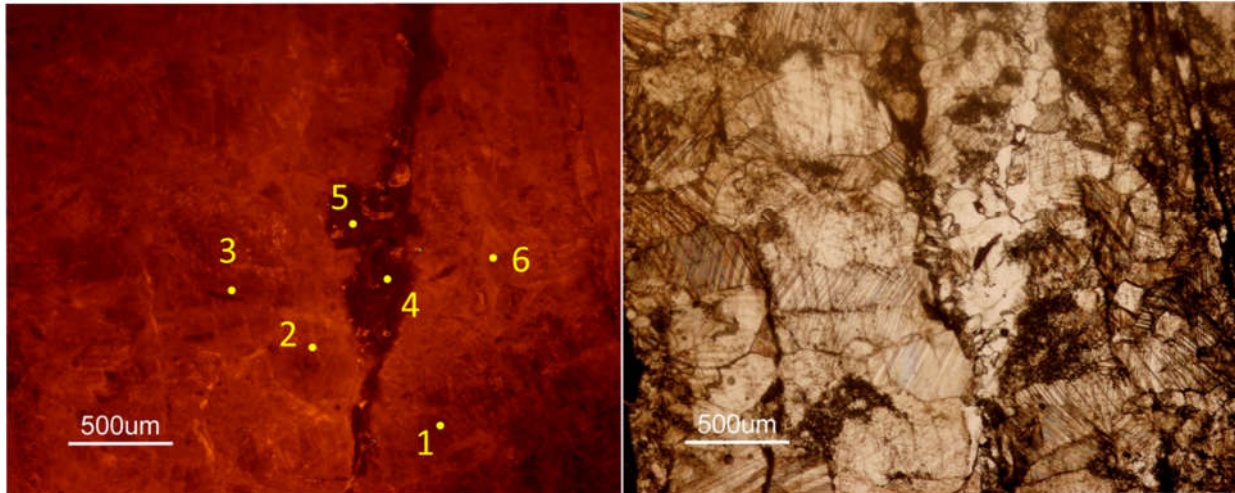
SA08-13 MAP 2
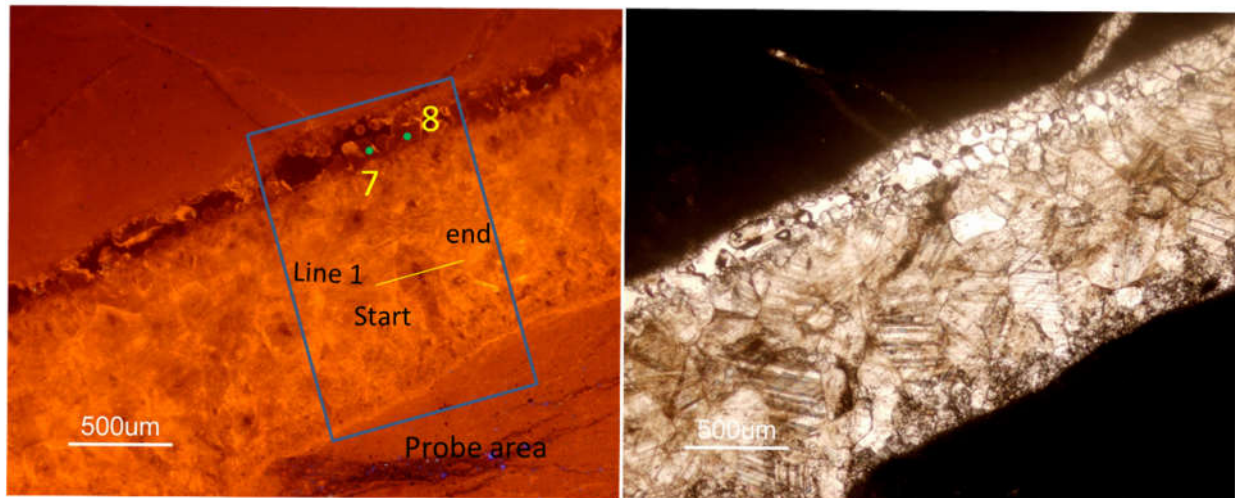
CMDI13-11 MAP 1
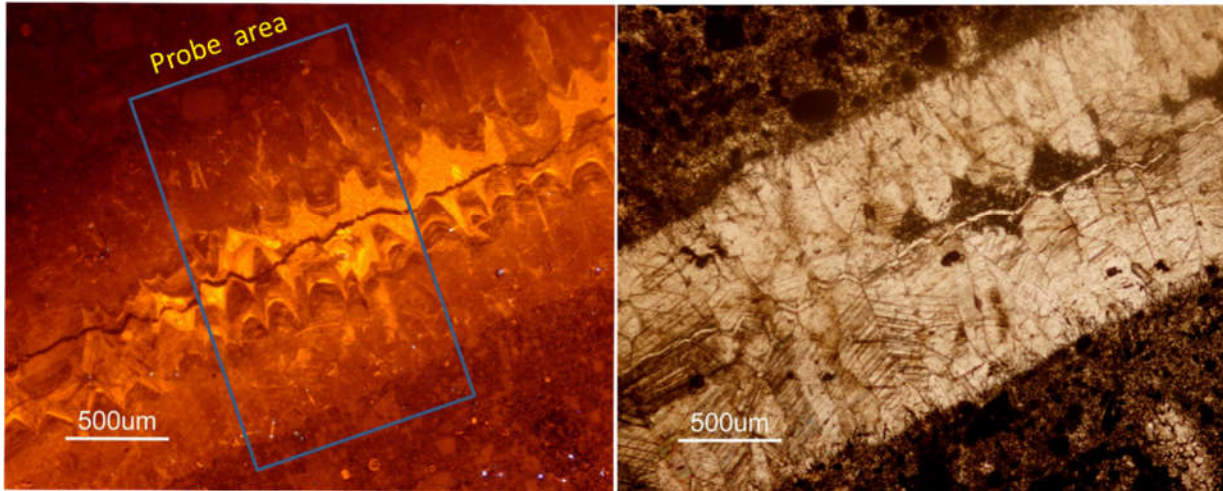
Note that additional detailed images and maps for CMDI13-11 are shown in Fig. 4.7.

CMDI13-11 MAP 2
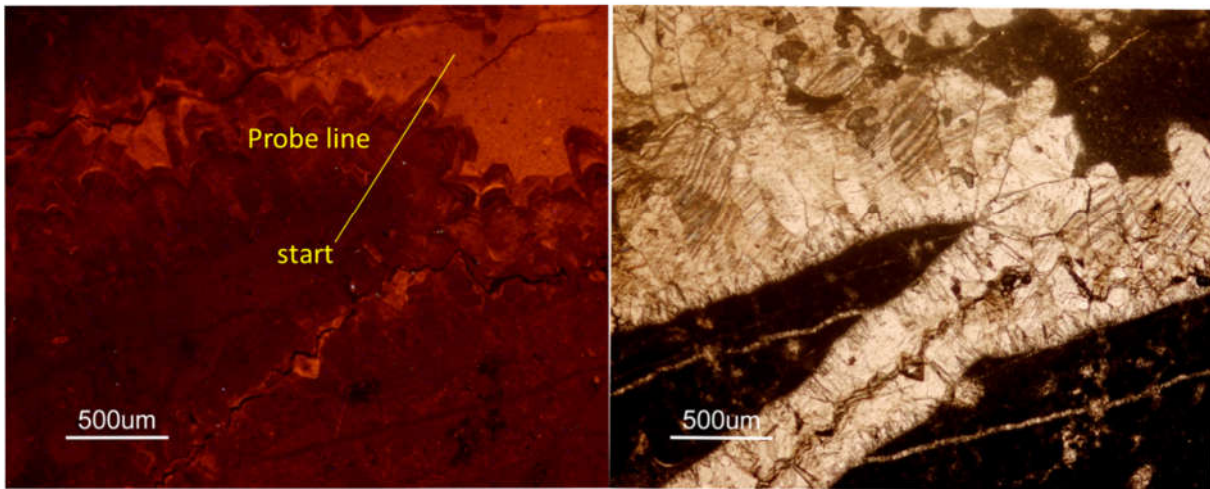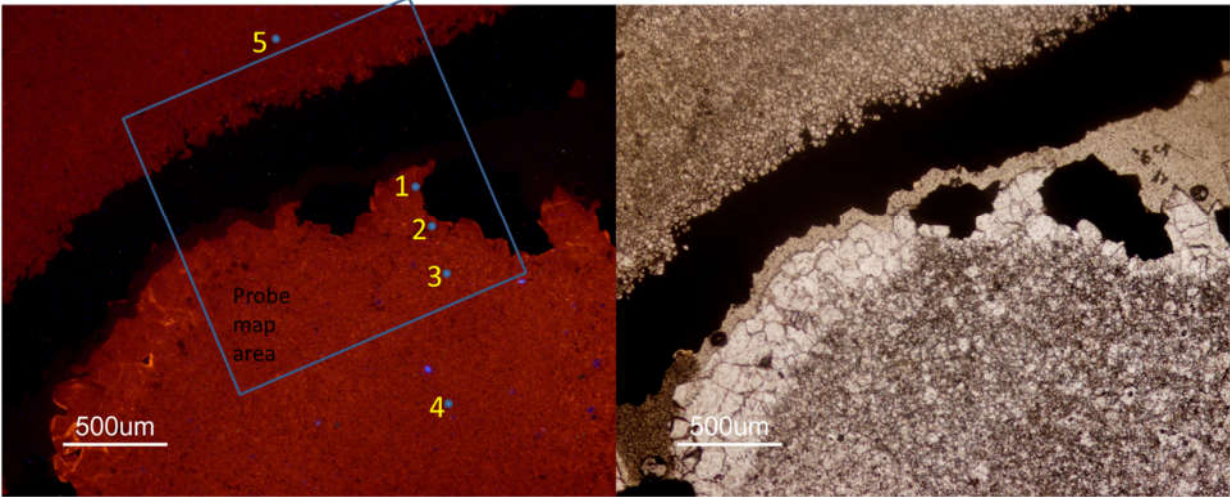
Context image for Fig. 4.12 (above).

HMP99-137 MAPS
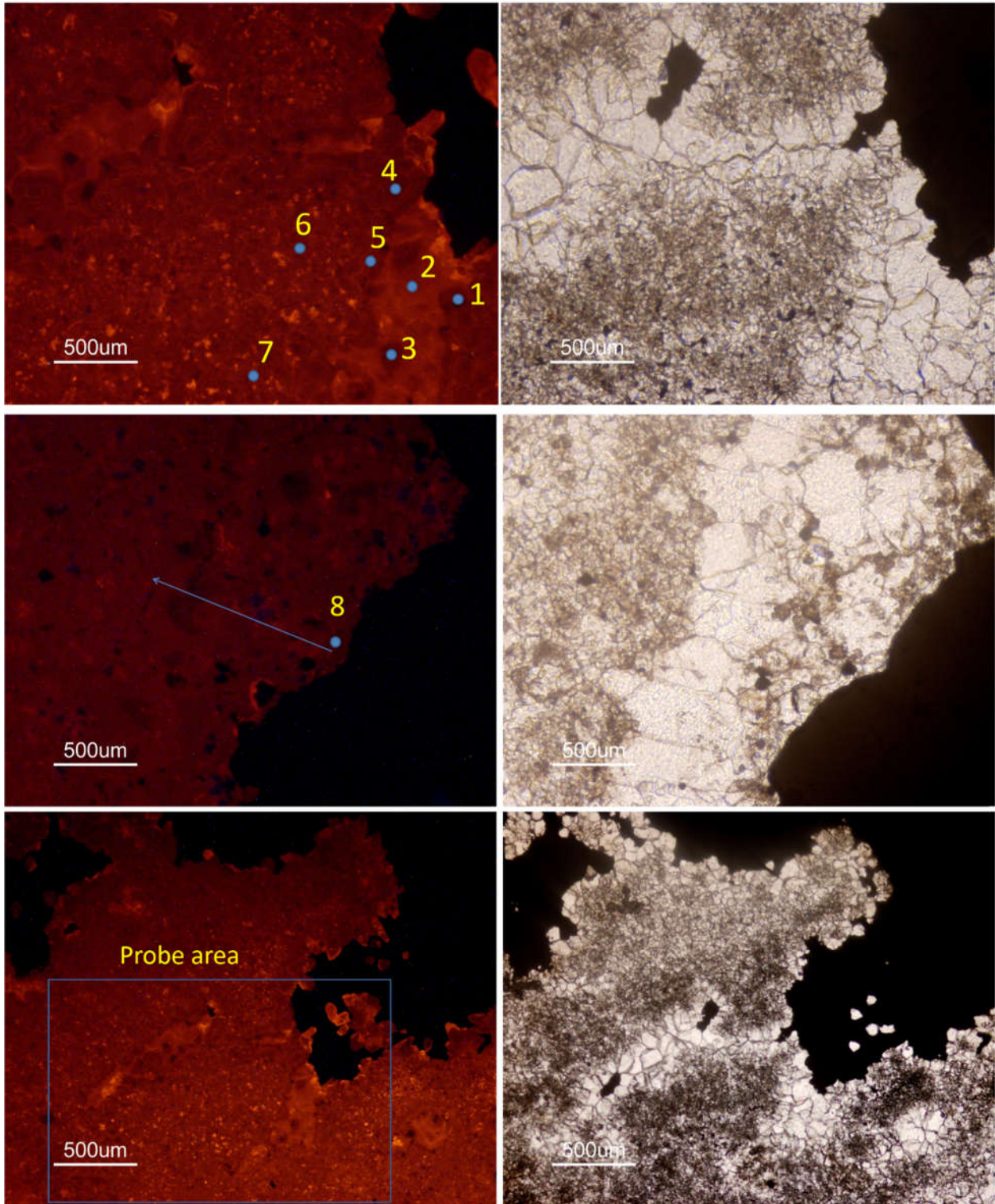
CMDI13-38 MAPS
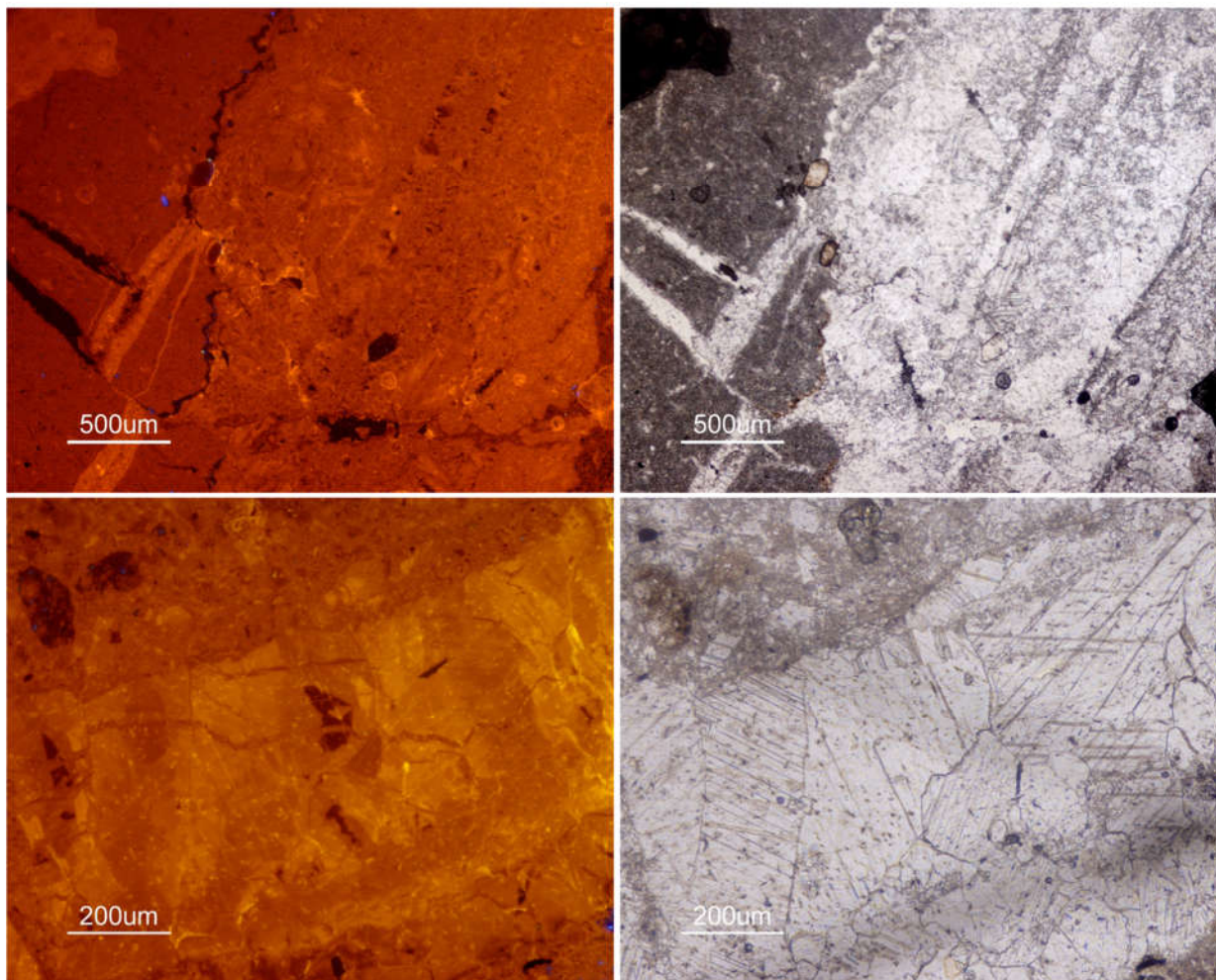
CMDI13-19 MAPS
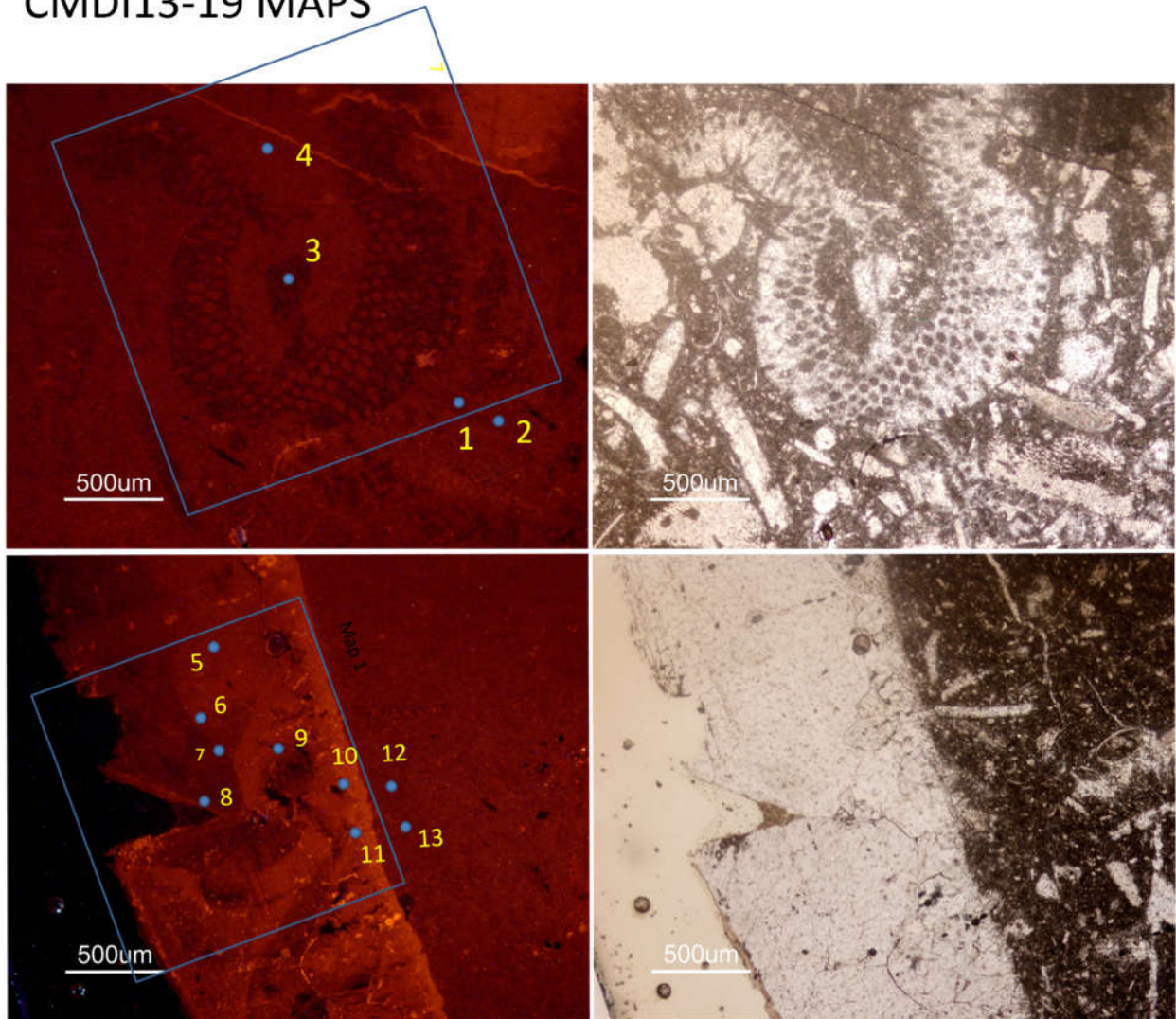
Appendix G   Raman Spectroscopy

Raman spectroscopy was used to identify a variety of phases, primarily silicates. Unfortunately, most of the clay mineral spectra either showed nothing at all, could not be indexed, fluoresced, or were overshadowed by more dominant phases (e.g. first spectra below). We also attempted to use Raman to identify the composition of both solid and fluid inclusions, with the same results. Below are some examples of successful identification. For some spectra, several peaks remain unidentified. Reference materials are from the RRUFF database. Details on the Raman use and methodology are provided in Chapter 3, section 3.3.2.
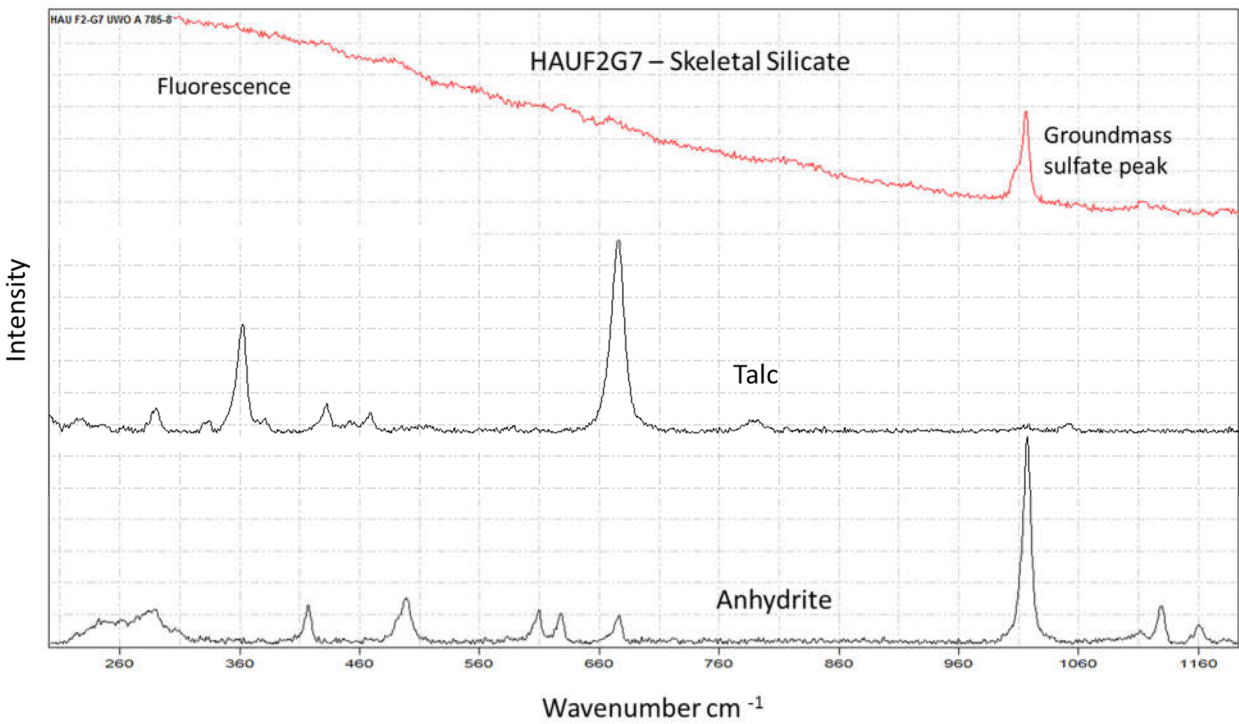
Anhydrite Reference 785nm_unoriented_R040061

Talc Reference 785nm_unoriented_21216
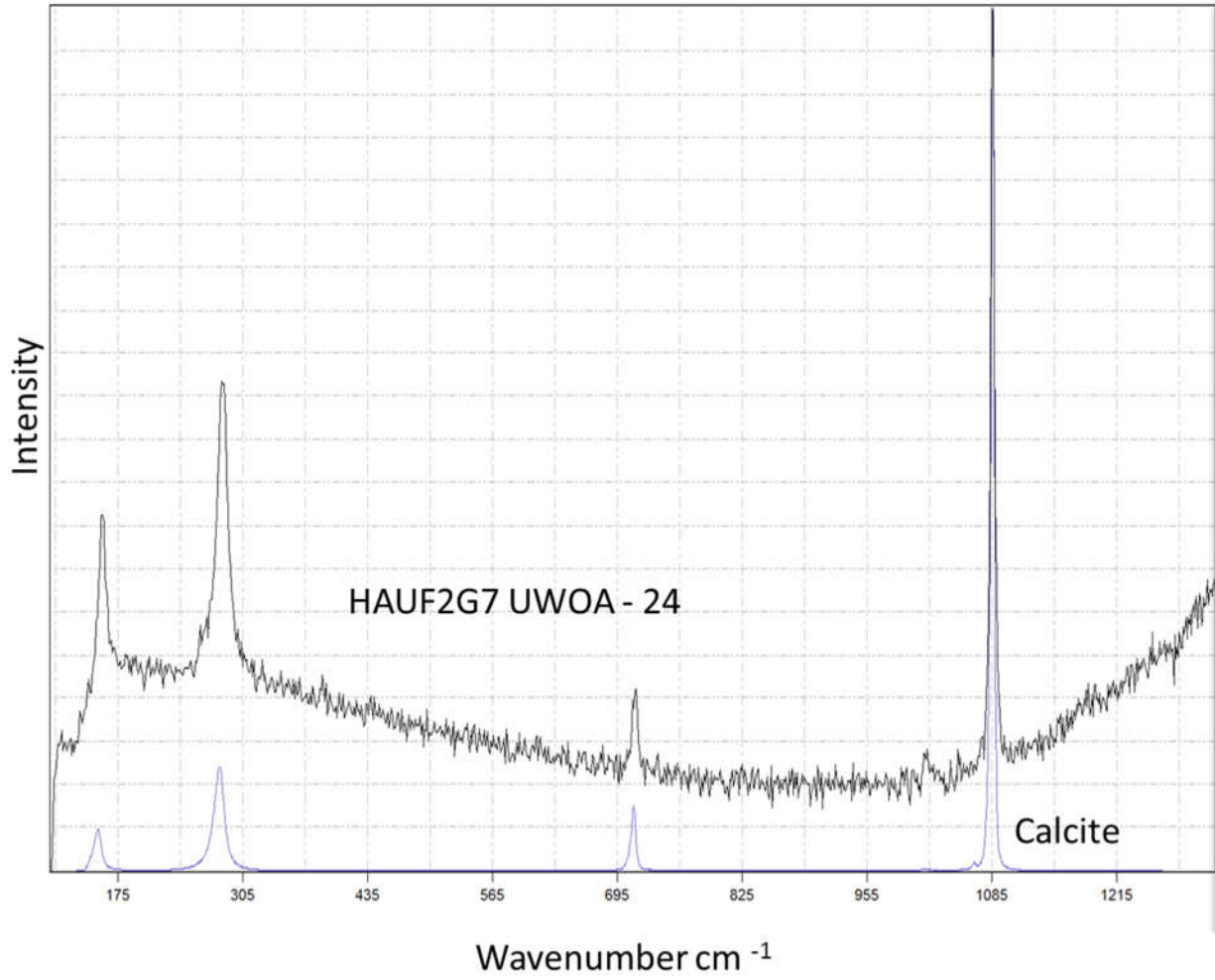
Calcite reference: Raman R050048_785nm_unoriented_21182
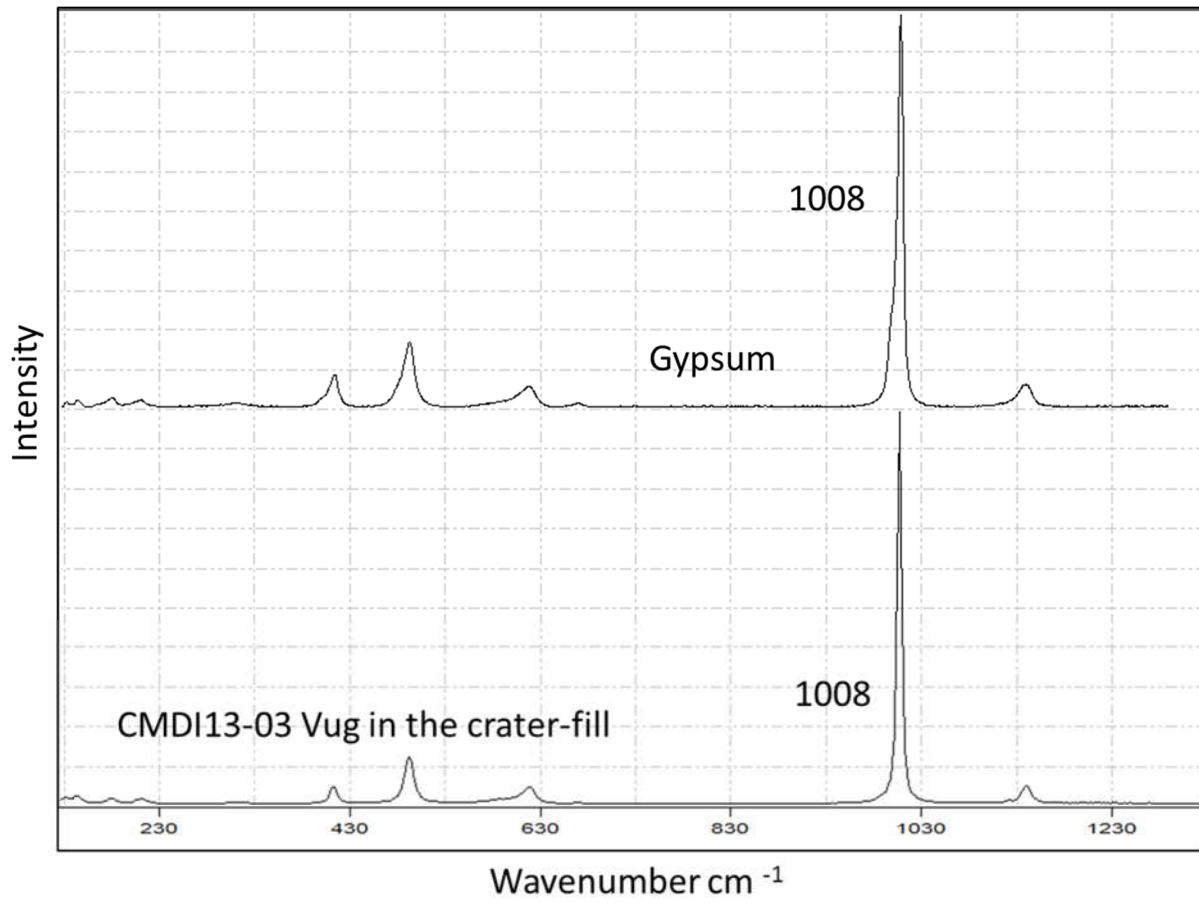
Gypsum reference: Gypsum :040029_532nm_26332
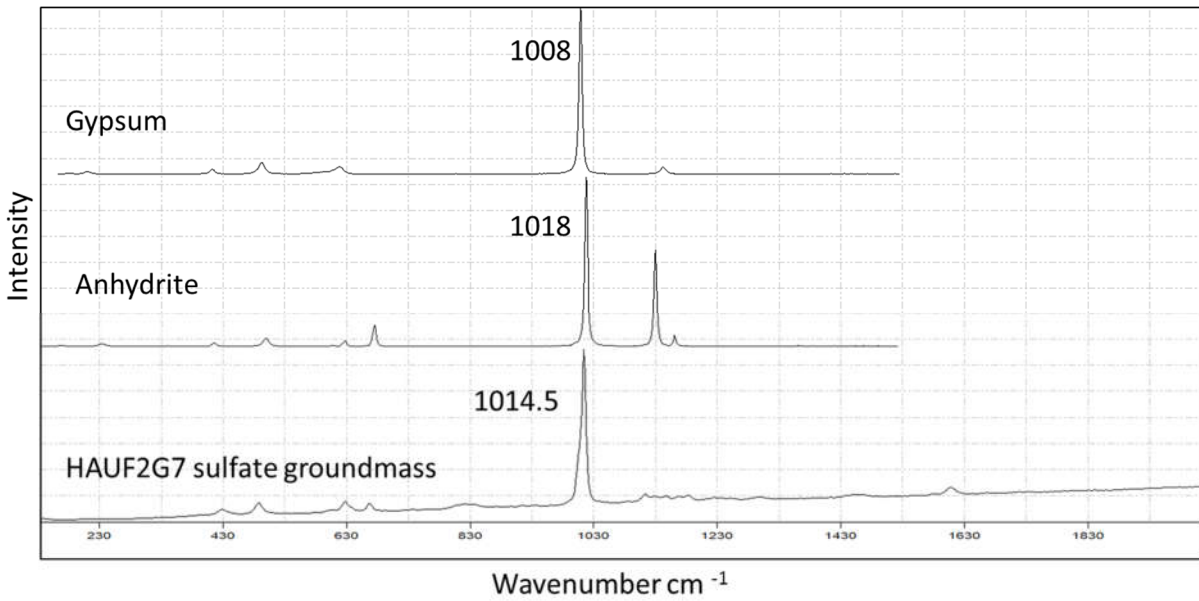
Gypsum ref: R040029, Anhydrite ref: R040061

Note that there was no bassanite in our reference database; however there are examples in Raman literature which indicate the main peak for bassanite is at 1015 cm^{-1} (e.g., Yang et al. (2009)), which is a match for our groundmass.
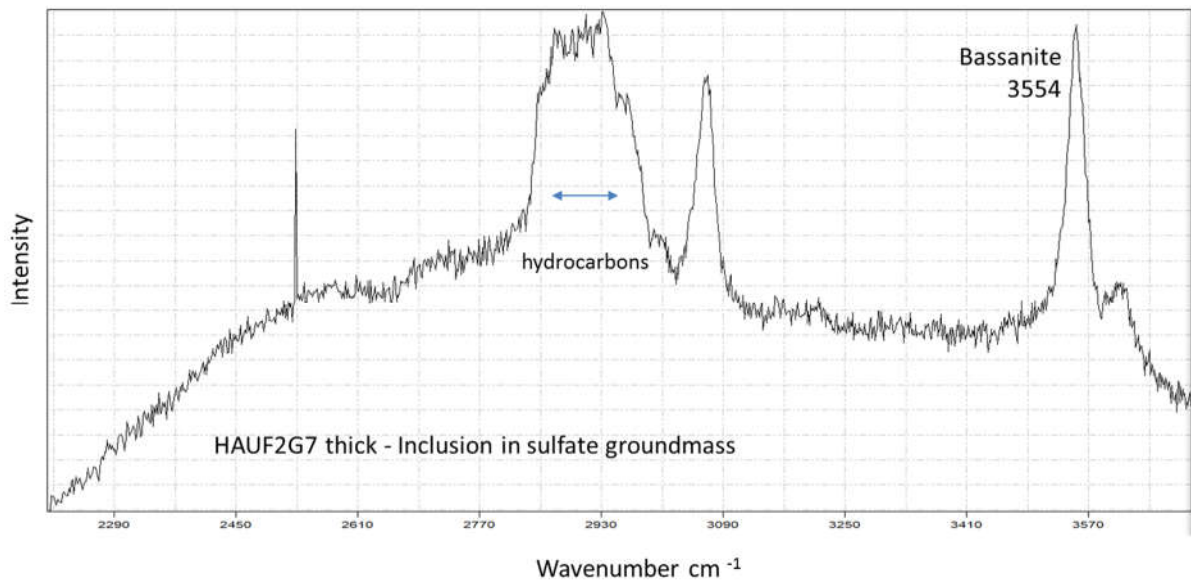
References:

Liu Y., Wang A. and Freeman John J. 2009. Raman, MIR and NIR spectroscopic study of calcium sulfates: gypsum, bassanite, and anhydrite. Lunar and Planetary Science Conference abstract #2128, Houston, Texas.

Appendix H   Image J analysis

	Core total pixel	Sulfate groundmass pixels	Carb Groundmass pixels	Silicate Groundmass pixels	Groundmass total	Clast pixels (by difference)
Table H-1. Image J analysis of clast and groundmass proportions in the F2 Core.						
	80678766	9630120	20825180	833921	31289221	49389545
Total Proportion		11.94	25.81	1.03	38.78	61.22
Proportion of groundmass		30.78	66.56	2.67		100.00

207
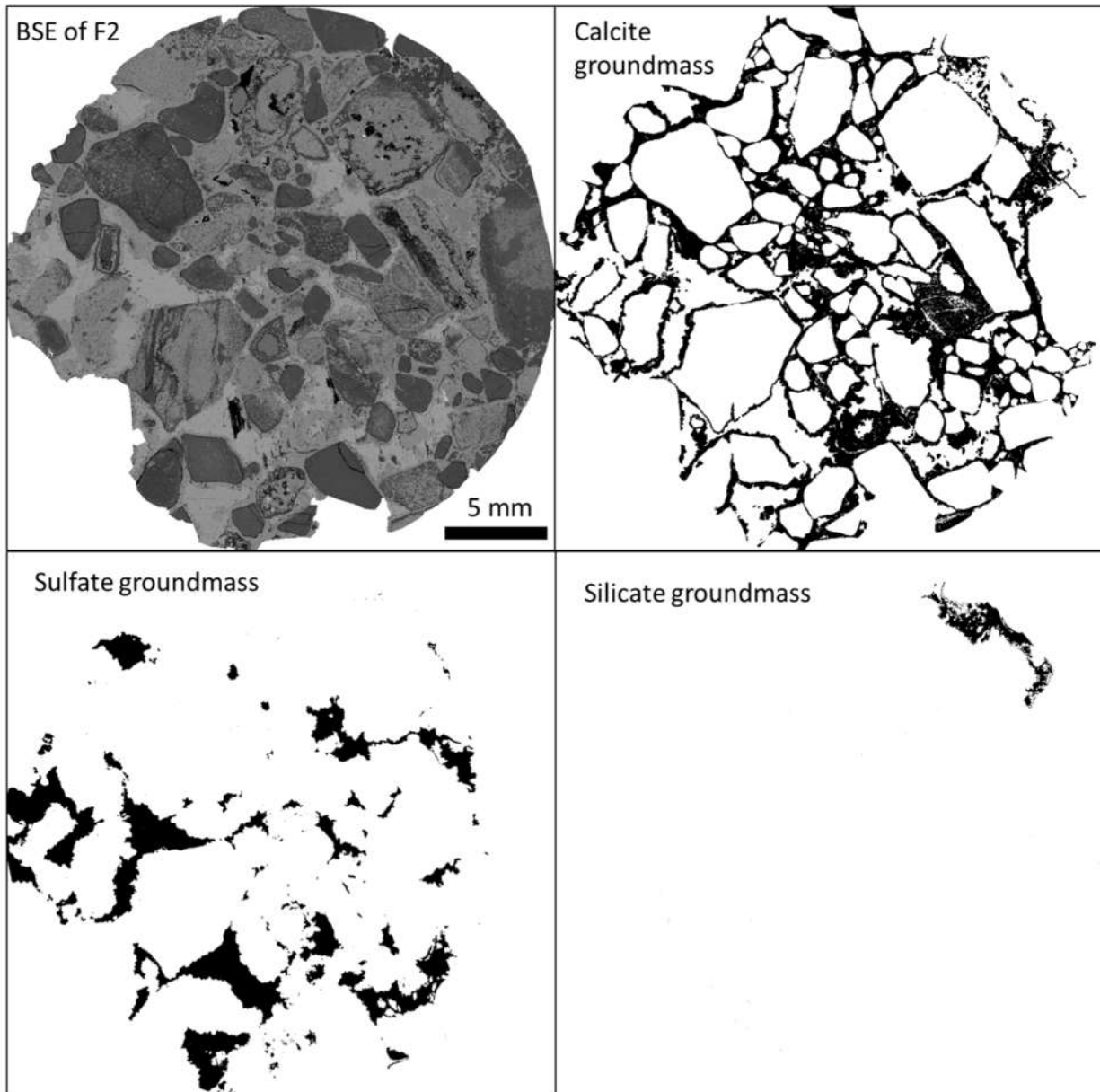
Appendix I   EPMA-EDS Analysis

Representative examples of the EPMA-EDS analysis of the F2 and F3 cores.

HAUF3F1B_matrix2
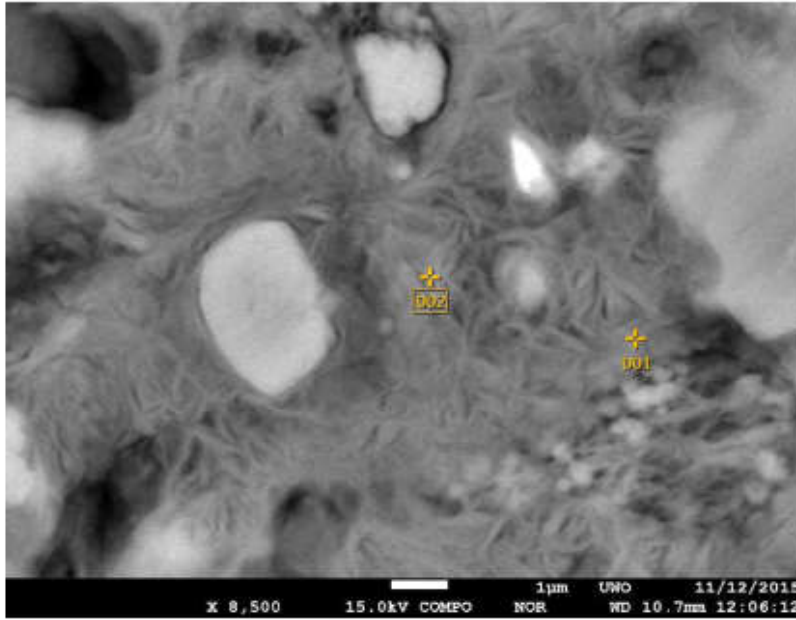
	Volt	: 15.00 kV
	Mag.	: x 8,500
	Date	: 2015/11/12
	Pixel	: 1280 x 960
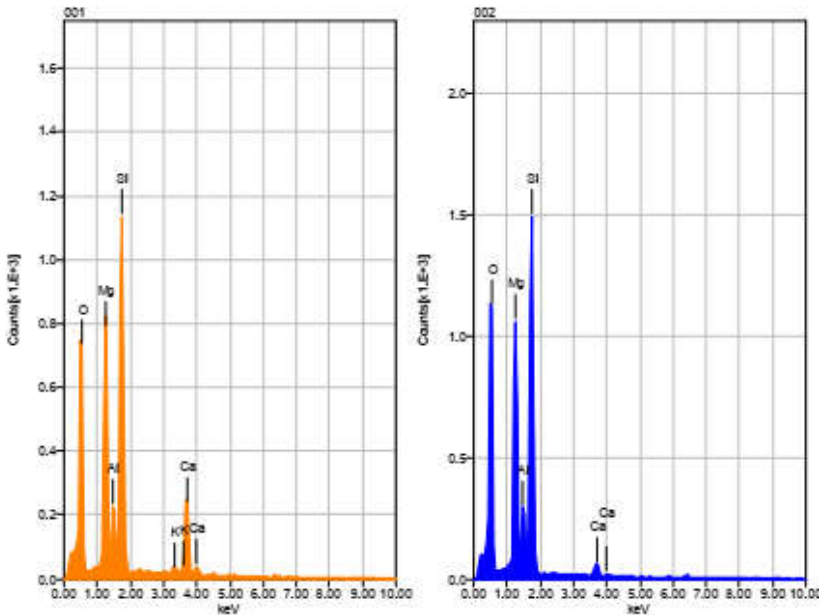
X 8,500   15.0kV COMPO   NOR   1µm   UWO   11/12/2015   WD 10.7mm 12:06:12

Acquisition Condition

Instrument	: 8530F
Volt	: 15.00 kV
Current	: ---
Process Time	: T2
Live time	: 10.00 sec.
Real Time	: 10.26 sec.
DeadTime	: 3.00 %
Count Rate	: 5097.00 CE

	K	O	Mg	Al	Si	Ca
001	0.77	44.26	14.57	4.04	23.94	12.42
002		46.49	17.36	5.17	28.70	2.28
Average	0.77	45.38	15.97	4.60	26.32	7.35
Deviation	0.00	1.58	1.97	0.80	3.36	7.17

HAUF2H11_C_clay matrix
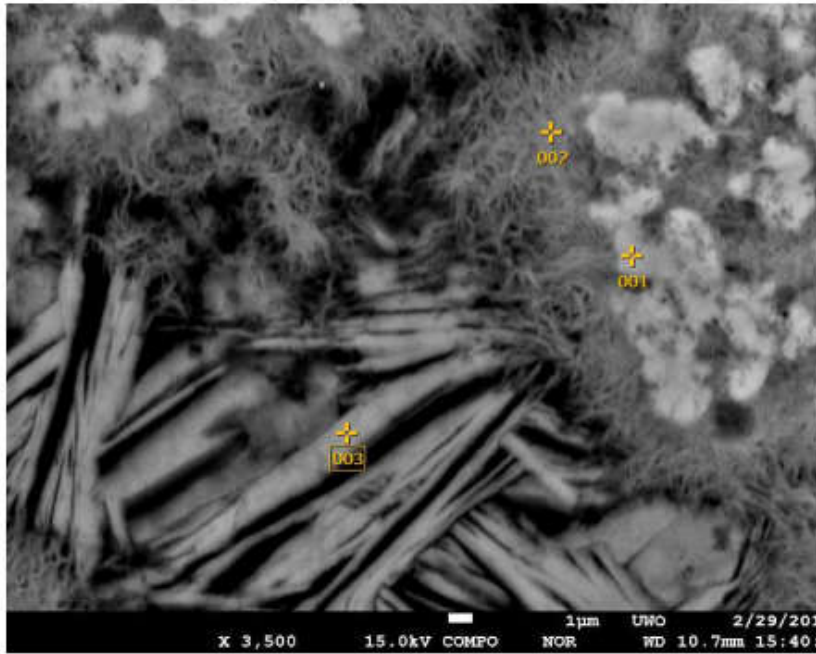
	Volt	: 15.00 kV
	Mag.	: x 3,500
	Date	: 2016/02/
	Pixel	: 1280 x 9
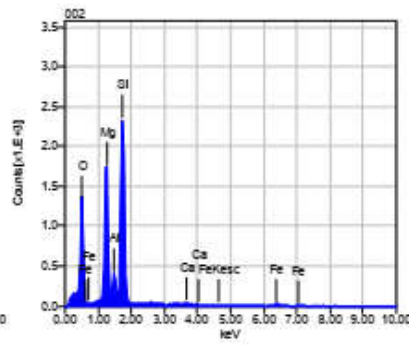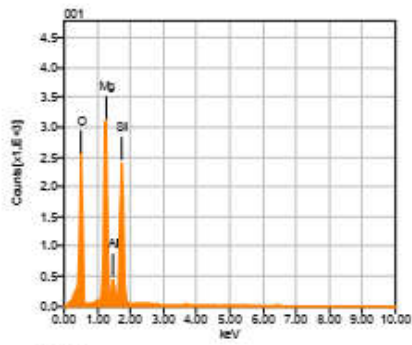
Acquisition Condition	
Instrument	: 8530F
Volt	: 15.00 kV
Current	: ---
Process Time	: T2
Live time	: 10.00 se
Real Time	: 10.37 se
DeadTime	: 3.00 %
Count Rate	: 6726.00
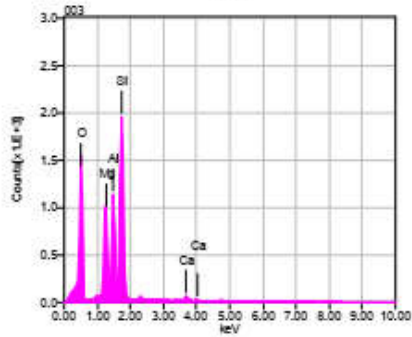
	Fe	O	Mg	Al	Si	Ca
001		47.04	24.96	4.07	23.92	
002	2.82	39.30	19.42	4.99	32.77	0.69
003		44.96	11.43	13.92	28.24	1.45
Average	2.82	43.77	18.60	7.66	28.31	1.07
Deviation	0.00	4.00	6.81	5.44	4.42	0.54

HAUF2H11 silica rim in silica matrix
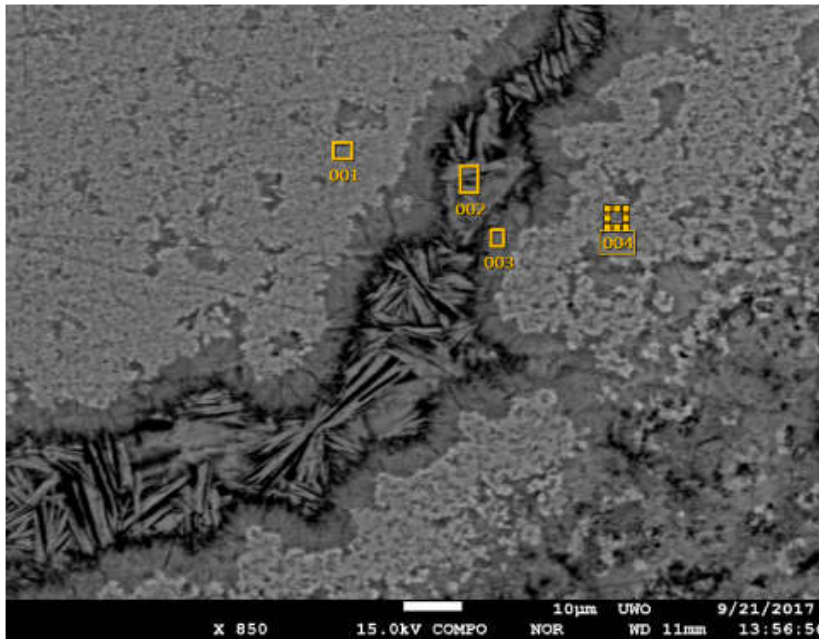
Volt : 15.00 kV
Mag. : x 850
Date : 2017/09/21
Pixel : 1280 x 960
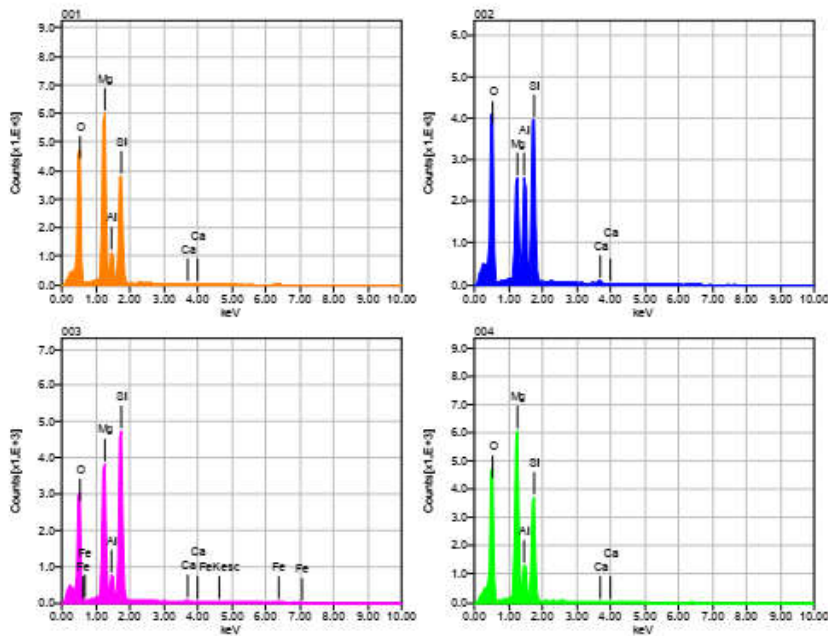
Acquisition Condition
Instrument : 8530F
Volt : 15.00 kV
Current : ---
Process Time : T2
Live time : 10.00 sec.
Real Time : 11.01 sec.
DeadTime : 9.00 %
Count Rate : 19267.00 CPS

	CaO	O	MgO	Al2O3	SiO2	FeO
001	0.57	0.00	42.24	11.20	46.00	
002	1.52	0.00	20.02	25.42	53.04	
003	0.99	0.00	30.69	6.84	59.30	2.18
004	0.72	0.00	42.66	13.10	43.52	
Average	0.95	0.00	33.90	14.14	50.46	2.18
Deviation	0.42	0.00	10.79	7.96	7.14	0.00

HAUF3F1B_matrix
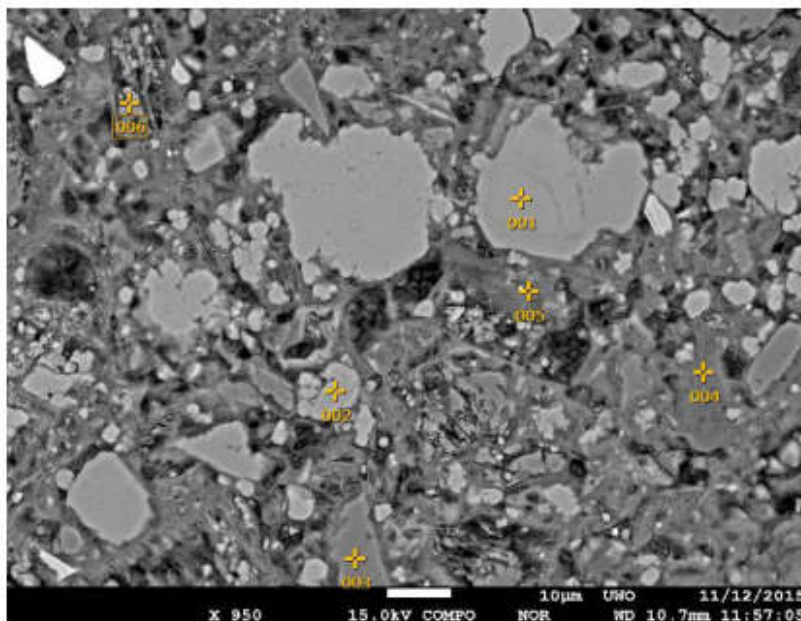
Volt   : 15.00 kV
Mag.   : x 950
Date   : 2015/11/12
Pixel   : 1280 x 960
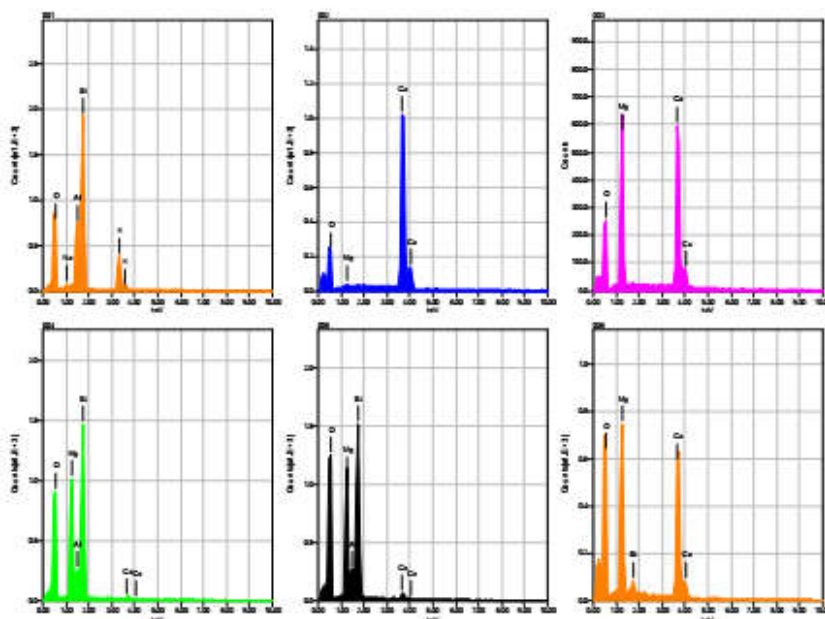
Acquisition Condition
Instrument   : 8530F
Volt   : 15.00 kV
Current   : ---
Process Time : T2
Live time   : 10.00 sec.
Real Time   : 10.18 sec.
DeadTime   : 2.00 %
Count Rate   : 3616.00 CE

	K	O	Na	Mg	Al	Si	Ca
001	14.88	41.97	0.65		9.99	32.50	
002		37.71		0.43			61.86
003		38.46		18.60			42.94
004		43.07		18.32	4.86	31.98	1.78
005		47.37		17.79	4.63	28.06	2.14
006		53.00		15.91		1.10	29.98
Average	14.88	43.60	0.65	14.21	6.49	23.41	27.74
Deviation	0.00	5.77	0.00	7.77	3.03	15.01	26.12

211

HAUF3F1B_laminated kinked lab
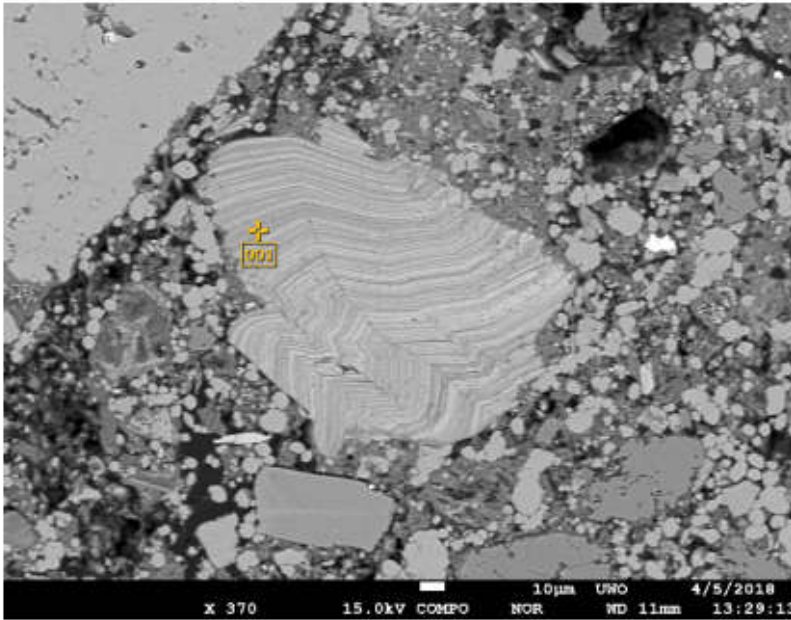
Volt	: 15.00 kV
Mag.	: x 370
Date	: 2018/04/05
Pixel	: 1280 x 960
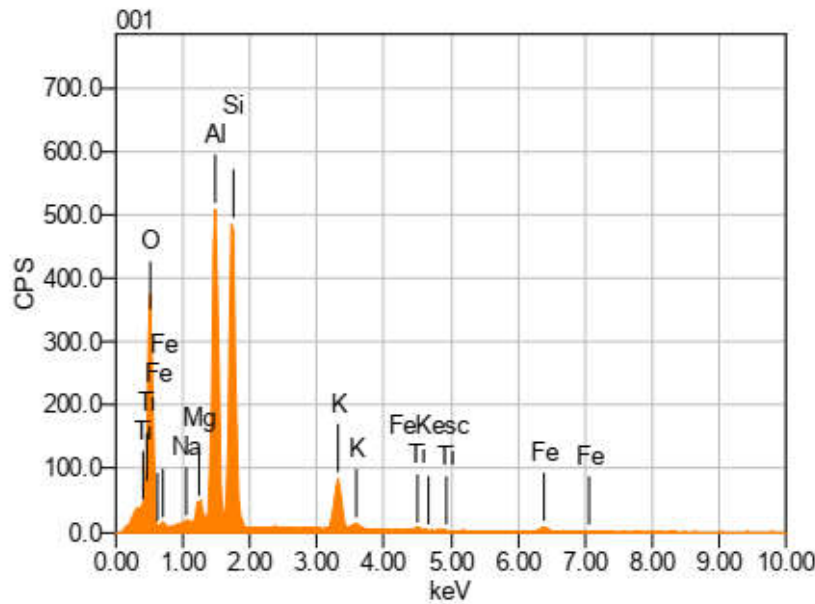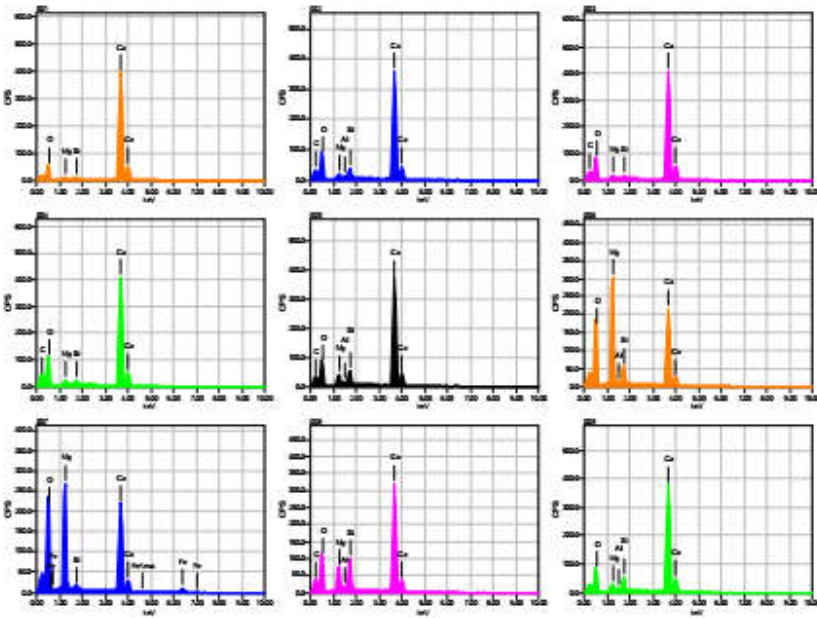
X 370   15.0kV COMPO   NOR   WD 11mm   13:29:13   10μm   UNO   4/5/2018

Acquisition Condition

Instrument	: 8530F
Volt	: 15.00 kV
Current	: ---
Process Time	: T2
Live time	: 10.00 sec
Real Time	: 11.03 sec
DeadTime	: 9.00 %
Count Rate	: 19445.00

Formula	mass%	Atom%	Sigma	Net	K ratio	Line
O	44.16	59.22	0.12	749796	4.2996025	K
Na	0.20	0.18	0.02	10570	0.0244362	K
Mg	1.42	1.26	0.03	92775	0.1735266	K
Al	19.67	15.64	0.08	1404701	2.7109183	K
Si	24.04	18.36	0.11	1471519	3.1764240	K
K	7.67	4.21	0.07	312643	1.2273191	K
Ti	0.55	0.25	0.04	14432	0.0811792	K
Fe	2.29	0.88	0.06	29856	0.3427182	K
Total	100.00	100.00				

HAUF3F1B_clasts4

	Fe	O	C	Mg	Al	Si	Ca
001		31.83		0.61		0.26	67.29
002		38.44	4.06	0.79	0.29	1.88	54.54
003		37.08	2.99	0.63		0.32	58.97
004		40.12	4.27	0.78		0.75	54.07
005		36.91	3.70	1.86	0.19	2.54	54.80
006		47.25		17.79	0.45	3.09	31.41
007	5.65	49.64		14.93		0.40	29.38
008		39.34	5.04	4.30	0.54	5.54	45.24
009		37.12		1.64	0.27	2.55	58.42
Average	5.65	39.75	4.01	4.81	0.35	1.93	50.46
Deviation	0.00	5.49	0.75	6.68	0.14	1.74	12.76

213

HAUF2H3 Gypsum vein
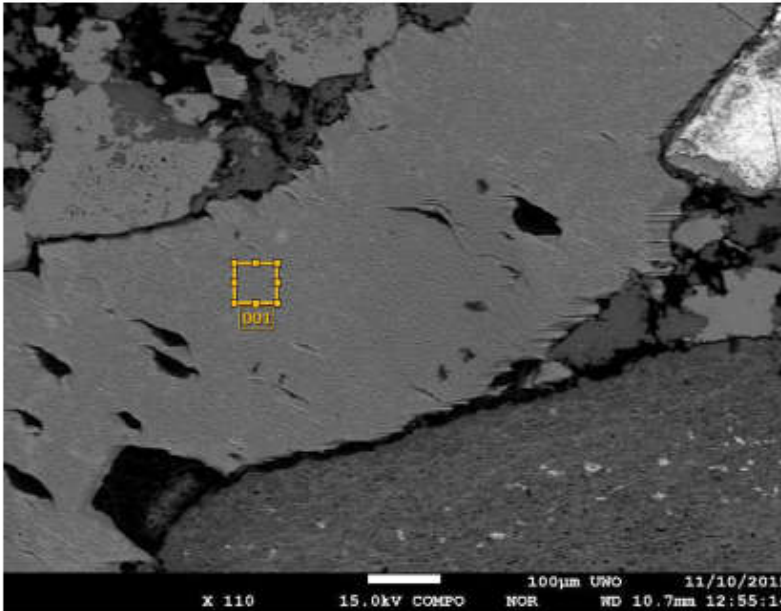
Volt   : 15.00 kV
Mag.   : x 110
Date   : 2015/11/10
Pixel   : 1280 x 960
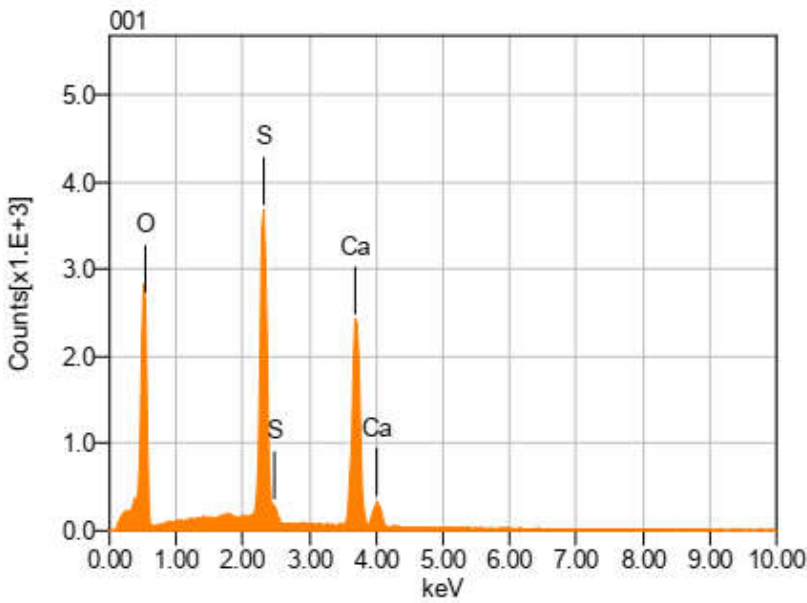
X 110   15.0kV COMPO   NOR   100μm UWO   WD 10.7mm 12:55:14   11/10/2015

Acquisition Condition
Instrument   : 8530F
Volt   : 15.00 kV
Current   : ---
Process Time : T2
Live time   : 10.00 sec.
Real Time   : 10.82 sec.
DeadTime   : 8.00 %
Count Rate   : 15405.00 C

Formula	mass%	Atom%	Sigma	Net	K ratio	Line
O	51.85	70.83	0.16	558113	2.1549923	K
S	21.33	14.54	0.07	1218691	2.8343938	K
Ca	26.83	14.63	0.12	1012230	4.0196781	K
Total	100.00	100.00				

214

HAUF2I6_glassy and acicular contacts zoom acicula
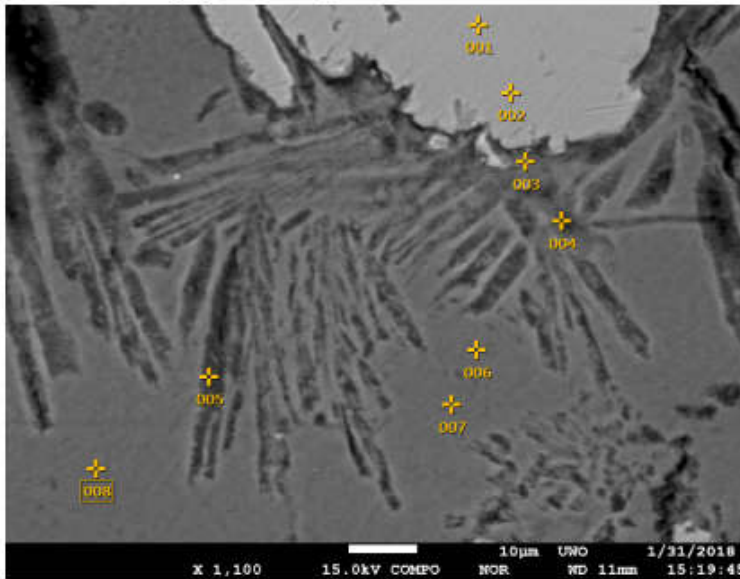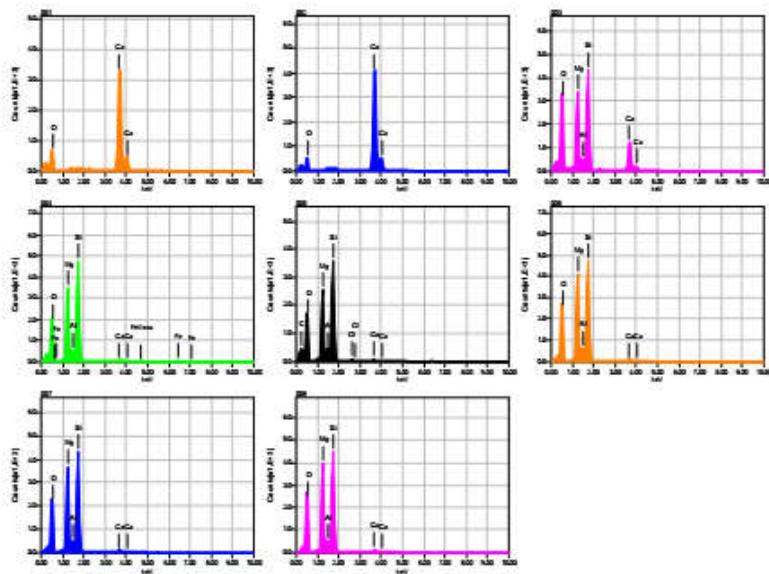
	CaO	O	C	MgO	Al2O3	SiO2	Cl	FeO
001	100.00	0.00						
002	100.00	0.00						
003	21.65	0.00		25.73	3.93	48.69		
004	1.39	0.00		28.76	5.42	62.60		1.83
005	1.24	0.00	15.50	24.69	4.56	53.54	0.46	
006	1.60	0.00		32.77	5.23	60.41		
007	1.73	0.00		32.65	4.65	60.97		
008	1.62	0.00		33.11	5.11	60.16		
Average	28.65	0.00	15.50	29.62	4.82	57.73	0.46	1.83
Deviation	44.58	0.00	0.00	3.78	0.55	5.41	0.00	0.00

215

HAUF2H11uwo_clast-comp-with zircon and Ap
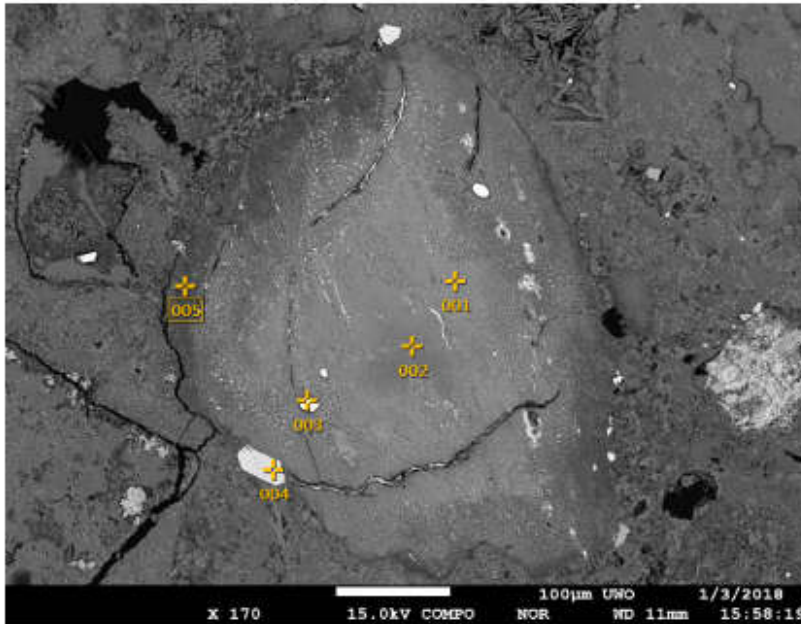
Volt	:	15.00 kV
Mag.	:	x 170
Date	:	2018/01/
Pixel	:	1280 x 9
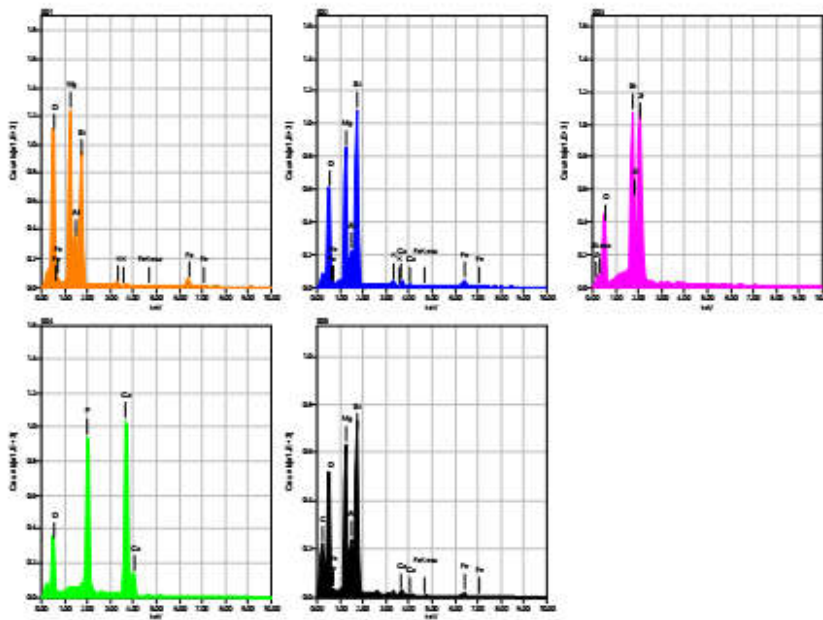
X 170   15.0kV COMPO   NOR   WD 11mm   15:58:19   100µm UWO   1/3/2018

Acquisition Condition

Instrument	:	8530F
Volt	:	15.00 kV
Current	:	---
Process Time	:	T2
Live time	:	10.00 se
Real Time	:	10.17 se
DeadTime	:	1.00 %
Count Rate	:	3255.00

	P	Fe	K	O	C	Mg	Al	Si	Ca
001		8.72	0.79	43.82		20.56	6.75	19.36	
002		7.49	1.39	37.18		19.20	4.75	28.54	1.45
003				30.60				15.95	
004	20.35			35.21					44.44
005		2.94		35.87	25.92	12.01	4.83	17.47	0.96
Average	20.35	6.39	1.09	36.54	25.92	17.26	5.44	20.33	15.61
Deviation	0.00	3.04	0.42	4.77	0.00	4.60	1.13	5.65	24.96

HAUF2H11_D_bt
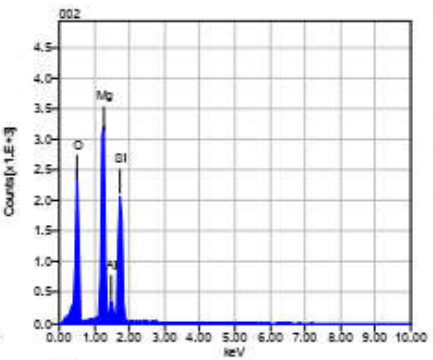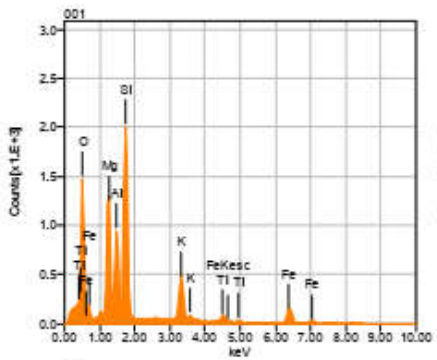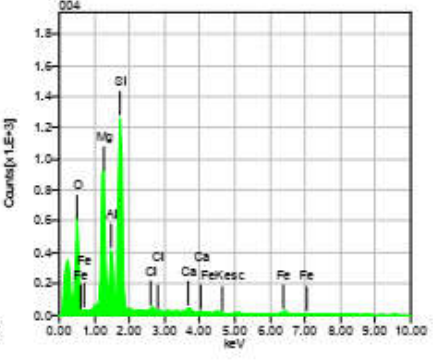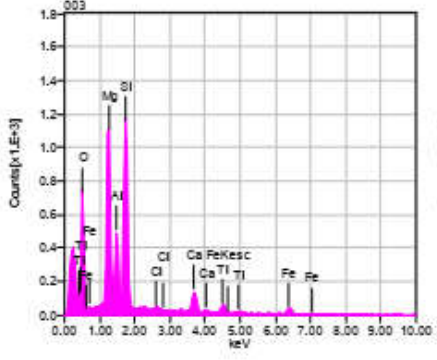
	Fe	K	O	Mg	Al	Si	Cl	Ca	Ti
001	11.55	8.91	36.78	11.13	8.85	20.24			2.53
002			47.53	26.65	3.57	22.25			
003	4.64		35.94	18.46	8.44	23.07	0.75	5.40	3.30
004	5.19		34.42	18.09	8.91	30.78	0.84	1.76	
Average	7.13	8.91	38.67	18.58	7.44	24.09	0.80	3.58	2.91
Deviation	3.84	0.00	5.99	6.35	2.59	4.62	0.07	2.57	0.55

217

HAUF2H11_B
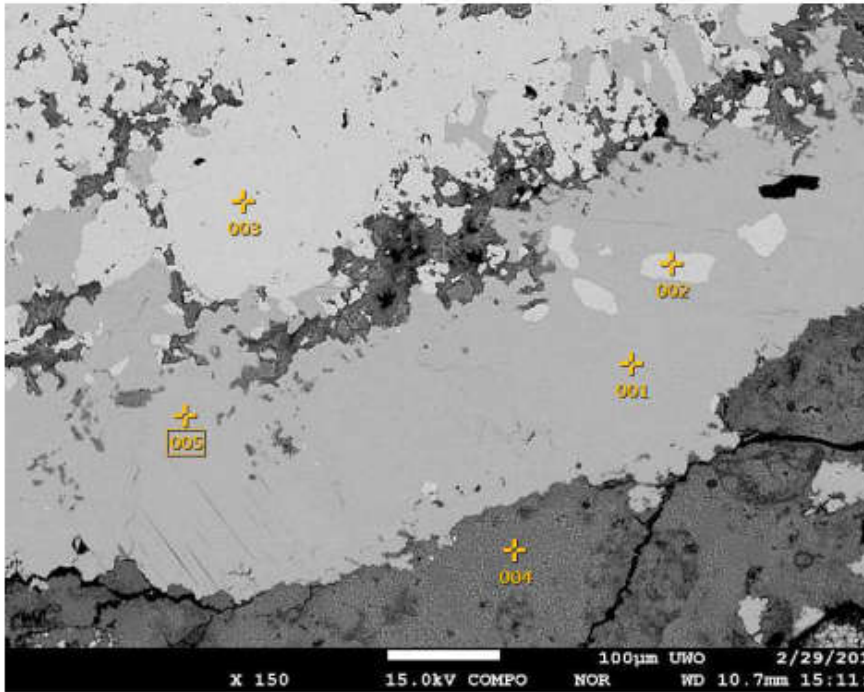
Volt   : 15.00 kV
Mag.   : x 150
Date   : 2016/02/
Pixel   : 1280 x 9
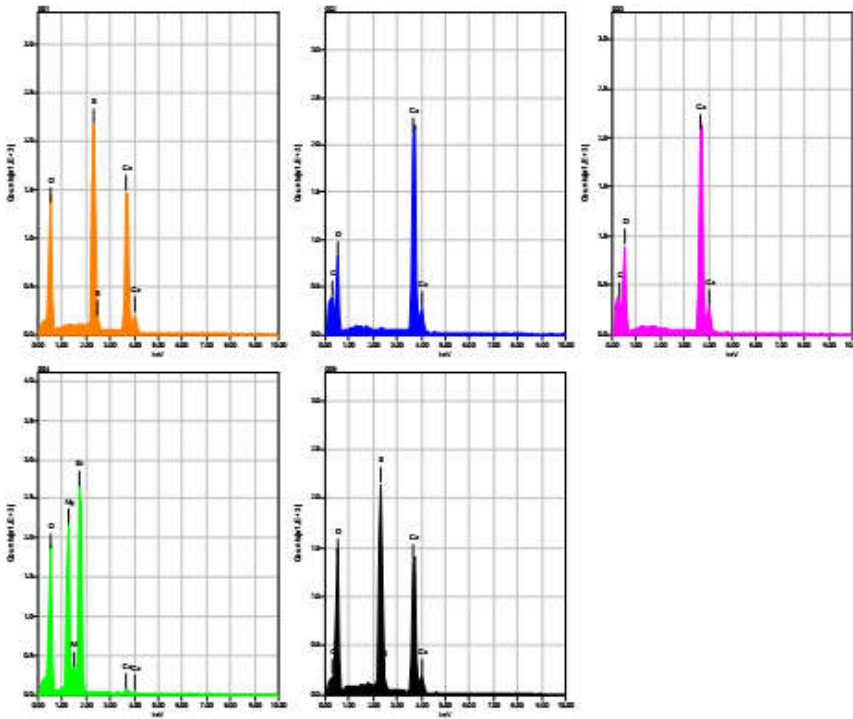
X 150   15.0kV COMPO   NOR   100µm UWO   2/29/201
WD 10.7mm 15:11:

Acquisition Condition
Instrument   : 8530F
Volt   : 15.00 kV
Current   : ---
Process Time : T2
Live time   : 10.00 se
Real Time   : 10.48 se
DeadTime   : 4.00 %
Count Rate   : 9325.00

	O	C	Mg	Al	Si	S	Ca
001	49.14					22.62	28.24
002	46.18	3.55					50.27
003	47.59	3.28					49.13
004	44.87		20.37	3.23	30.82		0.70
005	49.39	0.77				21.97	27.86
Average	47.44	2.53	20.37	3.23	30.82	22.29	31.24
Deviation	1.93	1.53	0.00	0.00	0.00	0.45	20.22

218

HAUF2G7uwo2_silicate intergrowth in Si2
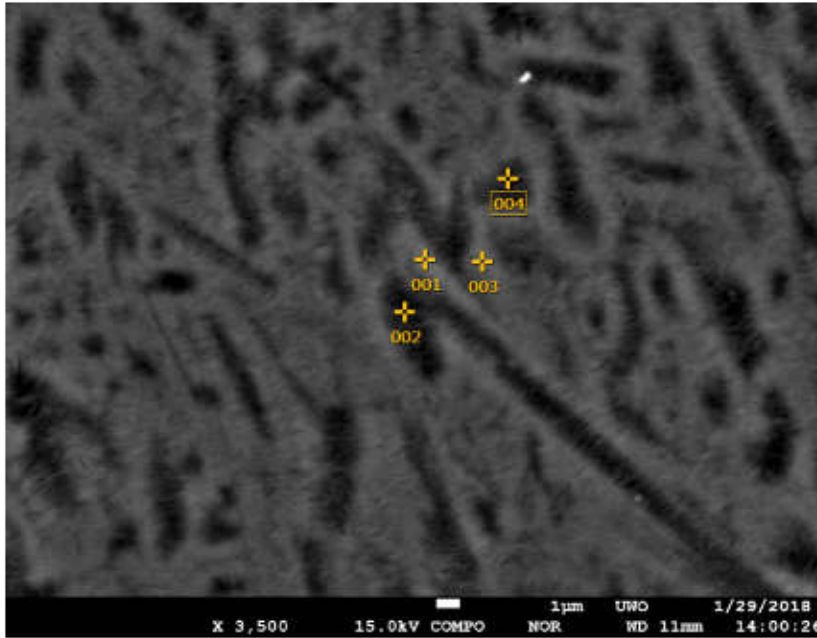
	Volt	: 15.00 kV
	Mag.	: x 3,500
	Date	: 2018/01/
	Pixel	: 1280 x 9
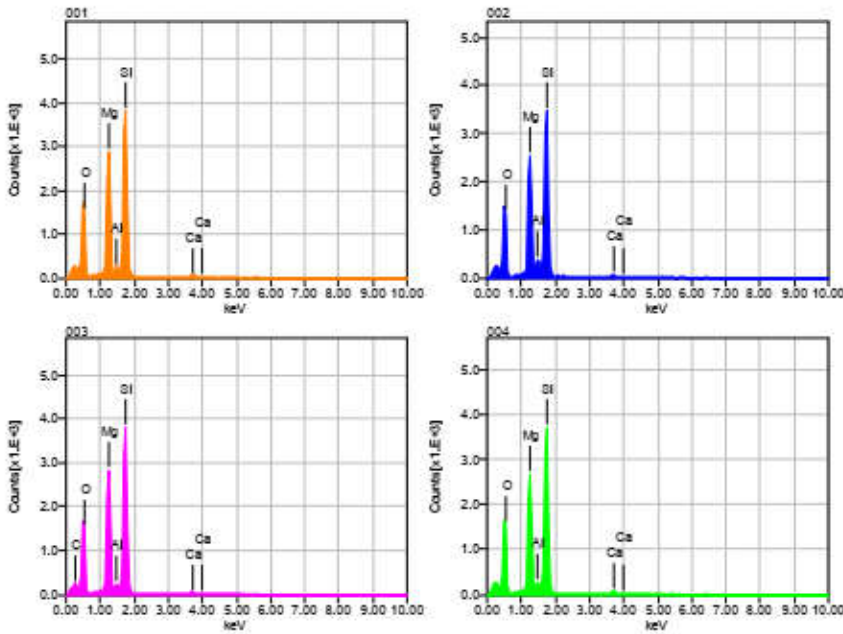
X 3,500   15.0kV COMPO   NOR   1μm   UWO   WD 11mm   1/29/2018   14:00:26

Acquisition Condition

Instrument	: 8530F
Volt	: 15.00 kV
Current	: ---
Process Time	: T2
Live time	: 10.00 se
Real Time	: 10.56 se
DeadTime	: 5.00 %
Count Rate	: 10395.00

	O	C	Mg	Al	Si	Ca
001	38.35		21.86	1.78	37.21	0.79
002	36.74		21.53	3.26	36.95	1.52
003	36.20	11.21	18.97	1.42	31.38	0.82
004	38.56		21.28	2.16	36.82	1.18
Average	37.46	11.21	20.91	2.16	35.59	1.08
Deviation	1.17	0.00	1.32	0.79	2.81	0.34

HAUF2G7uwo2_sulfides
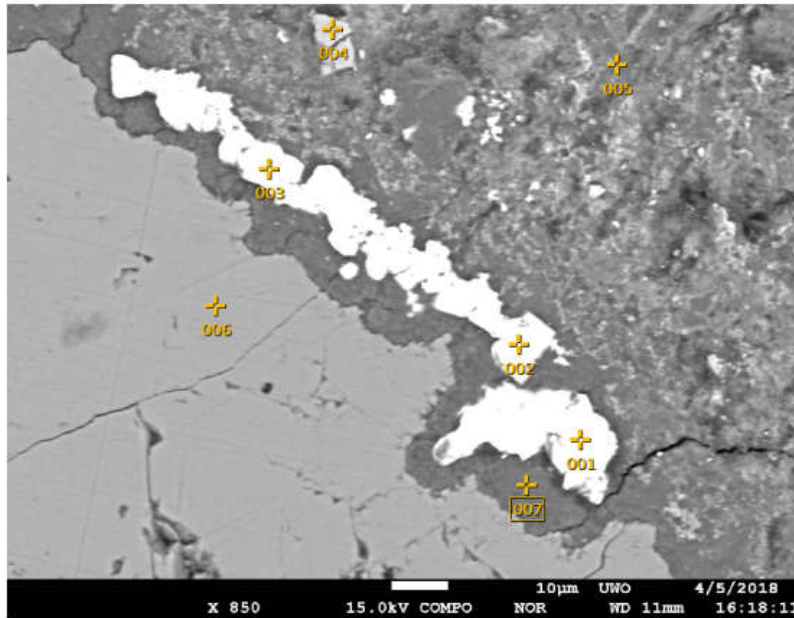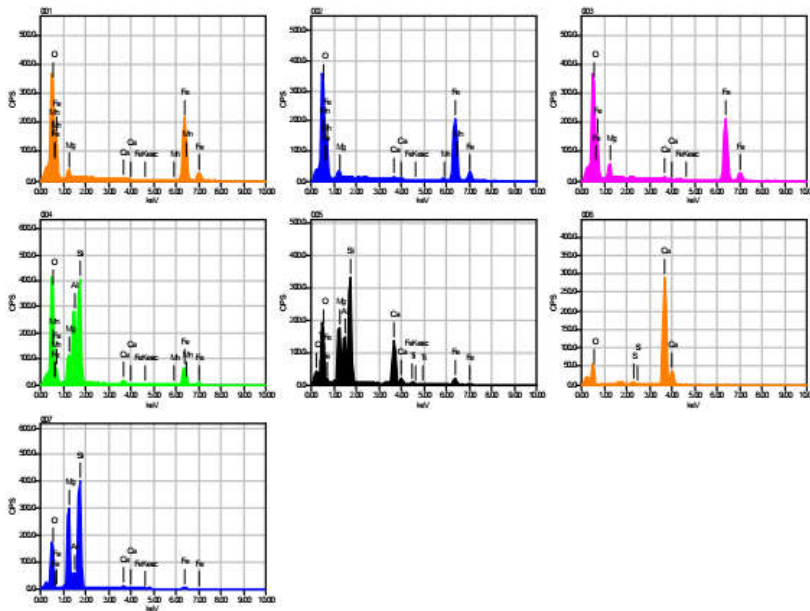
	Fe	O	C	Mg	Al	Si	S	Ca	Ti	M
001	74.44	22.66		1.40				0.48		1
002	74.86	21.95		1.32				0.53		1
003	73.67	23.24		2.50				0.59		
004	27.17	35.28		4.64	11.95	18.96		1.25		0
005	8.61	34.01	7.49	7.99	6.64	17.48		16.30	1.47	
006		35.57					0.33	64.10		
007	4.87	34.67		20.27	4.08	34.63		1.47		
Average	43.94	29.63	7.49	6.35	7.56	23.69	0.33	12.10	1.47	1
Deviation	34.13	6.58	0.00	7.27	4.02	9.50	0.00	23.64	0.00	0

HAUF2G7uwo_sulfate_talc_blades
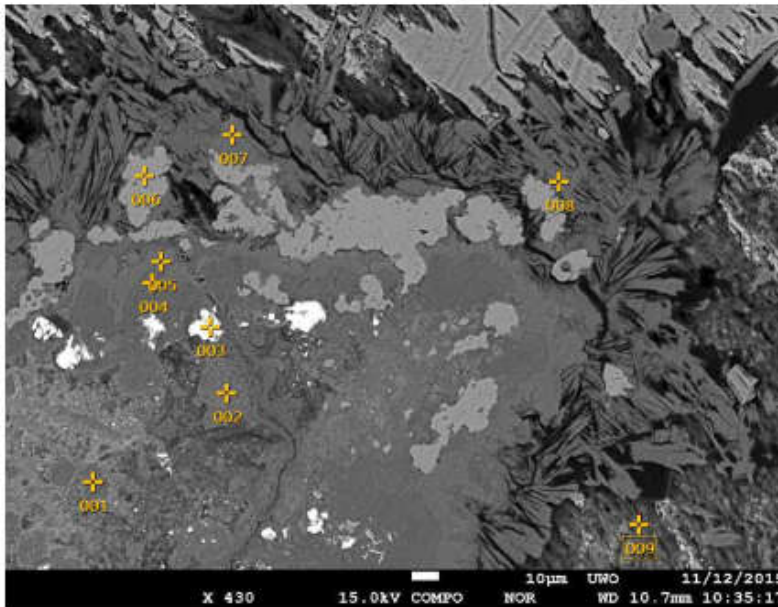
Volt   : 15.00 kV
Mag.   : x 430
Date   : 2015/11/12
Pixel   : 1280 x 960
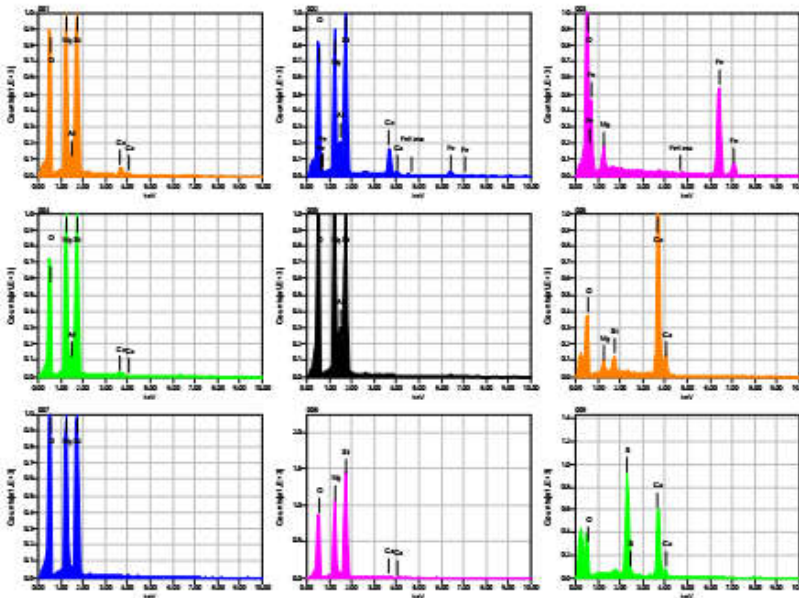
X 430   15.0kV COMPO   NOR   10μm UWO   11/12/2015
                                          WD 10.7mm 10:35:17

Acquisition Condition
Instrument   : 8530F
Volt   : 15.00 kV
Current   : ---
Process Time : T2
Live time   : 10.00 sec.
Real Time   : 10.21 sec.
DeadTime   : 2.00 %
Count Rate   : 4478.00 CP

	Fe	O	Mg	Al	Si	S	Ca
001		44.20	20.54	2.00	30.96		2.30
002	5.06	42.70	17.02	4.12	23.67		7.42
003	70.78	25.99	3.23				
004		41.94	22.54	2.90	31.76		0.87
005		49.26	24.50	5.56	20.68		
006		44.89	1.14		2.02		51.95
007		46.08	20.75		33.17		
008		43.86	20.78		34.77		0.59
009		38.76				27.34	33.90
Average	37.92	41.96	16.31	3.64	25.29	27.34	16.17
Deviation	46.47	6.65	8.98	1.54	11.48	0.00	21.63

221

HAUF2G7-D-near acicular
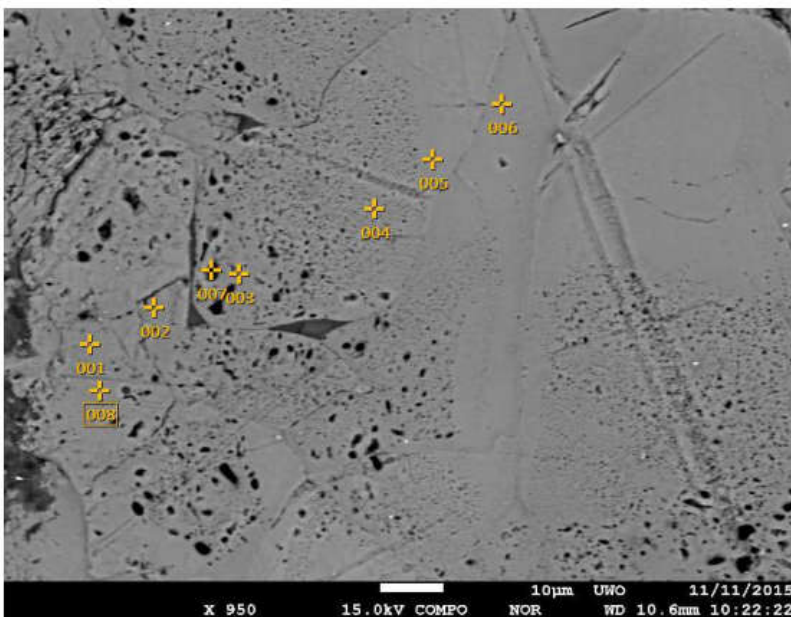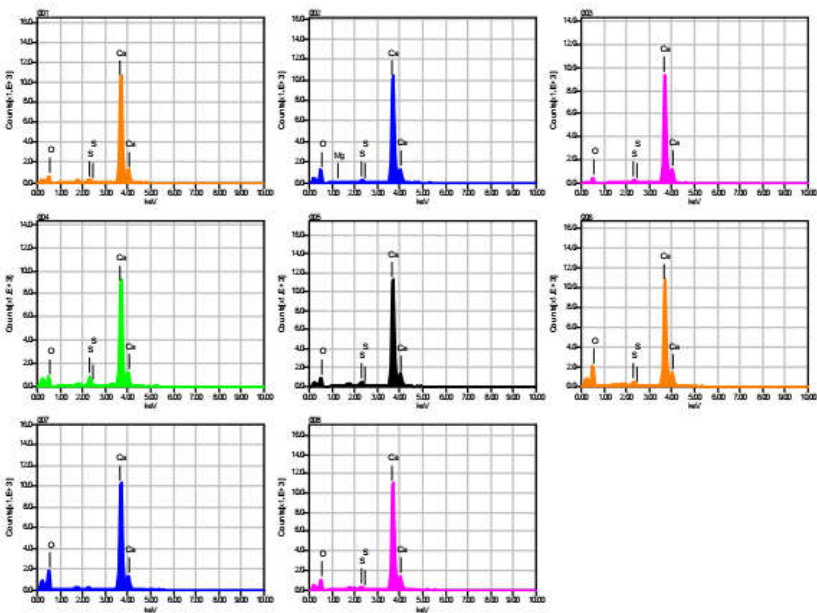
	O	Mg	S	Ca
001	18.80		0.79	80.41
002	28.15	0.20	0.58	71.07
003	13.81		0.54	85.65
004	22.20		2.99	74.81
005	19.77		1.67	78.56
006	34.32		1.29	64.39
007	34.27			65.73
008	25.01		0.60	74.39
Average	24.54	0.20	1.21	74.37
Deviation	7.37	0.00	0.89	7.24

HAUF2G7_mantled_blades
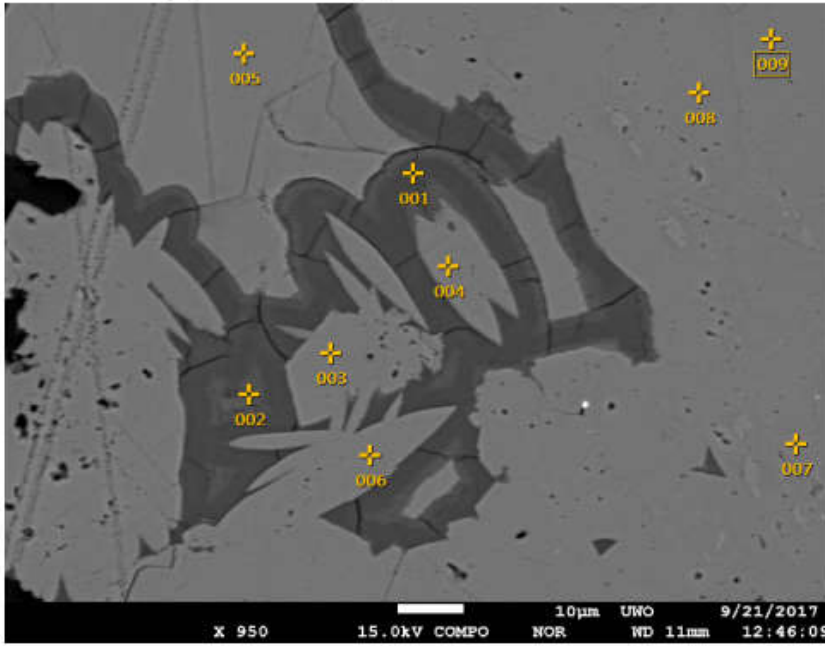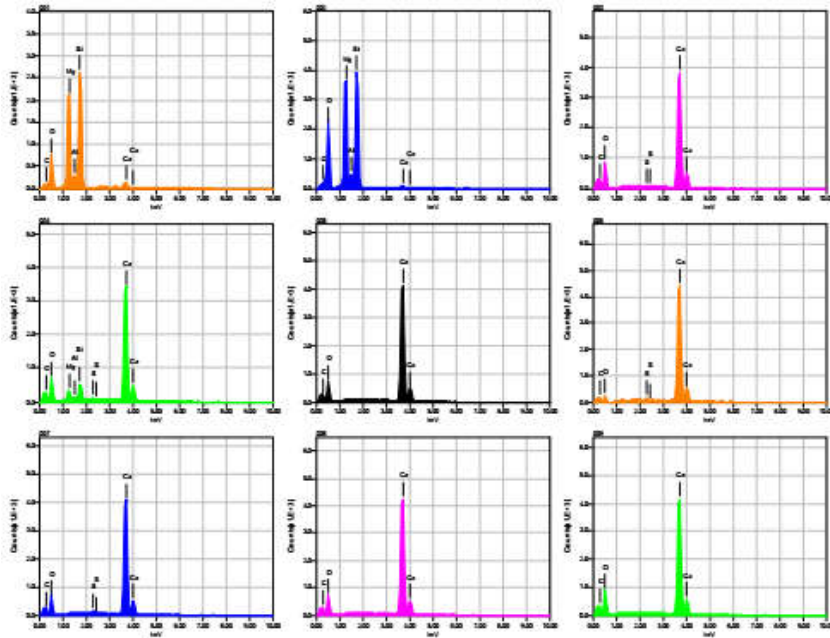
X 950   15.0kV COMPO   NOR   WD 11mm   12:46:09   10μm   UWO   9/21/2017

	CaO	O	C	MgO	Al2O3	SiO2	SO3
001	3.70	0.00	2.86	30.48	5.01	57.95	
002	1.42	0.00	3.31	33.10	5.56	56.61	
003	95.10	0.00	3.72				1.18
004	84.15	0.00	3.81	3.73	0.48	6.97	0.85
005	97.33	0.00	2.67				
006	96.25	0.00	2.21				1.54
007	95.65	0.00	2.47				1.88
008	96.72	0.00	3.28				
009	96.79	0.00	3.21				
Average	74.13	0.00	3.06	22.44	3.68	40.51	1.36

HAUF2G7uwo_celestite-sulfate incl in calcite corona
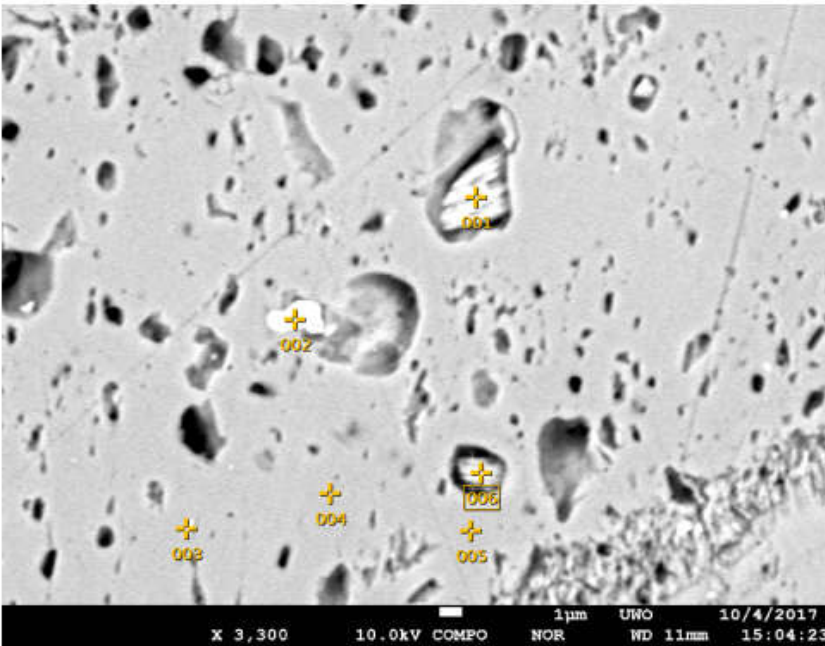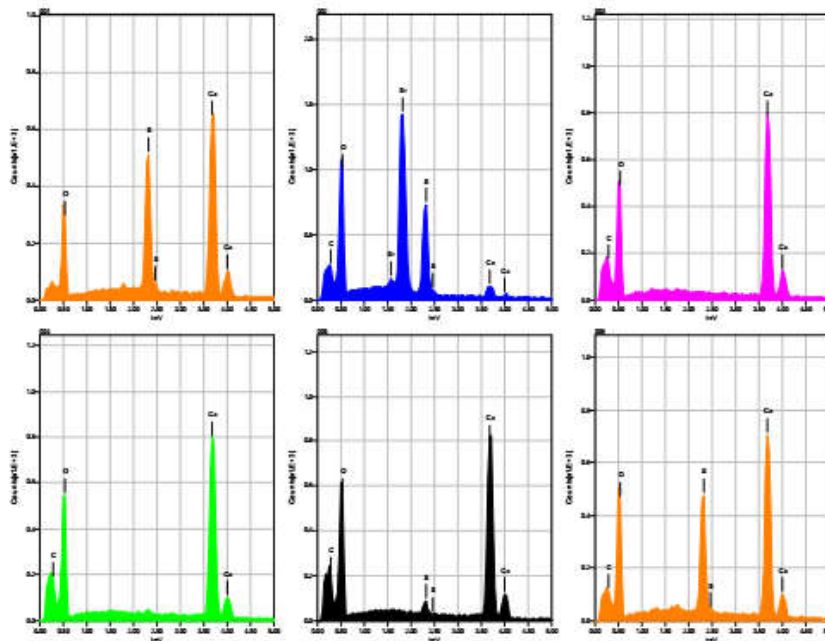
```
X 3,300        10.0kV COMPO      NOR        WD 11mm   15:04:23
                                     1µm    UWO       10/4/2017
```

	O	C	S	Ca	Sr
001	24.55		16.92	58.53	
002	29.31	7.10	15.38	4.56	43.65
003	33.98	3.14		62.87	
004	34.70	3.35		61.94	
005	34.46	4.13	1.39	60.02	
006	30.68	2.17	12.83	54.32	
Average	31.28	3.98	11.63	50.37	43.65
Deviation	3.97	1.88	7.03	22.65	0.00

Appendix J   Thin Section List

Table J-1 F2 and F3 core sections and their associated thin sections			
Core Sections	Description	# of thin sections	Thick doubly-polished sections
HAU F2 G1	Impact melt rock	2	0
HAU F2 G7	Impact melt rock	5	2
HAU F2 G8	Impact melt rock	2	0
HAU F2 H3	Impact melt rock	1	1
HAU F2 H4	Impact melt rock	2	0
HAU F2 H11	Impact melt rock	2	0
HAU F2 I1	Impact melt rock	2	1
HAU F2 I6	Impact melt rock	2	0
HAU F3 E1A	Impact melt rock	2	0
HAU F3 E1B	Impact melt rock	2	1
Thin sections made in France are labelled as shown above, those made at Western have a suffix uwo.			

Table J-2. Field samples collected for hydrothermal studies by C. Marion

sample number	date sampled	rock type	Host Formation	UTM coordinates		
CALCITE						
CMDI13-05	July 18, 2013	calcite	Eleanor River	16x	427834	8365650
CMDI13-10	July 19, 2013	calcite vein	Thumb Mountain			
CMDI13-10b	July 19, 2013	calcite vein	Thumb Mountain			
CMDI13-11	July 19, 2013	calcite vein	Thumb Mountain	16x	423969	8362404
CMDI13-14	July 19, 2013	calcite vein	Bay Fiord - Upper	16x	426668	8371129
CMDI13-15	July 19, 2013	calcite vein	Bay Fiord - Upper	16x	426690	8371163
CMDI13-18	July 21, 2013	calcite	Middle Allen Bay	16x	427516	8374623
CMDI13-18B	July 21, 2013	calcite vein	Middle Allen Bay	16x	427516	8374623
CMDI13-19	July 21, 2013	calcite?	Middle Allen Bay	16x	427516	8374623
CMDI13-22	July 22, 2013	crust	Eleanor River	16x	423055	8369271
CMDI13-31	July 22, 2013	calcite	crater-fill	16x	428055	8364690
CMDI13-32	July 22, 2013	calcite	crater-fill	16x	428055	8364690
CMDI13-33	July 22, 2013	calcite	crater-fill	16x	428062	8364668
CMDI13-34	July 25, 2013	calcite vein	Lower Allen Bay	16x	428022	8372061
CMDI13-35	July 25, 2013	calcite vein	Lower Allen Bay	16x	427525	8372128
CMDI13-36	July 25, 2013	calcite vein	Lower Allen Bay	16x	427408	8372173
CMDI13-37	July 25, 2013	calcite vein	Thumb Mountain	16x	426869	8371681
CMDI13-38	July 25, 2013	calcite vein	Bay Fiord - Upper	16x	426834	8371166
CMDI13-39	July 25, 2013	calcite vein	Bay Fiord - Upper	16x	426840	8371175
CMDI13-40	July 25, 2013	calcite vein	Upper Allen Bay	16x	426772	8370965
CMDI13-17	July 21, 2013	calcite	Middle Allen Bay	16x	429374	8372935
MARCASITE						
CMDI13-02	july 17, 2013	marcasite	crater-fill	16x	427482	8367016
CMDI13-04	July 18, 2013	marcasite	Eleanor River	16x	427896	8365778
CMDI13-06	July 18, 2013	marcasite	Eleanor River	16x	427711	8365511
CMDI13-38	July 25, 2013	marcasite	Bay Fiord	16x	426834	8371166
GYPSUM						
CMDI13-03	july 17, 2013	gypsum vug	crater-fill	16x	427905	8368344
CMDI13-41	July 27, 2013	selenite vein	Middle Bay Fiord	16x	426310	8363613
CMDI13-42	July 27, 2013	selenite vein	Middle Bay Fiord	16x		
CMDI13-43	July 27, 2013	selenite vein	Middle Bay Fiord	16x	426006	8363366
CMDI13-44	July 28, 2013	selenite vein	Middle Bay Fiord	16x	428900	8369285
CMDI13-45	July 27, 2013	selenite vein	Middle Bay Fiord	16x	429039	8370122
CMDI13-46	July 27, 2013	selenite vein	Middle Bay Fiord	16x	428556	8369743
rg-hmp-13-69	July 27, 2013	selenite vein	Middle Bay Fiord	16x	428624	8369631
CMDI13-20	July 21, 2013	sulfate	Lower Allen Bay - or Thumb Mountain	16x	426618	8375105
CMDI13-23	July 22, 2013	silica crust	Eleanor River	16x	424592	8366568
QUARTZ						
CMDI13-07	July 18, 2013	quartz	Eleanor River	16x	427295	8365771
CMDI13-08	July 19, 2013	quartz crust?	Eleanor River	16x	424957	8364798
CMDI13-09	July 19, 2013	quartz crust?	Eleanor River	16x	424247	8364884
CMDI13-13	July 19, 2013	silica crust	Eleanor River	16x	425824	8371878

Curriculum Vitae

Cassandra Marion

EDUCATION

2020: Western University, Institute for Earth and Space Exploration; Department of Earth Science, London, ON
Ph.D. Earth Science / Planetary Science

2009: Memorial University of Newfoundland, Department of Earth Sciences, St. John's, NL
M.Sc. Geology

2005: University of Ottawa, Department of Earth Sciences, Ottawa, ON
B.Sc. Honours Geology (completed in French)

HONOURS AND AWARDS

- 2018: Mineralogical Association of Canada Travel Award ($800)
- 2015: Northern Scientific Training Program (NSTP) Award ($3600)
- 2015-2017: NSERC CGS-Doctoral ($70,000)
- 2013-2014: Queen Elizabeth II Graduate Scholarship ($15,000)
- 2013: Northern Scientific Training Program (NSTP) Award ($3000)
- 2013: ASTRO-CPSX Travel Award ($1000)
- 2013: Lunar and Planetary Institute Career Development Travel Award ($1000)
- 2012: NSERC Collaborative Research and Training Experience (CREATE) Doctoral Fellowship ($8000/yr for 2 years + $1000/travel)
- 2012: Northern Scientific Training Program (NSTP) Award ($2405)
- 2009: Fellow of the School of Graduate Studies, Memorial University of
- Newfoundland, Canada
- 2008: Northern Scientific Training Program (NSTP) Award ($2800)
- 2007: Travel Grant, Canadian Space Agency, 58th International Astronautical
- Congress Hyderabad, India ($3100)
- 2004-2005: J.P. Bickell Foundation Geology Scholarship ($2000)
- 2004: World Petroleum Congresses Scholarship, Millennium Foundation ($1000)
- 2003-2004: Hogarts Geology Grant ($500)

WORK AND TEACHING EXPERIENCE

- **2019**: CanMoon Lunar Analogue Mission Operations Manager

Institute for Earth and Space Exploration, University of Western Ontario, London, Ontario, Canada.

- **2018**: Course Design and Instructor, X-Ray Fluorescence Spectroscopy for Acc. Masters Program

Dept. of Earth Sciences, University of Western Ontario, Canada

- **2012-2020**: Teaching Assistant, Dept. of Earth Sciences, University of Western Ontario, Canada

Courses: Introductory field mapping techniques; Catastrophic Events in Earth's History; Earth Science Seminar for graduate students; Education and Public Outreach for the Institute for Earth and Space Exploration

- **2010-2012**: Project Manager - Research Technologist
Impacts, lunar analogue mission to the South Pole-Aitken Basin analogue mission
Institute for Earth and Planetary Science (formerly CPSX), University of Western Ontario, London, Canada.

- **2009–2010**: Research Assistant and Coordinator
Centre for Planetary Science and Exploration (now the Institute for Earth and Space Exploration) Depts. of Earth Sciences and Physics and Astronomy, University of Western Ontario, London, Canada

- **2008-2009**: Science Technician - Electron Backscattered Diffraction (EBSD)
CREAIT Network: Microanalysis Facility, Memorial University of Newfoundland, Canada

- **2006-2008** Teaching Assistant
Dept. of Earth Sciences, Memorial University of Newfoundland, Canada
Courses: Earth Systems; Mineralogy and Petrography; High Temperature Geochemistry and Igneous Petrology.

- **2004**: Field Assistant, Caribou Mountains, British Columbia, Canada
Windermere Consortium, University of Ottawa, Canada.

SELECTED PUBLICATIONS

BOOK CHAPTERS:
Osinski G. R., Grieve R. A. F., **Marion C**., and Chanou A. 2013. Impact melt rocks and glasses. In: Impact Cratering: Processes and Products (Eds. Osinski G. R. and Pierazzo E.). Wiley Blackwell: Oxford. pp. 125–145.

ARTICLES IN REFEREED JOURNALS:
Osinski G.R. et al. 2019. The CanMars Mars Sample Return Analogue Mission. Planetary and Space Science 166: 110-130.

Zylberman W., Quesnel Y., Rochette P., Osinski G.R., **Marion C.,** Gattaccecca J. 2017. Hydrothermally enhanced magnetization at the center of the Haughton impact structure? Meteoritics & Planetary Science 52 (10): 2147-2165.

Greenberger R.N., Mustard J.F., Osinski G.R., Tornabene L.L., Pontefract A., **Marion C.L**., Flemming R.L., Wilson J.H. and Cloutis E.A. 2016. Hyperspectral mapping of alteration assemblages within a hydrothermal vug at the Haughton impact structure, Canada. Meteoritics & Planetary Sceince. 51(12): 2274-2292.

Hervé G., Gilder S.A, **Marion C.L**., Osinski G.R., Pohl J., Peterson N., Sylvester P.J. 2015. Paleomagnetic and rock magnetic study of the Mistastin Lake impact structure (Labrador, Canada): Implications for geomagnetic perturbation and shock effects. Earth and Planetary Science Letters.417: 151-163.

Antonenko I., Osinski, G.R., Battler M., Beauchamp M., Cupelli L., Chanou A., Francis R., Mader M.M., **Marion C**., McCullough E., Preston L.J., Shankar B., Unrau T., and Veillette D. 2012. Issues of geologically-focused situational awareness in robotic planetary missions: lessons from an analogue mission at Mistastin Lake Impact structure, Labrador, Canada. Advances in Space Research. 52 (2): 272-284.

Moores J.E. et al. 2012. A Mission Control Architecture for robotic lunar sample return as field tested in an analogue deployment to the Sudbury impact structure. Advances in Space Research 50: 12: 1666-1686.

Marion C.L. and Sylvester P.J. 2010. Composition and heterogeneity of anorthositic impact melt at Mistastin lake crater, Labrador. Planetary and Space Science 58: 552-573.

Osinski G. R., Grieve R. A. F., Collins G. S., **Marion C**., and Sylvester P. 2008. The effect of target lithology on the products of impact melting. Meteoritics & Planetary Science 43:12:1939–1954.

ABSTRACTS AND PRESENTATIONS

*__Marion C. L.,__ Osinski G.R., Bourassa M., Caudill C. M., Cloutis E. A., Christofferson P., Hill P. J. A., Morse Z. R., Newman J. D., Pilles E. A., Simpson S. L., Tornabene L. L. and Xie T. 2020. Overview of the CanMoon Lunar Sample Return Analogue Mission (abstract #2349). 51st Lunar and Planetary Science Conference, Woodlands, Texas, March 2020.

*__Marion C. L__., Morse Z. R., Newman J. D., Pilles E. A., Hill P. J. A., Osinski G. R., Cloutis E.A., Caudill C.M., Simpson S. L. and Xie T. 2020 Shift handovers for real-time lunar operations: methods from the CanMoon analogue mission (abstract #2400) 51st Lunar and Planetary Science Conference, Woodlands, Texas, March 2020.

*__Marion C.L__., Osinski G.R., Linnen R.L. An investigation of hydrothermal carbonate and quartz using combined microanalysis and cathodoluminescence at the Haughton impact structure. Resources for Future Generations,Vancouver 2018

*__Marion C.L.__, Osinski G.R., Linnen R.L., Zylberman W., Rochette P., Grieve R.A.F., Quesnel Y., Gattacceca J. A crystalline impact melt in drill core, Haughton Impact Structure? Women in Planetary Science and Exploration, Toronto, 2018.

*__Marion C.L__., Osinski G.R., Linnen R.L., Zylberman W., Rochette P., Grieve R.A.F., Quesnel Y., Gattacceca J. Textural evidence for impact melt in drill core at the Haughton Impact Structure, Nunavut, Canada. (abstract #2173) 47th Lunar and Planetary Science Conference, The Woodlands, Texas, March 2016.

*__Marion C.L.__, Osinski G.R., Grieve R.A.F., Bailey J., Péntek A., Smith D. and Clayton J. 2013. Mapping Sudbury Breccia in the North Range Footwall, Sudbury Impact Structure, Canada. Large Meteorite Impacts and Planetary Evolution V, Sudbury, Ontario, Canada.

Mader M.M., **Marion C.L**., Osinski G.R.O., Pickersgill A., Singleton A. and Tornabene, L.L. 2013. A Systematic multi-year Field Campaign at the Mistastin Lake Impact Structure, Labrador. Large Meteorite Impacts and Planetary Evolution V, Sudbury, Canada.

*__Marion C.L__., Osinski G.R., Linnen R.L. 2013. Hydrothermal Mineralization at the Prince Albert Impact Structure, Victoria Island, Canada. GACMAC Winnipeg, Canada.

*__Marion C.L.__, Osinski G.R., Linnen R.L. 2013. Characterization of hydrothermal mineralization at the Prince Albert impact structure, Victoria Island, Canada. (abstract #1635) 44th Lunar and Planetary Science Conference, Houston, Texas, March 2013.

*Osinski G.R., Abou-Aly S., Francis R., Hansen J., Marion C.L. and Pickersgill A.E. (2013) The Prince Albert impact structure, NWT Canada: 1 New 28-km diameter complex impact structure. (abstract #2099) 44th Lunar and Planetary Science Conference, Houston, Texas, March 2013.